Controls of sedimentary facies and diagenesis on reservoir and thermal properties in coal-bearing Upper Carboniferous siliciclastic rocks

Zur Erlangung des akademischen Grades eines

Doktors der Naturwissenschaften (Dr. rer. nat.)

von der KIT-Fakultät für Bauingenieur-, Geo- und Umweltwissenschaften des Karlsruher Instituts für Technologie (KIT)

genehmigte

DISSERTATION

von

Jonas Greve

aus Damme

Tag der mündlichen Prüfung: 24.April 2024
Erster Gutachter: Prof. Dr. Christoph Hilgers
Zweiter Gutachter: Prof. Dr. Harald Stollhofen

Karlsruhe (2025)

Acknowledgments

I would like to express my deep gratitude to Christoph Hilgers for his exceptional way of teaching Geology. His guidance, support, and enthusiasm for novel concepts and methods have been instrumental in shaping my doctoral thesis. Through numerous lengthy discussions, he has constantly inspired fresh ideas and motivated me for future tasks. Additionally, I am immensely grateful to him for making my research experience in Karlsruhe truly worthwhile.

Harald Stollhofen, who graciously served as the second referee for this thesis is also truly thanked. His profound knowledge and expertise greatly contributed to enhancing certain aspects of this work.

A special mention goes to Benjamin Busch for his invaluable introduction to diagenesis and the countless hours of engaging discussions we have had on various topics, ranging from sedimentology to structural geology. His optimistic and supportive attitude has promoted an encouraging work environment, and his careful reviews of my manuscripts significantly improved their quality. I am grateful for his patience in providing explanations in front of the microscope and addressing my numerous administrative challenges. Your commitment to teaching Geology and your attitude to work always inspired me.

I want to express my appreciation to the entire Structural Geology group at KIT for their contribution to making this journey an enjoyable experience. I am thankful to Martin von Dollen for his precise thin-section preparation, which has been indispensable for my research. I would also like to thank Ulrike Brecht for her guidance throughout the bureaucratic processes at KIT. To Felix Allgaier, Dennis Quandt, Bruno Mendes, and Agnes Kontny I am grateful for the insightful discussions we have had on geology and the shared joys of life, either in the field or in front of the coffee machine.

I extend my sincere gratitude to the Geological Survey of North Rhine-Westphalia for kindly providing access to the core material examined in this study and granting permission for sampling of the drill core and use of their laboratories. I would also like to acknowledge my colleagues at the Geological Survey of the former department 13 for their delightful company and enlightening discussions about geology as well as their help with any kind of problem. With their deep insights into the geology of the Upper Carboniferous Sascha Sandmann and Volker Wrede helped me to understand the regional geology of the Ruhr Basin. In particular, I am thankful to Mathias Knaak and Christoph Hartkopf-Fröder for their thorough review and valuable comments on my publications.

For their invaluable assistance during sample preparation and measurements, I extend my gratitude to Angelika Olders, Selim Gülsen, and Nina Pochorow. Additionally, I would like to express my appreciation to Jörg Schardinel for his exceptional camera skills, which greatly enhanced the visual aspect of this work. My sincere thanks also go to Dariusz Klugel for his invaluable assistance in the drill core archive.

I am grateful to the Federal Ministry of Education and Research, Germany (FKZ 03G0893A) for the research funding that has enabled this work.

Finally, but most importantly, I want to express my heartfelt appreciation to my family and friends for their unwavering support and presence during these challenging times. Their constant encouragement has been invaluable and has made this journey more pleasant.

Most of all, thank you Estefi.

Without the numerous night shifts, scientific discussions, and your support this thesis would have been much more demanding.

Abstract

The Upper Carboniferous of the Ruhr Basin, historically synonymous with coal mining, has transitioned into a region of multifaceted subsurface potential, including mine flooding and post-mining applications. This potential relies on the distribution of porosity and permeability as well as permeable faults and fractures in the targeted rock, facilitating fluid flow. Understanding the factors influencing permeability, ranging from micron-scale coatings to kilometer-scale bedding variations, promises better exploration success. Particularly, subsurface data provide valuable insights into these factors, as they display in-situ conditions of rock formations. A key novelty of this study is the systematic quantification of reservoir properties of the Upper Carboniferous of the Ruhr Basin based on drill core analyses, establishing a robust correlation with sedimentary attributes. While these formations have traditionally been classified as tight, their reservoir characteristics had not been extensively measured or systematically linked to lithological and diagenetic controls, providing a new framework for assessing their spatial variability and reservoir potential. This study focuses on subsurface samples from three drill cores across different stratigraphic substages particularly the Westphalian A (Langsettian) and Westphalian B (Duckmantian), using petrophysical, petrographical, and geochemical data.

The studied 270 m core material exhibits fourth-order delta sequences of coarsening- and fining-upward cycles in an overall shallowing upward trend. Thick sandstone beds are associated with the delta front, while mudstones and siltstones correspond to the lower delta plain and coal seams (up to some meters thick) are linked to wetland environments of the lower delta plain.

Upper Carboniferous sandstones and siltstones are generally tight (mean porosity 5.4 %; mean permeability 0.28 mD) but show significant heterogeneity in reservoir quality. The reservoir quality of these siliciclastics is largely controlled by sedimentary attributes, such as grain size, mineralogical composition, and diagenesis. Mechanical compaction is the dominant mechanism accounting for porosity loss (mean COPL 38.8 %) and poor reservoir properties, particularly in fine-grained lithologies containing abundant ductile rock fragments of the lower delta plain. Sandstones of the delta front exhibit slightly enhanced reservoir properties (> 8 %; > 0.01 mD) related to the development of intragranular dissolution porosity notably in feldspars during burial diagenesis (1.5 to 6 %). Further, sandstones are characterized by lower volumes of ductile rock fragments (< 38 %). In contrast, siltstones, containing fewer feldspars and unstable rock fragments, develop lower intragranular dissolution porosity while higher volumes of ductile rock fragments facilitate mechanical compaction (ICOMPACT > 0.99). Cementation has a minor impact on reservoir properties. Thus, the volumes of ductile rock fragments and feldspar or feldspar-rich rock fragments have large impacts on reservoir properties.

Generally, a change in mineralogical composition from litharenites to lithic subarkoses corresponds to an increase in grain size from silt to sandstone and an associated general increase in porosity.

Dissolution porosity in lithic subarkoses largely contributes to measured plug porosity and enhances reservoir properties. The dissolution porosity mostly relates to detrital K-feldspar and plagioclase grains resulting from acidic pore water from organic matter maturation and affects low present-day feldspar contents (mean 6.7 %). However, enhanced porosity in sandstones does not necessarily translate to increased permeability, since authigenic clays (i.e., kaolinite and illite) or late diagenetic carbonate cementation (i.e., siderite and ferroan dolomite/ankerite) clog secondary porosity.

Beyond influencing reservoir quality, these diagenetic processes also impact geomechanical and thermal properties. Low compressional wave velocities in sandstones of the delta front (2886 m/s) negatively correlate with high porosities (15.6 %). Likewise, porosity has major control over thermal conductivity with porous sandstones exhibiting values as low as 2.3 W/(m×K). For less porous samples, thermal conductivity becomes less dependent on porosity but mineralogy plays a more significant role. Generally, the high values of up to 5.3 W/(m×K) seem promising for geothermal applications, particularly when compared to available literature data.

The Si/Al ratio has been shown to be a reliable proxy for assessing grain sizes and may be a convenient tool for further exploration. The study also identified SiO_2, Al_2O_3, Fe_2O_3, MgO and K_2O contents from XRF analyses as promising proxies for quartz and phyllosilicate, helping to distinguish between sandstones and siltstones and to estimate reservoir properties.

Characterizing lithofacies types can offer a means to classify rock units according to differing styles of sedimentation and subsequent diagenetic overprint. Furthermore, the results of this study imply that grain size-based classification is superior to facies association classification in assessing geothermal potential. Nevertheless, fluid flow, whether for mine flooding, geothermal applications, or gas extraction will primarily rely on mined drifts and shafts. Natural faults may often be tight and natural fracture systems are confined to tight sandstone intervals. Considering the rock composition of ductile behaving schists and shales (often forming a pseudomatrix), quartz and minor feldspar, alteration of tight rocks due to mine flooding is unlikely.

Ultimately, this study provides an integrated framework for evaluating tight siliciclastic reservoirs of the Ruhr Basin, offering new insights into the interplay of sedimentary facies, diagenesis, and reservoir properties. The findings have direct implications for subsurface utilization strategies, particularly for post-mining geothermal applications, tight gas exploration, and fluid migration modeling in similar geologic settings worldwide.

Kurzfassung

Das Oberkarbon des Ruhrbeckens, historisch gleichbedeutend mit dem Kohlebergbau, hat sich zu einer Region mit vielfältigen Potentialen des Untergrunds entwickelt. Diese Potenziale hängen von der räumlichen Verteilung der Porosität und Permeabilität sowie von permeablen Störungen und Brüchen im Gestein ab, die den Fluidfluss steuern. Ein besseres Verständnis der Faktoren, die die Permeabilität beeinflussen – von mikroskaligen Kornüberwüchsen bis hin zu kilometerskaligen Änderungen der Lithofazies – ist daher entscheidend für eine verbesserte Exploration. Insbesondere Untergrunddaten bieten wertvolle Einblicke, da sie die in-situ Bedingungen der Gesteinsformationen widerspiegeln. Eine wesentliche Neuerung dieser Studie ist die systematische Quantifizierung der Reservoireigenschaften des Oberkarbons im Ruhrbecken anhand von Bohrkernanalysen, wodurch eine robuste Korrelation mit sedimentären Attributen hergestellt wird. Während diese Formationen traditionell als dicht klassifiziert wurden, fehlten bislang umfassende Messdaten zur räumlichen Variabilität der Reservoircharakteristika sowie eine systematische Verknüpfung mit lithologischen und diagenetischen Steuerungsfaktoren, was nun durch diese Arbeit adressiert wird.

Die Studie konzentriert sich auf Bohrkernproben aus drei Bohrungen, die verschiedene stratigraphische Einheiten des Westfal A (Langsettium) und Westfal B (Duckmantium) umfassen und kombiniert petrophysikalische, petrographische, geomechanische und geochemische Analysen. Die 270 m Kernmaterial zeigen zyklische Deltaablagerungen der 4. Ordnung mit Sohl- und Dachbankzyklen mit einem generell regressiven Trend. Mächtige Sandsteinlagen sind mit der Deltafront assoziiert, während Ton- und Siltsteine mit dem Prodelta bzw. der unteren Deltaebene in Verbindung gebracht werden. Mehrere Meter mächtige Kohleflöze sind den Überschwemmungsgebieten der unteren Deltaebene zugeordnet.

Die Sandsteine und Siltsteine des Oberkarbons sind im Allgemeinen undurchlässig (mittlere Porosität 5.4 %; mittlere Permeabilität 0.28 mD), weisen jedoch eine erhebliche Variabilität in ihren Reservoireigenschaften auf. Diese werden maßgeblich durch sedimentäre Eigenschaften wie Korngröße und mineralogische Zusammensetzung sowie durch diagenetische Alterationen gesteuert. Die mechanische Kompaktion stellt den dominierenden Mechanismus für den Porositätsverlust (mittlere mechanische Kompaktion 38,8 %) dar und führt insbesondere in den feinkörnigen Lithologien mit hohen Anteilen duktiler Gesteinsfragmente der unteren Deltaebene zu ungünstigen Reservoirbedingungen. Die Sandsteine der Deltafront weisen hingegen geringfügig verbesserte Reservoireigenschaften (> 8 %; > 0.01 mD) auf, die auf die Entwicklung intragranularer Lösungsporosität (1.5 bis 6 %), insbesondere in Feldspäten, während der Versenkung zurückzuführen sind. Zudem sind die Sandsteine durch geringere Volumina an duktilen Gesteinsfragmenten (< 38 %) charakterisiert. Im Gegensatz dazu entwickeln Siltsteine, die weniger Feldspäte und instabile Gesteinsfragmente enthalten, eine geringere intragranulare

Lösungsporosität, während höhere Volumina duktiler Gesteinsfragmente die mechanische Kompaktion begünstigen (ICOMPACT > 0.99). Zementation hat nur einen geringen Einfluss auf die Reservoireigenschaften. Somit haben die Volumina an duktilem Gesteinsfragmenten sowie Feldspat- oder feldspatreichen Gesteinsfragmenten einen entscheidenden Einfluss auf die Reservoirqualität.

Generell korreliert eine Veränderung der mineralogischen Zusammensetzung von Lithareniten zu lithischen Subarkosen mit einer Zunahme der Korngröße von Silt zu Sandstein, welche ebenfalls mit einem allgemeinen Anstieg der Porosität verbunden ist.

Die Lösungsporosität tritt hauptsächlich in detritischem Kalifeldspat und Plagioklas auf, die durch saure Porenwässer aus der Reifung organischen Materials entstanden ist und zu den niedrigen rezenten Feldspatgehalten (durchschnittlich 6.7 %) führt. Eine erhöhte Porosität führt jedoch nicht zwangsläufig zu einer verbesserten Permeabilität, da authigene Tone (d.h. Kaolinit und Illit) sowie spätdiagenetische Karbonate (d.h. Siderit und eisenhaltiger Dolomit/Ankerit) die sekundäre Porosität ausfüllen.

Neben der Reservoirqualität beeinflussen diese diagenetischen Prozesse auch die geomechanischen und thermischen Gesteinseigenschaften. Niedrige Kompressionswellengeschwindigkeiten in den Sandsteinen der Deltafront (2886 m/s) korrelieren negativ mit hohen Porositäten (15.6 %). Ebenso hat die Porosität einen wesentlichen Einfluss auf die Wärmeleitfähigkeit, wobei poröse Sandsteine minimale Werte von 2.3 W/(m×K) aufweisen. In weniger porösen Proben wird die Wärmeleitfähigkeit jedoch weniger von der Porosität, sondern stärker von der Mineralogie beeinflusst. Generell erscheinen die hohen Werte von bis zu 5.3 W/(m×K) vielversprechend für geothermische Anwendungen, insbesondere im Vergleich zu verfügbaren Literaturwerten.

Das Si/Al-Verhältnis hat sich als zuverlässiger Proxy zur Korngrößenabschätzung erwiesen und stellt ein praktisches Werkzeug für zukünftige Explorationsstudien dar. Zudem wurden SiO_2, Al_2O_3, Fe_2O_3, MgO und K_2O Gehalte aus XRF-Analysen als potenzielle Proxys für Quarz- und Phyllosilikatgehalte identifiziert, die dabei helfen, Sandsteine und Siltsteine zu unterscheiden und Reservoirparameter abzuleiten.

Die Charakterisierung der Lithofaziestypen stellt eine wertvolle Grundlage dar, Gesteinseinheiten anhand unterschiedlicher Sedimentationsbedingungen und diagenetischer Überprägung zu klassifizieren. Darüber hinaus deuten die Ergebnisse darauf hin, dass eine korngrößenbasierte Klassifikation gegenüber der Faziesassoziation überlegen ist, insbesondere zur Bewertung des geothermischen Potenzials. Dennoch wird der Fluidfluss – sei es für die Bergwerksflutung, Geothermie oder Gasförderung – primär auf künstliche Infrastrukturen wie Strecken und Schächte angewiesen sein. Natürliche Störungen sind oft undurchlässig, und natürliche Klüftungssysteme beschränken sich auf dichte Sandsteinhorizonte. Aufgrund der Gesteinszusammensetzung aus duktilen Schiefer- und Tonsteinfragmenten (die oft eine Pseudomatrix

ausbilden), Quarz und geringem Feldspatgehalt ist eine Veränderung der Gesteine durch die Grubenflutung unwahrscheinlich.

Letztendlich liefert diese Studie einen integrierten Rahmen zur Bewertung dichter siliziklastischer Reservoire im Ruhrbecken und bietet neue Erkenntnisse über das Zusammenspiel sedimentärer Fazies, Diagenese und Reservoirqualitäten. Die Ergebnisse haben direkte Implikationen für die untertägige Nutzung, insbesondere für geothermische Nachbergbaunutzung, Tight-Gas-Exploration und Fluidmigrationsmodellierung in vergleichbaren geologischen Systemen weltweit.

Contents

Declaration of originality

Chapter 2: As the first author during his PhD studies, Jonas Greve performed all sample acquisition, sedimentary core descriptions, petrophysical and thermal conductivity measurements and interpretation. He wrote the entire article with inputs from Benjamin Busch, Dennis Quandt, Christoph Hartkopf-Fröder, Mathias Knaak, and Christoph Hilgers. The discussions with all co-authors contributed to this manuscript.

Chapter 3: As the first author, Jonas Greve performed all sample acquisition, point counting, petrophysical measurements, x-ray fluorescence (XRF) and X-ray diffraction (XRD) analysis and interpretation. He wrote the entire manuscript with inputs from Benjamin Busch, Dennis Quandt, Mathias Knaak and Christoph Hilgers. The discussions with all co-authors contributed to this manuscript.

Chapter 4: As the first author, Jonas Greve performed all sample acquisition, point counting, petrophysical measurements, x-ray fluorescence (XRF), data analysis, and interpretation. He wrote the entire manuscript with inputs from Benjamin Busch, Dennis Quandt, Mathias Knaak and Christoph Hilgers. The discussions with all co-authors contributed to this manuscript.

1 Introduction

1.1 Motivation

The Upper Carboniferous has been fundamental for the European energy supply in recent decades (Andruleit et al., 2012; Littke et al., 2011; Littke & Zieger, 2019) not only because of its coal-bearing nature but also due to the gas reservoirs hosted in siliciclastic reservoirs (e.g., Besly, 1998; Kombrink, 2008; Teichmüller, 1986). Beyond the extraction of hydrocarbons, age-equivalent Upper Carboniferous siliciclastics contain geothermal resources in the Ruhr Basin (Bussmann et al., 2019). Moreover, an understanding of fluid migration in the subsurface is essential in assessing the performance of geothermal resources but also in forecasting the effect of rising mine water levels following the cessation of coal mining and enabling the former. Fluid migration is a function of reservoir quality (porosity and permeability), while heat conductivity is controlled by petrophysical and mineralogical properties. Thus, assessing rock composition and their diagenetic alteration in relation to lithotypes will facilitate a more detailed understanding of migration pathways and future reservoir utilization. Reservoir quality is influenced by differences in detrital composition and authigenic phases affecting the available pore space and permeability. Understanding the relationship between the reservoir quality and geological attributes of the reservoir is crucial to ensure operational efficiency (Becker et al., 2019; Busch et al., 2019).

The Ruhr Basin, situated in northwestern Germany, represents a Variscan foreland molasse-type basin that developed in response to the Late Carboniferous orogenic processes (Drozdzewski, 1993). The basin hosts a thick, siliciclastic sedimentary succession exceeding 4000 m, primarily composed of claystones, siltstones, sandstones, and interbedded coal seams, deposited in a fluvio-deltaic to paralic system (Drozdzewski, 1992; Süss et al., 2007). Sedimentation was governed by a complex interplay of subsidence dynamics, high sediment supply, and glacio-eustatic sea-level fluctuations, resulting in coarsening-upward sequences that reflect fourth- and fifth-order deltaic cycles (Rygel et al., 2008). The depositional framework encompasses delta-front sandstones, lower delta plain siltstones, wetland-associated mudstones, and prodelta claystones, each exhibiting distinct textural, mineralogical, and diagenetic characteristics that exert a primary control on reservoir properties (Guion & Fielding, 1988).

This study employs several analytical techniques applied to drill core samples from three boreholes to establish a quantitative correlation between sedimentological attributes, diagenetic overprint, and reservoir quality. A combination of petrophysical (porosity and permeability measurements), petrographic (thin-section analysis, point counting), and geochemical techniques (X-ray fluorescence (XRF), X-ray diffraction (XRD)) is applied to characterize the sedimentary and diagenetic controls on porosity and permeability

(e.g., Quandt et al., 2022a). Furthermore, compressional wave velocity (vP) and thermal conductivity analyses provide additional insights into the geomechanical and thermal properties of these lithologies.The diagenesis of siliciclastic rocks and its implications for reservoir quality have gathered substantial attention in past decades (e.g., Ajdukiewicz & Lander, 2010; Ehrenberg, 1990; Gaupp & Okkerman, 2011; Morad et al., 2000). Given the limitations of purely petrophysical assessments in accounting for complex mineralogical and temporal influences during burial on porosity-permeability relationships, an integrated approach that combines petrographic and petrophysical data is essential to understand reservoir quality controls comprehensively (Busch et al., 2020; Monsees et al., 2020; Schmidt et al., 2021). Especially in siliciclastic reservoirs, the inherent heterogeneity, i.e., variations in sedimentary facies, lithology, and depositional settings, presents a challenge in the accurate prediction of reservoir properties.

Grain parameters such as grain size, sorting, shape, and mineralogy (e.g., clay matrix content) determine the initial porosity and permeability of uncompacted sands (Beard & Weyl, 1973) as geometry and connectivity of the initial pore space is strongly dependent on these parameters (Fraser, 1935). In addition, sedimentary structures (e.g., cross-bedding, planar lamination) resulting from specific transport mechanisms and energies can impact directional permeabilities relative to the bedding. By incorporating lithology with sedimentary structures, lithofacies and corresponding depositional contexts can be classified for adequate characterization (Miall, 1977). In deltaic to shallow marine environments, the rapid changes in depositional facies caused by the interaction between sediment supply and sea level fluctuations affect the accommodation space and influence the lithofacies assemblages (Allen, 1965; Süss et al., 2007). This determines the diagenetic pathway and impacts the quality of reservoir rocks.

Diagenesis in siliciclastic sediments involves compaction and cementation processes. Compaction is a function of the detrital assemblage's response to overburden loading and temperature through grain rearrangement and pressure-solution processes (chemical compaction). Sediment compaction is generally quantified by the intergranular volume (IGV) (Ehrenberg, 1989; Paxton et al., 2002). Compaction is enhanced by ductile components, with mica-/clay-rich rock fragments particularly susceptible to it. Mica and illite also promote chemical compaction when in contact with quartz grains (Fig. 1.1 A), whereas compaction can be limited by pore-filling cements (Fig. 1.1 B). While cementation can occur throughout all burial stages, governed by temperature, pressure, and pore water chemistry, its distribution depends on the depositional environment, organic content, and rock texture (Morad et al., 2000). Furthermore, faults or fractures can act as fluid conduits, cementing the adjacent host rock (Busch et al., 2019). Point counting data enables the determination of whether compactional (COPL) or cementational porosity loss (CEPL) is the prevailing process responsible for porosity reduction (Lundegard, 1992) and quantifying correlations between compaction style and rock properties.

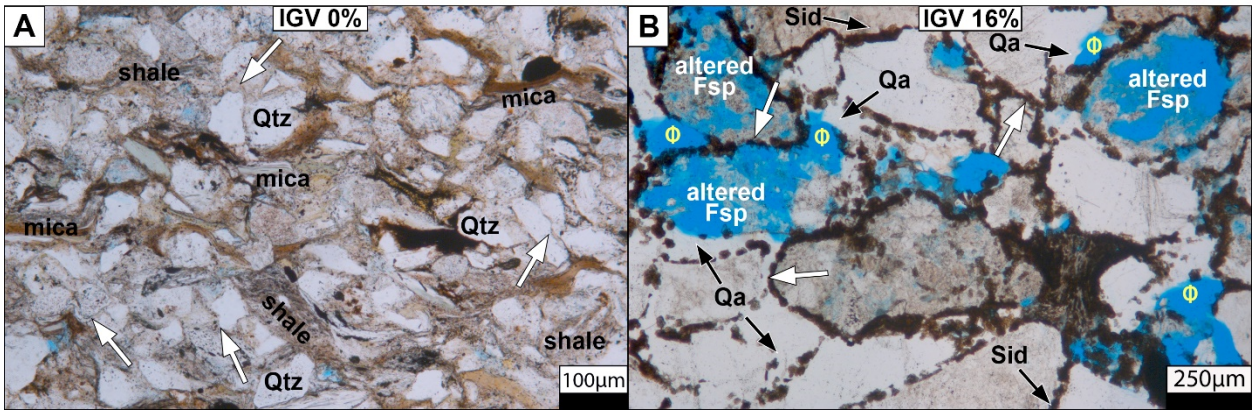

Figure 1.1 (**A**) Abundant micas and pseudomatrix, e.g., deformed shale clasts. Low porosity results from significant mechanical compaction of the grain framework, particularly the frequent ductile components have led to the formation of concavo-convex to sutured grain contacts (arrows). (**B**) The sample is distinguished by less frequent shale clasts in contrast to relatively rigid quartz (Qtz) or feldspar grains (Fsp). Siderite (Sid) and quartz (Qa) cement, partially filling some pore space, primarily support the grain framework. Compaction is mitigated, as evidenced by prevalent point and long grain contacts (arrows) and preserved primary porosity (Φ).

Detrital clasts also affect diagenesis because of their variable resistance against dissolution, i.e., feldspars and certain rock fragments are prone to dissolution (Fig. 1.1 B) by meteoric waters or by the release of acidic pore fluids during all stages of diagenesis (Gaupp et al., 1993). Therefore, the volume of feldspar dissolution is another critical aspect, either to result in porosity enhancement or to source authigenic clay mineral precipitation, such as kaolinite or illite (Lanson et al., 2002; Wilkinson et al., 2001).

The sediment composition and texture as well as the lithification of sediment into sedimentary rock carries substantial implications not only for reservoir quality but also for mechanical properties. This is particularly significant in the rock`s response to pressure variations induced by extraction or injection of fluids, defining the stress conditions under which the reservoir rock may undergo deformation and potential fracturing (Pijnenburg et al., 2019; Zhang et al., 2016). Especially during reservoir stimulation attempts, pivotal for tight reservoirs, through the injection of fluids the mechanical attributes are important and consequently influence reservoir performance. For the quantitative assessment of mechanical properties, the compressional wave velocity (v_P) can be determined, which is sensitive to the bulk density of rocks (controlled mostly by porosity), rather than to the mineralogical composition (Best et al., 2007; Quandt et al., 2022b; Stewart & Peselnick, 1978). Further, thermal properties, like heat conductivity are inherently interconnected with both porosity and the mineralogical composition of sandstones (Fig. 1.2 D) (Clauser & Huenges, 1995).

Regarding the Upper Carboniferous of the Ruhr Basin, the siliciclastic rocks show a range of tight matrix reservoir characteristics (Fig.1.2 A). Factors like the depositional setting, with delta front deposits dominated by sandstones exhibit higher porosity and permeability, while lower delta plain siltstones, wetland mudstones, and prodelta claystones display lower values. This relationship is further interlinked

with variations in mineralogical composition e.g., delta front deposits that are relatively enriched in feldspars and classified as lithic subarkoses, whereas higher contents of rock fragments in the other environments lead to their classification as litharenites (Fig. 1.2 B). Grain size has a further influence on reservoir properties as high porosities are associated with larger grain size (Fig. 1.2 C). A complex interaction of these factors as well as the diagenetic history and structural inventory, i.e., faulting and fracturing, complicates the efforts to predict not only the reservoir quality correctly but also other rock properties like heat conductivity and v_P (Fig.1.2 D), also controlled by petrophysical and mineralogical properties. In this work, the compressional wave velocity is rather positively correlated with the bulk density of sandstones than with their mineralogical composition, whereas thermal conductivity is correlated with both porosity and the mineralogical composition of sandstones. More quartz-rich samples generally have higher heat conductivity, as do samples with lower porosity (Fig. 1.2 D).

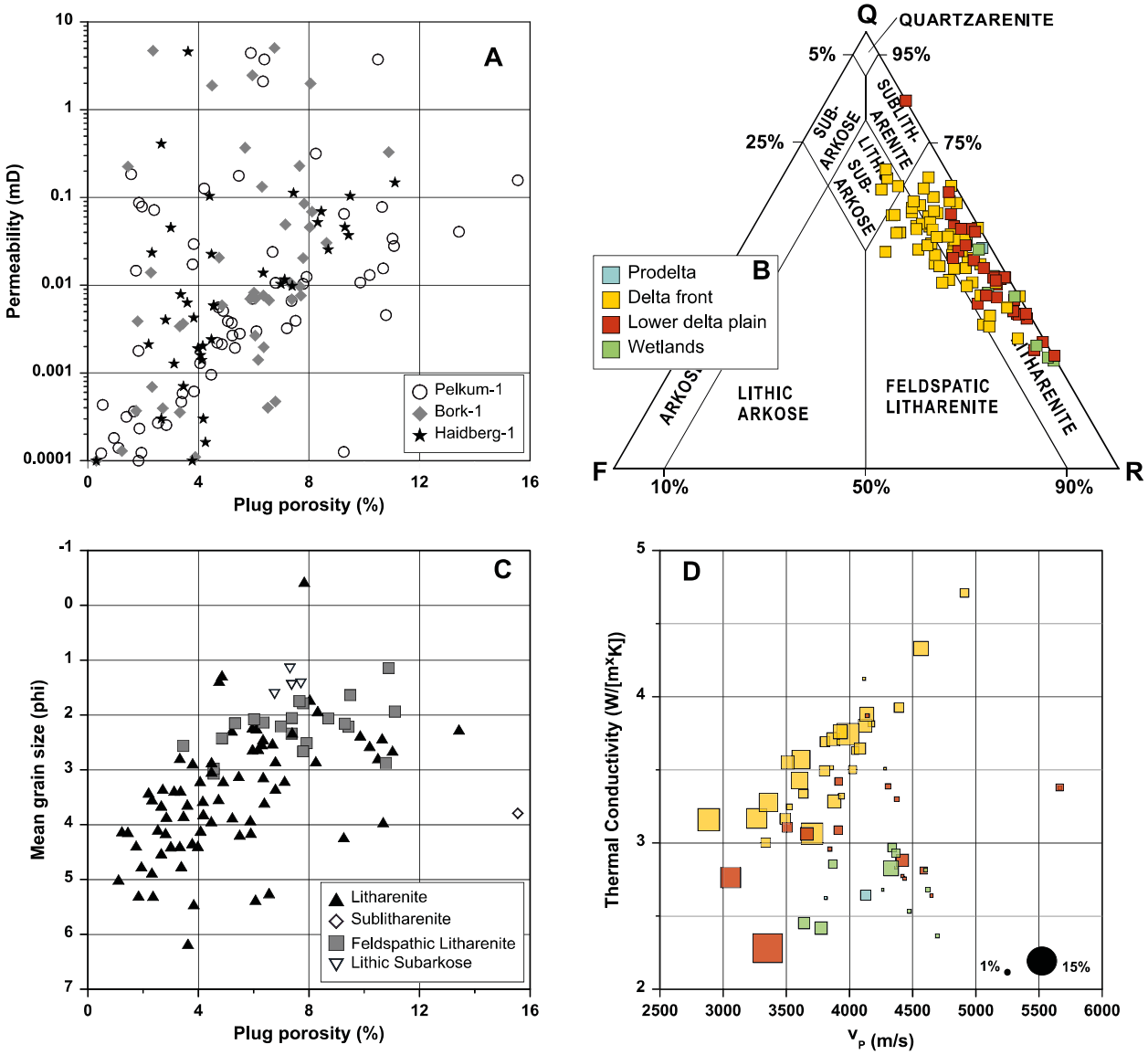

Figure 1.2 (**A**) The range of overall poor reservoir quality determined by samples in this study. (**B**) Studied samples are classified by their facies and characterized by their detrital mineralogy, showing their relationship. (**C**) Grain size plotted against porosity shows a positive correlation. (**D**) Cross plot for the depositional environments (sand dominated delta front, silt dominated lower delta plain and mud dominated wetlands and prodelta) of thermal conductivity versus v_P for dry conditions. Symbol size displays porosity values.

1.2 Aims & Objectives

This study aims to define the controlling factors that govern the reservoir quality of the Upper Carboniferous deltaic sedimentary rocks in the Ruhr Basin. Therefore, a detailed analysis of core material from three exploration wells of the eastern Ruhr Basin was performed focussing on their sedimentology and diagenesis. Furthermore, it is aimed to establish a coherent paragenetic sequence and subsequently correlate it with geological processes during its burial history. Therefore, a range of mineralogical and geochemical methods were applied to support the diagenetic data. By linking petrophysical and

petrographic data with the burial history, the reservoir quality development of the studied rocks over time is gained. This work focusses on the following four major aspects:

- Establish the relationships between sedimentary parameters and the deltaic depositional environment based on core material to evaluate the transferability of these relationships to reservoir modelling.

- Coupling petrography, permeability, porosity with compressional wave velocities (v_P), and geochemical data from X-ray fluorescence (XRF) analysis to assess the suitability of these parameters as proxies if core material is absent.

- Understanding the role of detrital mineralogy and diagenesis on mechanical and thermal parameters of sedimentary rocks.

- Establishing a uniform reservoir quality development trajectory for the Upper Carboniferous in the eastern Ruhr Area by incorporating diagenetic aspects from successive stratigraphic formations

1.3 Overview of thesis

1.3.1 Coupling heat conductivity and lithofacies of the coal-bearing Upper Carboniferous in the eastern Ruhr Basin, NW Germany (Chapter 2)

Subsurface coal mining spanning centuries has yielded a comprehensive understanding of the sedimentation patterns within Upper Carboniferous deposits (Wrede & Ribbert, 2005). A complex interplay involving rapid basin subsidence, high sedimentation rates, and eustatic sea-level fluctuations result in a cyclic clastic succession of deltaic deposits within the Variscan orogenic foredeep (Casshyap, 1975; Drozdzewski, 1992; Süss et al., 2000). In the context of the Ruhr Basin, sedimentation occurred across three distinct deltaic environments, specifically the lower delta plain including the wetlands, delta front, and subaquatic prodelta (Diessel, 1992). Types of lithofacies represent a classification scheme to characterize sedimentary deposits, including lithology and sedimentary structure (Miall, 1977). These lithofacies types are further subject to interpretation within the context of the depositional environment in which they formed. However, uncertainties persist regarding the correlation between porosity, permeability, thermal conductivity, and their association with changing sedimentary facies and mineralogy (Clauser & Huenges, 1995).

Chapter 2 examines rock properties, such as porosity, permeability, thermal conductivity, and compressional wave velocity and their relationship with sedimentary facies derived from core description

in wells Pelkum-1, Bork-1, Haidberg-1. Low compressional wave velocities are correlated with porous delta front sandstones. Moreover, the influence of porosity on thermal conductivity is a central aspect of sandstones. Nevertheless, as porosity diminishes in less porous samples, the dependence of thermal conductivity on mineralogy becomes dominant. In general, high thermal conductivity values suggest promising use of the lithology for geothermal applications. However, given the poor reservoir characteristics, the feasibility relies primarily on permeable fault and fracture networks or the abandoned mine galleries themselves.

1.3.2 The influence of sedimentary facies, mineralogy, and diagenesis on reservoir properties of the coal-bearing Upper Carboniferous of NW Germany (Chapter 3)

Porosity and permeability data from three wells within the Ruhr Basin highlight their poor reservoir quality (Greve et al., 2023). Variations in these properties are attributed to grain size differences and facies associations, with sandstone-dominated delta front deposits exhibiting the highest values. Despite studies on diagenetic sequences in the Upper Carboniferous of the Lower Saxony Basin (Becker et al., 2019; Busch et al., 2019; Wüstefeld et al., 2017), a comprehensive understanding of diagenesis and its impact on petrophysical properties of Westphalian A sandstones in the Ruhr Basin is lacking.

Based on point count data, sedimentary and diagenetic controls on reservoir properties are identified, and a paragenetic sequence for Westphalian A sandstones of well Pelkum-1 is defined. This analysis demonstrates the interrelation between varying grain sizes corresponding to distinct delta facies and shifts in mineralogical composition. Such mineralogical changes influence diagenetic alterations i.e., enhancing mechanical compaction in mud- and siltstones of the lower delta plain, wetlands, and prodelta is driven by the presence of ductile rock fragments like shale and phyllite rock fragments yielding a rapid decline in IGV during burial. In delta front sandstones lower volumes of ductile rock fragments result in less compactional porosity loss. The available pore space, not subjected to compaction, is accessible to pore-filling cements i.e., siderite and quartz overgrowth, preserving some IGV. Further, higher contents in feldspar and unstable rock fragments resulted in intragranular dissolution porosity, which enhances the total porosity. Yet, increased porosity does not necessarily lead to higher permeability since authigenic kaolinite and carbonate cement partially clog the pores. These changing mineral assemblages can also be quantified through X-ray fluorescence (XRF) analyses using the Si/Al ratio.

1.3.3 Understanding the interplay of sedimentary facies, mineralogy, and diagenesis on reservoir properties of the coal-bearing Upper Carboniferous Westphalian A and B of the Ruhr Area, NW Germany (Chapter 4)

Petrophysical insights into Upper Carboniferous siliciclastics underscore their tight reservoir characteristics. Dominant impacts on reservoir properties are identified as grain size and detrital mineralogy. A mineralogy shift was observed in tandem with increased grain size – from silt to sandstone – and is associated with an elevation in porosity and permeability (Greve et al., 2024; Quandt et al., 2022b).

Chapter 4 contributes supplemental petrophysical subsurface data from two wells within the eastern Ruhr Basin (wells Bork-1 and Haidberg-1), representing siliciclastic delta deposits of the Westphalian A and B. Employing point count data, the interplay of sedimentary and diagenetic factors governing reservoir properties can be discerned. This analysis encompasses evaluations of sedimentological attributes, detrital constituents, and textural parameters (e.g., grain size), along with a detailed assessment of prevailing authigenic phases. A paragenetic sequence based on textural relationships among these different authigenic phases establishes a uniform sequence across the Westphalian A and B. Further, dissolution porosity resulting from acidic pore waters during organic matter maturation significantly contributes to measured plug porosity and enhances reservoir qualities, particularly in sandstones. The origin of dissolution porosity primarily relates to detrital K-feldspar and plagioclase grains and results in low present-day feldspar contents. Yet, the genesis of dissolution porosity is interlinked with the provenance of silt- and sandstones within the Ruhr Basin. Additionally, to distinguish coarse-grained sections as delta front sandstones, the SiO2 content proves valuable. Conversely, the concentration of Al_2O_3, Fe_2O_3, MgO, and K_2O serves as a proxy, effectively identifying siltstones and clay minerals associated with the lower delta plain and wetland environments.

1.4 Parts of this thesis which have been published

Articles

Greve, J., Busch, B., Quandt, D., Knaak, M., Hartkopf-Fröder, C., Hilgers, C., 2023, Coupling heat conductivity and lithofacies of the coal-bearing Upper Carboniferous in the eastern Ruhr Basin, NW Germany, Journal of Applied and Regional Geology, Vol. 173(4), 673–695.

Greve, J., Busch, B., Quandt, D., Knaak, M., Hilgers, C., 2024, The influence of sedimentary facies, mineralogy, and diagenesis on reservoir properties of the coal-bearing Upper Carboniferous of NW Germany, Petroleum Geoscience, Vol. 30(1).

Greve, J., Busch, B., Quandt, D., Knaak, M., Hilgers, C., 2024, Understanding the interplay of sedimentary facies, mineralogy, and diagenesis on reservoir properties of the coal-bearing Upper Carboniferous Westphalian A and B of the Ruhr Area, NW Germany, International Journal of Earth Sciences, Vol. 113(8), 2275-2304.

Conference contributions

Greve, J., Busch, B., Quandt, D., Hilgers, C., Reservoir characterization of the coal-bearing Upper Carboniferous clastic succession, Ruhr area, Germany at DGMK Frühjahrstagung 2021 in Celle

Greve, J., Busch, B., Quandt, D., Hilgers, C., Reservoir characterization of the coal-bearing Upper Carboniferous clastic succession, Ruhr area, Germany at GeoKarlsruhe 2021 – DGGV annual conference

Greve, J., Busch, B., Quandt, D., Knaak, M., Hilgers, C., Reservoir properties of an Upper Carboniferous tight gas sandstone reservoir analogue, Ruhr Basin, NW Germany at EAGE conference and exhibition 2022 in Madrid

Greve, J., Busch, B., Quandt, D., Knaak, M., Hilgers, C., Coupling thermal conductivity and lithofacies of the coal-bearing Upper Carboniferous in the eastern Ruhr Basin, NW Germany at DGMK Frühjahrstagung 2022 in Celle

Greve, J., Busch, B., Quandt, D., Knaak, M., Hilgers, C., Coupling thermal conductivity, lithofacies and reservoir quality of the coal-bearing Upper Carboniferous in the eastern Ruhr Basin, NW Germany at GeoMinKöln 2022 – DGGV annual conference

2 Coupling heat conductivity and lithofacies of the coal-bearing Upper Carboniferous in the eastern Ruhr Basin, NW Germany

2.1 Abstract

The Ruhr Basin in Germany is one of the most extensively studied 3D rock volumes due to subsurface coal mining over the past centuries. With the final closure of the last coalfield in 2018, mine flooding was initiated and may result in induced ground movements. However, abandoned coal mines also provide the possibility for post-mining geothermal utilization. To improve the understanding of rock properties with respect to flow properties and heat flux in the Ruhr Basin, three drill cores of clastic sedimentary rocks of the Westphalian A (Langsettian) and Westphalian B (Duckmantian) were characterized and the facies analyzed. The studied 270 m core material shows 4th order sequences of coarsening- and fining-upward cycles in an overall shallowing upward trend. Up to 17 m thick sandstone beds are associated with the delta front, mudstones and siltstones are related to the lower delta plain and up to 4 m thick coal seams are linked to wetlands of the lower delta plain.

Rock properties show low compressional velocities with a minimum of 2886 m/s in sandstones of the delta front, which are negatively correlated with porosities of up to 15.6 %. Likewise, porosity is a major control on thermal conductivity with a minimum of 2.3 W/(m×K) for high porosity sandstones. For less porous samples, thermal conductivity becomes less dependent on porosity but more strongly on mineralogy. Comparing our results with accessible thermal conductivity data from North Rhine-Westphalia (NRW), the high values of up to 5.3 W/(m×K) seem promising for potential geothermal applications. Furthermore, the results of this study imply that the classification based on facies associations is less suitable than the classification based on grain sizes in order to assess the geothermal potential.

Overall, the Upper Carboniferous (Pennsylvanian) samples of this study show low porosity (mean 5.6 %) and permeability (mean 0.1 mD). Thus, fluid flow during mine flooding and potential future geothermal applications will primarily rely on permeable faults and fracture systems around the abandoned mine galleries as well as the galleries themselves.

2.2 Introduction

The Ruhr district in western Germany is a major urban region in Europe including one of the largest European district heating networks (Hannes, 1977; Schulte, 1975). Yet, it is subject to changes associated with the final closure of the last subsurface mines producing Upper Carboniferous (Pennsylvanian) coal in north-west Germany and has entered the post-mining stage (Kretschmann et al., 2017; Voß, 2018).

Post-mining in the Ruhr district is associated with subsurface mine water flooding, which can result in local stress perturbation and surface uplift and may be associated with induced microseismicity during the re-equilibration of mine waters (Rische et al., 2023). In the long term, subsurface mines in the Ruhr district offer opportunities for post-mining geothermal applications due to existing shafts and high-permeable galleries down to 1635 m depth (Balcewicz et al., 2021; Fritschle et al., 2021; Kruszewski et al., 2021; Philippe et al., 2019). Recent geothermal exploration activities aim for deep Upper Devonian and Lower Carboniferous (Mississippian) carbonate horizons in the Rhine-Ruhr area (Arndt et al., 2021) to further increase the share of geothermal energy on the German primary energy supply from currently 0.6 %, especially in the heat sector. When evaluating a geothermal system for the use of e.g., heat pump systems (Raymond, 2018), geothermal system simulations demonstrate the high sensitivity with respect to thermal conductivity (Raymond et al., 2017). However, this property varies among water saturated rocks from 0.75 to 8.1 W/(m×K) (Clauser & Huenges, 1995; their Tab. 2) and therefore needs to be understood for any geothermal application.

The Ruhr district is one of the world's best-documented subsurface 3D rock volumes due to widespread exploration and mining activity (Brix et al., 1988; Casshyap, 1975; Drozdzewski, 1992, 1993; Jessen, 1956; Krull & Wrede, 2005; Strehlau, 1990; Süss, 2005; Teichmüller & Teichmüller, 1982; Wrede & Ribbert, 2005). Thus, rock properties including thermal conductivity provide fundamental data for modelling uplift processes related to flooding and assessing the geothermal potential of the main lithologies of the Upper Carboniferous sedimentary rocks in the Ruhr district (Hahn, Jabs, et al., 2018).

A standard workflow used in industry and applied research (Busch et al., 2019; Wimmers & Koehrer, 2014) is the integration of core-based macroscopic geological elements, such as sedimentological facies, and facies associations with measured rock properties, and may be a helpful tool to predict rock properties in the absence of core data. To understand the distribution of the main lithological units and their rock properties we investigated three Upper Carboniferous (Westphalian A (Langsettian) and Westphalian B (Duckmantian) drill cores from the eastern Ruhr area (Fig. 2.1 B).

This study addresses the question if a standard workflow is required to outline how lithofacies or depositional environments can be coupled with petrophysical data and thermal conductivity. Especially this

link is crucial to the process understanding and may be a central input parameter for subsequent potential evaluation of suitable geothermal reservoirs.

2.3 Geological setting

The coal-bearing Upper Carboniferous strata of the Ruhr Basin are a 4000 m thick clastic succession of cyclically deposited clay-, silt-, and sandstones of fluvio-deltaic to paralic origin and contain about 250 coal seams (Drozdzewski, 1993; Süss et al., 2007). The overall coarsening-upward trend contains fourth-order sequences (400 ka) and fifth-order parasequences (112 ka) or sequences of higher periodicity, respectively (Süss et al., 2000). The cyclic successions are caused by the growing and shrinking of the Gondwana ice shield, leading to glacioeustatic fluctuations of 40 to 100 m magnitude during the Westphalian A, while Westphalian B fluctuations were less than 40 m (Rygel et al., 2008). The Ruhr Basin is a narrow, 150 km long and 80 km wide, NE-SW trending depression NW of the Rhenish Massif. While the SE border is erosive and conventionally located at the Remscheid anticline, the NE border is formed by the Lippstadt high and the Osning fault (Drozdzewski, 1993). To the W the Krefeld high forms the boundary, while the Aachen-Erkelenz coalfield to the SW is a continuation of the Ruhr Basin, as can be seen by its analogous sedimentary development (Wrede & Zeller, 1988). Northwards, the Upper Carboniferous strata of the Ruhr Basin are covered by Upper Cretaceous overburden with up to 2000 m thickness in the Münsterland region but continue northwards beyond the Osning Fault into the Lower Saxony Basin and extend 400 to 500 km to the central North Sea.

During the Late Carboniferous, the progressively NW-ward migrating Variscan orogenic belt in Central Europe initiated a northern peripheral foreland basin, which comprises the Ruhr Basin in central western Germany (Drozdzewski, 1992, 1993; Gayer et al., 1993; Süss et al., 2008; Ziegler et al., 1995). The tectonic style of deformation along the Variscan front changes at the Ruhr Basin from a thrust- into a fold-dominated type that is continuously widening westwards (Wrede et al., 1993; Wrede & Hilden, 1988).

The deformation of the Ruhr Basin is of post-Westphalian age, as displayed by folding of the strata. Deformation was strongest in the southeast, with a shortening of up to 50 %, decreasing continuously towards the north-west in the Dorsten anticline where shortening ranges from 5 to 10 % (Brix et al., 1988: their Fig. 7). The overall vergence is toward the NW, while some folds are upright or even verge southeastward. Fault-related folding is the prevailing deformation type in the Upper Carboniferous succession (Drozdzewski & Wrede, 1994). Seismic data suggest at 3 to 4 km depth a slightly SSE dipping structural discontinuity and a fault zone near Aachen (Faille du Midi), which is interpreted as a prominent and well lubricated thrust fault. Along the Faille du Midi, a vast horizontal nappe, displacement took place, indicating thin-skinned tectonics during the last stages of the Variscan orogeny (Meissner et al., 1981; Oncken et al., 1999) .

Thrusts strike NE-SW parallel to the fold axes. NW-SE striking faults were predominantly formed partly at the end of the Variscan deformation and partly prior to and during deposition of the Zechstein (Lopingian) strata (Wolf, 1985). The post-Carboniferous strata of the Ruhr Basin indicate further periods of active normal faulting during the Late Triassic (Drozdzewski, 1988) and during Late Cretaceous transpression, as pre-existing extensional faults in the Ruhr Basin were reactivated (Drozdzewski, 1993). During the Late Cretaceous the convergence of Africa, Iberia, and Europe lead to regional inversion resulting in NW-trending normal faults being reactivated as reverse faults (Kley & Voigt, 2008). During the Paleogene/Neogene, faults were mainly affected by extensional movements due to the formation of the Lower Rhine Embayment graben structure to the west, overprinting the pre-existing Paleozoic and Mesozoic structural framework (Arfai et al., 2014; Vinken, 1988).

The eastern Ruhr district (Fig. 2.1 B) hosts the mining water province Haus Aden. Subsurface data of this study originate from core material of three coal mining exploration wells (Fig. 2.1 B). The studied cores represent a typical clastic succession of the coal-bearing Upper Carboniferous Witten, Bochum, and Essen formations (Süss et al., 2000; Wrede & Ribbert, 2005) (Fig 1 C).

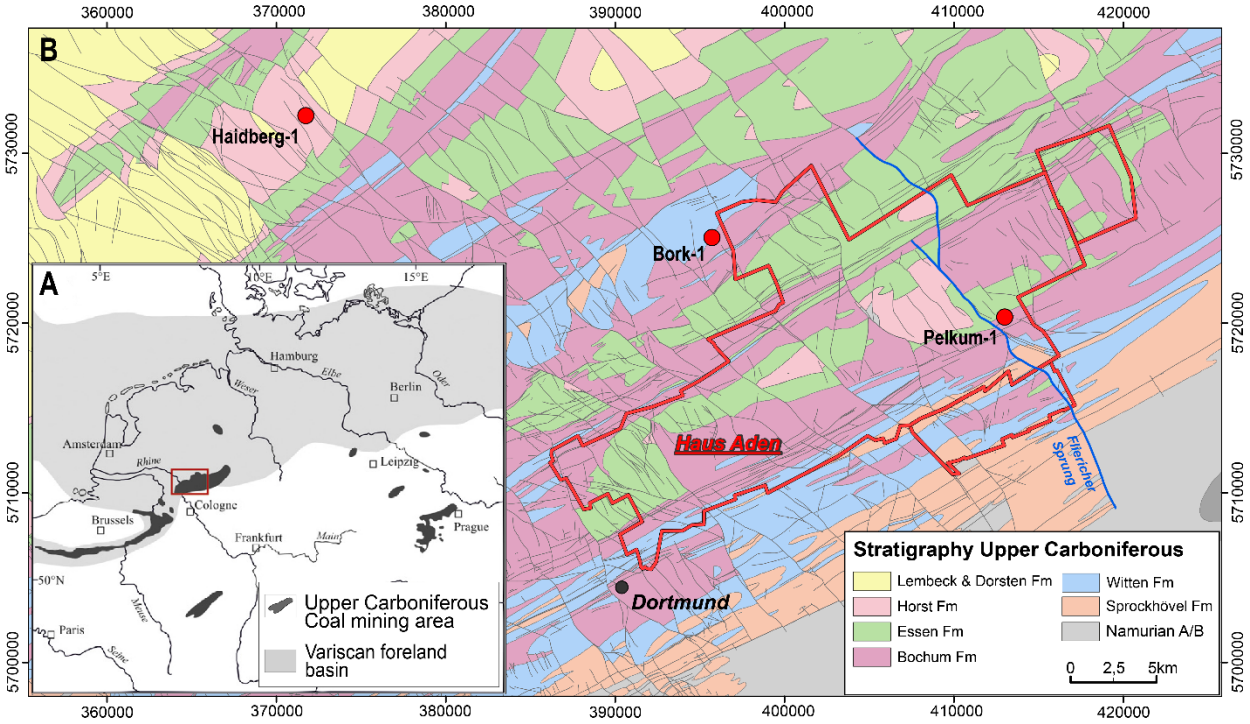
B
Haidberg-1
Bork-1
Pelkum-1
Haus Aden
Dortmund
Fliericher Sprung
A
Upper Carboniferous Coal mining area
Variscan foreland basin
Stratigraphy Upper Carboniferous
Lembeck & Dorsten Fm
Horst Fm
Essen Fm
Bochum Fm
Witten Fm
Sprockhövel Fm
Namurian A/B
0 2,5 5km
360000
370000
380000
390000
400000
410000
420000
5730000
5720000
5710000
5700000

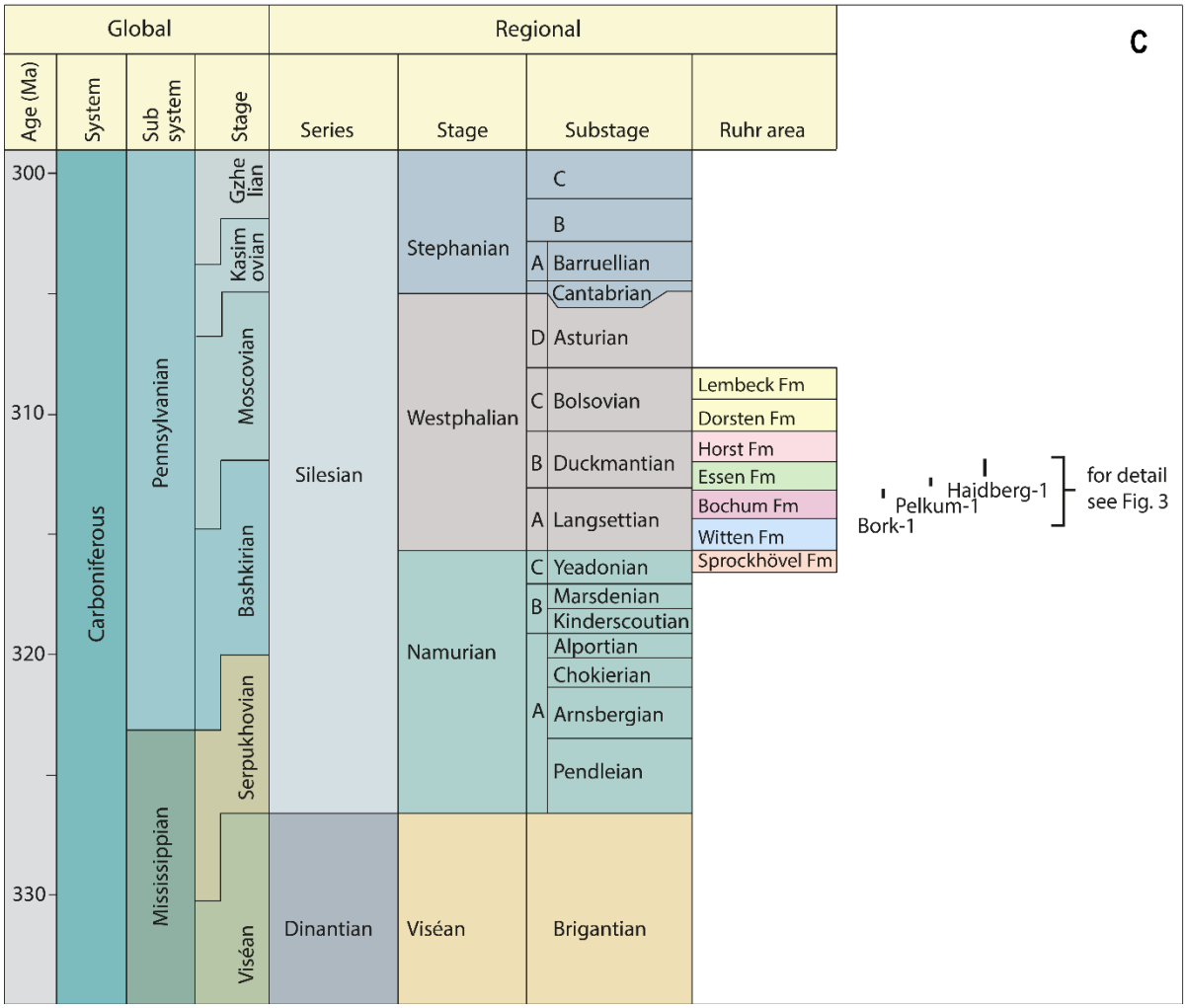
Global
Regional
C
Age (Ma)
System
Sub system
Stage
Series
Stage
Substage
Ruhr area
300
310
320
330
Carboniferous
Pennsylvanian
Mississippian
Gzhe lian
Kasim ovian
Moscovian
Bashkirian
Serpukhovian
Viséan
Silesian
Dinantian
Stephanian
Westphalian
Namurian
Viséan
C
B
A Barruellian
Cantabrian
D Asturian
C Bolsovian
B Duckmantian
A Langsettian
C Yeadonian
B Marsdenian
Kinderscoutian
A Alportian
Chokierian
Arnsbergian
Pendleian
Brigantian
Lembeck Fm
Dorsten Fm
Horst Fm
Essen Fm
Bochum Fm
Witten Fm
Sprockhövel Fm
Haidberg-1
Pelkum-1
Bork-1
for detail see Fig. 3

Figure 2.1 (**A)** The Variscan foreland basin in NW Europe with locations of Upper Carboniferous coalfields, modified from Jasper et al. (2009). (**B)** Location of the exploration wells, which encountered the stratigraphic units of the investigated area (Haus Aden; modified from the Geological Map of the Carboniferous of the Ruhr area 1:100.000, Geological Survey NRW, 1982). (**C**) Stratigraphic subdivision of the Carboniferous in Northern Germany (from the German Stratigraphic Commission (2016)) with stratigraphic ranges of the investigated drill cores indicated by the black bars, for details see Fig. 2.3.

2.4 Sedimentary evolution of the Ruhr Basin

The Upper Carboniferous deposits of the Ruhr Basin form a cyclic clastic succession in the Variscan orogenic foredeep including coal-bearing strata (e.g. Casshyap, 1975; Drozdzewski, 1992; Jessen, 1956; Littke & Zieger, 2019; Strehlau, 1990; Süss, 2005; Süss et al., 2000; Wrede & Ribbert, 2005). The Variscan shortening and uplift and the constant sediment supply into the northern foreland caused an overall regressive tendency of the depositional environment in the Ruhr Basin. This resulted in the narrowing of the sedimentation space from an open and deeper marine environment in the Early Carboniferous to a fluvio-deltaic/lagoonal system along the Variscan front, largely cut off from the sea in the Late Carboniferous (Wrede & Ribbert, 2005). Following Diessel (1992), delta environments can be subdivided into the subaquatic prodelta, the delta front, and the delta plain (Fig. 2.2). Subsequently, sedimentation in the Ruhr Basin occurred in three major sedimentary environments, the alluvial plain, marine/brackish subdeltas of the lower delta plain (Süss et al., 2000; their Fig. 10), and marine shelf deltas (Porębski & Steel, 2003: their Fig. 2). The shift from a marine basin to a marine prodelta environment at the basins southern margin in the Namurian B is accompanied by higher sedimentation rates and initial intercalations of thick sandstones that mark the advancing orogenic front (Drozdzewski, 2005). An increasing number of thick coal seams of the southern Ruhr Basin since the late Namurian C indicate a shift of the depositional environment to sedimentation in marine deltas and lower delta plains in this part of the basin (Strehlau, 1990). After the formation of a delta plain in the southeast during the early Westphalian A (Witten Formation), alluvial systems prograde repeatedly to the north-west indicating the proximity to the source area in the southeast during the late Westphalian A (Lower Bochum Formation). At that time, brackish-marine delta sequences form exclusively in the north-west but changed toward sedimentation in a subaqueous and lower delta plain environment in the late Westphalian A (Middle Bochum Formation) (Drozdzewski, 2005; Süss et al., 2000). A substantial reshaping of the subsidence pattern of the Ruhr Basin occurred throughout the latest Westphalian A (Upper Bochum Formation). The basin geometry changed from a ramp with the distal subsidence maximum in the early Westphalian A (Witten Formation) to a foreland basin geometry with a proximal subsidence maximum (Süss, 1996). This results in the initial occurrence of brackish deltaic sediments in the southeast, while lacustrine conditions prevailed in the north-west (Drozdzewski, 2005). The subaerial delta plain, forming on the marine delta front above sea level, is mainly composed of thin flood basin and flood plain deposits, which host smaller meandering channels.

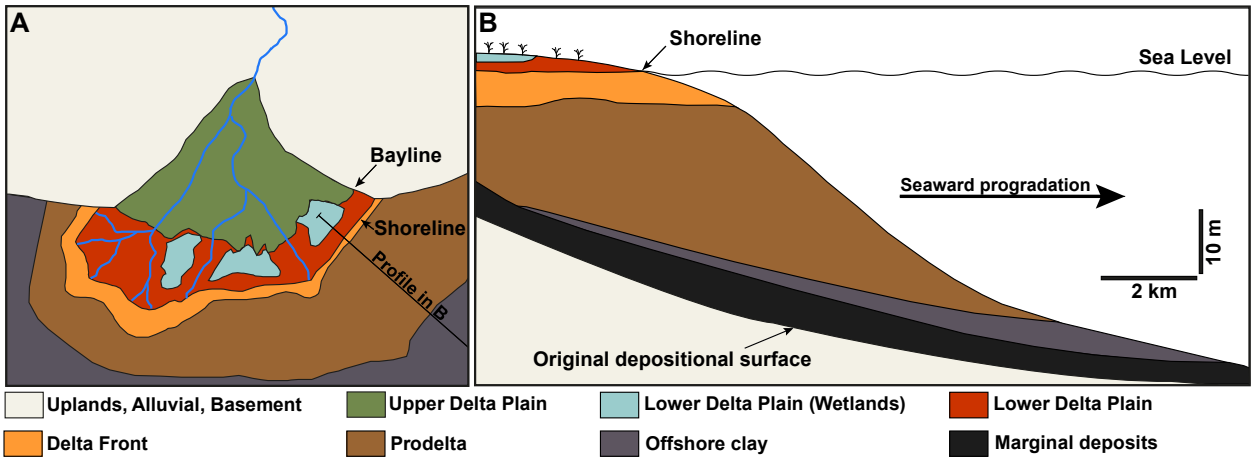

Figure 2.2 (**A**) Top view of the spatial associations of generalized facies associations. (**B**) Schematic cross section of the spatial associations of generalized facies associations in relation to the mean sea level. Modified and redrawn after Bhattacharya (2006).

The sedimentation pattern is controlled by an interplay of rapid basin subsidence, high sedimentation rate, and eustatic sea-level changes (Süss, 2005). In a tropical climate, prograding deltas and aggrading alluvial plains gave space for the development of extensive coal swamps along the lower and upper delta plain (Strehlau, 1990). Conditions most conducive for the development of swamps in a single depositional sequence occurred during the mid- to late-transgressive systems tracts when the sedimentation rate was balanced with the peat accumulation rate on a broad delta plain (Jerrett et al., 2011; their Fig. 11). In the Namurian C and Westphalian marine ingressions flooded the Ruhr Basin from the west (Strehlau, 1990). These marine ingressions were episodical and fainting already in the Westphalian B and C, indicated by the rare occurrence of marine horizons within the coal-bearing succession (Bless et al., 1980) (Fig. 2.3). Due to the migration of the Variscan deformation front, the depocenter and maximum coal formation shifted to the NW in the Westphalian. From the Westphalian C (Bolsovian) onwards, marine horizons no longer occurred, while the sedimentation area of North-west Germany was largely elevated above the sea level (Strehlau, 1990).

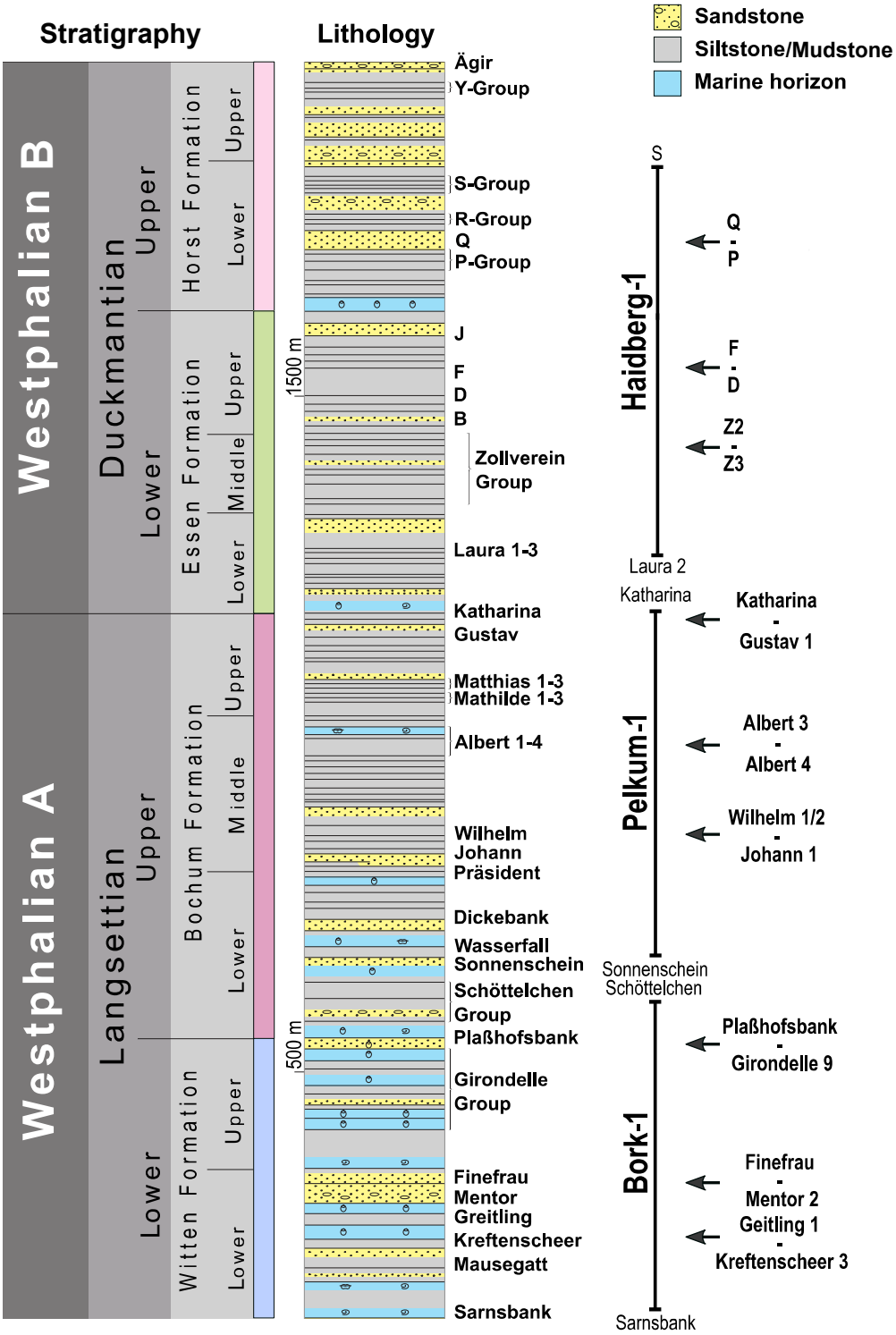

Figure 2.3 Stratigraphic column (colour code for formations as in Fig. 2.1 B) including a simplified lithological column comprising all relevant coal seams and the three drill cores with the examined cycles. Coal seam at the bottom and top of cored sections (Bork-1, Pelkum-1, and Haidberg-1) refer to coal seams to the left and are shown for the stratigraphic orientation. The names to the right indicate the studied cycles. Modified and redrawn after Hesemann (1975).

2.5 Methods

A sedimentological core description of approximately 270 m was performed on 10 cm diameter cores from three wells (Pelkum-1, Bork-1, and Haidberg-1) at the Geological Survey NRW. Sedimentary facies including grain size and sedimentary structures were defined based on available core descriptions, own observations and subsequently attributed to their corresponding facies association (see Tab. 2.1). The term "mudstone" is here defined as introduced by Folk (1954) and comprises samples with grain sizes finer than 0.0625 mm, i.e., silt plus clay, in which clay-sized material displays a substantial fraction. In contrast samples termed "siltstone" mostly comprise grains of the silt faction (between 0.0625 and 0.0039 mm).

Thermal conductivity is a physical rock property to deduce heat flow, the deep thermal regime and the thermal history of sedimentary basins (Clauser & Huenges, 1995; Fuchs & Förster, 2010; Littke et al., 1994). Thermal properties are related to mineral composition, compaction (and in consequence porosity), and the anisotropy of the rock (Labus & Labus, 2018; Popov et al., 2003; Zierfuss & Van der Vliet, 1956). The thermal conductivity of rock samples was determined using the optical scanning method on 60 slabbed core samples. This method is performed on a black-dyed rock sample surface with a mobile and continuously operating heat source (Popov et al., 1999). The rock samples were slabbed along the core axis perpendicular to bedding. Further thermal conductivity data were compiled from the database of the Geological Survey NRW for comparison. These data were determined using the same methodological approach and equipment. The dimensions of core samples varied in their length (5 to 50 cm), while the width was constant (10 cm). Measurements were performed on core samples, under ambient pressure and temperature, both in dry and water-saturated conditions. All samples were dried to constant weight at 70°C (dry). Following the dry measurements, the dehydrated samples were saturated with water and measured again (saturated). During the measurement, two infrared temperature sensors (initial and maximum temperature) simultaneously scan the planar surface perpendicular to bedding.

For further analyses, a total of 60 1-inch plugs were taken from the defined facies of the three studied wells, as they represent the main lithological units. The plugs were cored parallel to any apparent bedding plane. Porosity and density were measured using a micromeritics AccyPyc II 1340 Helium-pycnometer (Becker et al., 2017) on 1-inch core plugs at the Karlsruhe Institute for Technology (KIT). Permeability was measured on the same plugs at 12 bar confining pressure using dry, oil-free lab air (80 % N_2, 20 % O_2) as permeant in a Westphal Mechanik permeameter (Busch et al., 2022) at KIT.

Compressional wave velocity was measured using a Pundit Ultrasonic device (Pundit 200) at ultrasonic frequencies of 54 kHz at ambient temperature and pressure on the same 1-inch core plugs at KIT.

[1]Consequently, the velocity measurements were conducted parallel to the bedding. To provide a sufficient transmission between the transducer and the sample (maximize accuracy of the transit time measurement) a coupling agent (glycerine) was applied on the plug tops. v_P values were calculated by dividing the length of the core by the pulse transit time. The tests were repeated five times and the average value was taken as the v_P value.

2.6 Results

2.6.1 Lithology

The lithology of nine cycles from the three drill cores, 20 to 60 m thick (472.30 to 1281.50 m depth), exhibit alternating layers of claystone, mudstone, siltstone, and fine- to coarse-grained sandstone (see Fig. 2.4 and Tab. 2.1) intercalated with various coal seams (appendix A-C). The photographs in Fig. 2.4 show examples of facies types from the three drill cores as defined in Tab. 2.1.

2.6.1.1 Bork-1 (724.3 to 1031.7 m)

The coal seams of the lower cycle correspond after Fiebig (1977) to the coal seam group Kreftenscheer 3 and Greitling 1, constraining the lithostratigraphy of the 25 m thick cycle (1006.05 to 1031.70 m depth, appendix B.3) to the Lower Witten Formation of the Westphalian A. The coal seams of the 24 m thick middle cycle correspond to coal seam Mentor 2 to Finefrau/Finefrau Nebenbank, (941.0 to 964.40 m depth, appendix B.2) which separates the Lower and Upper Witten Formation (Fiebig, 1977). The 20 m thick upper cycle is constrained after Fiebig (1977) by the coal seams Girondelle 9 and Plaßhofsbank of the Upper Witten Formation (724.30 to 743.50 m depth, appendix B.1).

The base of the lower cycle is represented by structureless mudstone (mS, Tab. 2.1) with a sharp contact to 5 cm thick coal seams (C, Fig. 2.4 N) of a coal seam group. They are alternating with rooted mudstones (mR, Fig. 2.2.4 M), each layer with a thickness of 20 cm and forming a 2 m thick succession. The base of the middle and upper cycle consists of an up to 5 m thick succession of alternating parallel laminated sandstone (saPl, Fig. 2.4 B) and structureless (siS) or wavy laminated siltstone (siWl, Fig. 2.4 G), where the siltstone locally is bioturbated and siderite nodules apparent close to the overlying coal seam. The dip of these layers is 5 to 10°. Regardless of the facies, in all studied cycles a sharp erosional contact to the overlying medium-grained sandstone (saPl), dipping up to 20°, is present. The sandstone bodies are about 10 to 17 m thick and generally parallel laminated (dip 10 to 15°) but locally structureless. Another typical sedimentary structure is planar cross lamination. Furthermore, pebbles associated with shale clasts and coal

[1] For additional methodological considerations, see Addendum A.

fragments are locally present. The sandstones can be incised by sharp based, up to 1 m thick, structureless coarse-grained to pebbly sandstones (psaS, Fig. 2.4 D). Otherwise, the sandstone is incised by a 25 cm thick structureless mudstone (mS, Fig. 2.4 I) where the contact is undulating. The overlying fine-grained clastic rocks are wavy (siWl) to parallel laminated siltstone (siPl) or rooted mudstone (mR) and can be up to 4 m thick. The typical dip of these beds is ~5°.The contact is mainly sharp but occurs undulating or gradational as well. In the siltstone, thin (~20 cm) sharp-based sandstones can occur. A sharp contact to the overlying coal seam (C) is common, while the thickness of the coal seams varies from 5 cm to 1 m. The top of the section is just rarely formed by calcitic claystone (Fig. 2.4 A) but rather by a structureless mudstone showing a very faint lamination, dipping 5 to 10°. In general, the thickness of sandstone, siltstone and mudstone facies varies between the three sections but no thinning or thickening upward is noticed.

2.6.1.2 Pelkum-1 (472.30 to 1005.85 m)

The coal seams of the lower cycle correspond to the coal seam Johann 1 and Wilhelm 1/2 after Fiebig (1971), constraining the lithostratigraphy of the 24 m thick section (981.30 to 1005.85 m depth, appendix A.3) to the Middle Bochum Formation of the Westphalian A. The coal seams of the 50 m thick middle cycle correspond to Albert 4 and Robert/Albert1 (765.8 to 817.8 m depth, appendix A.2) of the Middle Bochum Formation (Fiebig, 1971). The 60 m thick upper cycle is constrained after Fiebig (1971) by the coal seams Gustav 1 and Katharina of the Upper Bochum Formation (472.3 to 530.2 m depth, appendix A.1), while the Katharina seam separates the Bochum Formation of the Westphalian A and the Essen Formation of the Westphalian B.

The base of all cycles consists uniformly of rooted mudstones (mR, Fig. 2.4 M) up to 3 m thick, in which siderite nodules and plant remains are apparent. The dip of these beds is 10 to 15°, while evident lamination can dip up to 15°. The top of the mudstones is sharp to the overlying coal seam (C, Fig. 2.4 N), which can be up to 30 cm thick. The contact from coal to the overlying sediments is sharp. In the lower and middle cycle, a 1 m thick mudstone facies is present (mS, Fig. 2.4 I), which locally is bioturbated (mBio), followed by either parallel laminated siltstone (siPl, Fig. 2.4 F) or sandstone (saPl, Fig. 2.4 B). The beds display a coarsening-upward trend, varying from 40 cm to 4 m. The upper cycle exhibits a sharp contact to the overlying medium-grained sandstone (saPl), alike in the cycles of the Bork-1. The sandstone beds are about 13 to 15 m thick and show parallel lamination (dip 15 to 20°), while the beds dip 15 to 23°. Another usual sedimentary structure is planar cross lamination (saCl). Shale clasts, plant remains and coal fragments are abundant throughout the entire sandstone facies. At the top of the sandstone beds a gradual contact to the overlying wavy (siWl) to parallel laminated siltstone (siPl, Fig. 2.4 F) is exhibited in the lower and upper cycle. Repetitive intercalated sand lenses (cm-scale) are common in the wavy laminated siltstones (see Fig. 2.4 G). The fining-upward continues, as the siltstone facies is followed by rooted mudstones (mR, Fig. 2.4 M) with apparent siderite nodules, resulting in a thickness of 4 m for the fining-upward succession (bedding dip ~15°). The fining-upward trend ends with an up to 3 m thick coal seam at the top. In the upper cycle

the coal seam is followed by a 30 m thick coarsening-upward trend grading from calcareous claystone (clC, Fig. 2.4 A) to a laminated calcareous siltstone (siPlC, Fig. 2.4 A) and wavy laminated sandstone (saWl, Fig. 2.4 E) at the top. Layers (cm-scale) in the wavy laminated sandstone contain high clay contents indicated by a brownish colour. A 60 cm thick section constrained by two clayey layers has a pale grey colour and appears to be poorly consolidated (see Fig. 2.4 E). In contrast in the middle cycle mainly structureless and rooted mudstones in sharp contact to coal seams build up a 23 m thick succession. The thickness of the coal seams varies from 5 cm to 3 m. The succession is repeatedly incised by siltstone beds of up to 4 m thickness that are locally bioturbated (siBio, Fig. 2.4 H). The lamination of siltstones dips 20°, while the beds dip 15°. The thicknesses of sandstone, siltstone and mudstone facies varies slightly between the three sections and no thinning or thickening upward is noticed.

2.6.1.3 Haidberg-1 (1010.40 to 1305.90 m)

The coal seams of the lower cycle correspond to the coal seams Zollverein 3 and Zollverein 1/2 (Von Sperber & Hettenberger, 1992), constraining the lithostratigraphy of the 25 m thick cycle (1281.50 to 1305.90 m depth, appendix C.3) to the Middle Essen Formation of the Westphalian B. The coal seams of the 34 m thick middle cycle (1159.45 to 1193.00 m depth, appendix C.2) correspond to D1 and F1 of the Upper Essen Formation (Von Sperber & Hettenberger, 1992). The 30 m thick upper cycle (1010.40 to 1040.20 m, appendix C.1) is constrained after Von Sperber & Hettenberger (1992) by the coal seams P4 and P3 of the Lower Horst Formation.

The base of all cycles consists of a mudstone facies (up to 3 m thick) that is rooted (mR, Fig. 2.4 M) or laminated with some mm-thick siltstone lenses (mPl, Fig. 2.4 J) or a laminated siltstone (siPl, Fig. 2.4 F) that fines up to a mudstone, in which siderite nodules and plant remains are apparent. The dip of these beds is 10 to 15°, while evident lamination dips 10°. The mudstones have a sharp contact to the overlying coal seams (C, Fig. 2.4 N), which are up to 80 cm thick. The top of the coal is sharp to the overlying mud facies. Here, the mudstone is structureless (mS, Fig. 2.4 I), varies in thickness from 10 cm to 3.5 m and comprises siderite nodules and plant remains. The mud facies is sharply overlain by medium-grained planar laminated sandstone (saPl, Fig. 2.4 B), dipping 5°. In the middle cycle the coal seam is sharply overlain by medium-grained sandstone (saPl). The sandstone beds are about 15 m thick and generally parallel laminated (dip 15°). Planar cross lamination is rarely present in a 30 cm thick section. Shale clasts and coal fragments occur frequently. The contact at the top of the sandstone bed is either sharp based to the overlying parallel laminated mudstone (mPl) or gradual from parallel laminated siltstones (siPl) to rooted mudstones (mR). The mudstone is sharply cut by layers of structureless siltstone (siS) and parallel laminated sandstone (saPl) with a thickness of 2.3 m. The dip of these beds is 5 to 10°. In the middle cycle no thick sandstone bed is developed but rather appears as thin lenses (<0.5 to 2 cm) within wavy (siWl, Fig. 2.4 G) and planar laminated (siPl Fig. 2.4 F) siltstone and planar laminated mudstones (mPl, Fig. 2.4 J) for about 17 m. Intercalated sand lenses (cm-scale) are common in the laminated siltstones (see Fig. 2.4 G). The top of this

succession is sharp to the overlying rooted mudstone (mR) that is 4 m thick and overlain by coal of up to 4 m thickness. 50 cm of structureless mudstones (mS, Fig. 2.4 I) overlays the coal seams (dip 5°) and either forms the top of the section or grades up to silt- and sandstone in the lower and upper cycle. The thickness of sandstone, siltstone and mudstone facies varies slightly between the three sections and no thinning or thickening upward is noticed.

2.6.2 Structures

As far as it could be observed in the cores, fractures in the cycles of the Bork-1 and Pelkum-1 well occur as up to 1 m long sub-vertical features (dip 75 to 85°). Barren fractures are present, but rare. Most fractures are completely mineralized by quartz or calcite and, where the aperture is >1 mm, additionally by pyrite/marcasite. Fractures are commonly restricted to the silt- and sandstone facies, where their presence is marked by bleaching of the host rock. This is reflected by an outer yellow to orange halo in the vicinity of the fracture.

In the Haidberg-1 well, fractures are sub-vertical (dip 75 to 85°), vary from 20 to 240 cm in length and are barren or mineralized. In contrast to the other wells, most fractures are predominantly mineralized by calcite and pyrite/marcasite. Fractures are mainly restricted to the silt- and sandstone facies.

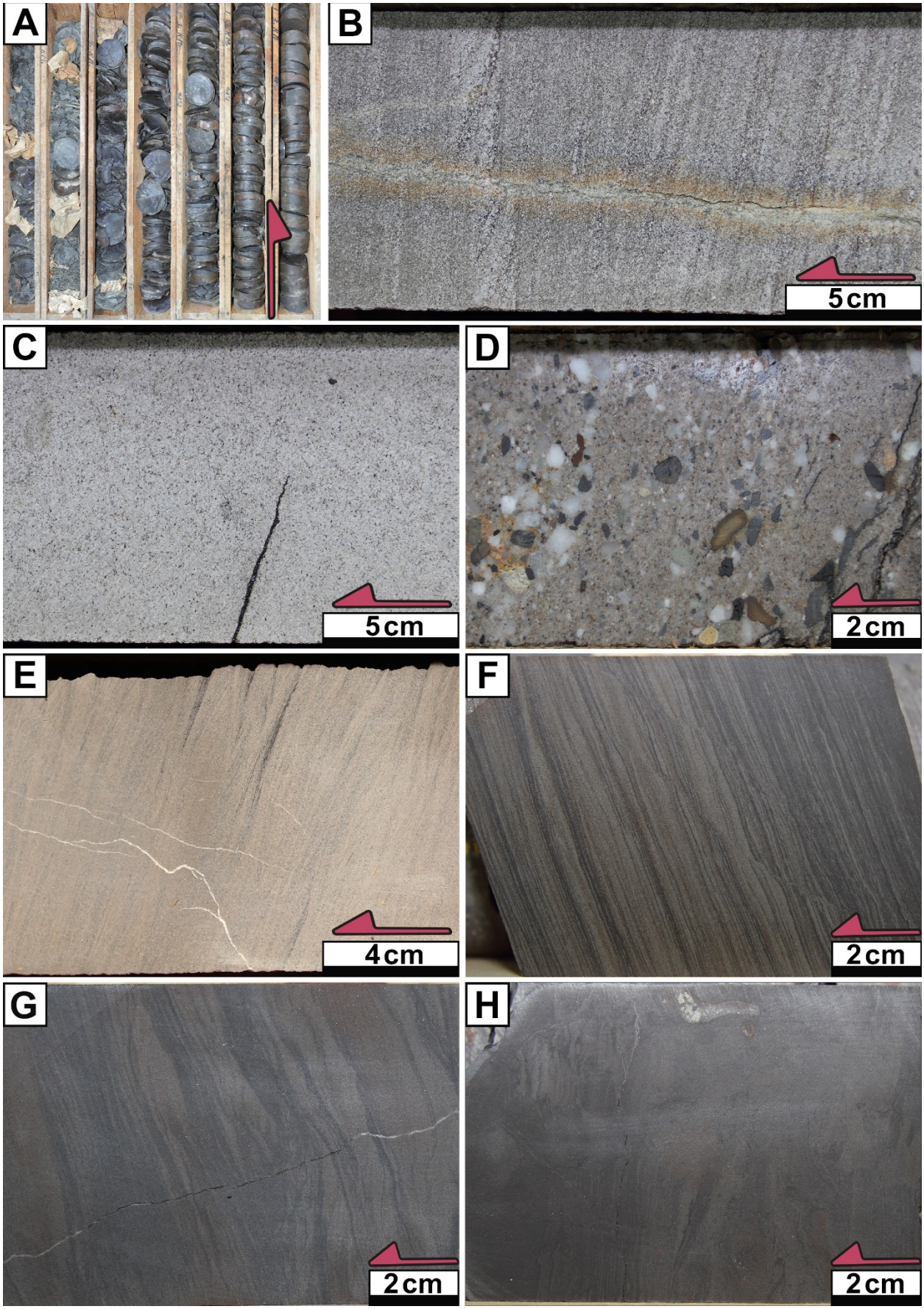
A
B
5 cm
C
5 cm
D
2 cm
E
4 cm
F
2 cm
G
2 cm
H
2 cm

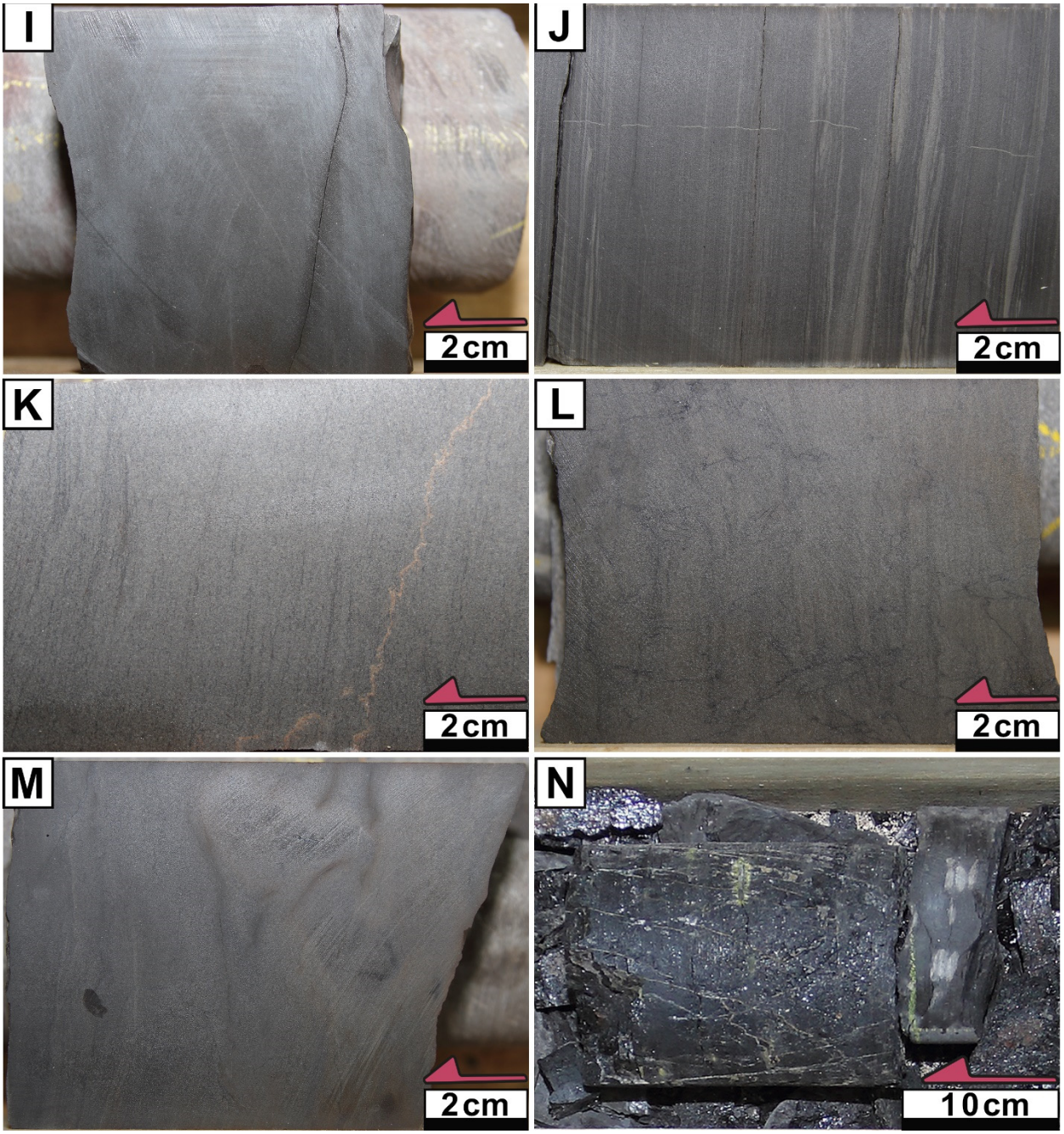

Figure 2.4 Photographs of defined facies of Table 1. The red arrows indicate the top. (**A**) Calcaerous claystone (clC) and heterolith, calcareous mud dominated (siPlC), Pelkum-1 478.4 to 487.3m; (**B**) Parallel laminated sandstone (saPl), Bork-1 1019.9m; (**C**) Structureless medium-grained sandstone (saS), Bork-1 1027.9m; (**D**) Coarse-grained to conglomeratic sandstone (psaS), Bork-1 1021.7m; (**E**) Poorly consolidated wavy laminated sandstone (saWl) with locally high clay content, Pelkum-1 525.3m; (**F**) Planar laminated heterolith, silt dominated (siPl) with increasing mud content to the right, Haidberg-1 1171.1m; (**G**) Wavy laminated heterolith, silt dominated (siWl) with sandy lenses, Haidberg-1 1140.1m; (**H**) Bioturbated siltstone (siBio), Pelkum-1 986.4m. (**I**) Mudstone structureless (mS), Haidberg-1 1013.5m; (**J**) Mudstone with silt laminae (mPl), Haidberg-1 1305.7m; (**K**) Structureless fine-grained sandstone (fsaS), Haidberg-1 1010.5m; (**L**) Siltstone with roots (siR), Haidberg-1 1285.4m; (**M**) Mudstone with roots (mR), Haidberg-1 1161.9m; N Coal (C), Haidberg-1 1160.8m (coal seam P3).

2.6.3 Facies and facies associations

Based on previously published studies (Bhattacharya, 2006; Van Yperen et al., 2019) the strata are divided into 16 facies recognized based on observations of lithology, grain size, and sedimentary structures (Tab. 2.1, Fig. 2.4). These facies are grouped into four facies associations, reflecting different sedimentary environments. Subsequent interpretations are based on their vertical relationships.

2.6.3.1 Prodelta

The prodelta facies association is classified following the description of Bhattacharya (2006). If present, the prodelta succession consists of fully marine, black calcareous claystone at the base (clC, Fig. 2.4 A) that is up to 6 m thick and contains marine fossils (e.g., goniatites). The black claystone shows a minor silt content, pyrite mineralization and sideritic clay-ironstone nodules. Lamination and bioturbation are lacking. In the overlying calcareous mud facies (mPlC), lamination is mainly planar. Bioturbation is scarce but apparent in small sections (dm-scale). The amount of plant remains increases towards the top of the succession.

2.6.3.2 Delta front

The claystones and mudstones of the prodelta facies grade continuously (coarsening-upward) to an alternating calcareous mud/silt laminated succession (siPlC , Fig. 2.4 A) of the distal delta front followed by a wavy laminated sandstone (saWl, Fig. 2.4 E) (Tab. 2.1) (cf. definition Bhattacharya, 2006). No differentiation between the distal and proximal delta front was made, as sedimentation mainly took place in the transitional zone from the lower to the upper delta plain during the Westphalian A and B (Strehlau, 1990). Delta front deposits consist of characteristic, fine- to coarse-grained sandstone successions, showing no signs of bioturbation, and are up to several metres thick. Sandstone colours alternate from yellowish to greyish white, while sedimentary structures are dominated by planar lamination (saPl, Fig. 2.4 B) with rare sections with planar cross lamination (saCl). The angle and direction of laminated beds are highly dynamic, with frequently changing angles and direction. In places, sedimentary structures are faint with sections of a structureless sandstone with scattered clasts (up to pebble size), coal flakes, and rip-up clasts (saS, Fig. 2.4 C) or appear as coarse-grained to pebbly (including rip-up clasts and coal flakes) structureless sandstone (psaS, Fig. 2.4 D). Bed boundaries are sharp but rarely erosional. In places, the top and base of the facies association is characterized by gradual contacts to structureless fine-grained sandstone (fsaS, Fig. 2.4 K)

2.6.3.3 Lower delta plain

Typical for the lower delta plain succession are heteroliths showing a vertical transition of their lamination type. It changes from planar lamination at the bottom through wavy to lenticular lamination at the top, where ripples are locally mud-draped, and mudstones capping the succession (Van Yperen et al., 2019). The mud layers drape ripple crests and fill the ripple troughs. Heterolith colours vary from dark grey to grey

corresponding to their TOC (total organic carbon) and mud/silt content. The silt dominated section exhibits planar lamination (siPl, Fig. 2.4 F) or wavy lamination due to oscillation ripples and less commonly asymmetric mud-draped current ripples (siWl, Fig. 2.4 G). The mud dominated section exhibits wavy to lenticular lamination with densely distributed mm-scale silt lenses to very fine-grained sand lenses. Bioturbation is scarce in the laminated heteroliths but apparent at the transition from silt dominated heteroliths (siBio, Fig. 2.4 H) grading to silt laminated mudstone (mBio). The overlying dark grey-black mudstone with a varying silt content is structureless (mS, Fig. 2.4 I) but may show partly faint parallel lamination with silty laminae (mP, Fig. 2.4 A J). Sideritic clay-ironstone nodules and plant remains appear in the entire succession, regardless of the facies. In places, this facies association is characterized by incursions of structureless (siS) and planar laminated siltstone (siPl, Fig. 2.4 F) and siltstone with root marks (siR, Fig. 2.4 L) into the structureless mudstone (mS, Fig. 2.4 I).

2.6.3.4 Lower delta plain (wetlands)

Typical deposits of this facies association are dark grey to black mudstones showing a faint wavy to planar lamination, are rich in plant remains and up to few metres thick, while root marks partly obliterate the primary sedimentary structures (mR). Commonly these rooted beds (term adapted from Mountney (2006)) are overlain by cm- to m-thick coal (C, Fig. 2.4 N). A black structureless mudstone with minor silt content that features sideritic clay-ironstone nodules and plant remains (mS, Fig. 2.4 I) in places drapes the coal seam and forms the top of the strata.

Table 2.1 Summary of facies associations and their constituting lithofacies in the studied wells, including a schematic sedimentary log that represents the main depositional environments.

SCHEMATIC LOG	FACIES ASSOCIATION	DESCRIPTION	FACIES	LITHOLOGY
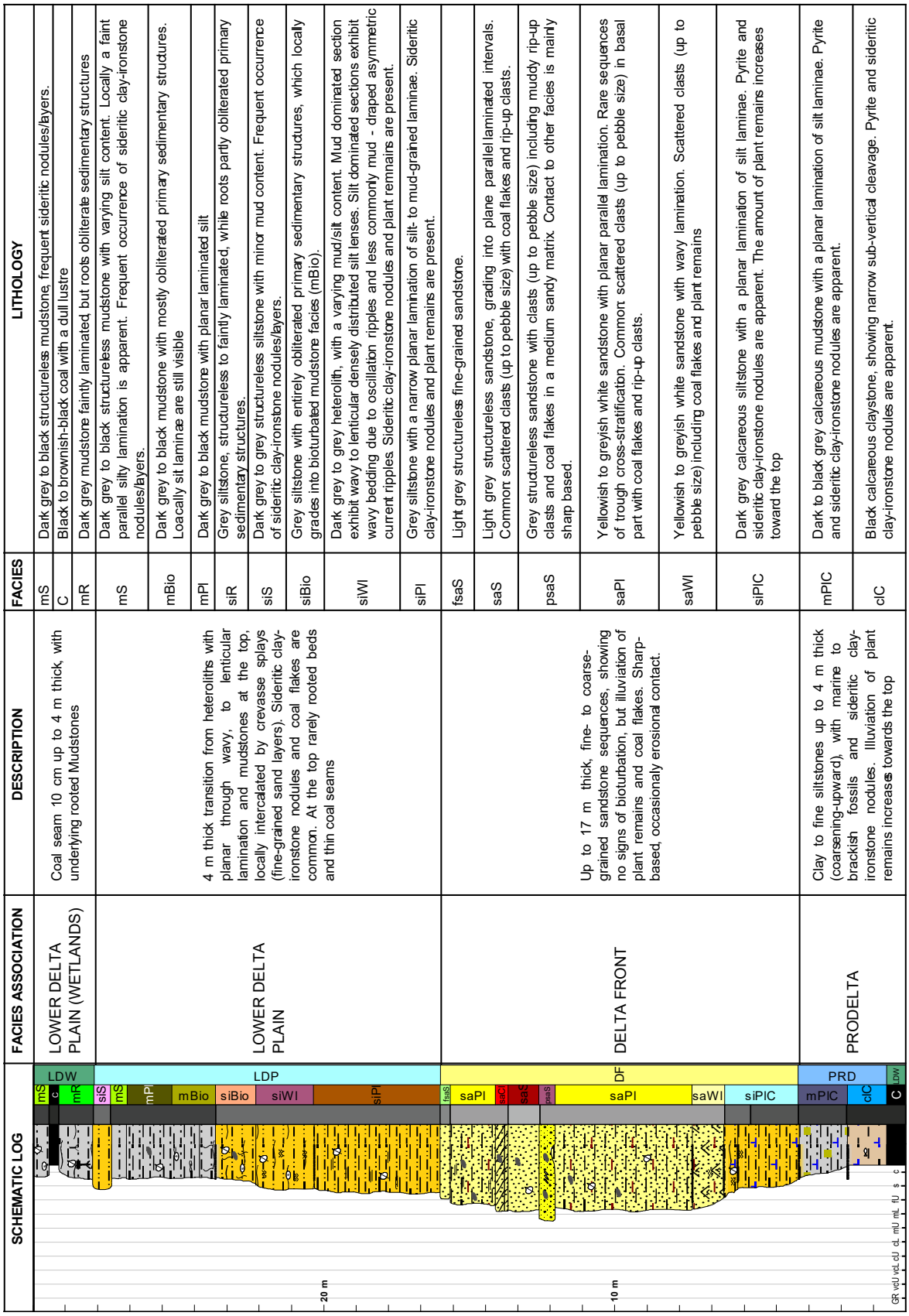	LOWER DELTA PLAIN (WETLANDS)	Coal seam 10 cm up to 4 m thick, with underlying rooted Mudstones	mS	Dark grey to black structureless mudstone, frequent sideritic nodules/layers.
			C	Black to brownish-black coal with a dull lustre
			mR	Dark grey mudstone faintly laminated, but roots obliterate sedimentary structures
	LOWER DELTA PLAIN	4 m thick transition from heteroliths with planar through wavy, to lenticular lamination and mudstones at the top, locally intercalated by crevasse splays (fine-grained sand layers). Sideritic clay-ironstone nodules and coal flakes are common. At the top rarely rooted beds and thin coal seams	mS	Dark grey to black structureless mudstone with varying silt content. Locally a faint parallel silty lamination is apparent. Frequent occurrence of sideritic clay-ironstone nodules/layers.
			mBio	Dark grey to black mudstone with mostly obliterated primary sedimentary structures. Loacally sit laminae are still visible
			mPl	Dark grey to black mudstone with planar laminated silt
			siR	Grey siltstone, structureless to faintly laminated, while roots partly obliterated primary sedimentary structures.
			siS	Dark grey to grey structureless siltstone with minor mud content. Frequent occurrence of sideritic clay-ironstone nodules/layers.
			siBio	Grey siltstone with entirely obliterated primary sedimentary structures, which locally grades into bioturbated mudstone facies (mBio).
			siWl	Dark grey to grey heterolith, with a varying mud/silt content. Mud dominated section exhibit wavy to lenticular densely distributed silt lenses. Silt dominated sections exhibit wavy bedding due to oscillation ripples and less commonly mud - draped asymmetric current ripples. Sideritic clay-ironstone nodules and plant remnains are present.
			siPl	Grey siltstone with a narrow planar lamination of silt- to mud-grained laminae. Sideritic clay-ironstone nodules and plant remains are present.
	DELTA FRONT	Up to 17 m thick, fine- to coarse-grained sandstone sequences, showing no signs of bioturbation, but illuviation of plant remains and coal flakes. Sharp-based, occasionaly erosional contact.	fsaS	Light grey structureless fine-grained sandstone.
			saS	Light grey structureless sandstone, grading into plane parallel laminated intervals. Common scattered clasts (up to pebble size) with coal flakes and rip-up clasts.
			psaS	Grey structureless sandstone with clasts (up to pebble size) including muddy rip-up clasts and coal flakes in a medium sandy matrix. Contact to other facies is mainly sharp based.
			saPl	Yellowish to greyish white sandstone with planar parallel lamination. Rare sequences of trough cross-stratification. Common scattered clasts (up to pebble size) in basal part with coal flakes and rip-up clasts.
			saWl	Yellowish to greyish white sandstone with wavy lamination. Scattered clasts (up to pebble size) including coal flakes and plant remains
			siPlC	Dark grey calcareous siltstone with a planar lamination of silt laminae. Pyrite and sideritic clay-ironstone nodules are apparent. The amount of plant remains increases toward the top
	PRODELTA	Clay to fine siltstones up to 4 m thick (coarsening-upward), with marine to brackish fossils and sideritic clay-ironstone nodules. Illuviation of plant remains increases towards the top	mPlC	Dark to black grey calcareous mudstone with a planar lamination of silt laminae. Pyrite and sideritic clay-ironstone nodules are apparent.
			clC	Black calcareous claystone, showing narrow sub-vertical cleavage. Pyrite and sideritic clay-ironstone nodules are apparent.

2.6.4 Petrophysical and wave velocity analysis

Measured plug porosity of investigated samples ranges from 0.9 % to 15.6 %, with a mean value of 5.6 %. Porosities are highest in sandstones (2.2 to 15.6 %; mean 6.9 %) compared to siltstones (0.9 to 8.4 %; mean 3.5 %) and mudstones (1.6 to 7.1 %; mean 3.5 %) (Fig. 2.5 A). Similarly, the highest porosities are measured in samples of the delta front environment (3.3 to 11.0 %; mean 6.8 %). Lower porosities are attributed to the lower delta plain (1.5 to 15.6 %; mean 4.6 %), the lower delta plain (wetlands) (0.9 to 8.4 %; mean 3.9 %), and the prodelta deposits (3.4 to 3.8 %; mean 3.6 %), respectively (Fig. 2.5 B). Measured permeability ranges from 0.0001 mD to 2.46 mD (mean 0.14 mD). Unlike the porosity the disparity in permeability, regarding the grain size is modest. Sandstones (0.0001 to 2.64 mD; mean 0.16 mD) have slightly higher permeabilities than siltstones (0.0001 to 0.23 mD; mean 0.03 mD) and mudstones (0.0004 to 1.89 mD mean 0.25 mD) (Fig. 2.5 A). Permeabilities are generally higher in delta front deposits (0.0001 to 2.46 mD; mean 0.18 mD). Lower permeabilities are measured in samples of the lower delta plain (0.0001 to 0.23 mD; mean 0.03 mD). The lowest values (0.00047 to 0.00062 mD; mean 0.00054 mD) are generally attributed to prodelta deposits (Fig. 2.5 B).

The compressional wave velocity (v_P) of dry core plugs ranges between 2886 and 5663 m/s, with a mean value of 4023 m/s (Fig. 2.5 C and D). The v_P values are higher in sandstones (2886 to 5663 m/s; mean 3869 m/s) than in siltstones (3814 to 4649 m/s; mean 4327 m/s) and mudstones (3641 to 4695 m/s; mean 4183 m/s) but variable (Fig. 2.5 C). In terms of facies associations (Fig. 2.5 D), the highest v_P values are measured in the delta front samples but show the widest spread, ranging from 2886 to 5663 m/s (mean 3920 m/s). Samples of the lower delta plain and lower delta plain (wetlands) spread across lower velocities ranging from 3060 to 4649 m/s (mean 4069 m/s) and from 3641 to 4695 m/s (mean 4271 m/s), respectively. Mean v_P values for prodelta deposits are 3971 m/s. When comparing the results from porosity measurements with the v_P values, a moderate negative correlation is displayed (R^2=0.6). This relationship is consistent when segregating into the lower delta plain (R^2=0.74) and wetlands (R^2=0.64). For the delta front samples, the trend is parallel, but the correlation is lower (R^2=0.48) (Fig. 2.5 D). Due to the low number of samples, no linear fit for prodelta deposits (n=2) is computed.

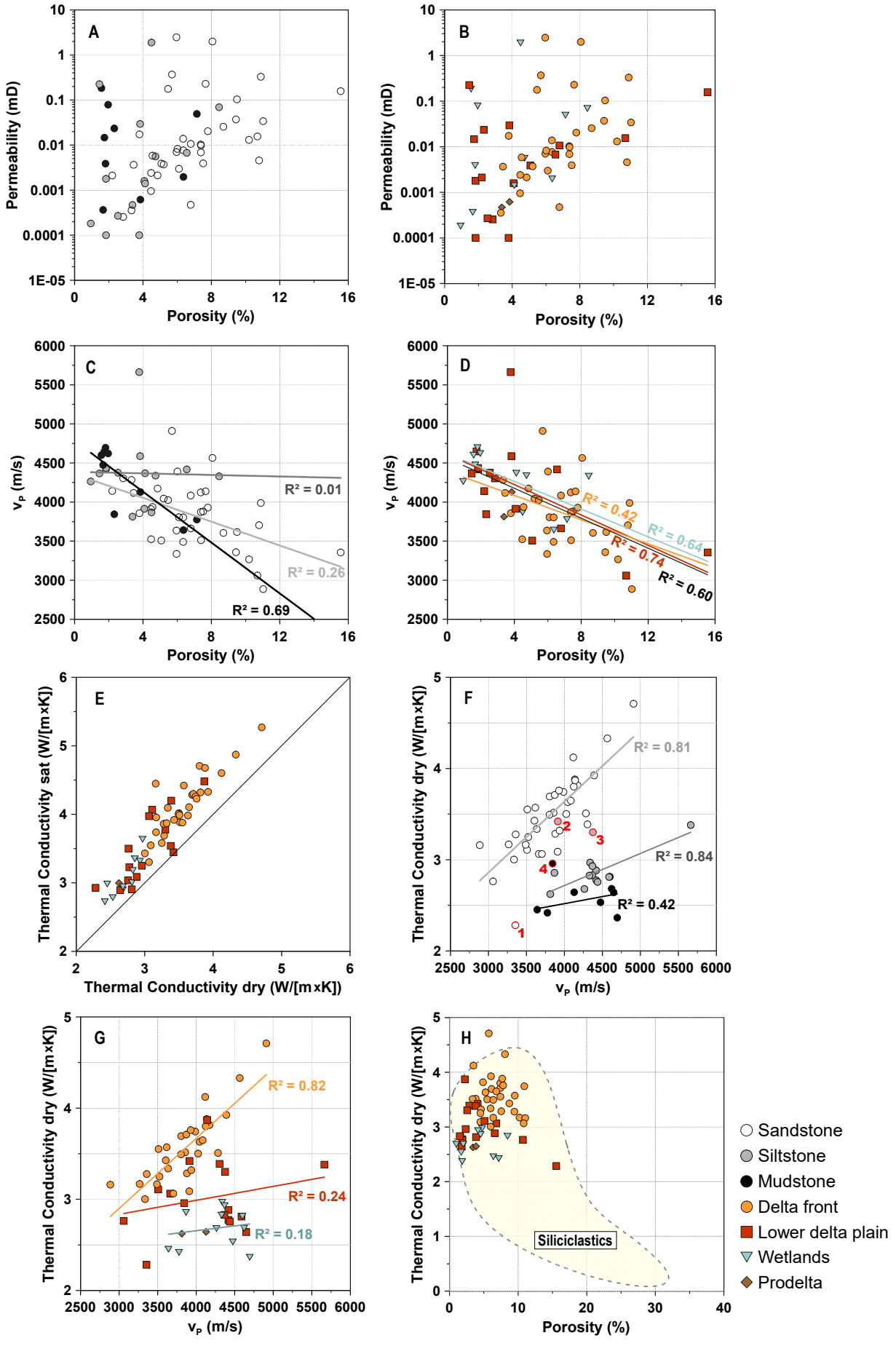
A
Permeability (mD)
Porosity (%)
B
Permeability (mD)
Porosity (%)
C
v_P (m/s)
R² = 0.01
R² = 0.26
R² = 0.69
Porosity (%)
D
v_P (m/s)
R² = 0.42
R² = 0.64
R² = 0.74
R² = 0.60
Porosity (%)
E
Thermal Conductivity sat (W/[m×K])
Thermal Conductivity dry (W/[m×K])
F
Thermal Conductivity dry (W/[m×K])
R² = 0.81
R² = 0.84
R² = 0.42
1
2
3
4
v_P (m/s)
G
Thermal Conductivity dry (W/[m×K])
R² = 0.82
R² = 0.24
R² = 0.18
v_P (m/s)
H
Thermal Conductivity dry (W/[m×K])
Siliciclastics
Porosity (%)
Sandstone
Siltstone
Mudstone
Delta front
Lower delta plain
Wetlands
Prodelta

Figure 2.5 Cross plots of the studied samples regarding either grain size or facies associations. (**A)** Measured porosities and permeabilities plot for samples subdivided by their grain size and (**B**) by their facies association. (**C**) The porosity-v_P relationship is plotted for dry samples subdivided by their grain size and (**D)** their facies associations including R^2-values. (**E)** Thermal conductivity in dry conditions versus saturated conditions. (**F)** The v_P-thermal conductivity relationship for dry samples subdivided by their grain size, with outliers marked in red that are not considered in the linear fit, and (**G**) their facies association. (**H**) Thermal conductivity of measured samples in dry condition and ambient temperature versus porosity, complemented by other siliciclastics values (coloured field, database Geological Survey NRW, unpubl.).

2.6.5 Thermal conductivity

Thermal conductivities of the Upper Carboniferous samples range between 2.3 and 4.7 W/(m×K)(mean 3.2 W/(m×K)) in dry conditions. For saturated samples, conductivity values are higher by a mean of 15 %, ranging from 2.7 to 5.3 W/(m×K), with a mean value of 3.7 W/(m×K) (Fig. 2.5 E).

Thermal conductivity is highest in sandstones, ranging from 2.3 to 4.7 W/(m×K) (mean 3.5 W/(m×K)) in dry conditions and 2.9 to 5.3 W/(m×K) (mean 4.1 W/(m×K)) in saturated condition (Fig. 2.5 F). Generally, conductivities are lower in siltstones and mudstones in dry conditions varying from 2.6 to 3.4 W/(m×K) (mean 2.9 W/(m×K)) and 2.4 to 3.0 W/(m×K) (mean 2.6 W/(m×K)), respectively. For saturated samples, values vary from 2.9 to 4.2 W/(m×K) (mean 3.0 W/(m×K)) and 2.7 to 3.4 W/(m×K) (mean 3.0 W/(m×K)), respectively (Fig. 2.5 F). Thermal conductivity is highest in samples of the delta front, ranging from 3.0 to 4.7 W/(m×K) (mean 3.6 W/(m×K)) in dry conditions and 3.3 to 5.3 W/(m×K) (mean 4.1 W/(m×K)) in saturated condition (Fig. 2.5 G). Lower conductivities in the lower delta plain and lower delta plain (wetlands) samples in dry conditions vary from 2.3 to 3.9 W/(m*K) (mean 3.0 W/(m×K)) and 2.4 to 3.0 W/(m×K) (mean 2.7 W/(m×K)), respectively. For saturated samples, the thermal conductivity varies from 2.9 to 4.5 W/(m×K) (mean 3.5 W/(m×K)) and 2.7 to 3.6 W/(m×K) (mean 3.1 W/(m×K)) of the lower delta plain and lower delta plain (wetlands), respectively (Fig. 2.5 G).

Thermal conductivity and P-wave velocity are positively correlating, as thermal conductivity increases with higher P-wave velocity (Fig. 2.5 F and G). Furthermore, a separation of the samples among different grain size (Fig. 2.5 F) and depositional environments can be observed (Fig. 2.5 G). For samples classified as sandstones and siltstones, a good linear fit of R^2=0.81 and 0.84, respectively is observed. Mudstones show a moderate correlation of R^2=0.42. Outliers are identified for sandstones (n=1), siltstones (n=2) and mudstone (n=1), which are not integrated in the linear fit (see outlier in Fig. 2.5 F). For the sandstone class, the outlier is attributed to a 60 cm thick section of pale grey (bleached) sandstone that is poorly consolidated (see Fig. 2.4 E). Outliers for the siltstone and mudstone classes refer to samples that incorporate <0.5 to 2 cm-thick sand lenses (see Fig. 2.4 G) and mm-thick siltstone lenses (Fig. 2.4 J), respectively, altering the thermal conductivity. Calculated slope values display a relatively high gradient for sandstones (b=0.00078 Tc/v_P) and siltstones (b=0.00035 Tc/v_P) compared to a lower gradient for mudstones (b=0.00015 Tc/ v_P). For delta front samples a good linear fit of R^2=0.82 is determined. Samples of the lower delta plain and the

wetlands show a poor correlation of R^2=0.24 and 0.18, respectively. Calculated slope values display a relatively high gradient for delta front deposits (b=0.00077 Tc/v_P) compared to lower gradients for lower delta plain (b=0.00015 Tc/v_P) and wetland deposits (b=0.00015 Tc/v_P). When comparing to thermal conductivity data of common siliciclastics from North Rhine-Westphalia (Fig. 2.5 H), the values presented here are within the range of available thermal conductivities.

2.7 Discussion

2.7.1 Depositional environment

2.7.1.1 Prodelta

The fossil content (i.e., goniatites) of the calcareous claystone (clC, Fig. 2.4 A) and its coarsening-upward trend suggest shallow marine conditions, with water depths ranging from several tens to a maximum of 100 m, marking the distal areas of the delta (Süss et al., 2000) and act as sequence stratigraphic reference horizons (e.g., Katharina horizon). Clay/mud is deposited by suspension out of buoyant river plumes, below the fair-weather wave base. The muddy sediment is deposited at the seabed and may have been resuspended by waves (Kineke et al., 1996) or by storms (Allison et al., 2000). Mud may also be introduced directly onto the seafloor by hyperpycnal flows (Bhattacharya, 2006). As sedimentation rates of hyperpycnal flows are much higher than by suspension settling, their importance in the construction of the shelf has classically been underestimated (Mulder & Syvitski, 1995). The low to absent bioturbation in the claystone is characteristic of prodelta environments that experience river-induced stresses (MacEachern et al., 2005). As the delta front progrades, the proportion of plant remains increases towards the top due to the increasing sedimentary input, caused by higher flow energy. The presence of authigenic pyrite marks anoxic conditions. High organic influx in a shallow marine milieu and anoxic, sulphidic pore waters results in Fe-sulphides (pyrite/marcasite) precipitates in marine and transitional sediments (Coleman, 1985; Morad et al., 2000). An increase in alkalinity due to bacterial sulphate reduction that previously lead to the formation of pyrite, can further promote carbonate precipitation (Morad et al., 1998) and the growth of sideritic clay-ironstone nodules.

2.7.1.2 Delta front

The delta front facies, an intrinsically heterogeneous succession, is interpreted as a complex stacking pattern of estuarine bars and distributary channels (Süss et al., 2000), forming the transition between the subaqueous prodelta (saPl, saS and psaS, Fig. 2.4 B to D) and the lower delta plain. Low to almost absent bioturbation is related to high sedimentation rates with increased flow turbidity and reduced salinity, which is characteristic of river-dominated delta front deposits (Gani et al., 2007). The dynamics of palaeocurrent directions is leading to unconfined, frequently changing flow at the channel mouth, with consequent lateral,

downstream, and upstream growth of the delta front (Van Yperen et al., 2019). Architectural features i.e., erosional unconformities that could be interpreted as the base of larger distributary channels may be related to the facies psaS (Fig. 2.4 D), as reworking of the more proximal delta sequence. Yet, their modest dimension and a missing fining-upward trend rather imply a genetic relationship to the internal dynamic of its depositional environment. This interpretation is supported as the reworking of the upper delta plain strata might occur without an eustatic sea-level drop (Süss et al., 2000).

2.7.1.3 Lower delta plain

The lower delta plain facies association is considered as tide-influenced deposits of a lower delta plain based on their vertical transition from planar (siPL, Fig. 2.4 F) and wavy (siWl, Fig. 2.4 G) to lenticular bedding (mPl, Fig. 2.4 J). It is regarded as the development to a more proximal shallow environment and subsequently a stagnant water zone. The lower delta plain is characterized by the occurrence of oscillation wave ripples and current ripples that are locally mud-draped, while locally root marks represent periods of subaerial exposure. Mud draping of ripples has previously been interpreted as flaser bedding (Melehan et al., 2021 : their Fig. 5), but are not necessarily linked to any tidal bedding, i.e., to tidal currents and to tidal slack water, in this case (Reinieck & Wunderlich, 1968). Their formation is rather linked to local changes in stream velocity that leads to the deposition of the silt fraction in these river-dominated delta deposits (Sundborg, 1956: their Fig. 13). The clay-rich sections were formed by flocculation from hypopycnal suspensions widely distributed in the basin, while silt to fine sandstones (fsaS, Fig. 2.4 K) might originate from flooding events of nearby rivers (Guion, 1987). A further separation of a brackish estuarine environment and lacustrine environment may be inferred from the fossil record (Süss et al., 2000), which is not considered in this study. The frequent occurrence of sideritic clay-ironstone nodules and layers might be related to the deposition in a more enclosed basin, in which sapropelic mudstones form and faunal remains decline. In consequence of this setting, a combination of iron reduction and microbial methanogenesis causes alkalinity and iron concentrations to rise, promoting precipitation of either siderite or ferroan carbonate, depending on the presence of other mineral species (e.g. Coleman, 1985). The incursions of structureless fine-grained clastics (siS and fsaS) into the mudstone may be interpreted as crevasse splays (David, 1987). These fine-grained sediments are deposited by the spreading with high energy, as the levee bank breaches during flood periods, which normally separates the delta plain from the fluvial channel, away from the breach in the levee bank. In the lower delta plain the frequency of crevassing increases because of lower depositional stability and flatter, more narrow levees, separating the distributaries of the lower delta plain from the surrounding bays and marshes compared to the higher, wider levee banks flanking the channels in the upper delta plain (Diessel, 1992).

2.7.1.4 Lower delta plain (wetlands)

Usually, rooted mudstones (mR, Fig. 2.4 M), and to a minor degree siltstones (siR, Fig. 2.4 L), of the floodplain sediments are underlying the coal seams (c, Fig. 2.4 N). These rooted facies indicate a rising of the groundwater table, prior to peat formation in wetlands. Following Teichmüller & Teichmüller (1982), coal deposits derive from autochthonous peats which accumulated in mires. Besides terrestrialization by infilling shallow lakes, paludification by swamping poorly drained areas, e.g., flood plains of rivers, are the two main processes leading to the formation of mires (Boron et al., 1987). However, swamp formation in the Late Carboniferous is related to paludification, while ideal conditions for the formation of extensive mires prevailed during Westphalian A and early B (Strehlau, 1990). Sedimentation mainly took place in the transitional zone from the lower to the upper delta plain throughout the Westphalian A and the early Westphalian B, while during the late Westphalian B and C sedimentation shifted towards fluvial conditions (Drozdzewski, 2005). For the draping black mudstone (mS, Fig. 2.4 I), which forms the top of the logged strata (appendix A-C), lacustrine and shallow lagoonal facies are considered as depositional sites, after drowning of the swamp. Its black colour is associated with a high amount of organic material, mainly of plant origin that could be preserved in the waterlogged sediments under reducing (sapropelic) conditions. Furthermore, Strehlau (1990) states that these roof strata including sapropelic coals, as the uppermost part of the seam, demonstrates that peat formation was terminated by the rising of the groundwater table and prevented plants from growing. Reducing conditions are deduced from the presence of sideritic clay-ironstone nodules, in consequence of bacterial sulphate reduction (Morad et al., 1998).

2.7.1.5 Vertical succession

Cyclically occurring sandstones, siltstones, and claystones are categorized into different delta facies by their lithology and sedimentary structures of the studied core material. They represent a typical Upper Carboniferous sedimentary succession of a Variscan foredeep basin, demonstrating coarsening- and fining-upward trends. The occurring sedimentary facies succession can be represented by an upward lithological transition as follows: Calcareous claystone of the subaqueous prodelta draping coal; laminated siltstone and sandstone of the distal and proximal delta front; wave and current rippled siltstone formed on the shallow subtidal lower delta plain; rooted silt- and mudstone beds overlain by coal demonstrate the subaerial peat swamps of the wetlands (Fig. 2.2 and Tab. 2.1). Reversible and alternating transitions occur frequently between some lithologies. In general, this order of sedimentary succession is closely comparable with that suggested for the Upper Carboniferous sedimentary cycles in England (Elliott, 1976; Guion, 1987), and the coarsening-upward and shallowing-upward succession of a Cenomanian deltaic sandstone from New Mexico (Van Yperen et al., 2019). Likewise, it matches with the concepts of deltaic cycles presented by Casshyap (1975) and Süss et al. (2000). According to these concepts, the sedimentation pattern is controlled by the interplay of sediment inflow, basin subsidence, and eustatic sea-level changes. Further autocyclic

sedimentation, especially on the delta plain, plays part in the lateral and vertical distribution of sedimentary facies (Süss, 2005).

2.7.2 Petrophysical data and v_P

Generally, the porosities measured in this study range between 0.3 and 15.6 %. They are in the same range as subsurface Westphalian B/C samples from the Ibbenbüren district 80 km to the north (1 to 10.9 %, Quandt et al., 2022b), Westphalian C/D samples from two tight gas reservoirs (1.8 to 16.9 %, Busch et al., 2019) but lower than outcrop samples from the Westphalian C/D (15 to 30 %, Becker et al., 2019; Becker et al., 2017) from the Schafberg region near Ibbenbüren.

Permeabilities from this study range between 0.0001 and 2.46 mD and are in the same range as the subsurface Westphalian B/C samples from Ibbenbüren (0.0001 to 1.6 mD, Quandt et al., 2022b) and outcrop samples from the Westphalian C/D (0.001 to 0.1 mD, Becker et al., 2019) indicating that most samples can be classified as tight (Pusch et al., 2005). Permeabilities are lower than in Westphalian C/D samples from two tight gas reservoirs in the Lower Saxony Basin, (0.01 to 40.47 mD, Busch et al., 2019) but high permeabilities are due to open fractures. Matrix permeability, however, is in the same range as the values of this study.

Similarly, measured v_P values between 2886 and 5663 m/s are within and slightly below the range recorded for Westphalian B/C sandstones from Ibbenbüren. Nevertheless, the measured v_P velocities are in good agreement with the v_P values from Upper Carboniferous sandstones and siltstones of northeast England (Best et al., 2007), ranging from 3266 to 6299 m/s.

The wide ranges of v_P and porosity data suggest that these values are the consequence of an interaction between several parameters. A linear correlation between v_P and porosity values could be shown (Fig. 2.5 C and D). This supports the findings by Stewart & Peselnick (1977, 1978), who investigated v_P velocities of various sedimentary and metasedimentary rocks at high pressure and temperature of 8 kbar and 300°C, respectively. Their results display that v_P depends on bulk density (which is reciprocal to porosity) but only weakly on the mineralogy of sandstones. The presence of clay/organic-rich laminations or coal flakes and plant remains (Best et al., 2007) may result in lower v_P values of samples of the lower delta plain and wetlands (Fig. 2.5 D). Further, v_P values in fine-grained or laminated samples of these facies associations might be lower due to preferential alignment of microfractures opening at ambient pressure (Best et al., 2007). However, the wide range in v_P values (2886 to 5663 m/s) and porosity (0.9 to 15.6 %) are not only dependent on sedimentary attributes such as grain size, as indicated by similar v_P values in sandstones (mean 3869 m/s), siltstones (mean 4327 m/s) and mudstones (mean 4183 m/s) (Fig. 2.5 C). In general, velocity-density correlations for sandstones improve significantly when the samples are categorized by their clay content (Han et al., 1986; Miller & Stewart, 1991). This matches our macroscopic estimation of the clay/grain ratio in the measured plugs, as plugs with low velocities have high contents of sheet-silicates.

Thus, knowledge of the target lithologies may enable using v_P data to derive lithological information and ranges of porosity.

2.7.3 Thermal conductivity

Generally, the recorded thermal conductivities are in good agreement with values of thermal conductivities from Mesozoic sandstones of the Northeast German Basin that range from 3.4 to 7.4 W/(m×K) even though their porosities (16 to 30 %) are much higher (Fuchs & Förster, 2010). Thermal conductivities from Jurassic and Triassic sandstones (1.2 to 2.4 W/(m×K)) of the Upper Rhine Graben (Harlé et al., 2019) are slightly below the values of this study, but porosities are much higher (3 to 35 %). Our results demonstrate that thermal conductivity is highest for sandstones with a steep gradient (b=0.00078 Tc/v_P). For relatively low thermally conductive siltstones and mudstones the gradient is less steep with b=0.00035 and b=0.00015, respectively (Fig. 2.5 F). Similarly to the grain size, for the facies associations thermal conductivity is highest for the sand dominated delta front deposits with a steep gradient (b=0.00077 Tc/v_P), while for relatively low thermally conductive silt and clay dominated samples of the lower delta plain and wetland gradients (b=0.00015 and b=0.00011 Tc/v_P) are lower compared to gradients of silt- and mudstones (Fig. 2.5 F and G). This observation emphasizes that thermal conductivity is dependent on lithology, but still there is no characteristic conductivity for a given lithology which is supported when comparing these results with the range of thermal conductivity values for sandstones (0.9 to 6.6 W/(m×K)) or siltstones (0.7 to 4.0 W/(m×K)) provided by Čermák & Rybach (1982). Samples of the delta front with the highest values of thermal conductivity seem to be related to a high quartz content, relative to feldspar, mica, and shale clasts. This observation is in agreement with macroscopically observed frequent grain/grain contacts of quartz and/or quartz-rich rock fragments. Thus, the quartz content is regarded to be a significant influence on the thermal conductivity, since quartz has ideal heat transmission characteristics, leading to high thermal conductivity, especially parallel to its optical c-axis (Clauser & Huenges, 1995). In contrast, the low thermal conductivity of clay and silt dominated deposits (Fig. 2.5 F) of the lower delta plain and prodelta may be related to the presence of organic matter, i.e., coal flakes and plant remains or sheet-silicate minerals, such as clays and micas that are characterized by low thermal conductivities (Clauser & Huenges, 1995; their Tab. 3). Furthermore, Labus & Labus (2018) demonstrate that the thermal conductivity measured on fine-grained sedimentary rocks parallel to bedding is usually 1.5 to 3.8 times higher than perpendicular to bedding and that this anisotropy is related to the presence of laminae of e.g., organic matter and sheet-silicates. This is also shown for sheet-silicates (i.e., muscovite, biotite and phlogopite), where thermal conductivity parallel to the crystal planes is up to 9 times higher than in perpendicular direction (Gray & Uher, 1977; Horai & Simmons, 1969). Therefore, mudstones or claystones may add to an anisotropic thermal conductivity in the studied area.

The general correlation of thermal conductivity and v_P values (Fig. 2.5 F, G) very likely corresponds to the porosity, which is confirmed by the results discussed before (Fig. 2.5 C, D). Thus, porosity is a predominant control on the thermal conductivity of the studied samples (Fig. 2.6 A, B). The variation in gradient values of the presented trends is related to the difference in mineralogy in contrast to the low thermal conductivity of water (0.6 W/(m×K); Clauser & Huenges, 1995; their Fig. 7) filling the pores. Thus, the steep gradient for sandstone samples may results from the high thermal conductivity contrast between quartz (7.7 W/(m×K); Clauser & Huenges, 1995; their Fig. 7) and water. The flat gradient for silt- and mudstone samples may result from the lower thermal conductivity contrast between non-quartz minerals (1.5 to 5 W/(m×K); Clauser & Huenges, 1995; their Fig. 7). Hence, for less porous sandstone samples (high v_P values) the influence of porosity becomes less pronounced and thermal conductivity depends more on the mineralogy. This behaviour has also been observed in previous studies (Harlé et al., 2019; Popov et al., 2003).

Additional diagenetic factors (including compaction) controlling porosity and permeability, such as cementation or dissolution of unstable minerals and rock fragments (i.e., feldspars) that may also influence the thermal conductivity, may further be evaluated. When taking permeabilities of investigated samples into account no correlation is observed (Fig. 2.6 C and D). However, in the Upper Carboniferous sedimentary rocks, permeabilities show little correlation with porosity (e.g., Becker et al., 2019). Differences in permeabilities are mostly due to clay mineral contents (Busch et al., 2019), or carbonate cement dissolution in outcrops (Becker et al., 2019), which were not considered here.

According to Harlé et al. (2019) for more porous samples, the disparity of the thermal conductivity measured in dry and saturated states is more significant, as the effect of water saturation strongly depends on the porosity of the sample and very little on the sample's mineralogy. This relationship has already been observed in sedimentary rocks by Popov et al. (2003). In a few high porosity samples of the present study, the increase from unsaturated to saturated thermal conductivity is very pronounced, partly supporting this statement.

The best R^2 values for correlations between thermal conductivity and v_P are observed when the grain sizes of the samples are considered (sandstones R^2=0.81, siltstones R^2=0.84 and mudstones R^2=0.42). In contrast, the consideration of facies provides less good R^2 values (delta front R^2=0.82, the lower delta plain R^2=0.24 and the wetlands R^2=0.18). The only exception are sandstones and delta front samples, which are characterized by very similar R^2 values. This suggests that, apart from the delta front category, the classification in facies associations is less suitable to be integrated with measured rock properties than the classification in grain sizes. This may be related to the similarity of fine grain sizes of the lower delta plain and the wetland deposits whereas delta front sandstones are distinctively coarser grained. The combination of measured petrophysical properties, including thermal conductivity, with sedimentological facies and facies associations represents a standard workflow in industry and applied research (Busch et al., 2019;

Wimmers & Koehrer, 2014). However, thermal conductivity can only be integrated into 3D reservoir models with constraints. Nevertheless, for potential reservoir modelling and simulation, facies associations still may be useful, when it is necessary to simplify the complex architecture of facies encountered in reservoir sections (e.g., Bushell, 1986; Harding et al., 2005).

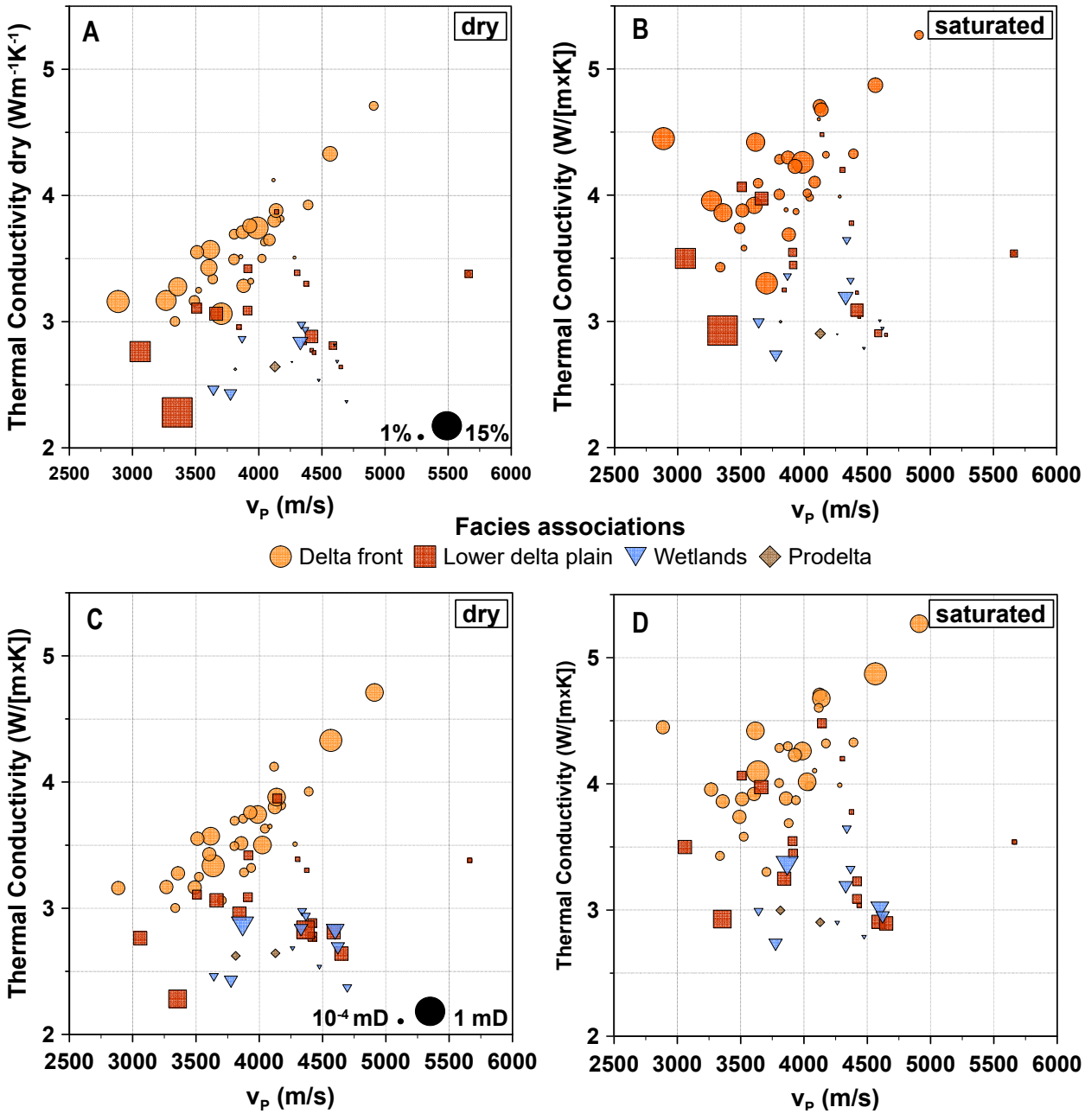

Figure 2.6 Cross plot for the depositional environments (sand dominated delta front, silt dominated lower delta plain and mud dominated wetlands and prodelta) of thermal conductivity versus v_P for dry conditions (**A, C**) and saturated conditions (**B, D**). Symbol size indicates porosity in **A, B** and permeability in **C, D**.

2.7.4 Implications for post-mining geothermal applications

Various factors control the temperature structure in sedimentary basins (Blackwell & Steele, 1989 : their Tab. 2.1). Particularly, the thermal conductivity has a major impact on the temperature distribution. Blackwell & Steele (1989) highlight the importance of understanding the thermal conductivity of the lithological facies in a sedimentary basin before attempting to understand its temperature distribution. Thus, the Upper Carboniferous cyclic deposits need to be characterized to accurately assess the geothermal potential of the Ruhr area. Comparison with literature data for sandstone (mean 2.47 W/(m×K)), siltstone (mean 2.04 W/(m×K)) and claystone (mean 2.46 W/(m×K)) from Čermák & Rybach (1982) shows that the mean thermal conductivity provided here for sandstone of the delta front environment, for siltstones of the lower delta plain and mudstones of the prodelta are about 40 %,40 % and 6 % higher, respectively. Lower thermal conductivity of mud- and siltstone is at the upper end of the range recorded for similar lithologies in North Rhine-Westphalia (Fig. 2.5 D). Yet, the thermal conductivity of claystone appears to be within error margins of 50 to 100 % (Blackwell & Steele, 1989). Since clay-, mudstones and laminated siltstones form a significant fraction of the sedimentary succession of the basin, accurate subsurface temperature-depth predictions cannot be made if the thermal properties of these units are not well understood. Nevertheless, relatively high thermal conductivities of i.e., sandstone beds seem to be promising for post-mining geothermal applications.

Previous studies demonstrated that the thermal conductivity of rocks (in dry conditions) tends to decrease with increasing temperature (Clauser & Huenges, 1995; Guo et al., 2017; Harlé et al., 2019). Although temperature is a major factor that influences the thermal conductivity of rocks, the decrease in thermal conductivity with increasing temperature seems nonlinear (Guo et al., 2017), which makes it problematic to extrapolate. Harlé et al. (2019), however, demonstrated a linear trend for temperatures between 18 to 160°C that could be used to compute an estimated thermal conductivity at an assumed temperature. Regardless, measurements at appropriate in-situ temperatures may be essential for a conclusive thermal conductivity assessment.

In a complex geological setting, such as the Ruhr Basin, thermal conductivity patterns may be affected by vertical variations in a layered section or due to lateral juxtapositions of contrasts in thermal conductivity associated with folds and faults. Nevertheless, because of the low porosity of most Upper Carboniferous clastic deposits of the Ruhr Basin, it is inferred that most lithological units are tight and fluid flow is limited through low matrix permeability. Thus, upcoming post-mining applications (i.e., geothermal use) will rather rely primarily on permeable faults and fracture systems or old mine infrastructure. According to Allgaier et al. (2023) and Niederhuber et al. (2023) a fault and fracture strike of N-S and NW-SE is most likely to present a suitable strike orientation for advective fluid transport as they are nearly to critically stressed in the in-situ stress state in the Ruhr Basin resulting in higher dilation tendency.

2.8 Conclusion

In the three studied cores of the Westphalian A and B, sand-, silt-, mud- and claystones occur in 20 to 40 m thick cycles and exhibit a typical sedimentary succession of the Ruhr Basin. In most cycles, basal coal seams are unconformably overlain by 10 to 17 m thick sandstone beds of the delta front followed by up to 4 m thick fining- and shallowing-upward successions of silt- and mudstones of the lower delta plain and the supratidal wetlands. The cycles end with coal (up to 3 m thick) that is locally draped with up to 1 m thick mudstone beds. Generally, the thickness of sandstone, siltstone and mudstone lithologies varies between the studied cycles but no overall thinning or thickening pattern of the sequences between the cycles nor the cores is observed. The porosity and permeability range from 0.9 % to 15.6 % and 0.0001 mD to 2.46 mD, respectively. The value ranges are related to grain size variations and the facies associations. Sandstone dominated delta front deposits show high porosity and permeability values (mean 6.8 %; 0.18 mD), while properties in siltstone dominated lower delta plain deposits (mean 4.6 %; 0.03 mD), mudstone dominated wetland deposits (mean 3.9 %; 0.21 mD) and prodelta deposits (mean 3.6 %; 0.0005 mD) are lower. v_P values range from 2886 to 5663 m/s and are mainly dependent on the porosity and only weakly controlled by mineralogy. Sedimentary attributes e.g., grain size have little impact, as indicated by similar v_P values in sandstones (mean 3869 m/s), silt- (mean 4327 m/s) and mudstones (mean 4183 m/s). Samples of the delta front with the highest values of thermal conductivity ranging from 3.0 to 4.7 W/(m×K) in dry conditions and from 3.3 to 5.3 W/(m×K) in saturated condition are related to a high quartz content. The low thermal conductivity of silt and mud dominated deposits of the lower delta plain (2.33.9 W/(m×K); 2.94.5 W/(m×K)) and wetlands (2.4 to 3.0 W/(m×K); 2.7 to 3.6 W/(m×K)) is probably due to the presence of organic matter and sheet-silicates. The thermal conductivity in saturated conditions is on average 15 % higher than in dry conditions, and ranges from 2.7 to 5.3 W/(m×K) compared to 2.3 to 4.7 W/(m×K) in dry samples. While porosity is considered to be the major influence on thermal conductivity values, for less porous samples the influence of the porosity becomes less pronounced and depends more on the mineralogy. High values (2.7 to 5.3 W/(m×K)) of the Upper Carboniferous samples seem promising for potential geothermal applications. Furthermore, the comparison of the results from this study indicates that the classification into facies associations is less suitable to be integrated with measured rock properties than the classification into grain sizes. Yet, for potential reservoir modelling and simulation, facies associations still may be useful when it is necessary to simplify the complex facies architecture encountered in reservoirs. The up to 17 m thick sandstones of the investigated cores have a porosity of 2.2 to 15.6 % but low permeabilities of 0.0001 to 2.46 mD, which is considered tight. Thus, mine flooding is mainly restricted to galleries and shafts. Thus, post-mine geothermal utilization will rather rely on permeable faults and fracture systems around abandoned mine galleries and the mine galleries themself.

Remark: For additional methodological considerations, see appendix A

3 The influence of sedimentary facies, mineralogy, and diagenesis on reservoir properties of the coal-bearing Upper Carboniferous of NW Germany

3.1 Abstract

Former coal mines hosted in Upper Carboniferous silt- and sandstones in the Ruhr Basin, NW Germany, are currently examined for post-mining applications (e.g., geothermal energy) and are also important tight-gas reservoir analogs. Core material from well Pelkum-1, comprising Westphalian A (Bashkirian) delta deposits, was studied. The sandstones and siltstones are generally tight (mean porosity 5.5 %; mean permeability 0.26 mD). Poor reservoir properties primarily result from pronounced mechanical compaction (mean COPL 38.8 %) due to deep burial and high contents of ductile rock fragments. Better reservoir properties in sandstones (> 8 %; > 0.01 mD) are due to (1) lower volumes of ductile grains (< 38 %) that deform during mechanical compaction and (2) higher volumes in feldspar and unstable rock fragments. During burial these form secondary porosity (> 1.5 %) resulting from acidic pore water from organic matter maturation. Still, sandstones with enhanced porosities only show a small increase in permeability since authigenic clays (i.e., kaolinite and illite) or late diagenetic carbonates (i.e., siderite and ferroan dolomite/ankerite) clog secondary porosity. Quartz cementation has a minor impact on reservoir properties. Evaluating the Si/Al ratio can be a suitable proxy to assess grain sizes and may be a convenient tool for further exploration.

3.2 Introduction

Over the past years, natural gas production from unconventional reservoirs has risen worldwide since innovations in horizontal drilling and hydraulic fracturing enabled their development (Conti et al., 2016). Understanding the variability in reservoir properties (porosity and permeability), their spatial distribution, and driving mechanisms forming tight reservoirs can be highly complex, and the standard workflows for conventional reservoir characterization may not be appropriate for unconventional reservoirs (Wimmers & Koehrer, 2014). Poor reservoir properties often result from deep burial processes involving mechanical and chemical compaction. However, they can significantly depend on secondary porosities from mineral

alteration (e.g., Becker et al., 2019; Higgs et al., 2007) or permeabilities that often are enhanced by natural open fractures (Becker et al., 2017; Busch et al., 2019).

The Ruhr and Lower Saxony Basins in NW Germany contain tight sandstones from the coal-bearing Upper Carboniferous (Littke et al., 2011). In the Lower Saxony Basin, studies on Upper Carboniferous tight gas reservoir analogues (e.g., Wüstefeld et al., 2017), as well as borehole samples (e.g., Busch et al., 2019; Quandt et al., 2022b), evaluated its tight gas potential including past exploration attempts which were shown to be successful (Hedemann, 1985; Kombrink et al., 2010; Pasternak et al., 1998). However, little is known about the tight gas potential of the Upper Carboniferous of the Ruhr Basin, even though the region is one of the world's best-documented subsurface 3D rock volumes due to widespread hard coal mining over centuries until 2018 (Brix et al., 1988; Casshyap, 1975; Drozdzewski, 1992, 1993; Strehlau, 1990; Teichmüller & Teichmüller, 1982; Wrede & Ribbert, 2005). Previous studies provided little porosity and permeability data from Upper Carboniferous outcrop samples of the Ruhr Basin (Brenne, 2016; Duda & Renner, 2013; Stöckhert et al., 2015). Recently, Greve et al. (2023) provided porosity and permeability values from borehole samples from three wells in the Ruhr Basin, evaluating their impact on the geothermal potential of the strata. While studies on diagenetic sequences for the Upper Carboniferous exist for the Lower Saxony Basin (e.g., Busch et al., 2019), diagenesis and controls on reservoir properties in the Ruhr Basin are poorly understood.

This study aims to provide additional subsurface data, including a paragenetic sequence based on petrography, and to identify sedimentary and diagenetic controls on reservoir properties using point count data. Lithological units based on sedimentary core description (Greve et al., 2023) are adopted to identify the depositional environments. Using a published burial history scenario (Bruns et al., 2013), the relative timing of diagenetic modification can be related to the tectonic and thermal development of the studied area. Furthermore, petrographic observations are supported by X-ray powder diffraction (XRD) data. X-ray fluorescence (XRF) data is provided and compared with point count data to identify suitable geochemical proxies to evaluate reservoir properties.

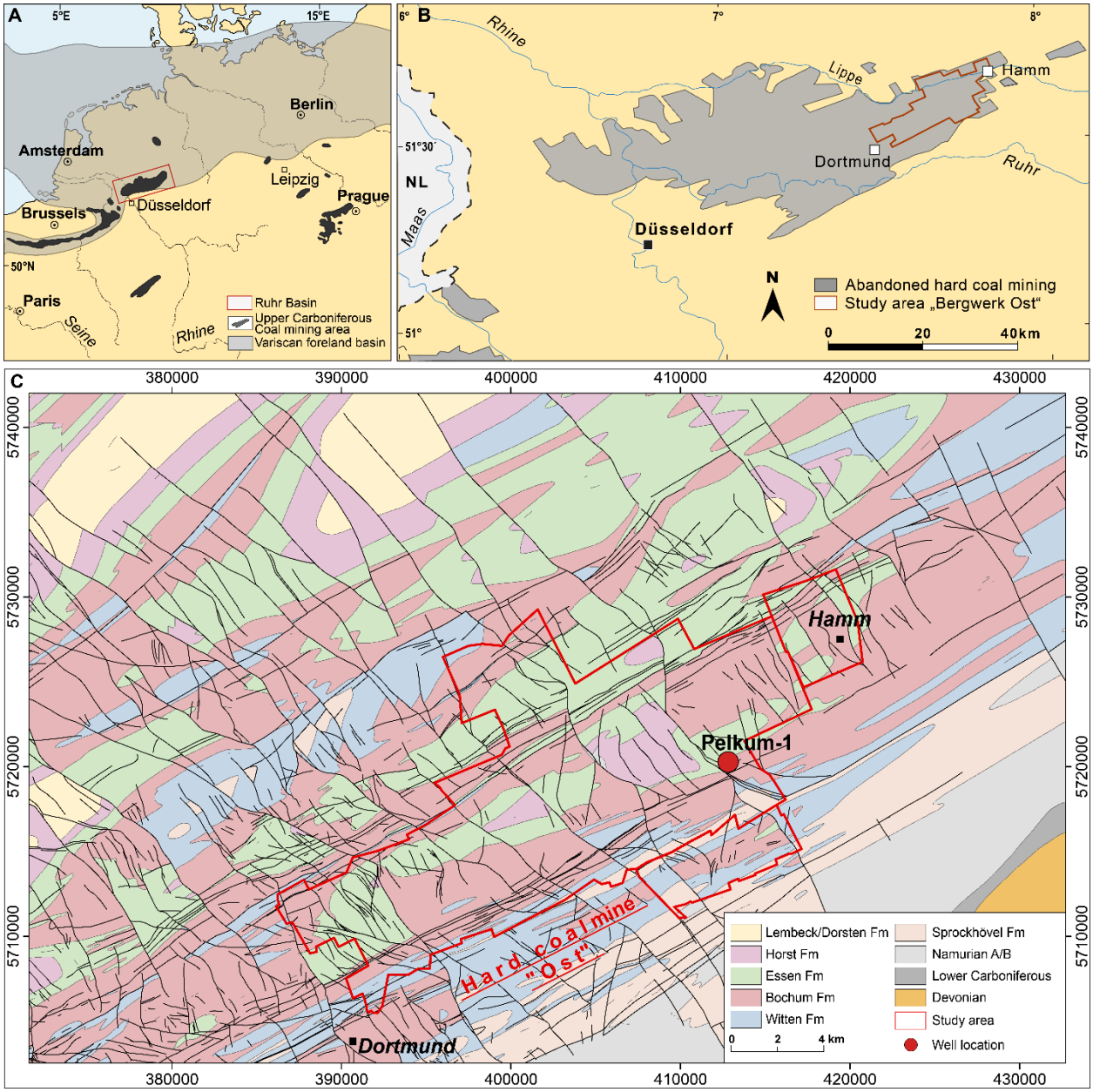

Figure 3.1(**A**) The Variscan foreland basin in NW Europe with locations of Upper Carboniferous coalfields, modified from Jasper et al. (2009). (**B**) The Ruhr Basin in NW Europe with locations of abandoned Upper Carboniferous coal mines, modified from Thielemann et al. (2004). (**C**) Location of the exploration well Pelkum-1 (mine Bergwerk Ost; modified from the Geological Map of the Carboniferous of the Ruhr area 1:100.000, Geological Survey North Rhine-Westphalia, 1982).

3.3 Geological setting

The Ruhr Basin in Germany outlines a narrow, 150 km long and 80 km wide, NE-SW trending foreland molasse-type basin NW of the Rhenish Massif and represents the Variscan orogenic foredeep in central Europe. The basin formed during the Late Carboniferous (Pennsylvanian) (Drozdzewski, 1992, 1993; Gayer et al., 1993) and comprises a 4000 m thick Upper Carboniferous clastic succession. The succession

consists of cyclically deposited clay-, silt-, and sandstones of fluvio-deltaic to paralic origin containing about 250 coal seams (Drozdzewski, 1993; Süss et al., 2007). While fourth-order sequences (400 ka) and fifth-order parasequences (112 ka) or sequences of higher periodicity (Süss et al., 2000) are initiated by the growing and shrinking of the Gondwana ice shield (Rygel et al., 2008), an overall coarsening-upward trend is noticeable throughout the Westphalian (Drozdzewski, 2005; Süss et al., 2007: their Fig. 2). This change in sedimentary facies from marine through paralic to continental deposits is apparent in the Variscan foreland basins of NW Europe during the Pennsylvanian (Gayer et al., 1993; Guion, 1987; Guion & Fielding, 1988; Süss et al., 2007).

The deformation of the Ruhr Basin is of post-Westphalian age and originated from the progressively northwestward migration of the Variscan orogenic belt (Brix et al., 1988). At its southern margin, the Upper Carboniferous strata overlie the northern front of the Rhenish Massif and exhibit Variscan thrusting and folding (Drozdzewski, 1992, 1993; Drozdzewski & Wrede, 1994; Gayer et al., 1993). Different periods of active faulting are indicated by the post-Carboniferous strata of the Ruhr Basin, overprinting the pre-existing Paleozoic and later Mesozoic structural framework (cf. Arfai et al., 2014; Vinken, 1988). Variscan thrusts strike NE-SW parallel to the fold axes, while NW-SE striking normal faults were formed partly at the end of the Variscan deformation and partly before and during the Zechstein (Lopingian) (Geluk, 1999; Wolf, 1985). Northwards, the Upper Carboniferous of the Ruhr Basin is unconformably covered by an Upper Cretaceous overburden with up to 2000 m thickness in the Münsterland region that consists of shallow-marine strata.

3.3.1 Lithological units

The studied core material was retrieved from well Pelkum-1 located within the study area (Fig. 3.1 A) in the eastern Ruhr district, Germany (Fig. 3.1 B). Well Pelkum-1 reaches a depth of 1221.7 m and encounters the typical clastic succession of the coal-bearing Upper Carboniferous Bochum Formation of the Westphalian A (Bashkirian; Langsettian Substage) at 465.6 m (Fiebig, 1971) (Fig. 3.1 C). Based on three sections of 24 to 60 m in length that stratigraphically cover the middle and upper Bochum-Formation, cyclically occurring sandstone, siltstone, and claystone are categorized into different delta facies by their lithology and sedimentary structures (appendix A), demonstrating coarsening- and fining-upward sequences (Greve et al., 2023). This sedimentation pattern is controlled by the interplay of sediment inflow, basin subsidence, and eustatic sea-level changes (Casshyap, 1975; Süss et al., 2000). Greve et al. (2023) provide a characteristic sedimentary facies succession for well Pelkum-1 that is represented by an upward lithological transition from up to 30 m thick calcareous claystone of the subaqueous prodelta draping coal seams at the base. Subsequent 13 to 15 m thick parallel and cross-laminated siltstone and sandstone beds of the distal and proximal delta front are interpreted as a complex stacking pattern of estuarine bars and distributary channels. The subsequent up to 4 m thick wave and current rippled siltstone formed on the

shallow subtidal lower delta plain and is overlain by 3 m thick rooted silt- and mudstone beds. It marks the development into a more proximal shallow environment, which transitioned into a stagnant water zone, where bioturbation can be apparent. Localized root marks and the overlying up to 3 m thick coal seam represent the subaerial peat swamps of the wetlands. Aside from this provided succession (cf. Fig. 2 and Tab. 1 in Greve et al., 2023), other Upper Carboniferous sedimentary cycles in England are closely comparable (e.g. Guion, 1987).

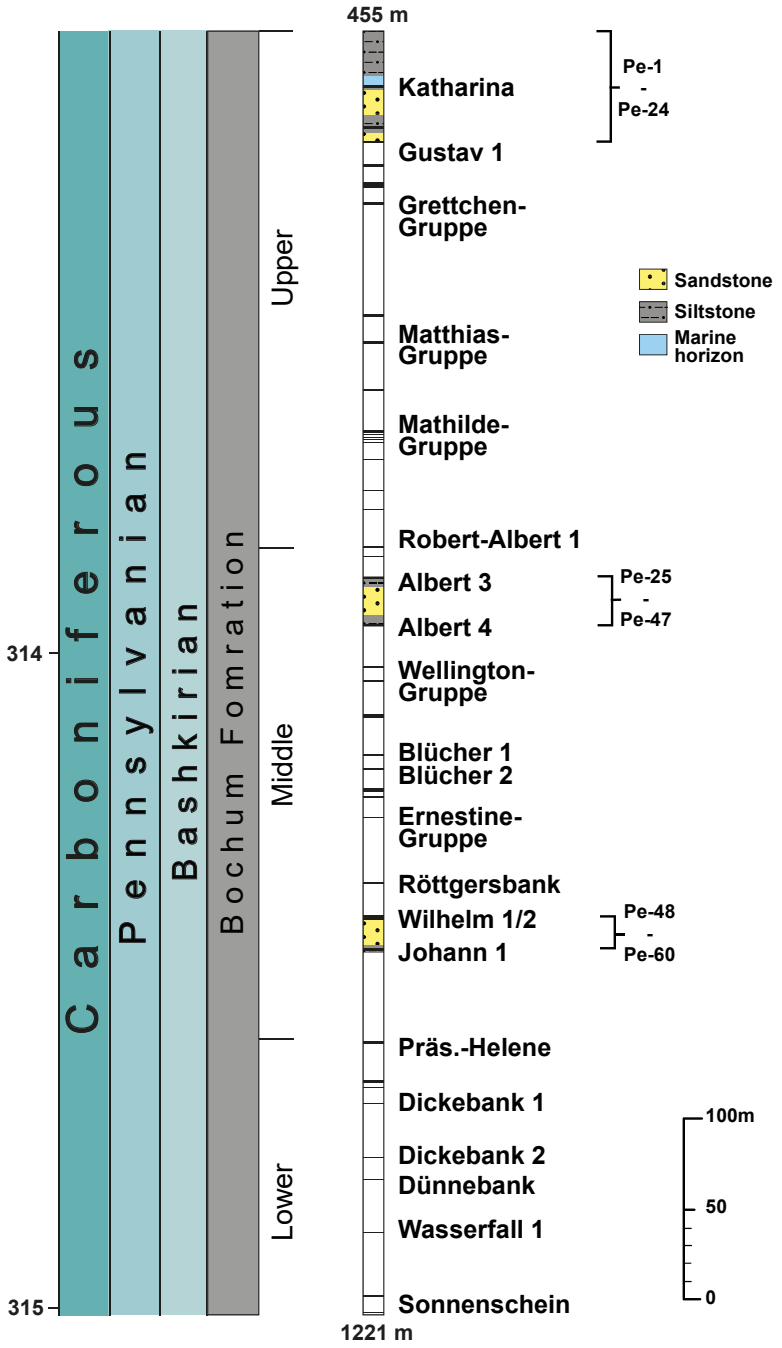

Figure 3.2 Stratigraphic column (colour code for formations as in Fig. 3.1 B) including a simplified lithological column comprising all relevant coal seams (black lines) of well Pelkum-1. Yellow, blue and grey coloured sections indicate the studied cycles. Modified and redrawn after Fiebig (1971).

3.4 Materials and methods

A total of 60 cylindrical plug samples (2.51 cm diameter and 1.4 to 3.5 cm length) with their cylindrical axis aligned parallel to bedding were prepared from the available core material (appendix D.1). Trim ends of 39 plug samples were embedded in blue dyed epoxy resin to prepare 30 µm thick thin sections, which were half stained with a combined alizarin red S and potassium ferricyanide solution in 0.3 % HCl to aid in identifying carbonate minerals (Dickson, 1965). Individual samples (Pe-1 and Pe-15) were polished for further reflected light and cathodoluminescence (CL) analyses.

The long axes of 150 grains per thin section were measured (appendix D.1) using a regularly spaced grid that covered the entire thin section to gain area-weighted grain size data. Grain size parameters such as sorting, mean, and median diameter were calculated after (Folk & Ward, 1957). Grain sizes are classified after Udden (1914) and Wentworth (1922). Roundness (Tucker, 2001) was determined using standardized comparison charts.

For a quantitative evaluation, 300 points per thin section have been counted using a Pelcon Automatic Point Counter mounted on a Zeiss DM 2700. The step size was adjusted to the maximum observed grain size (Busch et al., 2017).

Point-counting data were further used to derive the intergranular volume (IGV) as an indicator for compaction, as the sum of intergranular porosity, intergranular cement, and depositional clay mineral matrix (Paxton et al., 2002). To further assess the compactional (COPL) and cementational porosity loss (CEPL), as well as the compactional index (Icompact), point-counting data were processed according to Lundegard (1992). Initial porosity (Pi) values of unconsolidated sands range between 27.9 and 42.4 %, considering different sorting and grain size (Beard & Weyl, 1973). Therefore, sample partitioning in terms of sorting (among poorly and moderately sorted samples) was done to circumvent the impact of different initial porosities (appendix D.1). Yet, to illustrate the relative influence of compaction and cementation on porosity loss, an initial porosity of 40 % was consistently assumed for calculations. This decision does not change the outcome when compared to varying initial porosities.

To further assess carbonate vein cements, CL investigations were conducted on two polished thin sections (Pe-15 and Pe-54.2), using a CITL Mk5 Optical Cathodoluminescence Microscope Stage mounted on a Leitz Dialux Microscope equipped with a Jenoptik Gryphax Naos camera (e.g., Monsees et al., 2020). The electron beam current and voltage were adjusted to excite luminescence (325-350 µA, 15 kV for carbonates, 20 kV for quartz). CL emissions depend mainly on the crystal structure, lattice defects, and distribution of trace elements (Götze et al., 2013).

Porosity was measured on 30 samples for this study using a Micromeritics™ AccyPyc II 1340 Helium-pycnometer (Becker et al., 2017) on core plugs at the Karlsruhe Institute for Technology (KIT).

Permeability was measured on the same plugs at 12 bar confining pressure using dry, oil-free lab air (80 % N_2, 20 % O_2) as permeant in a Westphal Mechanik permeameter (Busch et al., 2022) at KIT and was Klinkenberg-corrected.

Whole rock element data were determined by X-ray fluorescence (XRF) at the Geological Survey of North Rhine-Westphalia, Krefeld, Germany, using a Spectro Xepos He X-ray spectrometer. 18 samples from the deltaic facies associations from core material were crushed into pieces of < 2 mm and then powdered using an agate mill. The sample powder was annealed before mixing with lithium tetra/metaborate and fused in platinum crucibles at 1150°C to prepare fused discs. Loss of ignition (LOI) was determined gravimetrically by heating the samples to 1050°C. Total iron is expressed as Fe_2O_3. The concentration of $CaCO_3$ was thermally determined. Consequently, siderite is not incorporated since it is thermally unstable compared to calcite and decomposes at 550°C (Bisutti et al., 2007).[2] Following the lithologic identification of sandstone, mudstone (shale) based on element logging (Yin et al., 2018; their Fig. 4) the Si+Ca+K/Al+Fe ratio was applied to differentiate between the different facies associations.

To support the petrographical differentiation of carbonate cement and clay minerals, for three samples (Pe-1, Pe-20, Pe-35), X-ray powder diffraction (XRD) data were determined using a Rigaku Miniflex 600 C (Cu anode) with a 2θ scan range of 3 to 80° at a step size of 0.02°. For the sample preparation core material was crushed into pieces of < 2 mm and powdered using an agate mill. The powder was reverse mounted into an aluminium sample holder. The phase identification and the determination of relative phase amounts are done using the Rigaku Smart Lab software.

3.5 Results

3.5.1 Petrography

3.5.1.1 Textural parameters

The analyzed siltstones and sandstones (n=39) are mostly laminated (Fig. 3.3 A), as samples contain aligned elongated constituents (mostly mica or coal flakes, Fig. 3.3 B). The mm-scale bedding (laminae) results from more than one predominant grain size. In contrast, some fine-grained sandstones are structureless (Fig. 3.3 C). Sample P38 is bioturbated, which obliterates any sedimentary texture. On a thin section scale, the bioturbated texture cannot be distinguished from structureless textures (Fig. 3.3 D).

[2] For additional methodological considerations, see Addendum B.

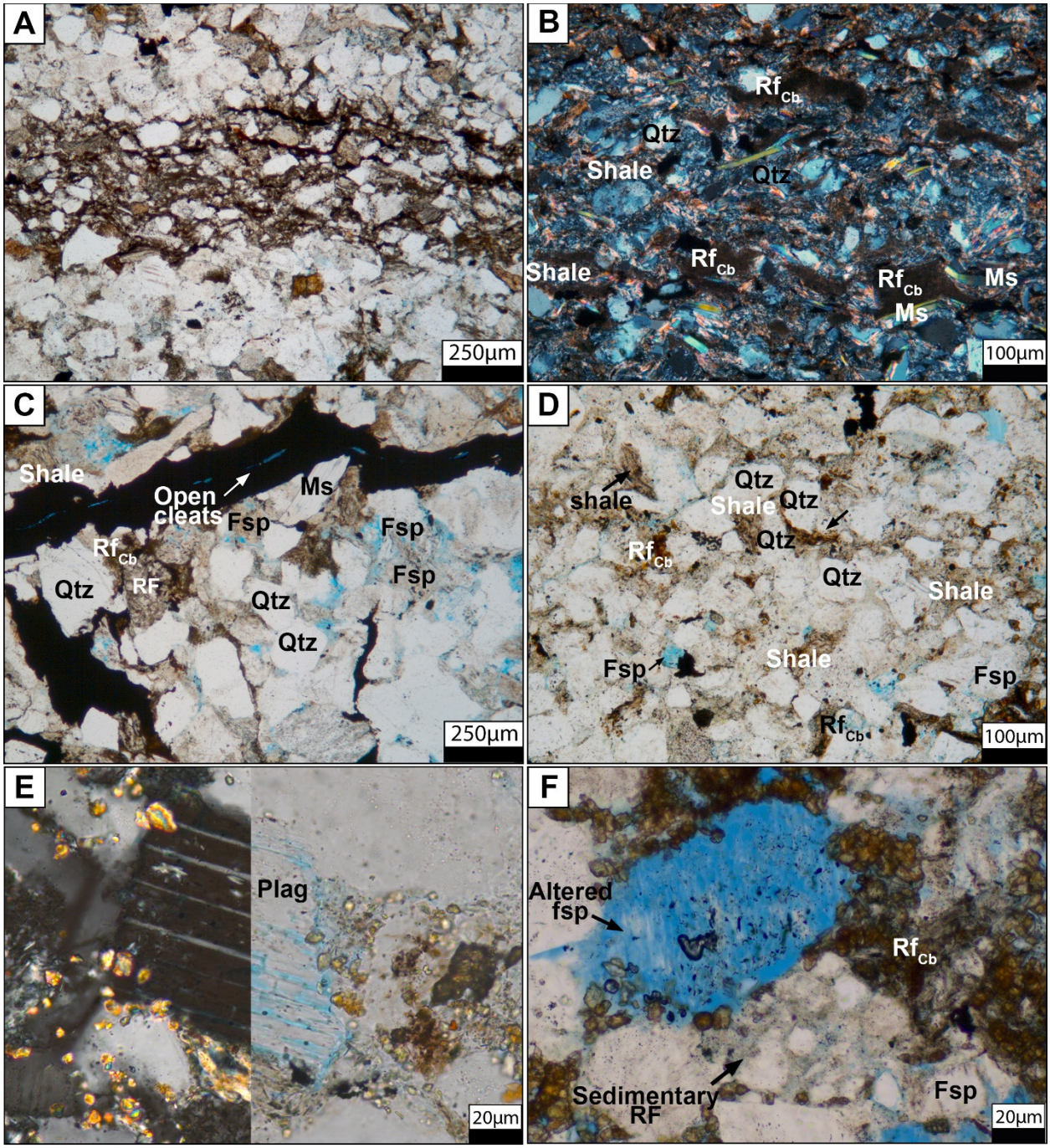

Figure 3.3 Prominent textures in Upper Carboniferous sand and siltstones. (**A**) Lamination in sample Pe-1 shows a change in mineralogical composition, i.e., high occurrence of shales, carbonatic rip-up clasts and stretched constituents (e.g., mica flakes) that are aligned. (**B**) Alignment of elongated stretched micas in an mm-scale lamination texture in sample Pe-44. (**C**) Structureless samples including coal layer (250 µm thick) with open cleats in sample Pe-40. (**D**) Bioturbated texture in sample Pe-6 cannot be distinguished from structureless textures. (**E**) Plagioclase (Plag) exhibits synthetic albite twins in cross-polarized light and has often undergone alteration, resulting in secondary pore space in sample Pe-10. (**F**) Sedimentary rock fragment (siltstone clast with clay cement) in a sandstone sample (Pe-17), classified as sedimentary rock fragment. Qtz: quartz grain, Plag: plagioclase, Fsp: feldspar, RF: rock fragment, RFCb: Carbonatic rip-up clasts, Ms: muscovite.

The sandstones are fine-grained (mean grain size 0.063 to 0.22 mm) and poorly to well sorted, while siltstones are fine to coarse-grained (mean grain size 0.02 to 0.062 mm) and moderately to moderately well sorted. All samples are nearly symmetrical to positively skewed, indicating the grain size distribution to be prone towards the coarser grain sizes relative to finer grain sizes (Fig. 3.4). A positive correlation between increasing grain size and better sorting is noticeable (Fig. 3.4) while no relationship between skewness and sorting or grain size can be established. The grain shape of framework grains is commonly sub-angular to rounded with moderate sphericity.

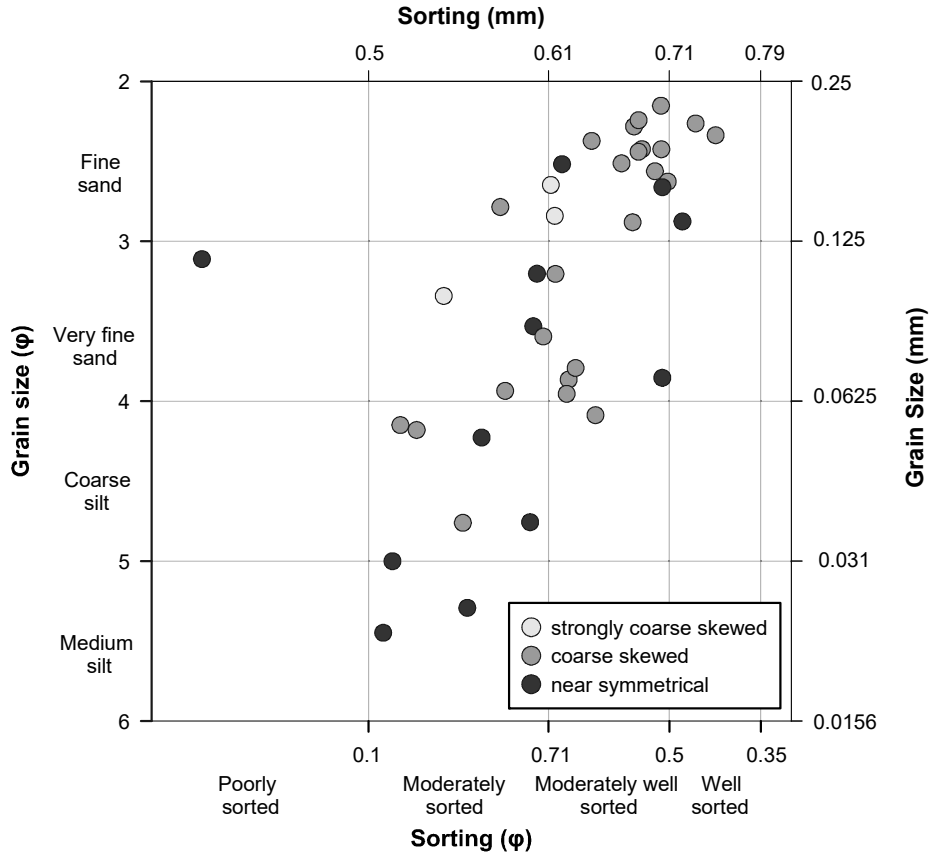

Figure 3.4 The samples are mainly moderately to well sorted and characterized by a nearly symmetrical to strongly coarse skewed, indicated by the gray shades. All thresholds are taken from Folk (1980).

3.5.1.2 Detrital constituents

The detrital grains are composed of monocrystalline quartz (Qm), polycrystalline quartz (Qp), K-feldspar (Kfs), plagioclase (Plag) and rock fragments (R). The latter is further subdivided into metamorphic (MRF), plutonic (PRF), volcanic (VRF), sedimentary rock fragments (SRF), shales, carbonate intraclasts, phyllites, schists, and quartzites. Polycrystalline quartz (Qp) is the most dominant grain type (14.0 to 45.7 %, mean 27.7 %, appendix D.1), while monocrystalline quartz (Qm) is less dominant (6.0 to 25.3 %, mean 12.3 %).

Quartzite, containing quartz subgrains and aligned micas, generally ranges from 0.0 to 3.3 %, with a mean of 1.2 %. K-feldspar grains occur frequently (0.0 to 10.3 %, mean 3.2 %) and prominently contain intragranular pore space (Fig. 3.3 F). Plagioclase exhibits synthetic albite twins in cross-polarized light (Fig. 3.3 E), often showing alteration that includes illitization and intragranular dissolution but is less frequent than potassium feldspar (0.0 to 4.7 %, mean 1.3 %). Shale rock fragments (Fig. 3.3 D) are common in all samples (2.3 to 46.7 %, mean 17.2 %). Especially in siltstones, shale rock fragments appear deformed in a ductile manner and are likely to be embayed by adjacent rigid grains. Siderite clasts (carbonatic rip-up clasts) occur widely (0.3 to 65.0 %, mean 13.0 %) and consist of microcrystalline siderite and clay minerals (Fig. 3.3 F).

Fragments classified as schists are common (0.7 – 8.0 %, mean 3.9 %) and comprise foliated fragments composed of quartz and muscovite. Other typically foliated rock fragments are phyllites (0.3 to 10.7 %, mean 3.6 %). Plutonic rock fragments (Fig. 3.3 C) are common (0.0 to 6.0 %, mean 1.3 %) and the included plagioclase and K-feldspar are partially altered to sericite or dissolved, resulting in intragranular porosity. Rare volcanic rock fragments (0.0 to 3.7 %, mean 0.9 %) contain small euhedral plagioclase phenocrysts in an aphanitic matrix (Fig. 3.3 C). The plagioclase and matrix are usually degraded, resulting in intragranular pore space. Present sedimentary rock fragments (0.0 to 9.0 %, mean 1.6 %) comprise fine-grained sandstone and siltstone clasts with clay mineral cement (Fig. 3.3 F).

Micas are primarily represented by muscovite (Fig. 3.3 B) (0.3 to 15.7 %, mean 3.3 %). Zircon and tourmaline are the main accessory heavy minerals observed (0.0 to 0.7 %, mean 0.1 %) but were only point-counted in a few samples (n=12). Coal layers and fragments appear in most samples (Fig. 3.3 C) and contain open coal cleats aligned parallel to the coaly layer (Fig. 3.3 C, arrow).

Based on their mineralogical composition, sedimentary rocks are classified as litharenites (n=16), feldspathic litharenites (n=13) and sublitharenites (n=1) after McBride (1963) (Fig. 3.5), while siltstones are classified as litharenites (n=9). Generally, samples with coarser grain sizes show a more quartz-rich composition than those with finer grain sizes. Similarly, samples retrieved from the delta front contain fewer rock fragments than samples from wetlands or the lower delta plain (Fig. 3.5).

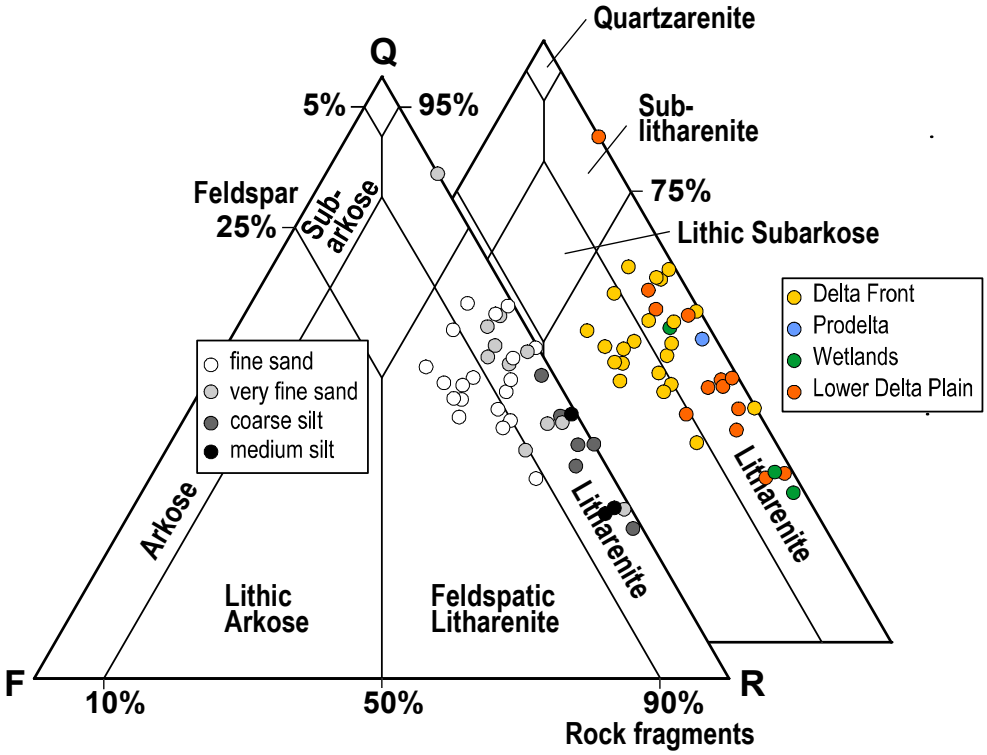

Figure 3.5 Rock classification diagram after McBride (1963), used for the silt- and sandstone samples of the Pelkum-1 well with gray shades indicating grain sizes. In addition, the samples are classified after their facies association, as indicated by the color code.

3.5.1.3 Optical porosity

Optical porosity from point counting ranges from 0.0 to 6.3 % (mean 2.3 %). It comprises intergranular porosity (0.0 to 1.0 %, mean 0.7 %) as well as intragranular porosity due to the dissolution of rock fragments (0.0 to 6.0 %, mean 1.6 %), K-feldspar (0.0 to 1.3 %, mean 0.3 %), and plagioclase (0.0 to 1.7 %, mean 0.3 %). Intragranular pores, resulting from dissolution, remain grain-shaped (Fig. 3.6 G, H), and ductile particles have deformed around the previous grain outline (Fig. 3.6 G).

3.5.1.4 Authigenic mineralogy

Authigenic minerals comprise 0.0 to 38.7 % (mean 4.7 %) of the rock mineralogy. The carbonate phases are recognised through a combination of thin section staining and XRD analysis (Tab.1). Authigenic kaolinite, carbonate cement (e.g., syntaxial siderite and equant calcite), as well as quartz overgrowths, are the dominant phases. Furthermore, fracture-filling marcasite/pyrite, kaolinite and carbonates are observed.

Siderite is the predominant authigenic mineral, as an intergranular cement coating framework grains or forming isopachous bladed siderite cement on detrital carbonatic rip-up clasts (0.0 to 6.3 %, mean 0.8 %). Siderite further fills the intragranular pore space of previously dissolved unstable grains, e.g., feldspars and volcanic rock fragments (0.0 to 7.0 %, mean 0.7 %). Siderite is readily recognized because it forms small,

strongly flattened or equant yellowish-brown rhombs with a high relief (Fig. 3.6 A). Furthermore, sample Pe-5 exhibits a vertical and sub-horizontal vein filled with coarse crystalline siderite (Fig. 3.7 B and C). XRD analyses also show siderite in samples Pe-1 and Pe-20 (Tab. 3.1).

Authigenic quartz is common as syntaxial overgrowths on detrital quartz gains (0.0 to 4.7 %; mean 0.4 %), especially in the interstices of coarse-grained samples of the delta front (Fig. 3.6 B). Monocrystalline quartz grains host relatively larger volumes of partly non-euhedral quartz overgrowth, while polycrystalline quartz grains host small volumes of isopachous, small (~10 µm) overgrowths with rhombohedral or prismatic crystal faces. In contrast to inclusion-rich detrital quartz grains, the overgrowths are commonly inclusion-poor. Locally, detrital grain outlines are marked by a rim of scattered siderite crystals, pigmented hematite rims, or solid inclusions, aiding the identification of quartz overgrowths. Syntaxial quartz overgrowth cement is also rarely observed to form in intragranular dissolution pores on the residual quartz of dissolved rock fragments (Fig. 3.7 A).

The grain-rimming siderite is mostly enclosed by quartz overgrowth cement (Fig. 3.6 B). However, some siderite crystals are also present at the interface between syntaxial quartz overgrowth cements and the intergranular pore space and are not encased in quartz cements (Fig. 3.6 B, lower right). Further, siderite cement encases intergranular pyrite/marcasite (Fig. 3.6 I). Sulfides, in general, are present in traces (0.0 to 1.0 %, mean 0.1 %) and only occlude negligible volumes of intergranular porosity.

Carbonates are locally abundant as equant to blocky calcite spar cement and in samples with apparent fractures (Pe-1 and Pe-40) as fracture-filling carbonates (0.0 to 1.0 %, mean 0.1 %). In sample Pe-1 ferroan carbonate cement was identified in thin sections through staining (Fig. 3.6 A) and was identified by XRD analyses (Tab.1) as ferroan dolomite/ankerite (8.8 %) and ferroan calcite (1.1 %). Carbonates are composed of light blue stained, non-luminescent ferroan dolomite/ankerite (D/A) and deep blue stained, bright luminescent ferroan calcite (Cf) (Fig. 3.6 C and D). A sharp contact of ferroan dolomite/ankerite to ferroan calcite is strongly marked under cathodoluminescence, also displaying fractures crosscutting the non-luminescent ferroan dolomite/ankerite that are filled by bright luminescent ferroan calcite. Pervasive equigranular, xenotropic textured ferroan dolomite/ankerite (13.7 %, Tab.1) and ferroan calcite cementation (0.6 %, Tab.1) in sample Pe-20 is present (Fig. 3.6 E). A patchy pore-filling cement distribution is present in sample Pe-35, where ferroan dolomite/ankerite (21.0 %, Tab.1) and ferroan calcite (1.2 %, Tab.1) clog preferentially intergranular porosity while intragranular porosity seems widely unaffected. In contrast, intragranular pore space in partially dissolved rock fragments is filled by ferroan dolomite/ankerite and ferroan calcite, while other intragranular pores appear unfilled (Fig. 3.7 G). Ferroan dolomite/ankerite and ferroan calcite, filling intergranular and intragranular porosity, is also observed to encase euhedral quartz overgrowth cement (Fig. 3.7 E).

Tab. 3.1 *Quantitative XRD data for three selected samples of this study to better constrain the carbonate cement type.*

Sample	*Quartz*	*Fe-Dolomite/Ankerite*	*Siderite*	*Calcite*	*Muscovite*	*Albite*	*Kaolinite*	*Chlorite*
Pe-1	55.0	8.0	6.2	1.1	15.7	11.0	2.1	1.1
Pe-20	71.8	13.7	1.8	0.6	6.4	0.0	2.0	3.7
Pe-35	46.1	21.0	0.0	1.2	8.7	15.9	3.8	3.2

Fracture-filling pyrite/marcasite (0.0 to 6.0 %, mean 0.2 %) is present in individual samples (Pe-1, Pe-15, Pe-18, Pe-20), cementing fractured detrital grains (Fig. 3.6 F). The fractured quartz grains do not show syntaxial overgrowth on their fractured surfaces. Alongside pyrite/marcasite veins, goethite staining of clay mineral cements and clay-bearing rock fragments is observed (Fig. 3.6 F).

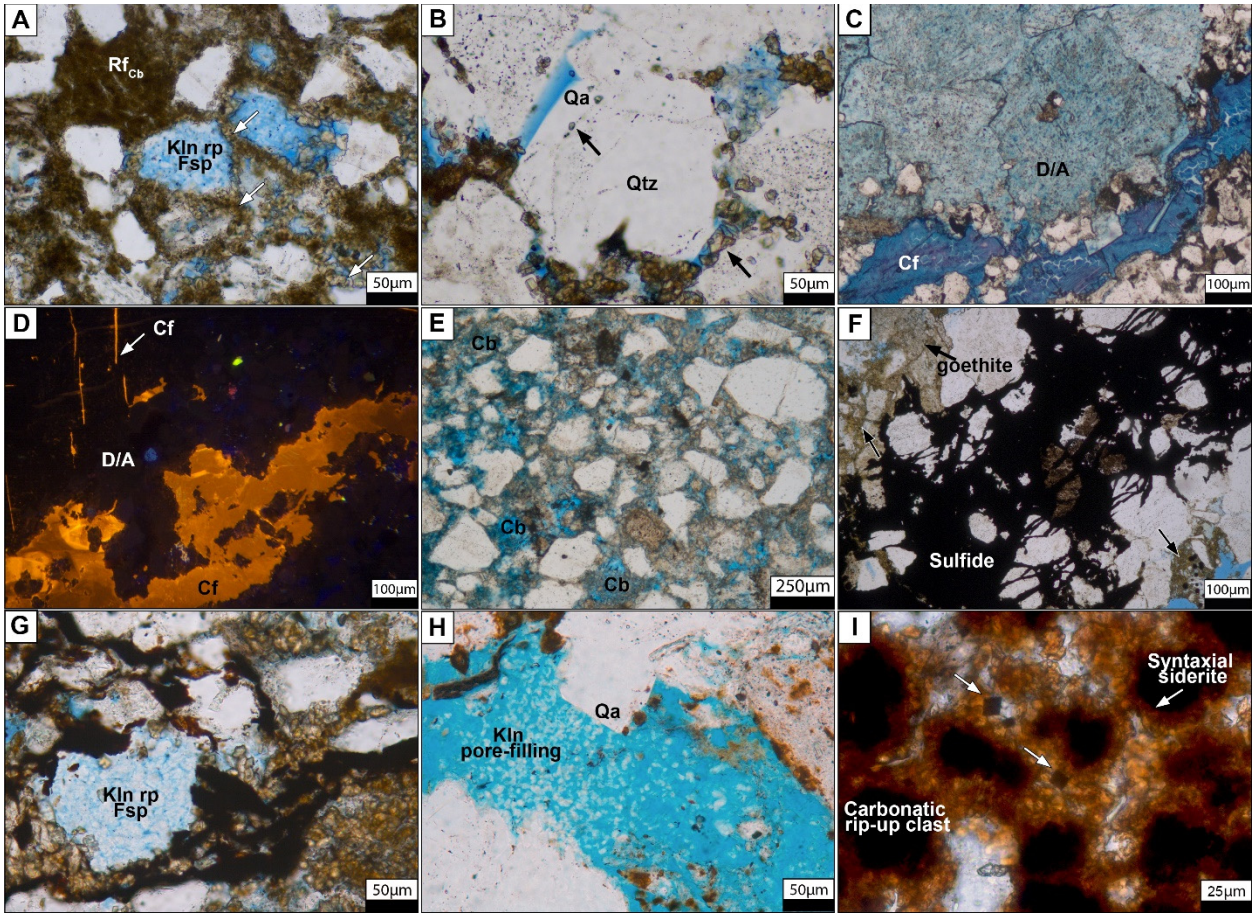

Figure 3.6 (**A**) Intergranular siderite cement (arrows) that is recognized by its small, strongly flattened or somewhat more equant rhombs in sample Pe-21. The siderite cement encases feldspars replaced by kaolinite, still exhibiting grain outlines. (**B**) Authigenic quartz is common in sample Pe-12 as syntaxial overgrowths on a detrital quartz gain. The boundary between the detrital grain and quartz overgrowth is marked by siderite (arrow), while in the lower right the arrow marks the interface of quartz overgrowth and intergranular siderite. (**C**) Fracture-filling calcite composed of poikilotopic calcite in sample Pe-1. (**D**) The CL picture displays a distinct change in carbonate composition between ferroan dolomite/ankerite (D/A) and ferroan calcite (Cf). (**E**) Pervasive equigranular, xenotropic textured ferroan

calcite cementation (Cb) (sample Pe-20). (**F**) Fracture-filling sulfides cementing fractured framework grains in sample Pe-15. Goethite covers authigenic minerals (arrows). (**G**) Kaolinite exhibits aggregates of randomly oriented coarse crystalline booklets within former grain outlines (Pe-19). (**H**) Euhedral quartz delimits the growth of kaolinite. Here the kaolinite exhibits aggregates of randomly oriented finely crystalline (4-20 µm) booklets (Pe-15). (**I**) Intergranular cubic pyrite (arrows) is encased by isopachous bladed siderite cement syntaxially growing on carbonatic rip-up clasts (Pe-5). Qtz: quartz grain, Qa: Authigenic quartz, D/A: Ferroan dolomite/ankerite, Cf: Ferroan calcite, Kln rp Fsp: Kaolinite replacing feldspar, RF_{Cb}: Carbonatic rip-up clasts.

3.5.1.5 Authigenic clay minerals

Authigenic kaolinite and illite are recorded mainly in coarse-grained samples from the delta front in minor amounts (0.0 to 4.3 %, mean 0.7 %). Kaolinite exhibits aggregates of randomly oriented booklets of very fine to fine crystalline (4-20 µm) or coarse crystalline size after Folk (1980) (Fig. 3.6 G). Coarse-crystalline kaolinite is marginally less prominent (0.0 to 1.7 %, mean 0.2 %) than fine-crystalline kaolinite (0.0 to 2.7 %, mean 0.3 %). XRD analyses determined a kaolinite content of 2.0 to 3.8 % (Tab.1). Kaolinite either replaces unstable grains such as igneous rock fragments or feldspar, outlined by residual grain limits or is widely occluding pores (pore-filling). Euhedral quartz delimits the growth of kaolinite (Fig. 3.6 H). Authigenic illite is documented in traces as an alteration product within feldspar grains (Fig. 3.7 H) or optically non-resolvable small plates (0.0 to 0.7 %, mean 0.1 %). Coarse-crystalline kaolinite booklets locally fill fractures or cover fracture surfaces, covering quartz overgrowth cement and fracture-filling coarse crystalline siderite (Fig. 3.7 C and D).

An illitization of kaolinite booklets could only be determined in sample Pe-15 (0.7 %). Illite coatings rarely occur as finely disseminated aggregates on detrital grain outlines, forming tangential illite.

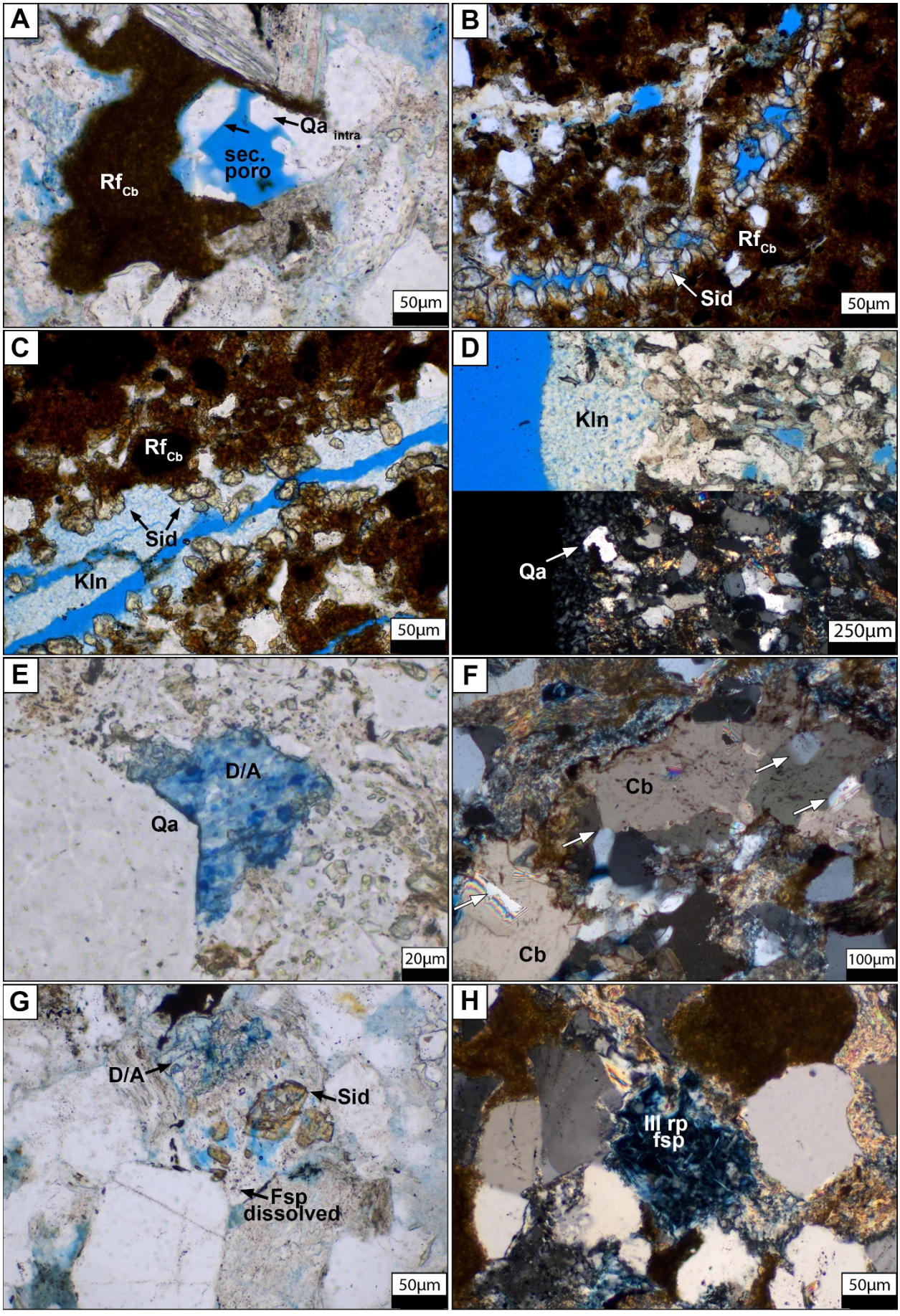
A
Qa intra
sec. poro
Rf Cb
50µm
B
Rf Cb
Sid
50µm
C
Rf Cb
Sid
Kln
50µm
D
Kln
Qa
250µm
E
D/A
Qa
20µm
F
Cb
Cb
100µm
G
D/A
Sid
Fsp dissolved
50µm
H
Ill rp fsp
50µm

Figure 3.7 (**A**) Syntaxial quartz overgrowth cement filling intragranular dissolution pores on the residual quartz of dissolved rock (Pe-38). (**B**) Coarse crystalline siderite syntaxially filling fractures subparallel to the lamination in sample Pe-5 with residual fracture porosity (dark blue). (**C**) Fracture-filling kaolinite overlays coarse crystalline siderite in the same sample. (**D**) Fracture-filling kaolinite composed of coarse booklets covers a fractured surface, including quartz overgrowth cement (arrow) in sample Pe-34. (**E**) Quartz overgrowth (euhedral) is enclosed by ferroan dolomite/ankerite (centre) in sample Pe-1. (**F**) Fracture-filling calcite in sample Pe-39 encloses quartz overgrowth cement (arrows). The fracture is oriented normal to the bedding. (**G**) Siderite and ferroan dolomite/ankerite filling intragranular porosity in a partly dissolved felspar (Pe-55). (**H**) Illite (mesh) replacing a feldspar in sample Pe-36. Sid: Siderite, Ill rp Fsp: Illite replacing feldspar. Qa_{intra}: Intragranular authigenic quartz, Qa: Authigenic quartz, Cb: Carbonate, Kln: Kaolinite, RF_{Cb}: Carbonatic rip-up clasts, D/A: Ferroan dolomite/ankerite, Cf: Ferroan carbonate.

3.5.2 Compaction

The samples show low intergranular volumes (IGV) values (0.0 to 7.0 %, mean 1.7 %) and low contents of intergranular cement (0.0 to 6.3 %, mean 1.6 %). Calculated compactional porosity loss (COPL) values range from 35.5 to 40.0 % (mean 38.8 %), while low cementational porosity loss (CEPL) values vary from 0.0 to 4.1 % (mean 1.0 %). Consequently, compaction index (ICOMPACT) values are high (0.9 – 1.0). Thus, all samples fall in the area of compaction-dominated porosity loss (Fig. 3.8).

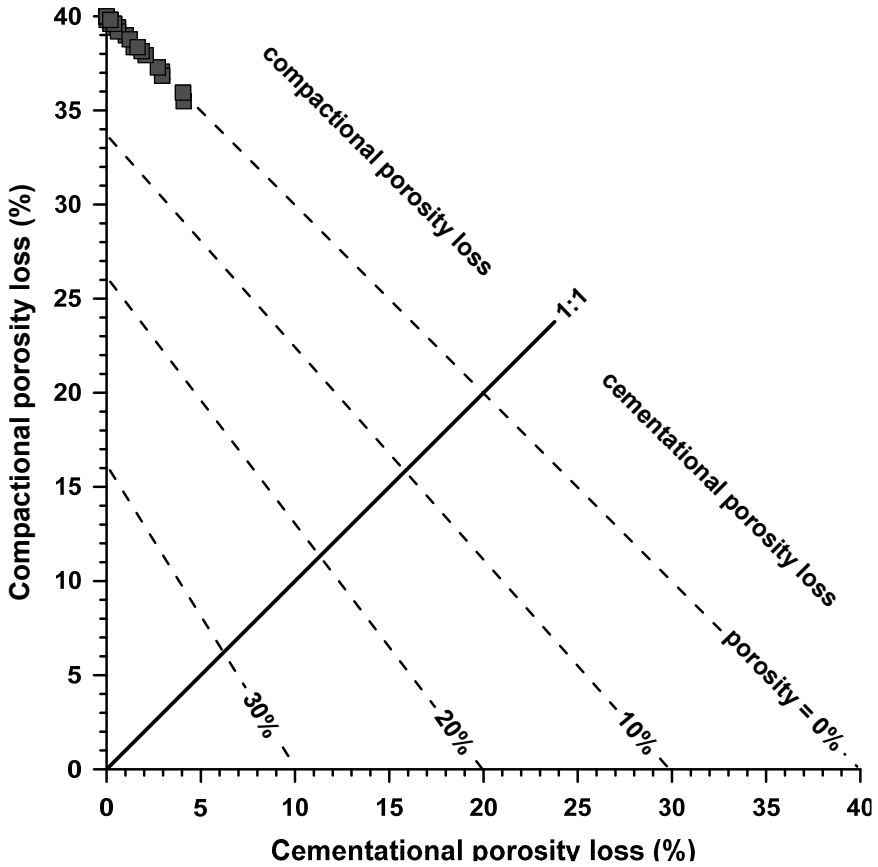

Figure 3.8 Evaluation of relative porosity loss stated due to mechanical (COPL) and cementational (CEPL) compaction for present samples, after Lundegard (1992). All samples plot in the field for compactional porosity loss.

3.5.3 Porosity and permeability

Porosity ranges from 0.5 to 15.6 % (mean 5.5 %), while permeabilities range from 0.0001 to 4.43 mD (mean 0.26 mD) (Fig. 3.9 A). No differentiation between stratigraphic units is observable, but samples of the delta front have better reservoir properties (Fig. 3.9 B). Samples with low porosity but a permeability > 1 mD mostly contain a thin (~ 250 µm) coal layer (Fig. 3.3 C). In addition, notably fine-grained samples tend to have cracks subparallel to the present lamination (fracture porosity) and are treated carefully, as, i.e. permeability might be amplified and are not representative values. Sample Pe-21 shows a very low permeability (0.0001 mD) despite high porosity (9.26 %).

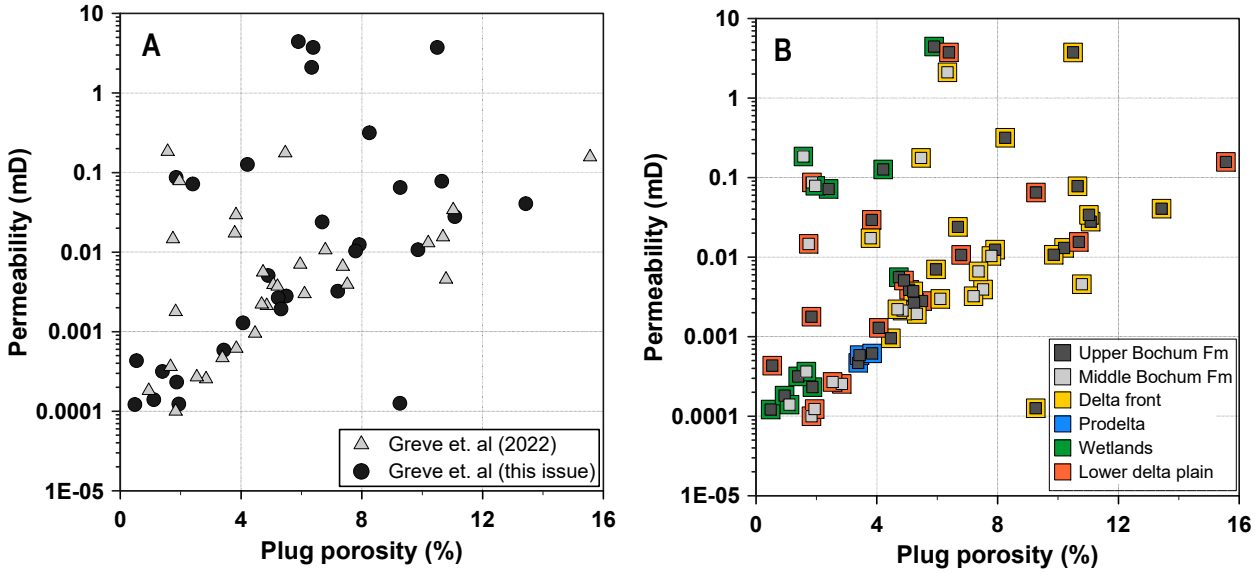

Figure 3.9 (**A**) Porosity – permeability cross plot of the samples used in this study, separated by their issue. (**B**) Samples of this study were separated by their formation (as in Fig. 3.2) and their facies associations, marked by the coloured rims.

3.5.4 Rock typing

The impact of various aspects on reservoir quality in samples of well Pelkum-1 is visualized on porosity-permeability cross plots colour-coded for petrographic properties (Fig. 3.10). An increase in grain size (from medium silt to fine sand) generally corresponds to enhanced reservoir properties, with a higher porosity (> 8 %) and higher permeabilities (> 0.01 mD) (Fig. 3.10 A). Higher volumes of ductile-behaving grains (> 38 %), such as shale and phyllite fragments, carbonatic rip-up clasts, micas and ferric oxyhydroxides are associated with lower porosity and lower permeabilities (Fig. 3.10 B).

The volume of secondary porosity (1.5 – 6.0 %) also positively correlates with enhanced reservoir properties (Fig. 3.10 C). Samples with enhanced reservoir properties are also often characterized by high volumes of authigenic clay minerals (> 0.5 %) as well as high cementational porosity loss (CEPL) (Fig.

3.10 D and E). When it comes to intergranular volumes (IGV), the correlation is almost identical to the characterization by CEPL (Fig. 3.10 F), since primary porosity is negligible (0.0 to 1.0 %, mean 0.7 %). High quartz cement contents correspond with better reservoir properties (Fig. 3.10 G). Carbonate cements occur widely in the samples, but higher volumes correlate with better reservoir properties (Fig. 3.10 H). A very low permeability despite high porosity in sample Pe-21 corresponds to pervasive cementation by intergranular siderite (Fig. 3.6 A). High volumes of authigenic cements, in general, correspond with coarser-grained samples. In contrast, ductile grains appear mainly in fine-grained samples (Fig. 3.10 H).

The cracks subparallel to the present lamination result in fracture porosity due to relaxation of the rock material, enhancing the permeability. Furthermore, cleats in coal fragments lead to an enhancement in permeability. However, the measurements were performed at a confining pressure (1.2 MPa), not representing reservoir conditions. Measurements at higher confining pressures show that the permeability enhancement diminishes. Therefore, samples containing fractured porosity or coal fragments are treated carefully.

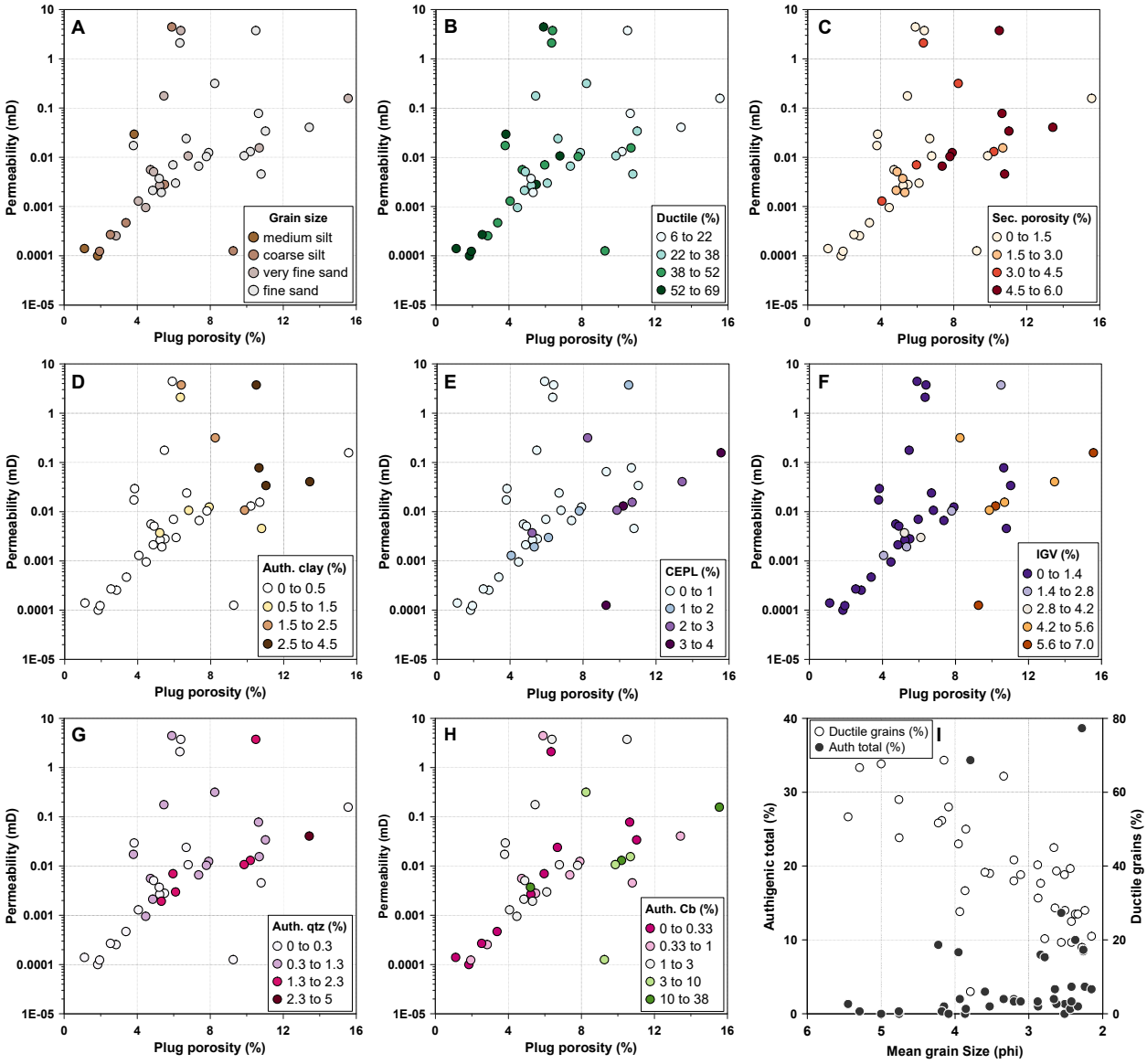

Figure 3.10 Porosity – permeability cross plots characterized by (**A**): The mean grain size. (**B**) Volume of ductile grains. (**C**) Volume of secondary porosity. (**D**) Authigenic clay content. (**E)** Cementational porosity loss (CEPL). (**F**) Intergranular volume (IGV). (**G**) Authigenic quartz. (**H)** Authigenic carbonates (Cb). (**I**) Grain size vs total authigenic minerals and ductile grains (shales, phyllites, carbonatic rip-up clasts).

3.5.5 Geochemistry

Major and trace element results from XRF for 18 sand and siltstones samples from well Pelkum 1 are grouped into their facies association to highlight facies-dependent differences (Fig. 3.11). The SiO_2 content is highest in samples of the delta front (n=9, 59.3 to 83.7 %, median 73.7 %), while volumes for the lower delta plain (n=5, 56.8 to 75.4 %, median 68.4 %), the wetlands (n=3, 59.6 to 71.8 %, median 62.9 %) and the prodelta (n=1, 62.8 %) are decreasing stepwise. The content of $CaCO_3$ is considerably higher for samples of the delta front (0.2 to 9.1 %, median 1.4 %), including a positive outlier (24.5 %), and the lower delta plain (0.3 to 9.3 %, median 3.4 %) compared to lower contents in the wetlands (2.2 to 4.6 %, median

3.9 %) and prodelta (1.4%) samples, respectively. Volumes of Al_2O_3 are lowest in samples of the delta front (4.7 to 13.5 %, median 9.9 %), while volumes for the lower delta plain (8.5 to 17.6 %, median 15.7 %), the wetlands (10.5 to 18.7 %, median 14.3 %) and the prodelta (17.5 %) are increasing stepwise. Alike, the Fe_2O_3 content is lowest in samples of the delta front (2.1 to 5.3 %, median 4.0 %), including a positive outlier (17.8 %), while volumes for the lower delta plain (1.9 to 7.7 %, median 4.4 %), the wetlands (5.5 to 10.4 %, median 6.9 %) and the prodelta (5.3%) are higher. The TiO_2 content is low in all samples (0.3 to 0.9 %, median 0.6 %) regardless of the facies association. Regardless of the facies associations, the content of MgO (0.4 to 2.4 %, median 1.5 %), CaO (0.1 to 0.7 %, mean 0.3 %) and K_2O (1.1 to 3.6 %, median 1.9 %) are generally low in all samples. A positive outlier for MgO is observed in a sample of the delta front (4.2 %). Positive outliers for CaO are displayed for samples of the delta front (6.7 %) and the lower delta plain (2.9 %).

The distribution of some minor elements does not relate to the facies associations. In general, outliers are restrained to the delta front samples. For the MnO content, values are highest for the wetland samples (830 to 1823 ppm, median 1138 ppm) compared to lower values of the lower delta plain (529 to 1020 ppm, median 832 ppm), prodelta (762 ppm) and delta front (58 to 4038 ppm, median 732 ppm). Regardless of the facies associations, the content of SrO is generally low (77 to 190 ppm, median 108 ppm). It is similar for the BaO (10 to 630 ppm, median 259 ppm) and Rb_2O (43 to 168 ppm, median 81 ppm). ZrO_2 values of the delta front (146 to 306 ppm, median 181 ppm) are slightly lower compared to the lower delta plain (279 to 382 ppm, median 297 ppm), wetlands (248 to 484 ppm, median 307 ppm) and prodelta (290 ppm).

When comparing the Si+Ca+K/Al+Fe ratio with mean grain size, a general increase in the ratio can be observed with increasing grain size (Fig. 3.11 C to F). The classification based on facies association shows that most coarse-grained samples with a relatively high Si+Ca+K/Al+Fe ratio are associated with the delta front facies (Fig. 3.11 C). When classifying based on the SiO_2 (wt%) and the detrital quartz content (%), an increase in both values is observed with increasing grain size (Fig. 3.11 D to E). In contrast the Al_2O_3 (wt%) content is generally lower in coarse-grained samples (Fig. 3.11 F). A positive correlation (R^2=0.54) is evident when comparing the Si+Ca+K/Al+Fe ratio and helium porosity (%), as the ratio tends to increase with increasing porosity (Fig. 3.11 G).

In addition to the differentiation of authigenic carbonate species, XRD-analyses of the three samples show that quartz is the dominant component (46.1 to 71.8 %) in all samples (Tab.1). Muscovite (6.4 to 15.7 %) and albite (0.0 to 15.9 %) are present as minor constituents. Chlorite is also present in small quantities (1.1 to 3.7 %).

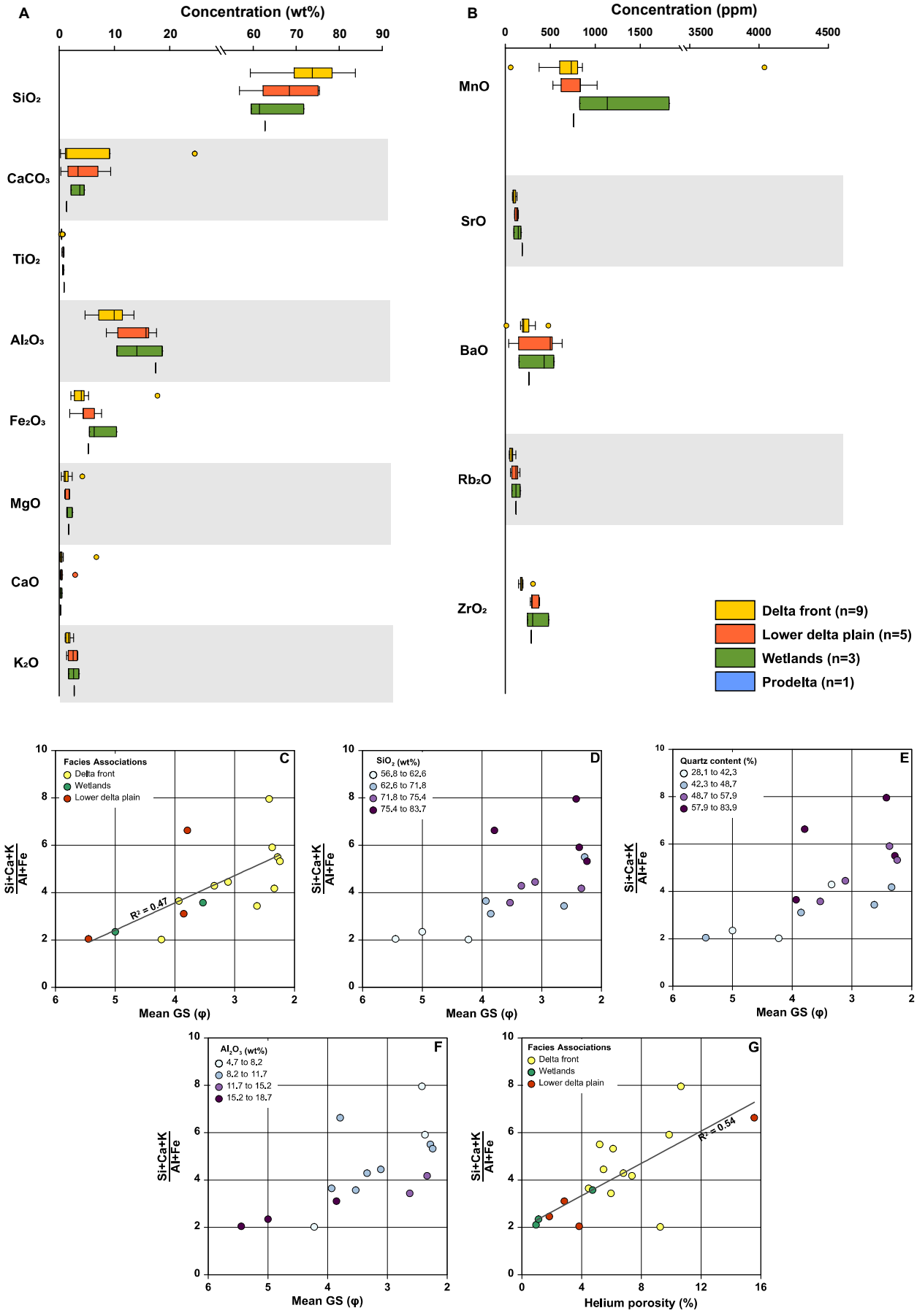
A
Concentration (wt%)
0
10
20
60
70
80
90
SiO₂
CaCO₃
TiO₂
Al₂O₃
Fe₂O₃
MgO
CaO
K₂O
B
Concentration (ppm)
0
500
1000
1500
3500
4000
4500
MnO
SrO
BaO
Rb₂O
ZrO₂
Delta front (n=9)
Lower delta plain (n=5)
Wetlands (n=3)
Prodelta (n=1)
C
Facies Associations
Delta front
Wetlands
Lower delta plain
R² = 0.47
D
SiO₂ (wt%)
56.8 to 62.6
62.6 to 71.8
71.8 to 75.4
75.4 to 83.7
E
Quartz content (%)
28.1 to 42.3
42.3 to 48.7
48.7 to 57.9
57.9 to 83.9
F
Al₂O₃ (wt%)
4.7 to 8.2
8.2 to 11.7
11.7 to 15.2
15.2 to 18.7
G
Facies Associations
Delta front
Wetlands
Lower delta plain
R² = 0.54
Si+Ca+K / Al+Fe
Mean GS (φ)
Helium porosity (%)

Figure 3.11 Box-and-whisker bars plotted for (**A**) concentration in wt% of major and minor elements. (**B**) Concentration (ppm) of trace elements for samples of the Pelkum-1 well (appendix D.1: Modal data). (**C**) Comparison of the Si+Ca+K/Al+Fe ratio with the mean grain size displays a positive correlation (R^2=0.47). The classification based on facies association shows a good agreement as coarse-grained samples with relatively high Si/Al ratios are associated with the delta front facies. (**D**) When classifying based on SiO_2 (wt%) and (**E**) the detrital quartz content (%), an increase in both values is observed with increasing grain size. (**F**) In contrast, when classifying based on Al_2O_3 (wt%) a decrease with increasing grain size is observed. (**G**) The comparison of helium porosity and Si+Ca+K/Al+Fe ratio shows a positive correlation (R^2=0.54) and is in good agreement with the facies associations.

3.6 Discussion

3.6.1 Paragenetic sequence

Based on the described paragenetic interactions in combination with a published burial history, a relative paragenetic sequence can be established (Fig. 3.12). The sequence is split up into early, burial and uplift diagenesis.

Throughout early diagenesis, the alteration of sediments was controlled by meteoric waters and the depositional environment's physical, geochemical, as well as biological characteristics. In terms of burial, the maximum depth limit of early diagenetic alteration is about 1 to 2 km, which equals approximately 30 to 70°C in most basins (Morad et al., 2000). Burial diagenesis persists once the sediment is no longer controlled by the depositional environment and meteoric waters (Worden & Burley, 2003). Uplift diagenesis characterizes phases where the sedimentary rocks once again interact with meteoric fluids, following a phase of burial diagenesis.

3.6.2 Early diagenesis

Authigenic clay minerals and hematite are observed at grain contacts and their emplacement is interpreted as the earliest diagenetic alteration, suggesting that they formed before mechanical compaction. The term "clay rim" is used for clay phases that form at the site of deposition, primarily controlled by sediment transport and subordinately by bioturbation or clay illuviation/mechanical infiltration (Dowey et al., 2017; Molenaar, 1986). Tangential illite, aligned parallel to the grain surface (Busch et al., 2020; their Fig. 1), is most likely a product of recrystallization from clay rims that act as precursory minerals. The whole rock XRD data (Tab.1) could not be used to differentiate between detrital muscovite and authigenic illite. However, a small proportion of the muscovite component is likely to be authigenic illite. Chlorite is interpreted as a detrital constituent of phyllites originating from the Variscides since no authigenic chlorite is observed. On the southern edge of the Rhenish Massif to the Saxothuringian (Phyllite zone), Middle to Upper Devonian metasediments of the greenschist-facies are exposed, which are classified as chlorite-sericite-phyllites (Meisl et al., 1982).

Euhedral pyrite is encased by isopachous bladed siderite cement growing on carbonatic rip-up clasts (Fig. 3.6 I). Thus, an early diagenetic origin of Fe-sulfides disseminated in the intergranular pore space is interpreted. The high organic influx in the waterlogged sediments of the lower delta plain could have favored the pyrite formation,since it is an environment suitable for biogenic sulfate reduction, promoting anoxic, sulfidic pore water conditions favorable for the precipitation of pyrite (Coleman, 1985; Morad et al., 2000). Yet, the volumes of pyrite are low (0.0 to 1.0 %, mean 0.1 %), considering the amount of organic matter stored in the Upper Carboniferous coal seams. Frequent remobilized sideritic rip-up clasts and early siderite cement indicate that sufficient reactive iron was abundant in the system. However, the limited availability of reactive organic matter in sandstones of the distal delta front is likely to restrict the abundance of pyrite. In contrast, low levels of available sulphate to maintain sulphate reduction due to the influence of meteoric water on the proximal delta plain may have been limited the production of H_2S, necessary for the pyrite formation. Siderite cement filling the intergranular pore space and coating detrital framework grains is present at grain-to-grain contacts, indicating a formation shortly after pyrite formation and prior to mechanical compaction (Fig. 3.6 A and B). Siderite can form where insufficient H_2S cannot precipitate the available reduced iron as pyrite (Curtis & Spears, 1968). Meteoric water containing low sulfate concentrations limits pyrite precipitation but can lead to methanic conditions promoting siderite precipitation (Curtis & Coleman, 1985; Gautier, 1982). However, in late Holocene marsh and sandflat sediments siderite may also form wherever the iron reduction rate exceeds the sulphate reduction rate (Pye et al., 1990). An internal source of iron may be the alteration of Fe-bearing silicates or the de-watering of Fe-bearing clay minerals during early diagenesis, while the inflow of basinal brines transporting iron could have acted as an external source.

Given that most siderite coats detrital quartz grains and is overgrown by quartz cement (Fig. 3.6 B), a formation before quartz cement precipitation is assumed. However, some siderite is inferred to have been formed during burial diagenesis. Pervasive pore-filling ferroan calcite parageneses are restricted to samples Pe-20 and Pe-35 (Fig. 3.6 B), and these samples lack quartz cement or are enclosed by authigenic quartz. Thus, their formation is interpreted to predate quartz formation and is interpreted to have been formed during early diagenesis. Early diagenetic ferroan calcite is common in sediments with marine-influenced pore waters (Curtis & Coleman, 1985).

3.6.3 Burial diagenesis I

Since no absolute dating methods were applied, the relative timing of fractures is based on textural relationships to other authigenic minerals and preceding works. However, thrust tectonics (e.g. Becker et al., 2011; Sindern et al., 2012) and fracturing of the Upper Carboniferous lithologies are widespread throughout its burial history (e.g. Drozdzewski, 1988; Drozdzewski & Wrede, 1994; Vinken, 1988). As fractured quartz grains in pyrite/marcasite veins do not show quartz overgrowth precipitation, the formation

of fracture-filling pyrite/marcasite is interpreted to predate quartz precipitation. A possible source for Fe could be the dewatering and fluid expulsion from mudrocks and shales during compaction (Miocic et al., 2020).

Suitable pathways for fluids might have been NW-SE striking faults. Faults predominantly formed partly at the end of the Variscan deformation and partly before and during the deposition of the Zechstein (Lopingian) strata (Wolf, 1985).

Syntaxial quartz overgrowths are very common in coarse-grained samples. Based on their paragenesis, authigenic quartz post-dates early siderite, ferroan dolomite/ankerite, and pyrite/marcasite cementation. Still, it is interpreted to be either synchronous with or predates pore-lining illite as well as kaolinite that replaces feldspar. Dissolution of framework grains that results in intragranular porosity in feldspars or plutonic rock fragments must predate quartz precipitation since quartz overgrowths form in those dissolved rock fragments (Fig. 3.7 A). Quartz overgrowth is typically the dominant cement type in sandstones at temperatures above 70-100°C (Bjørlykke & Egeberg, 1993; Walderhaug, 1996). According to burial and heat flow reconstructions by Bruns et al. (2013), temperatures have exceeded 70°C since the Late Carboniferous/Early Permian to form quartz cement for nearly 20 Ma. Concerning the maximum burial during the Early Permian with contemporaneous elevated heat flow and the observed paragenetic relationships, most quartz cementation is interpreted to have been formed during this burial phase.

The silica to form authigenic quartz may have been provided by clay mineral transformations and feldspar dissolution since pressure dissolution along dissolution seams is widely absent. The alteration of kaolinite with K-feldspars to form illite and quartz occurs at similar temperatures as quartz precipitation (Bjorkum & Gjelsvik, 1988) and represents an additional suitable source of silica.

As grain-shaped pores, occasionally containing kaolinite, are still present and on occasion surrounded by deformed ductile rock fragments (Fig. 3.3 A, 6 A and G), the dissolution of unstable rock fragments and feldspars in the studied samples is interpreted to post-date early diagenesis and the main phase of mechanical compaction. Commonly, the dissolution of unstable rock fragments and feldspars as well as feldspar replacement by kaolinite are early diagenetic alterations in humid climates in contact with meteoric waters (Bjørlykke et al., 1979; Hancock & Taylor, 1978; Lønøy et al., 1986). However, the pervasive formation of siderite points to slightly alkaline pH conditions (Zhang et al., 1997; their Fig. 4), under which feldspar is stable at atmospheric pressure and low temperature (Jackson & Sherman, 1953). The introduction of organic acids and carbonic acids formed during thermal maturation of organic matter within the Upper Carboniferous strata during burial (Barth & Bjørlykke, 1993) is interpreted to cause feldspar dissolution during burial diagenesis. The interpretation of acidic pore waters being responsible for K-feldspar dissolution is additionally supported by the presence of kaolinite, which is more stable under acidic conditions (Lanson et al., 2002).

As pore-lining illite is intergrown with quartz cements (Fig. 3.6 H), it must predate or is contemporaneous with quartz precipitation. The partial or complete illitization of feldspar grains is prominently observed (Fig. 3.7 H), while the illitization of kaolinite is barely evident. As illite replacements of feldspars remained grain-shaped (Fig. 3.7 H), their formation is also interpreted to post-date mechanical compaction. The illitization of K-feldspar can initiate at temperatures of 90 to 120°C if there is a source of acidity that promotes extensive, contemporaneous breakdown of K-feldspar, as long as the supply of K^+ can be maintained to form illite rather than kaolinite (Berger et al., 1997; Lanson et al., 2002). Acidic fluids originating from the maturation of organic matter analogously to Gaupp et al. (1993) in a closed geochemical system have been reported to be capable of dissolving K-feldspar and releasing K^+. The illitization of detrital clay rims (e.g., smectite) is likely to be a product of the same mechanism by incorporating the released K^+ from feldspar dissolution (McKinley et al., 1999).

3.6.4 Uplift diagenesis I/II

Vertical and sub-horizontal fractures are partially filled by coarse crystalline siderite (Fig. 3.7 B and C) and are interpreted to uplift related stress release and fracturing. Fracture-filling ankerite and siderite in Westphalian strata were previously linked to an ascending fluid during the Upper Cretaceous inversion (Mumm & Wolfgramm, 2002; Rieken, 1988), which agrees with findings from Wüstefeld et al. (2017) from the Upper Carboniferous of northwestern Germany. Therefore, the second phase of uplift diagenesis during Cretaceous basin inversion is interpreted to account for sub-horizontal fracturing.

Goethite is staining all other detrital and authigenic phases in the vicinity of sulfide-filled fractures and is interpreted to post-date all other authigenic minerals (Fig. 3.6 F). The formation of goethite is related to the alteration of abundant fracture-filling sulfide minerals during uplift diagenesis, which can lead to the oxidation of pyrite to goethite (Abouessa & Morad, 2009).

These phases of uplift diagenesis may also have been responsible for further feldspar dissolution and kaolinization, promoted by the flushing of meteoric waters at shallow depths (Bjørlykke et al., 1979; Hancock & Taylor, 1978).

3.6.5 Burial diagenesis II/III

Siderite crystals also occur on quartz overgrowth cements, interpreted as a second phase of siderite precipitation post-dating or synchronous to quartz cementation (Fig. 3.6 B, lower right). Some kaolinite fills fractures and covers quartz overgrowth cements as well as fracture-filling siderite (Fig. 3.7 C and D), and thus represents another phase of kaolinite precipitation. Generally, fracture-filling kaolinite is not widely discussed by other authors. Kaolin minerals in fractures are described in core samples of Cretaceous shales from the Gibraltar Strait area at burial depths of 2 to 3 km and formed from smectite dissolution

(Cruz & Reyes, 1998). The previously discussed low pH of formation fluids related to organic matter maturation may again favor kaolinite precipitation in the presented fractures.

Staining highlights two phases of carbonate precipitation in veins, which are a light blue stained, non-luminescent ferroan dolomite/ankerite (D/A) and a deep blue stained, bright luminescent ferroan calcite (Cf) (Fig. 3.6 C and D). Bright orange cathodoluminescence suggest that the ferroan calcite is enriched in manganese (Götze et al., 2013). Bright luminescent ferroan calcite precipitated within fractures in non-luminescent ferroan dolomite/ankerite, indicating that the calcite post-dates the dolomite/ankerite. Ferroan dolomite/ankerite, cementing intragranular porosity in feldspars and rock fragments as well as some intergranular porosity, formed simultaneously. Fluids were introduced by fracture conduits since ferroan dolomite/ankerite also encases quartz overgrowths (Fig. 3.7 E). This is supported by mineralization within coal cleats from the Ruhr Basin, confirming that first ferroan dolomite/ankerite precipitated from a basinal brine (Dawson et al., 2012). A basinal brine may also be a suitable source of manganese in the fracture-filling ferroan calcite. Likely, periods of emplacement are the early Kimmerian phase with normal faulting in the Late Triassic and the Late Cretaceous transpression, where pre-existing extensional faults in the Ruhr Basin were reactivated as reverse faults (Drozdzewski, 1988; Kley & Voigt, 2008).

Burial history and heat flow reconstructions indicate relatively shallow burial (~2 km) and normalized heat flow during burial diagenesis II/III (Bruns et al., 2013). Thus, quartz cementation and illitization of detrital K-feldspars and diagenetic kaolinite were likely to be limited.

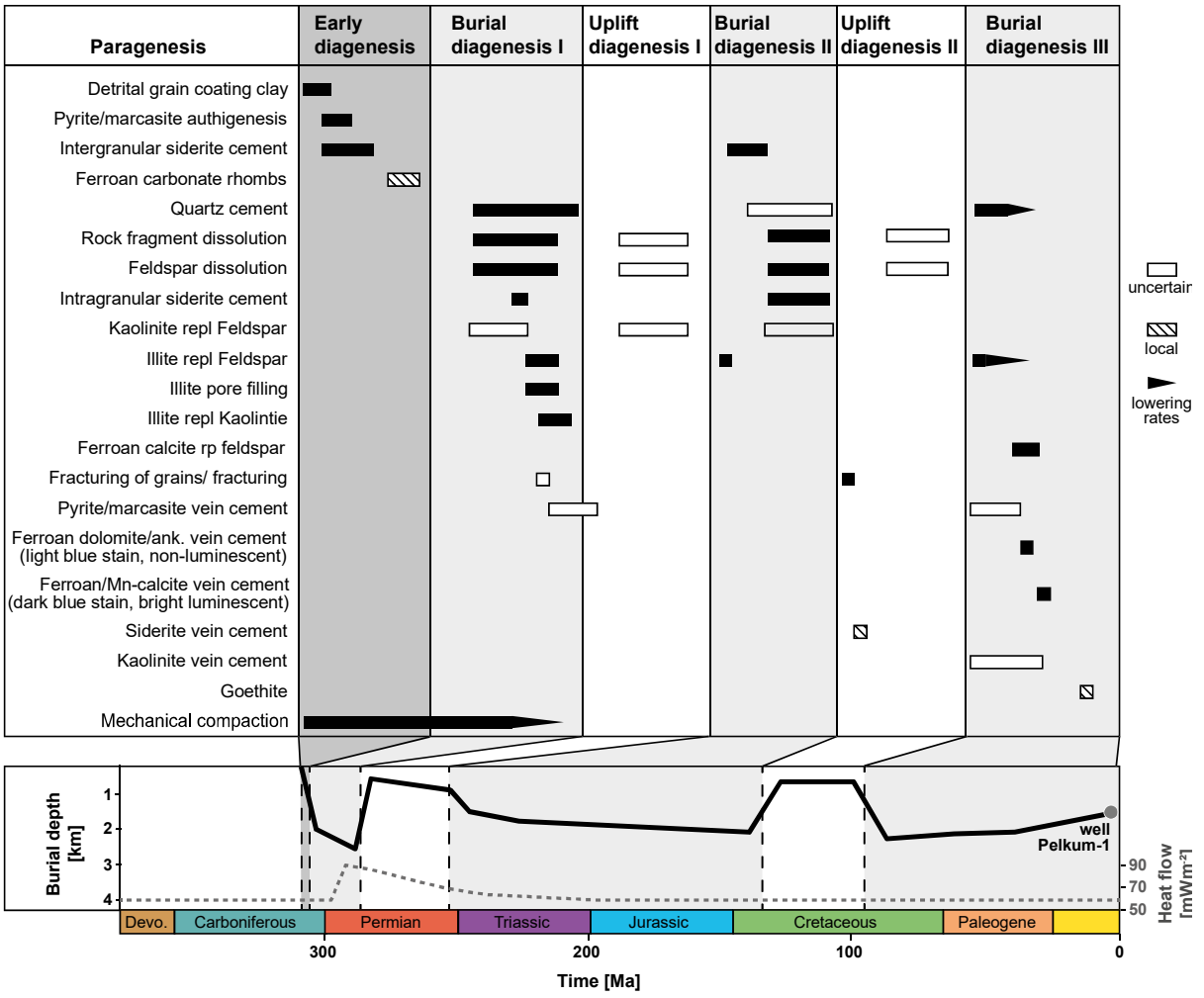

Figure 3.12 The paragenetic sequence of well Pelkum-1, based on petrographic evidence from this work, is associated with the burial and thermal reconstruction of the Münsterland Basin (modified after Bruns et al., 2013). The burial path was projected based on their reconstruction regarding the stratigraphic units encountered by the well.

3.6.6 Controls on reservoir properties and rock typing

The petrophysical data presented in this study demonstrate that the Upper Carboniferous sandstones and siltstones are generally tight. In some studied samples, coal fragments (Fig. 3.3 C) enhance permeability by about 100 mD under non-reservoir conditions at a confining pressure of 1.2 MPa. However, samples containing coal fragments are assumed to be tight at reservoir pressures at > 455 m depth. It agrees with measurements from previous studies in the Ruhr area (Brenne, 2016; Duda & Renner, 2013; Greve et al., 2023; Stöckhert et al., 2015) as well as from the Lower Saxony Basin (Becker et al., 2017; Busch et al., 2019; Quandt et al., 2022b; Wüstefeld et al., 2017), stating that the Upper Carboniferous siliciclastic rocks are generally tight. Post-mine geothermal utilization is thus limited to fractures, zones of enhanced permeability around galleries, and the galleries themselves as suitable targets.

The controls on the reservoir properties are deduced from rock typing, integrating petrographic analysis combined with porosity and permeability values. In Upper Carboniferous samples, the main aspect controlling reservoir properties seems to be the grain size (Fig. 3.10 A). A shift in grain size from fine (silt) to coarse (fine sand) corresponds with changes in mineralogy from litharenites towards feldspathic litharenites (Fig. 3.5). Coarse-grained samples also contain more quartz cement (2.3 to 5 %) than siltstones. In siltstones most surfaces of detrital quartz where cement could precipitate were in contact with ductile grains, resulting in a smaller substrate area. In sandstones, however, fewer grain surfaces were covered with ductile grains, thus providing a larger reactive surface area for syntaxial cement precipitation. It is thus similar to grain-coating clay minerals inhibiting quartz precipitation (Busch et al., 2020; Busch et al., 2017; Monsees et al., 2020). Furthermore, quartz cement grows at a faster rate in sandstones with larger grain sizes, in contrast to smaller or polycrystalline grains with individual subgrains. This is due to the more rapid development of euhedral crystal faces on smaller grains, leading to a reduced growth rate after euhedral faces develop (Lander et al., 2008; Prajapati et al., 2020).

Additionally, the presence of ductile rock fragments (i.e., shales and phyllites) enhances mechanical compaction, indicated by higher COPL values (Fig. 3.10 E). As siltstones contain higher volumes of ductile rock fragments (> 38 %) than sandstones (< 38 %), their COPL is higher. Subsequently, this change in mineralogy is interpreted to be the major control on IGV values, as high volumes of ductile grains increase the effect of mechanical compaction. Therefore, the presence of ductile rock fragments is the main mechanism that accounts for the porosity loss in the studied samples (Fig 8). The petrographic observations support this interpretation, e.g., ductile shale fragments are deformed and squeezed between rigid grains (e.g. Fig. 3.7 A). The effect of ductile grains on the IGV is in agreement with previous studies on the compactional behavior of sandstones (Paxton et al., 2002; Pittman & Larese, 1991). Thus, the quartz grain size and the volume of ductile grains control the distribution and volumes of cement, which subsequently control mechanical compaction.

The effect of cementation on the mitigation of compactional porosity loss is considered subsidiary since the volumes of early diagenetic siderite are too low to keep surrounding pore space open during ongoing compaction. Siderite rimming detrital quartz grains or clay mineral coatings, e.g., pore-lining illite do not interfere and thus predate with quartz overgrowths.

Grain size and mineralogy affect the formation and occurrence of dissolution porosity, generally formed within feldspars and unstable feldspathic rock fragments (cf. Quandt et al., 2022b). Sandstones are mostly classified as feldspathic litharenites and tend to show higher volumes of dissolution porosity (> 1.5 %) compared to siltstones (< 1.5 %). The occurrence of authigenic clays, i.e., replacive kaolinite and illite, increased in sandstones since feldspars were the main source of subsequent authigenic clays (Worden & Morad, 1999). Burial diagenetic, ferroan dolomite/ankerite and siderite account for higher carbonate cement volumes that appear mostly in coarse-grained samples (Fig. 3.10 H). They fill intergranular and

intragranular porosity (Fig. 3.7 G). Compared to other deeply buried tight reservoirs where poor reservoir properties are associated with extensive authigenic illite (e.g., Higgs et al., 2007), poor reservoir properties result from pronounced mechanical and chemical compaction, but dissolution porosity slightly enhances porosity. However, samples with enhanced dissolution porosity do not correspond with higher permeabilities (Fig. 3.13). This may be a consequence of the simultaneous increase in authigenic clay minerals, i.e., kaolinite and illite, which impair the reservoir quality, and carbonate cements, which partially clog dissolution porosity.

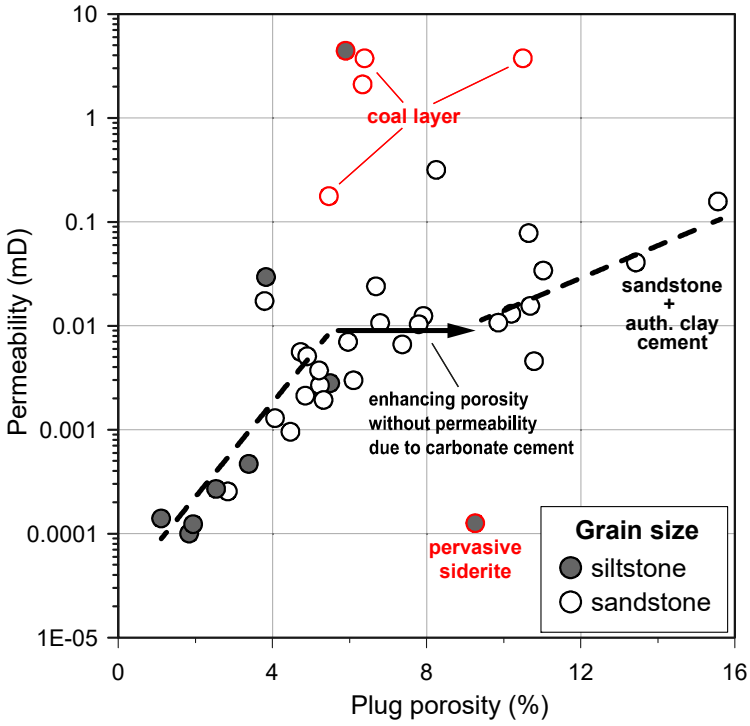

Figure 3.13 Porosity – permeability cross plot of the studied samples separated in silt- and sandstone, including the corresponding exponential best fit (dashed lines), to highlight samples with enhanced secondary porosity but no increase in permeability due to the occurrence of authigenic clays and intragranular cement. Red marked high permeability sandstone plugs contain coal layers (Pe-15, Pe-22, Pe-40, and Pe-59) or cracks (Pe-5), while the sample with reduced permeability is siderite cemented (Pe-21). These samples were treated as outliers and not included in the best fits in this plot.

3.6.7 Comparison of petrographic (point counting) with geochemical (XRF) data

The sample mineralogy from point count data (Fig. 3.5) and geochemistry from XRF analysis (Fig. 3.11) were compared to identify proxies for reservoir properties when core material is absent. Considering that sandstones primarily constitute delta front deposits while siltstones being characteristic of the lower delta plain and the wetlands (Greve et al., 2023a), facies associations are compared to each other. The results indicate that coarse-grained samples with high Si+Ca+K/Al+Fe ratios, along with abundant detrital quartz and feldspars, are predominantly linked to the delta front facies (Fig. 3.11 C). Delta front samples also exhibit elevated SiO_2 concentrations (wt%) (Fig. 3.11 D), suggesting a direct correlation between SiO_2

content and detrital quartz abundance (Fig. 3.11 E). It implies that SiO_2 content can serve as a proxy to identify delta front deposits. On the other hand, low Si+Ca+K/Al+Fe ratios in delta front deposits correspond to higher contents of non-quartz rock fragments (i.e., shales and phyllites) in siltstones samples (Fig. 3.5). Considering the negative correlation of grain size and Al_2O_3 wt% (Fig. 3.11 G) the low Si+Ca+K/Al+Fe ratio may be also used as a proxy for fine-grained sections that are designated as siltstones, assigned to the lower delta plain and wetland environment. The Si/Al ratio represents the detrital quartz relative to aluminosilicate components derived from the source area (Hofmann et al., 2001) and extended by Ca, K and Fe to identify between mudstones and sandstones (Yin et al., 2018). In the case of Fe_2O_3, carbonatic rip-up clasts seem like a suitable source (Curtis & Coleman, 1986), while K_2O and CaO reflect K-feldspar and plagioclase. Thus, XRF data can be suitable proxies to assess grain sizes and differentiate between sandstones and siltstones of their respective depositional environment and may be a tool for further exploration in the absence of core material. Since slightly better reservoir properties (mean porosity 6.8 %; mean permeability 0.18 mD), including high thermal conductivities (up to 5.3 W/(m*K)), are recorded in sandstones samples (Greve et al., 2023a), the presented geochemical analyses may be suitable proxies. This is furthermore reflected by the positive correlation between Si+Ca+K/Al+Fe ratio and helium porosity (Fig. 3.11 G).

The MgO concentration shows a similar distribution compared to Al_2O_3 and Fe_2O_3 (Fig. 3.11 A) and is likely to result from clay minerals. Since deposits of other environments (fluvial or aeolian) in the Upper Carboniferous are not considered, their relationship still needs to be investigated. $CaCO_3$ is present in low concentrations but is higher in samples from the delta front (Fig. 3.11 B). It may be related to high volumes of late diagenetic carbonates, filling intragranular pore space since outliers have enhanced volumes of mesodiagenetic carbonate cement (appendix D.1). TiO_2, MnO, SrO, BaO, Rb_2O, and Zr_2O concentrations seem to be no diagnostic proxies to estimate the sedimentary facies from the Upper Carboniferous.

3.7 Conclusions

The studied Upper Carboniferous sandstones and siltstones from Pelkum-1 core material shows poor reservoir properties (mean porosity 5.5 %; mean permeability 0.26 mD) and is considered tight (< 1 mD). Coal fragments in plugs enhance the permeability by c. 100 mD under non-reservoir conditions (1.2 MPa) but are not representative since under reservoir conditions the permeability enhancement diminishes. Poor reservoir quality primarily results from pronounced mechanical compaction (mean COPL 38.8 %) due to deep burial. Yet, petrographical data highlights slightly better reservoir properties in sandstones mostly found in delta front deposits (> 8 %; > 0.01 mD). Rock typing that integrates point counting and petrophysical data emphasizes that grain size and mineralogical composition are the main parameters controlling reservoir quality.

Better reservoir properties in delta front sandstones are a result of (1) lower volumes of ductile grains (< 38 %), such as shales, phyllites, (2) carbonatic rip-up clasts that facilitate mechanical compaction, and (3) higher volumes in feldspars and unstable rock fragments, which during burial forms dissolution porosity (> 1.5 %), which enhances the total porosity (> 8 %).

The dissolution of unstable rock fragments such as feldspars is probably related to acidic pore waters derived from organic matter maturation. However, sandstones with enhanced porosities only show a small increase in permeability since authigenic clays (i.e., kaolinite and illite) replace feldspathic fragments or late diagenetic carbonates (i.e., siderite and ferroan dolomite/ankerite) clog dissolution porosity. Cements, such as quartz overgrowths and early diagenetic siderite in sandstones seem to have a minor impact on reservoir properties.

Evaluating the Si+Ca+K/Al+Fe ratio can be a suitable proxy to assess grain sizes and differentiate between sandstones of the delta front and siltstones of the lower delta plain deposits in the studied environment. Better reservoir qualities are expected in delta front deposits (mean 6.8 %; 0.18 mD). Thus, it may be a convenient tool for further exploration in the absence of core material.

Remark: For additional methodological considerations, see appendix B.

4 Understanding the interplay of depositional rock types, mineralogy, and diagenesis on reservoir properties of the coal-bearing Upper Carboniferous Westphalian A and B of the Ruhr Area, NW Germany

4.1 Abstract

Deltaic silt- and sandstones from the Upper Carboniferous in the Ruhr Basin are currently being examined for post-mining applications (e.g., geothermal) but are also an important tight-gas reservoir analog in NW Germany. Core material from two wells in the eastern Ruhr Basin, comprising Westphalian A and B (Bashkirian) delta deposits, were studied using petrographic and petrophysical data to assess their reservoir properties and factors controlling these. The samples are generally tight, with low porosity and permeability (mean porosity 5.5 % well Bork-1 and 5.1 % well Haidberg-1; mean permeability 0.41 mD and 0.16 mD, respectively). Grain size and detrital mineralogy are the main factors affecting reservoir properties. The a change in mineralogy from litharenites to lithic subarkoses corresponds to an increase in grain size from silt to sandstone and is associated with a general increase in porosity and permeability. Dissolution porosity largely contributes (up to 6 %) to measured plug porosity. The dissolution porosity mostly relates to detrital K-feldspar and plagioclase grains and affects low present-day feldspar contents (6.0 to 6.8 %). Present ductile rock fragments, such as shales and phyllites, reduced porosity due to facilitated mechanical compaction, especially in siltstones (ICOMPACT > 0.99). Reservoir quality is related to the depositional rock type, controlling the detrital grain size. The study also identified SiO2 and Al_2O3 contents from XRF analyses as promising proxies for estimating reservoir properties and distinguishing between sandstones and siltstones. These findings help identify sections with better reservoir properties for potential exploration and production strategies in similar geological settings.

4.2 Introduction

Natural gas production from unconventional reservoirs has increased during the past several years thanks to advancements in horizontal drilling and hydraulic fracturing (Conti et al., 2016). Tight gas is a major unconventional resource in the global hydrocarbon inventory (IEA, 2009). Yet, the production performance

of tight gas reservoirs must be optimized due to narrow profit margins. In this context, the term "tight gas" is used to refer to low permeability sandstone reservoirs characterized by porosity < 12 % and permeability ≤ 1 mD, which necessitate production intervention such as fracturing and horizontal drilling for commercial viability (Surdam et al., 1997). Understanding the variability in reservoir parameters (porosity and permeability), their driving factors, as well as spatial and temporal distribution is key to successful exploration. Unlike conventional reservoirs, tight reservoirs tend to be complex and the standard workflows for conventional reservoir characterization may not be suitable (Wimmers & Koehrer, 2014), demanding a systematic integration of large-scale geologic elements and small-scale rock petrology with physical flow and storage properties (Rushing et al., 2008).

Sandstones hosting tight gas reservoirs can develop in a wide range of depositional environments. Their further classification depends on the formation mechanisms, comprising primary depositional types or structurally diagenetically modified types (Zou et al., 2010). However, if poor reservoir properties are depositionally related due to a matrix-support texture, high clay content or poor sorting of the depositional rock types, tight reservoir characteristics further result from processes during deep burial involving mechanical and chemical compaction and cementation (Gong et al., 2016; Zhu et al., 2008). The tight gas sandstone reservoirs in most Chinese basins are characterized by low lithological and textural maturity i.e., high content of feldspars and lithic fragments (Zou et al., 2012; their Tab. 2), poorly sorted, angular to subangular gains and high mud content. These sedimentary features facilitate compaction, resulting in narrow and less effective pore throats as well as poor pore size distribution, resulting in overall poor reservoir quality (Lai et al., 2016). Yet, intragranular dissolution porosity caused by mineral alteration can greatly influence reservoir properties (e.g., Becker et al., 2019; Higgs et al., 2007). Furthermore, the relationship between porosity and permeability is often poor, suggesting that the permeability is unrelated to the porosity but rather controlled by pore structures and the presence of microfractures and natural fractures that enhance permeabilities (Busch et al., 2019)

Tight sandstones from the coal-bearing Upper Carboniferous are found in the Ruhr and Lower Saxony Basins of NW Germany (Andruleit et al., 2012; Littke et al., 2011). Studies on Upper Carboniferous tight gas reservoir analogs and borehole samples (Becker et al., 2019; Becker et al., 2017; Busch et al., 2019; Quandt et al., 2022b; Wüstefeld et al., 2017) evaluated the tight gas potential of the Lower Saxony Basin, including previous successful exploration efforts (Hedemann, 1985; Kombrink et al., 2010; Pasternak et al., 1998). Although the Ruhr Basin has one of the best-documented subsurface 3D rock volumes in the world (including core material and geophysical log suites) as a consequence of centuries of hard rock coal mining, little is known about the tight gas potential of the Upper Carboniferous in North-Rhine Westphalia (NRW) (Brix et al., 1988; Casshyap, 1975; Drozdzewski, 1992, 1993; Jessen, 1956; Krull & Wrede, 2005; Strehlau, 1990; Süss, 2005; Teichmüller & Teichmüller, 1982; Wrede & Ribbert, 2005). In contrast to the Lower Saxony Basin, however, studies on diagenetic sequences for the Upper Carboniferous are rare for

the Ruhr Basin. The controls on reservoir properties, including the influence of diagenesis on the coal-bearing Upper Carboniferous Westphalian A, were recently presented by Greve et al. (2024) for well data of the Upper and Lower Bochum Formation (Bashkirian) in the former mining district "Haus Aden" in the eastern Ruhr Basin.

In addition to its use as a tight gas reservoir analog, it may be convenient to extract geothermal heat from abandoned hard coal mines, including shafts and galleries at depths of more than 1000 m (Hahn, Bussmann, et al., 2018). Porosity and permeability measurements from Upper Carboniferous outcrop samples of the Ruhr Basin range from 4.5 to 5.0 % and 0.0005 to 0.008 mD (Brenne, 2016; Duda & Renner, 2013; Stöckhert et al., 2015). Samples from core material (478 to 1005 m depth) presented by Greve et al. (2023) range from 0.5 to 15.6 % and 0.0001 to 4.43 mD. As the core material records lower minimum values, the accurate use of subsurface data and the understanding of controls on reservoir properties is necessary to correctly assess their influence on post-use case scenarios of the lithological units.

By integrating new samples and data (from wells Bork-1 and Haidberg-1) and previously published data (well Pelkum-1), we aim to further understand sedimentary and diagenetic influences on reservoir parameters using point count data from thin sections of the Westphalian A and B. The petrographic and petrophysical results are supplemented by X-ray fluorescence (XRF) data to find appropriate geochemical proxies concerning sedimentary rock types to assess reservoir attributes.

4.3 Geological setting

The Variscan orogenic foredeep in central Europe is represented by the Ruhr Basin in Germany (Fig. 4.1 A). It outlines a 150 km long and 80 km wide, NE-SW trending molasse-type foreland basin NW of the Rhenish Massif. The basin developed during the Late Carboniferous (Pennsylvanian) period and comprises an up to 4000 m thick Upper Carboniferous clastic succession (Drozdzewski, 1992, 1993; Gayer et al., 1993; Süss et al., 2008; Ziegler et al., 1995). Around 250 coal seams are contained in the sequence, comprised of cyclically deposited clay, silt, and sandstones of fluvio-deltaic (paralic) origin (Süss et al., 2007). While the growing and shrinking of the Gondwana ice shield (Rygel et al., 2008) initiated fourth-order sequences (400 ka) and fifth-order parasequences (112 ka) or sequences of higher periodicity (Süss et al., 2000), an overall coarsening-upward trend is apparent throughout the Westphalian (Drozdzewski, 2005; Süss et al., 2007; their Fig. 2). In the Variscan foreland basins of NW Europe during the Pennsylvanian, sedimentary facies changed from marine to paralic to continental deposits (Gayer et al., 1993; Guion, 1987; Guion & Fielding, 1988; Süss, 1996).

The deformation of the Ruhr Basin is of post-Westphalian age and resulted from the gradual northwestward movement of the Variscan orogenic belt (Brix et al., 1988). Near its southern edge, the Upper Carboniferous strata overlie the northern front of the Rhenish Massif and contain Variscan thrust faults and folds

(Drozdzewski, 1992, 1993; Drozdzewski & Wrede, 1994; Gayer et al., 1993). The post-Carboniferous strata of the Ruhr Basin reflect multiple periods of active faulting, overprinting the earlier Paleozoic and later Mesozoic structural framework (cf. Arfai et al., 2014; Vinken, 1988). Variscan thrusts strike NE-SW parallel to the fold axes, while NW-SE striking normal faults were developed partly at the end of the Variscan deformation and partly before and during the Zechstein (Lopingian) (Geluk, 1999; Wolf, 1985). As nearshore and hemipelagic conditions predominated since the Albian-Turonian, the Upper Carboniferous of the Ruhr Basin is unconformably covered by an Upper Cretaceous overburden in the Münsterland region that can be up to 2000 m thick and is made up of shallow-marine strata (Dölling et al., 2018).

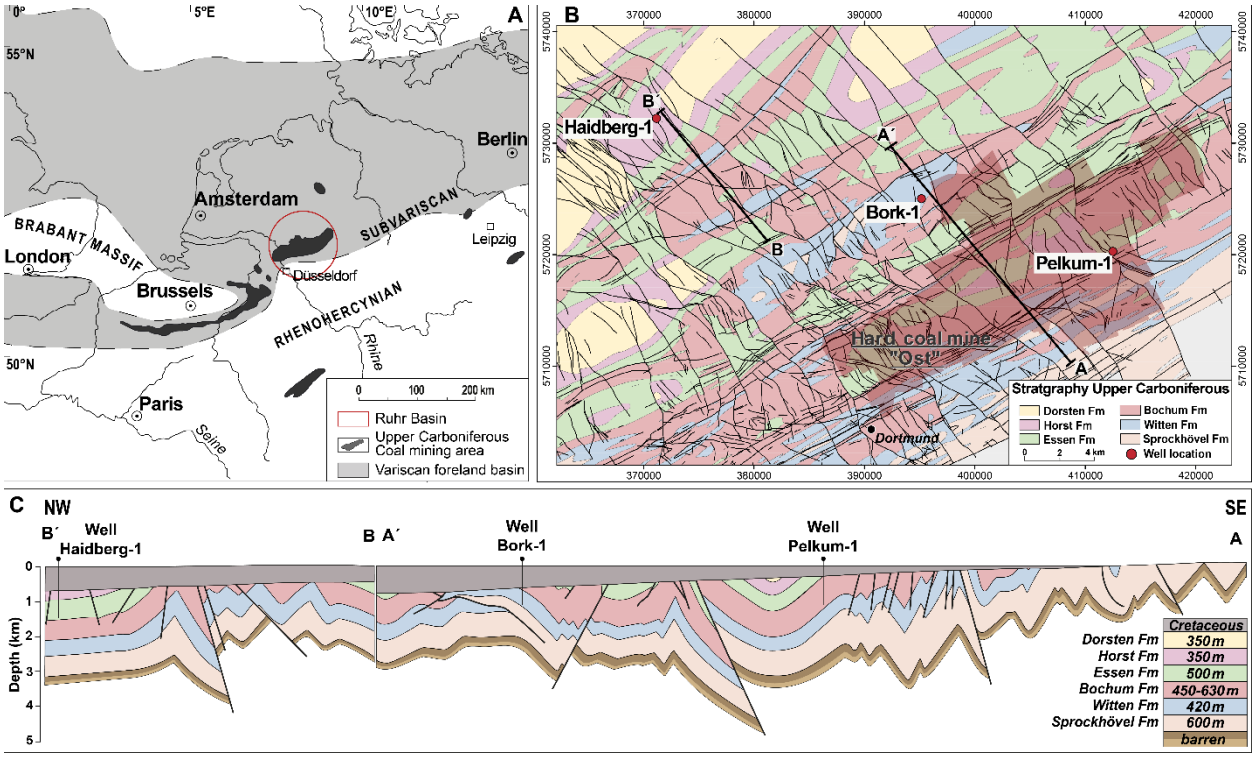

Figure 4.1 (**A**) The Variscan foreland basin in NW Europe with locations of Upper Carboniferous coalfields, modified from Jasper et al. (2009). (**B**) Location of the exploration wells Haidberg-1, Bork-1, and Pelkum-1 (mine Bergwerk Ost). Modified from the Geological Map of the Carboniferous of the Ruhr area 1:100.000, Geological Survey North Rhine-Westphalia (1982). (**C**) Cross section of the area along the studied wells, encountering the different stratigraphic levels of the Upper Carboniferous. Modified and redrawn from the Tectonic Map of the Carboniferous of the Ruhr area 1:50.000, Westphalian Mining Union Fund (1956).

4.4 Lithological units

The studied wells, Bork-1 and Haidberg-1 are located NW of the mining area “Bergwerk Ost” (now water province “Haus Aden”) in the eastern Ruhr district, Germany (Fig. 4.1 B). The wells lie on a 40 km long NW-SE oriented cross-section with well Pelkum-1 (Fig. 4.1 C). Based on three segments per well, each 20 to 34 m long, cyclically occurring sandstone, siltstone, and claystone are assigned to delta facies associations by their lithology and sedimentary structures (appendix B-C). The lithological columns

demonstrate repeating coarsening- and fining-upward sequences, resulting from sedimentation shifting from prodelta to lower delta plain (Greve et al., 2023). This sedimentation pattern is controlled by the interplay of sediment inflow, basin subsidence, and eustatic sea-level changes (Casshyap, 1975; Süss et al., 2000). Greve et al. (2023) provide characteristic successions of depositional rock types for well Pelkum-1, Bork-1, and Haidberg-1. The cycles of wells Bork-1 and Haidberg-1 demonstrate autocyclic sedimentation (Süss, 2005), resulting in a complex sequence of alternating siltstones, mudstones, and coal seams of the delta plain facies, often with sharp contacts. However, in all cycles, up to 17 m thick planar laminated sandstone bodies are present and are interpreted to represent a stacking pattern of estuarine bars and distributary channels (Greve et al., 2023).

4.4.1 Well Bork-1

Well Bork-1 reaches a depth of 1216.3 m and encounters the cyclic clastic succession of the coal-bearing Upper Carboniferous Witten Formation of the Westphalian A (Bashkirian; Langsettian Substage) at 688.8 m (Fiebig, 1977) (Fig. 4.2). Greve et al. (2023) recognize a succession of depositional rock types that at the base consists of a 2 m thick succession of rooted mudstones (Greve et al., 2023; their Fig. 4 M) (each layer with a thickness of 20 cm) sharply alternating with 5 cm thick coal seams.

The subsequent 10 to 17 m thick medium-grained sandstones of the proximal delta front with parallel-lamination (or locally structureless) are interpreted as a complex stacking pattern of estuarine bars and distributary channels (Greve et al., 2023; their Fig. 4 B and C). Sharp erosional contacts to the overlying sandstone beds are interpreted to result from internal basin dynamics, leading to a change in paleocurrent directions.

The sandstones can be incised by sharp-based, up to 1 m thick, structureless coarse-grained to pebbly sandstones in which pebbles are locally associated with shale clasts and coal fragments (Greve et al., 2023; their Fig. 4 D). The up to 4 m thick overlying fine-grained clastic rocks are made up of wavy to parallel laminated siltstone (Greve et al., 2023; their Fig. 4 F) of the shallow subtidal lower delta plain. It marks the development into a more proximal shallow environment, where root marks in siltstones and mudstones as well as the overlying up to 1 m thick coal seam (Greve et al., 2023; their Fig. 4 N) represent the subaerial peat swamps of the wetlands. Alternatively, an up to 5 m thick succession of parallel laminated sandstone alternating with structureless or wavy laminated siltstone (Greve et al., 2023; their Fig. 4 G) documents the transition between the delta front and lower delta plain environment. Toward the top, the lower delta plain environment is established, where the siltstone is locally bioturbated, and siderite nodules are observed close to the overlying coal seam. The frequent occurrence of sideritic clay-ironstone nodules and layers is related to a combination of iron reduction and microbial methanogenesis, causing alkalinity and iron concentrations to rise, promoting precipitation of either siderite or ferroan carbonate, depending on the presence of other mineral species. The tops of the sections are often formed by calcitic claystone, displaying

marine ingressions, which inundated the Ruhr Basin from the west since the Namurian C and Westphalian A (Strehlau, 1990) but were fainting already in the Westphalian B and C (Bless et al., 1980).

4.4.2 Haidberg-1

Well Haidberg-1 reaches a depth of 1459.0 m and encounters the typical clastic succession of the coal-bearing Upper Carboniferous Horst Formation of the Westphalian B (Bashkirian; Duckmantian Substage) at 947.7 m (Von Sperber & Hettenberger, 1992) (Fig. 4.2). Greve et al. (2023) have interpreted a sedimentary succession that are represented at the base by up to 3 m thick rooted mudstones of the subaerial wetlands, laminated with some mm-thick siltstone lenses with apparent siderite nodules and plant remains. The up to 80 cm thick overlying coal is again overlain by 10 cm to 3.5 m thick structureless mudstones (Greve et al., 2023; their Fig. 4 I) that comprise siderite nodules and plant remains. The overlying 15 m thick medium-grained sandstone marks the continuous shift from the lower delta plain to the delta front. Planar lamination in the sandstone bed is dominant, while planar cross lamination is rarely present in a 30 cm thick section. The shallowing of the depositional environment is displayed by the contact at the top of the sandstone body to the overlying parallel laminated mudstone (Greve et al., 2023; their Fig. 4 J) or by the gradual transition from parallel laminated siltstones to rooted mudstones (Greve et al., 2023; their Fig. 4 M). Structureless siltstone and parallel laminated sandstone incising the mudstone display tidal creek deposits on the lower delta plain. At the top of this succession, the 4 m thick rooted mudstone is overlain by coal of up to 4 m thickness, displaying the subaerial wetlands of the lower delta plain.

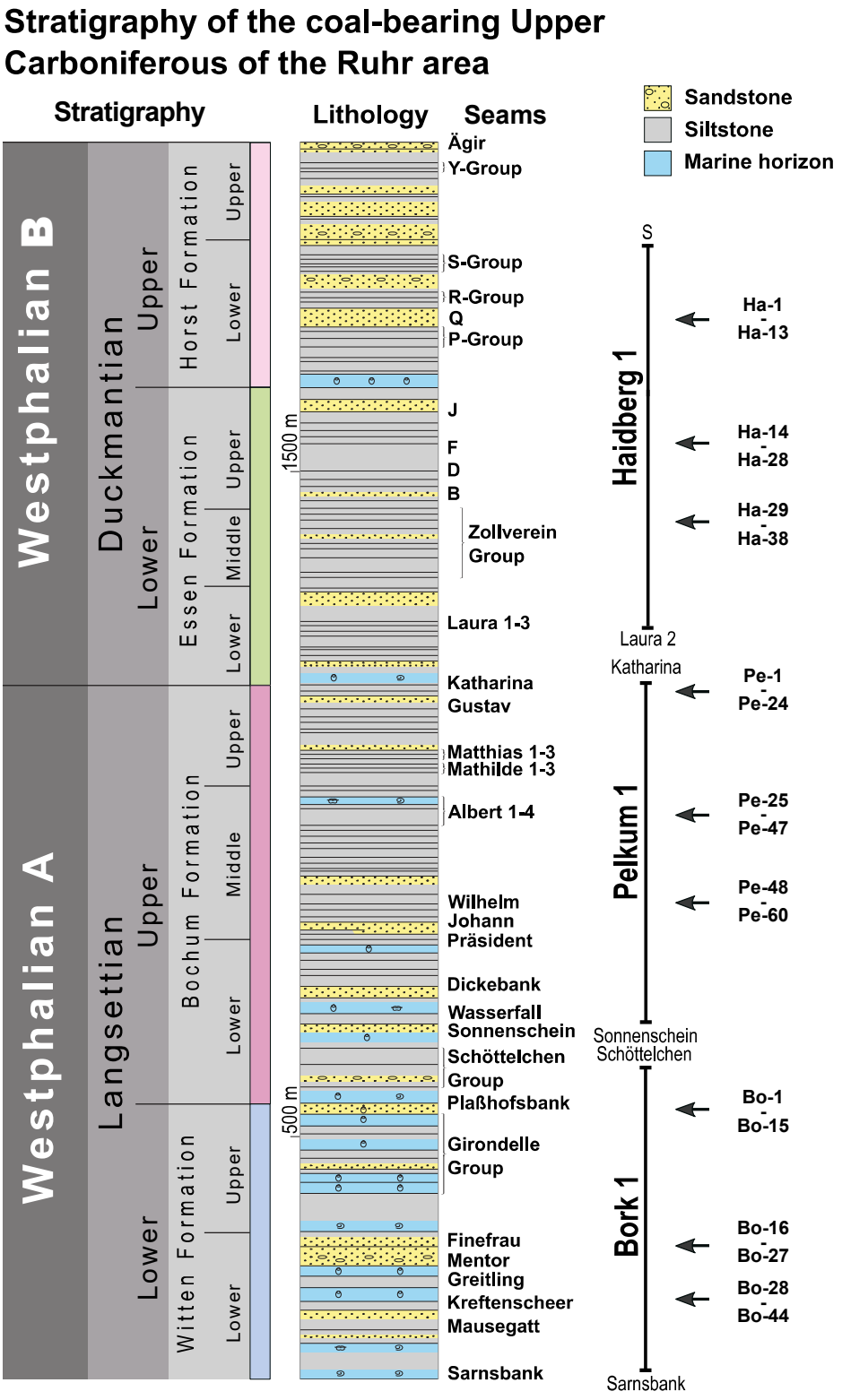

Figure 4.2 Stratigraphic column (color code for formations as in Fig. 4.1 B and C) including a simplified lithological column comprising all relevant coal seams, the accumulated thickness and the three drill cores with the examined cycles. Coal seam at the bottom and top of cored sections of the three wells Bork-1 (688.8 - 1216.3 m), Pelkum-1 (472.30 - 1221.70 m), and Haidberg-1 (947.7 - 1459.0 m) refer to coal seams to the left and are shown for the stratigraphic correlation. The names to the right indicate the studied samples. Modified and redrawn after Hesemann (1975).

4.5 Methods

For petrophysical measurements, 44 cylindrical plug samples (2.51 cm in diameter) with their long axes parallel to bedding were prepared for this work and correlated with 99 plug samples from previous works (for details, see appendix D.2-3). For 61 plug samples of the studied wells, trim ends are embedded in blue-dyed epoxy resin to prepare thin sections with a thickness of 30 µm. Thin sections are half stained with a combined Alizarin red S and potassium ferricyanate solution in 0.3% HCl to allow the identification carbonate minerals and covered by a glass slide. Six samples were polished for further reflected light and cathodoluminescence analyses of vein and host rock cements (Bo-7, Bo-13, Bo-34, Ha-27, Ha-34, and Ha-35).

The long axes of 150 grains per thin section were measured (appendix D.2-3) using a regularly spaced grid that covered the entire thin section to gain area-weighted grain size data. Grain size parameters such as sorting, mean, and median diameter were calculated after Folk & Ward (1957). Grain sizes are classified after Udden (1914) and Wentworth (1922). Roundness was determined using standardized comparison charts after Tucker (2001).

For a quantitative assessment, 300 points per thin section have been counted, according to McBride (1963), using a Pelcon Automatic Point Counter mounted on a Zeiss DM 2700 microscope. The Q pole includes quartz, chert, and quartzite, the F pole has feldspars, and the R pole contains rock fragments other than mica. Rock fragment classification was based on textural characteristics described by Ulmer-Scholle et al. (2014). The step size was adjusted to the maximum observed grain size (Busch et al., 2017) to gain area-weighted results.

Point-counting data were used to reconstruct the feldspar volume during deposition by quantifying and adding the intragranular dissolution porosity and replacive cement phases to the present-day contents. Though they do not include information about the hosted grain, most replacive cements are observed in feldspars. Furthermore, point-counting data were utilized to obtain the intergranular volume (IGV) as an indicator for compaction, which is the sum of intergranular porosity, intergranular cement, and depositional clay mineral matrix (Paxton et al., 2002). To assess the compactional (COPL) and cementational porosity loss (CEPL), point-counting data were processed to calculate the COPL and CEPL after equations [1] and [2] and the compaction index ICOMPACT after [3] from Lundegard (1992). For this purpose, the initial porosity (P_i), intergranular optical porosity (P_o), and volume percent of pore-filling cement (C) were determined (appendix D.2-3). The minus-cement porosity (P_{mc}), here, equals the intergranular volume (IGV), as no detrital clay mineral matrix is present, and equals the sum of P_o and C (Ehrenberg, 1989). According to calculations after Beard & Weyl (1973) using sorting and grain size of the samples, P_i values vary between 30.4 and 39.7 %. Sample division in terms of sorting (among poor and moderate) was done to avoid the impact of different initial porosities (appendix D.2-3). Yet, to demonstrate the relative impact

of compactional and cementational porosity loss, an initial porosity of 40 % in all samples was supposed for calculations since the conclusion remains identical.

$$\text{Compactional porosity loss (COPL)} = P_i - (100 \times IGV) - (P_i \times IGV) / (100 - IGV) \quad [1]$$

$$\text{Cementational porosity loss (CEPL)} = (P_i - COPL) \times (C / IGV) \quad [2]$$

$$ICOMPACT = COPL / (COPL + CEPL) \quad [3]$$

To assess carbonate vein cements, cathodoluminescence (CL) investigations were conducted on polished thin sections (Ha-27 and Ha-34), using a CITL Mk5 Optical Cathodoluminescence Microscope Stage mounted on a Leitz Dialux Microscope equipped with a Jenoptik Gryphax Naos camera (e.g., Monsees et al., 2020). The electron beam current and voltage were adjusted to excite luminescence (100 µA and 10 kV for carbonates; 325-350 µA and 15-20 kV for quartz). CL emissions depend mainly on the crystal structure, lattice defects, and distribution of trace elements (Götze et al., 2013).

Porosity was measured on 43 1-inch core plug samples using a micromeritics AccyPyc II 1340 Helium-pycnometer (Becker et al., 2017) at Karlsruhe Institute for Technology (KIT). Permeability was measured on the same plugs at 12 bar confining pressure using dry, oil-free lab air (80 % N_2, 20 % O_2) as permeant in a Westphal Mechanik permeameter (Busch et al., 2022) at KIT and was Klinkenberg-corrected. The samples used for correlation were measured in the same setup. The limits for presented permeability measurements are 0.0001 and 10000 mD. The measurement setup includes mass flow meters with a specified accuracy of 0.1 % of the flow rate, resulting in an error of 0.1 % of the final permeability value. The reproducibility of measurements is within on average 1.8 % of the given value.

X-ray fluorescence (XRF) was used to determine whole rock element data at the Geological Survey of North Rhine-Westphalia, Krefeld, Germany, using a Spectro Xepos He X-ray spectrometer. XRF was used to determine the major and minor elemental composition qualitatively and quantitatively of 17 samples from the deltaic facies associations and combined with XRF values from 18 samples from Greve et al. (2024). The elements were determined in their oxidized state as a composition percentage and are required for geochemical characterization. For the geochemical analyses, samples from core material were crushed into pieces of < 2 mm and then powdered using an agate mill. The sample powder was annealed before mixing with lithium tetra/metaborate and fused in platinum crucibles at 1150°C to prepare fused discs. The fused discs produced in this way correspond to the classical silicate analysis, in which the element contents are calculated as oxides. Loss of ignition (LOI) was determined gravimetrically by heating the samples to 1050°C. Total iron is expressed as Fe_2O_3. The concentration of $CaCO_3$ was determined thermally. Consequently, siderite is not included since it decomposes at 550°C, while calcite is thermally stable

(Bisutti et al., 2007).[3] All data derived from previous studies (Greve et al., 2023; Greve et al., 2024) used for correlation are also added in appendix D1-3.

4.6 Results

4.6.1 Petrography

4.6.1.1 Textural parameters

The sandstones in well Bork-1 (n=23) are very fine- to very coarse-grained (0.063 to 1.3 mm) and poorly to well-sorted, whereas sandstones in well Haidberg-1 (n=24) are very fine- to medium-grained (0.063 to 0.3 mm). Siltstones in well Bork-1 (n=7) are fine to coarse-grained (0.02 to 0.062 mm), and sorting is moderate to moderately well, while siltstones in well Haidberg-1 (n=7) are fine- to coarse-grained (0.01 to 0.062 mm), and sorting is moderate to moderately well. The grain shape of framework grains is commonly sub-angular to rounded with modest sphericity (equant to discoidal grains). Most grain size distributions are nearly symmetrical (n=47) or coarse skewed (n=44). Only a few samples are strongly coarse skewed (n=3) or fine skewed (n=6), indicating the grain size distribution to be generally prone towards finer grain sizes relative to coarser grain sizes (Fig. 4.3). Further, the increase of grain size and better sorting are correlated. However, no correlation is noticed between skewness with sorting and grain sizes (Fig. 4.3).

[3] For additional methodological considerations, see Addendum B.

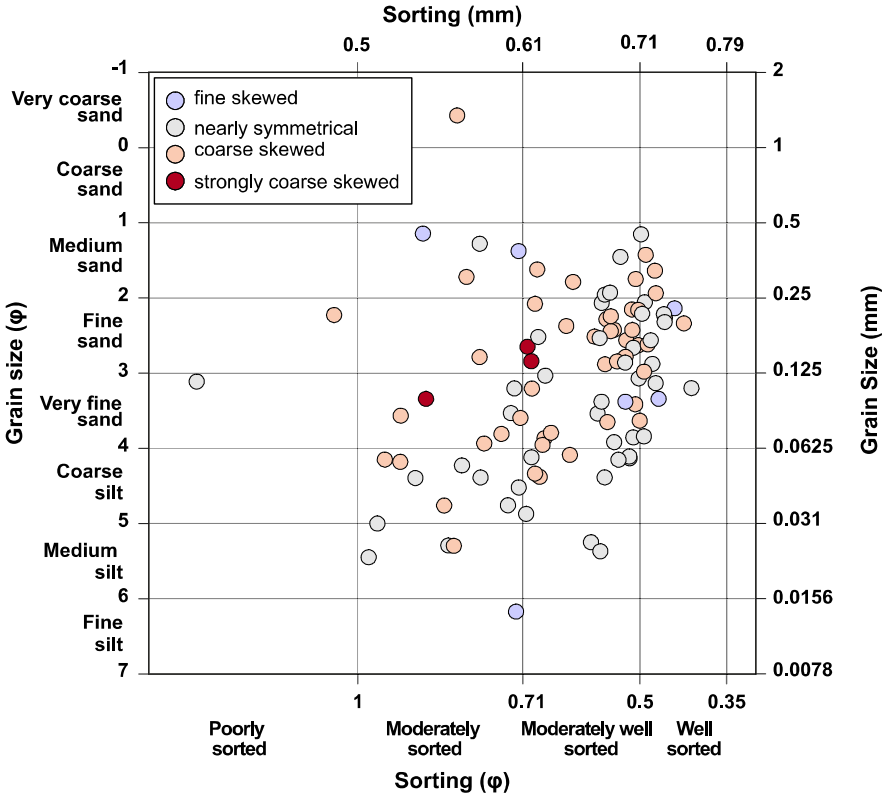

Figure 4.3 Sorting plotted against mean grain size for the investigated samples and samples from Greve et al. (2024), primarily composed of fine-grained siltstones to very coarse-grained sandstones. The samples are poorly to well sorted and characterized by a fine to strongly coarse skewness, indicated by the color code. All thresholds are taken from Folk (1980).

The analyzed silt and sandstones plugs (n=60) usually exhibit planar or wavy lamination accompanied by elongated constituents (mostly mica flakes) that are aligned (Fig. 4.4 A). The mm-scale bedding (lamina) texture results in more than one predominant grain size. Several pebbly to coarse-grained sandstones are structureless (Fig. 4.4 B). In sample Bo-24, roots or minor bioturbation slightly obliterated the lamination (Fig. 4.4 C).

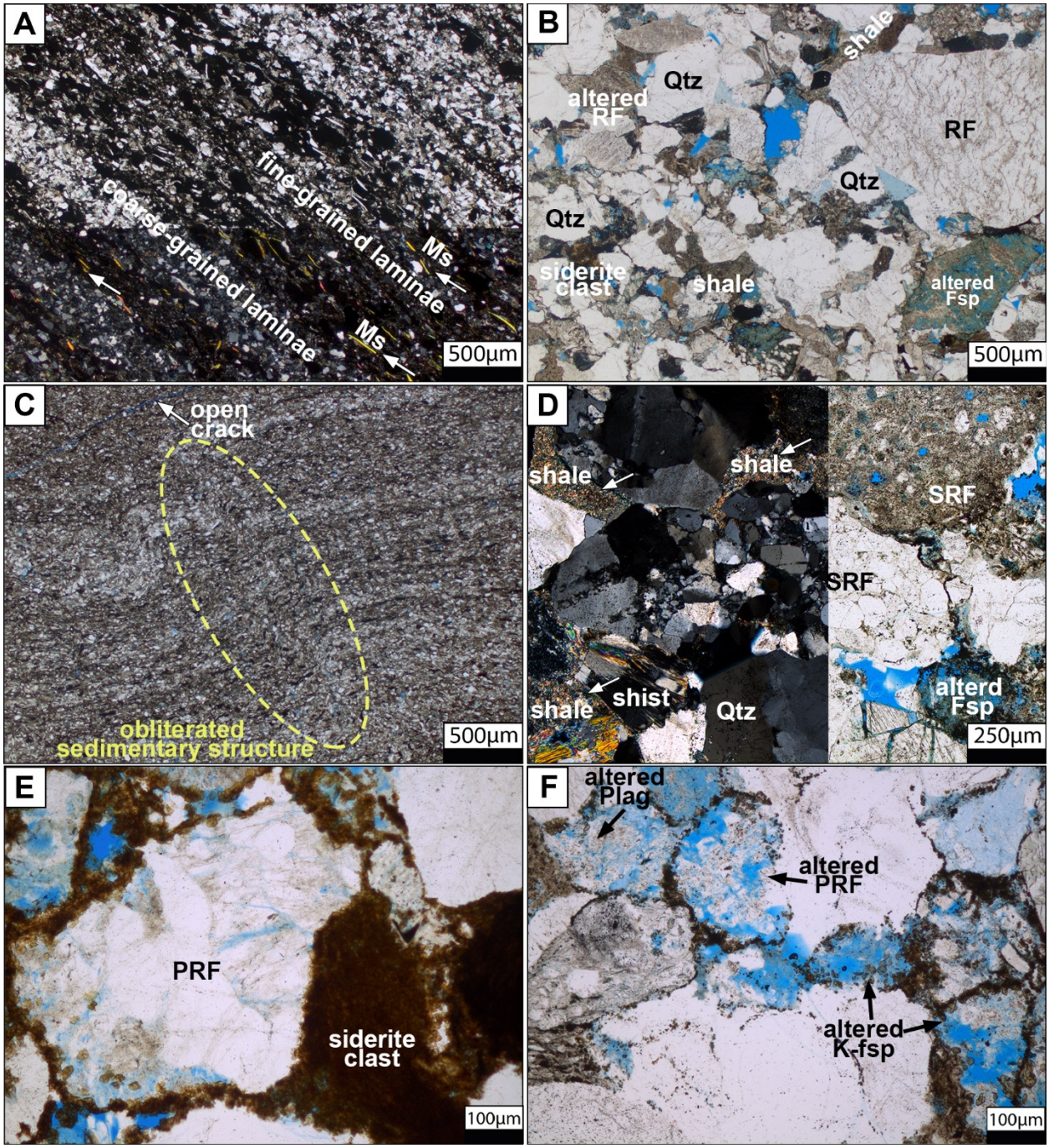

Figure 4.4 Prominent textures in Upper Carboniferous sand- and siltstones. (**A**) Lamination in sample Ha-19 shows a change in mineralogical composition, i.e., high occurrence of shales, carbonatic rip-up clasts, and stretched constituents (e.g., mica flakes) that are aligned (arrows). (**B**) Structureless texture in a moderately sorted sample (Bo-9) (**C**) Sedimentary texture that is weakly obliterated in sample Bo-24 and might be due to roots or small burrows (yellow dashed). The sample includes an open crack sub-parallel to its lamination. (**D**) Ductile shale fragments with relatively poor internal clay mineral orientation (arrows) appear deformed and are likely to be embayed by adjacent rigid grains, such as sedimentary rock fragment (SRF) composed of silt-sized clasts with clay cement (Bo-9). (**E**) Plutonic rock fragment (PFR) composed of quartz and feldspar intergrowth with highly embayed quartz in a sandstone sample (Bo-13). Feldspar dissolution of the PFR can lead to residual quartz. (**F**) Extensive alteration of plagioclase (Plag), K-feldspar (K-fsp), and plutonic rock fragments (PRF) results in secondary pores, which retain their grain

shape (Bo-12). Qtz: quartz grain, Plag: plagioclase, K-fsp: K-feldspar, PRF: plutonic rock fragment, SRF: sedimentary rock fragment, Ms: muscovite.

4.6.1.2 Detrital constituents

Monocrystalline quartz (Qm), polycrystalline quartz (Qp), plagioclase (Plag), K-feldspar (Kfs), and rock fragments (R) make up the detrital grains. Rock fragments are further subdivided into sedimentary rock fragments (SRF), metamorphic rock fragments (MRF), plutonic rock fragments (PRF), volcanic rock fragments (VRF), shales, carbonate intraclasts, phyllites, schists, and quartzites (for details see supplemental material 2). The most prevalent grain type is polycrystalline quartz (Qp), which consists of recrystallized and stretched subgrains as well as quartz with undulose extinction (18.0 to 50.0 %, mean 32.8 % in Bork-1; 14.0 to 50.0 %, mean 30.2 % in Haidberg-1). The monocrystalline quartz (Qm) class is dedicated to quartz grains with non-undulatory extinction and contains fewer grains (2.0 to 16.3 %, mean 8.9 % in Bork-1; 2.0 to 25.3 %, mean 10.5 % in Haidberg-1).

Quartzites are mostly composed of equant quartz subgrains and aligned micas and typically range from 0.0 to 7.7 %, with a mean of 2.5 % in well Bork-1 and 0.0 to 7.7 %, with a mean of 1.7 % in well Haidberg-1. K-feldspar grains (0.0 to 9.7 %, mean 4.1 % in Bork-1; 0.0 to 14.3 %, mean 4.0 % in Haidberg-1) prominently contain intragranular pore space (Fig. 4.4 D). Plagioclase exhibits synthetic albite twins under cross-polarized light and is less common than K-feldspar (0.0 to 5.3 %, mean 2.4 % in Bork-1; 0.0 to 5.3 %, mean 1.9 % in Haidberg-1). Felspars are frequently altered to illite and intragranular dissolution pores. All samples include a high percentage of shale rock fragments (6.0 to 37.7 %, mean 19.5 % in Bork-1; 2.3 to 46.7 %, mean 18.1 % in Haidberg-1). Shale rock fragments with poor internal clay mineral orientation, particularly in siltstones, are ductile and prone to be embayed by nearby rigid grains. Microcrystalline siderite and clay minerals are the main constituents of siderite clasts (carbonatic rip-up clasts) (Fig. 4.4 E), which appear brown under plane-polarized light and are widely distributed (0.0 to 36.0 %, mean 6.3 % in Bork-1; 0.0 to 65.0 %, mean 11.1 % in Haidberg-1). Schists are widespread (0.0 to 8.7 %, mean 3.0 % in Bork-1; 0.0 to 8.7 %, mean 3.1 % in Haidberg-1) and consist of foliated fragments with micas distributed between the elongated quartz crystals. Phyllites are another common foliated rock fragment (0.0 to 8.0 %, mean 2.8 % in Bork-1; 0.0 to 10.7 %, mean 2.9 % in Haidberg-1), which include very fine-crystalline mica with well-developed crystal orientation.

Plutonic rock fragments comprising quartz, plagioclase, or K-feldspar (Fig. 4.4 E) are common (0.0 to 6.0 %, mean 1.9 % in Bork-1; 0.0 to 6.0 %, mean 1.8 % in Haidberg-1). Intragranular porosity in these PRF (Fig. 4.4 E, F) can occur when plagioclase and K-feldspar are partially dissolved or altered to illite. Rare volcanic rock fragments (0.0 to 4.0 %, mean 0.7 % in Bork-1; 0.0 to 4.0 %, mean 0.9 % in Haidberg-1) contain small euhedral plagioclase phenocrysts in an aphanitic matrix, which are usually degraded, resulting in intragranular pore space (Fig. 4.4 F). Sedimentary rock fragments (0.0 to 8.0 %, mean 1.6 % in Bork-1;

0.0 to 9.0 %, mean 1.7 % in Haidberg-1) consist of fine-grained sandstone and siltstone clasts cemented by clay minerals (Fig. 4.4 D). Muscovite is the most prominent mica (0.0 to 17.3 %, mean 4.2 % in Bork-1; 0.0 to 17.3 %, mean 4.1 % in Haidberg-1), while biotite and chlorite occur in traces (< mean 0.3 %). Zircon is the main accessory heavy mineral observed (0.0 to 0.7 %, mean 0.1 % in both wells), while tourmaline occurs in traces (< 0.7 %). Most samples contain coal layers and fragments (Fig. 4.4 C), with open coal cleats oriented parallel to the coaly flakes.

Regarding their mineralogical composition, the studied sandstones are classified as litharenites (n=51), feldspathic litharenites (n=25), subarkose (n=4), and sublitharenites (n=1), while siltstones are classified as litharenites (n=24). Furthermore, samples from the delta front contain fewer rock fragments than the wetland or lower delta plain samples. Generally, samples with coarser grain sizes tend to have a more quartz-rich composition than those with finer grain sizes (Fig. 4.5). In contrast, samples with finer grain sizes show a more rock fragment-rich composition than those with coarser grain sizes. Often these rock fragments deform in a ductile manner (Fig. 4.4 D).

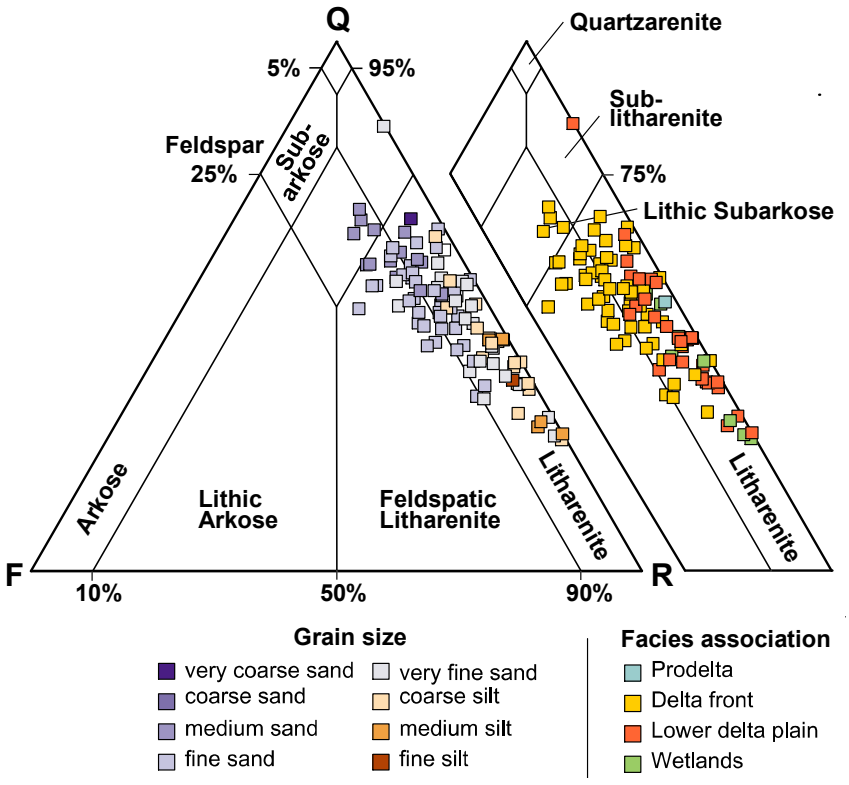

Figure 4.5 Rock classification diagram for the silt- and sandstone samples of the wells Pelkum-1, Bork-1, and Haidberg-1 with the color code indicating grain sizes (plot after McBride (1963)). In addition, the samples are color-coded for their respective facies association.

4.6.1.3 Optical porosity

The range of optical porosity is 0.0 to 5.3 % (mean 1.7 %) in well Bork-1 and 0.0 to 3.7 % (mean 1.2 %) in well Haidberg-1. It comprises intergranular porosity (0.0 to 0.7 %, mean 0.1 % in Bork-1; 0.0 to 0.3 % in Haidberg-1) as well as intragranular porosity resulting from the dissolution of K-feldspar (0.0 to 2.3 %, mean 0.4 % in Bork-1; 0.0 to 2.0 %, mean 0.6 % in Haidberg-1), plagioclase (0.0 to 2.3 %, mean 0.6 % in Bork-1; 0.0 to 1.7 %, mean 0.3 % in Haidberg-1), and rock fragments (0.0 to 3.3 %, mean 0.6 % in Bork-1; 0.0 to 1.3 %, mean 0.3 % in Haidberg-1). Intragranular pores remained grain-shaped, and ductile particles have deformed around the prior grain outline (Fig. 4.4 F).

4.6.1.4 Authigenic mineralogy

Authigenic minerals comprise 0.0 to 31.7 % (mean 5.0 %) of the rock mineralogy in well Bork-1 and 0.3 to 44.0 % (mean 5.5 %) in well Haidberg-1. The predominant phases are authigenic kaolinite and carbonate cement, including syntaxial siderite and equant calcite, as well as quartz overgrowths. Furthermore, fracture-filling carbonate, kaolinite, and marcasite/pyrite are observed.

The most prominent authigenic mineral is siderite, which appears as intergranular cement forming isopachous bladed siderite cement on detrital carbonatic rip-up clasts or covering framework grains (0.0 to 11.0 %, mean 0.8 % in both wells). Siderite is readily identified since it produces small, yellowish-brown, noticeably flattened, or equal rhombic structures with high relief (Fig. 4.6 A). Furthermore, the intragranular pore space of previously dissolved unstable grains, such as feldspars and volcanic rock fragments, can be filled by siderite (Fig. 4.6 B) (0.0 to 3.0 %, mean 0.5 % in Bork-1; 0.0 to 7.0 %, mean 0.7 % in Haidberg-1).

Authigenic quartz overgrowth cements are frequently observed (0.0 to 5.7 %, mean 1.5 % in Bork-1; 0.0 to 5.7 %, mean 0.9 % in Haidberg-1) (Fig. 4.6 C) and are more prominent in coarse-grained samples of the delta front. They form syntaxial overgrowths on monocrystalline and polycrystalline quartz and can prominently be identified based on solid inclusion rims (Fig. 4.6 D, mostly hematite or siderite) on the detrital grain outline. Polycrystalline quartz grains include small (10 µm) isopachous overgrowths with rhombohedral or prismatic crystal faces, while monocrystalline quartz grains are substrates to greater volumes of partially non-euhedral quartz overgrowths. The overgrowths are frequently inclusion-poor in contrast to detrital quartz grains that are inclusion-rich. Syntaxial quartz overgrowth cement has also been observed to form in intragranular dissolution pores on the residual quartz of dissolved rock fragments but is rare in both wells (< 0.7 %). Most quartz overgrowth cement encloses the grain-rimming siderite (Fig. 4.6 A, C). Yet, some siderite crystals are also limited by quartz cement (Fig. 4.6 E).

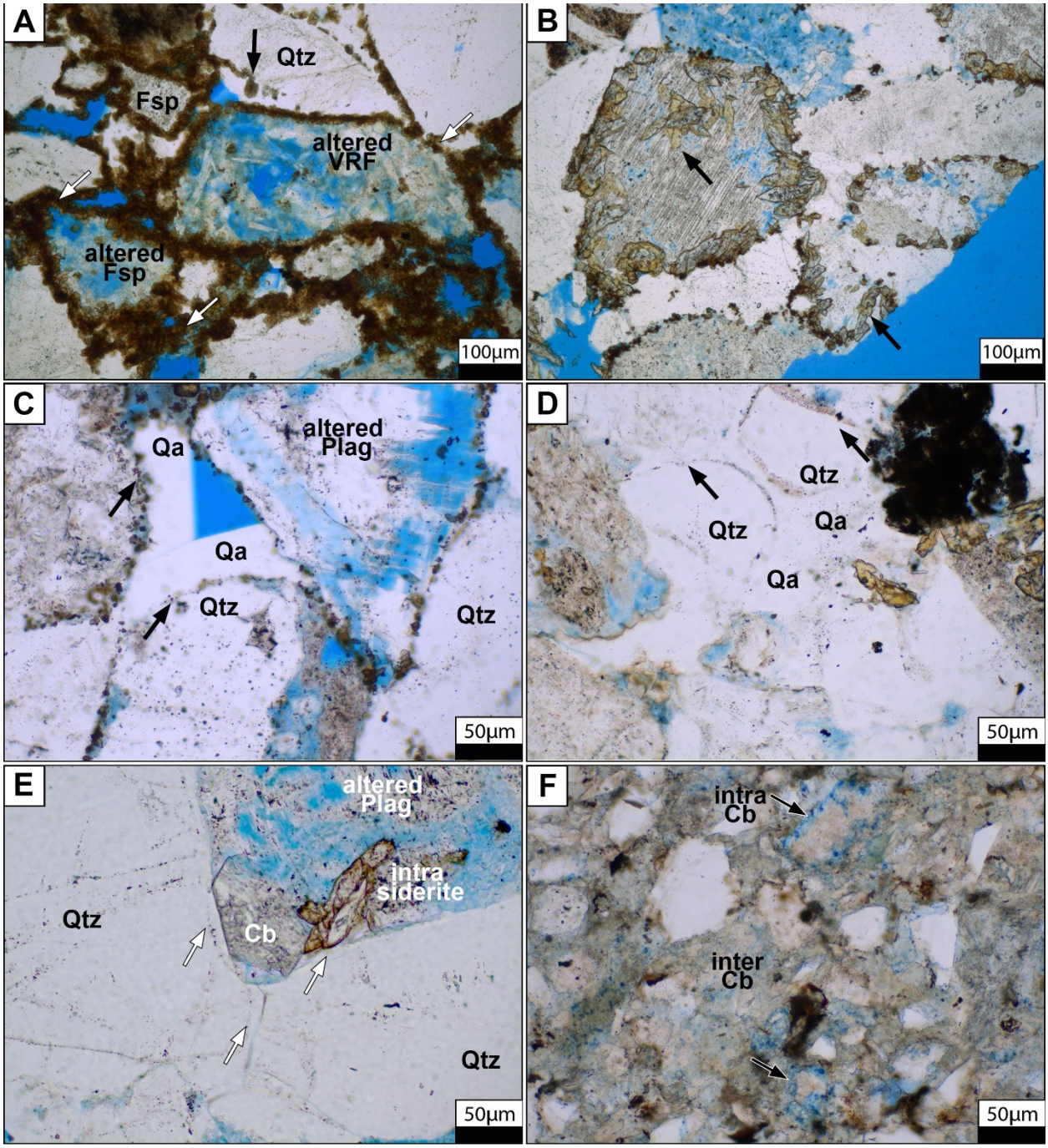

Figure 4.6 (**A**) Intergranular siderite cement (arrows) is recognized by its small, strongly flattened, or equant rhombs in sample Bo-10. Authigenic quartz is overgrowing detrital quartz. The boundary between the detrital grain and quartz overgrowth is marked by siderite (arrow). (**B**) Siderite filling intragranular porosity (arrows) in a partly dissolved plagioclase (Bo-36). (**C**) Authigenic quartz is common as syntaxial overgrowths on a detrital quartz gain. The interface between the detrital grain and quartz overgrowth is marked by siderite (arrow). (**D**) Colored hematite rims indicate quartz overgrowths in sample Bo-29 on detrital quartz. Yet, hematite rims are rare in the studied samples. (**E**) Quartz overgrowths (arrows) delimit intragranular calcite (Cb) and siderite (unstained half, Ha-6). Further, calcite restricts the growth of siderite. (**F**) Pervasive equigranular, xenotropic textured slightly ferroan calcite cementation (inter Cb). It can be distinguished from intragranular calcite (intra Cb), which is more deeply stained (sample Ha-17). Plag: Plagioclase, VRF: Volcanic rock fragment, Qtz: Quartz grain, Qa: Authigenic quartz, Cb: Ferroan calcite, Kln rp Fsp: Kaolinite replacing feldspar.

Pervasive equigranular, xenotropically textured, slightly ferroan calcite cements (stained blue) are present in sample Ha-17 (Fig. 4.6 F). Calcite is locally abundant in samples of well Haidberg-1 (Ha-9, Ha-10, Ha-24, Ha-25, Ha-26, and Ha-33) as equant to blocky calcite spar cement filling fractures (Fig. 4.7 A) (0.0 to 3.7 %, mean 0.4 %). During CL analyses, the fracture-filling carbonate can be differentiated into less-luminescent ankerite (Ank) and brightly luminescent manganese-rich ferroan calcite (Cmf, Fig. 4.7 B). Manganese-rich ferroan calcite encases the (partly) euhedral ferroan calcite and fills fractures and pores (Fig. 4.7 B, C, arrows). Both calcite phases overgrow cubic sulfides, which are present at the host-rock vein interface (Fig. 4.7 C, white arrows). Adjacent to fractures filled by ferroan calcite, intragranular pore space in partially dissolved rock fragments are filled by luminescent manganese-rich ferroan calcite (Cmf), while other intragranular pores appear unfilled (Fig. 4.7 C and D, black arrow). Manganese-rich ferroan calcite (Cmf), filling intergranular and intragranular porosity, is also observed to encase euhedral quartz overgrowth cement and siderite (Fig. 4.7 D, arrows).

Fracture-filling pyrite/marcasite (Fig. 4.7 A) is present in some samples of well Haidberg-1 (Ha-9, Ha-10, Ha-33) (0.0 to 2.3 %, mean 0.1 %). The quartz grains show thin syntaxial quartz overgrowths on their surfaces, which are in contact with the sulfides (Fig. 4.7 E, arrows). Sulfides, in general, are present in traces (0.0 to 0.3 %, mean 0.0 % in Bork-1; 0.0 to 1.3 %, mean 0.0 % in Haidberg-1) and only occlude negligible volumes of intergranular porosity. The intergranular pyrite/marcasite is encased by isopachous bladed siderite cement growing on carbonatic rip-up clasts. Near pyrite/marcasite filling fractures, goethite staining of clay mineral cements and clay-bearing rock fragments is observed (Fig. 4.7 E and 8 C).

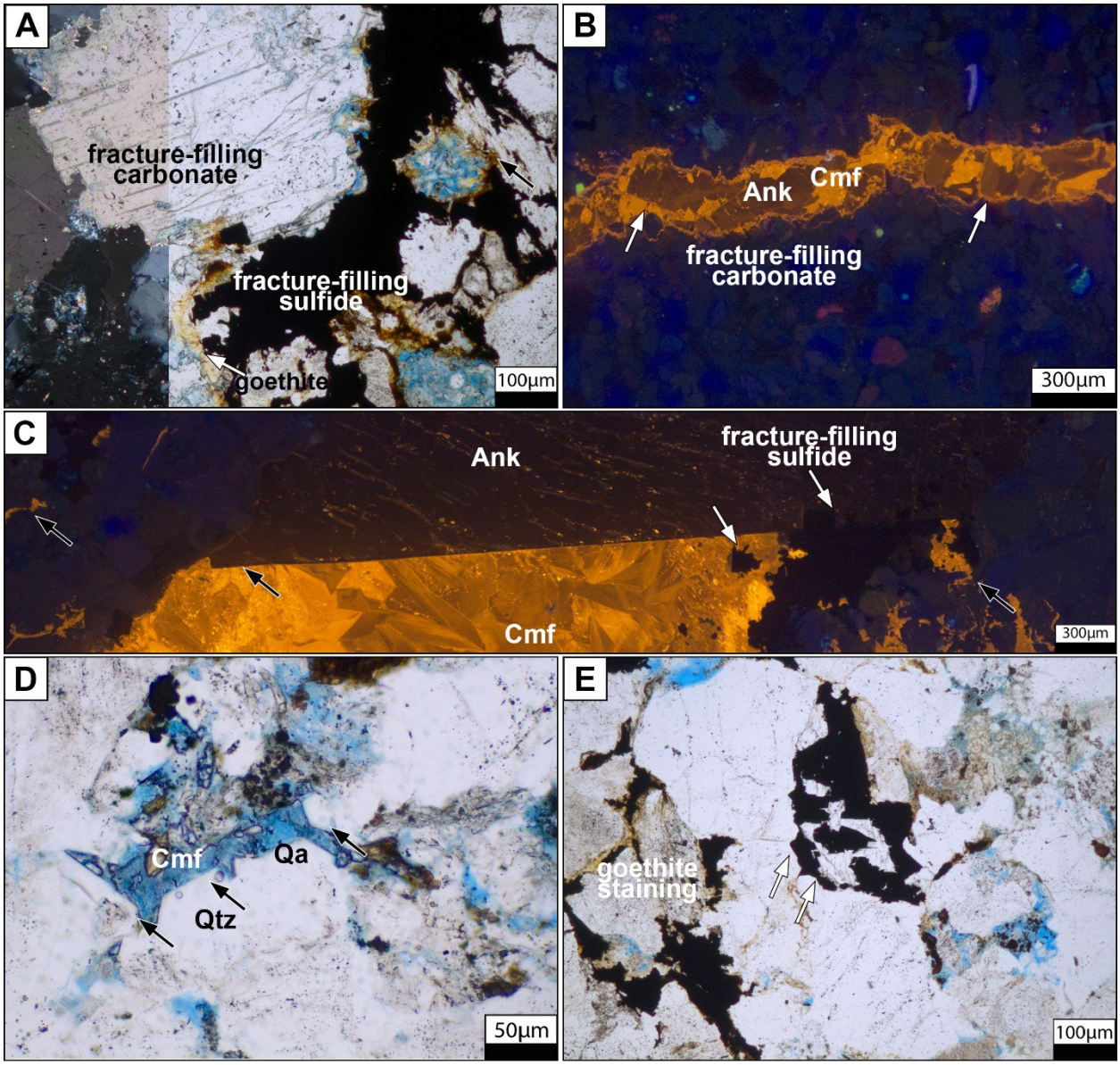

Figure 4.7 (**A**) Fracture-filling sulfides are cementing framework grains next to fracture-filling calcite in sample Ha-9. Fracture-filling calcite is composed of poikilotopic calcite. The sulfide exhibits euhedral cubic crystal faces at the interface with calcite. Goethite covers authigenic minerals (arrows). (**B**) The CL picture (Ha-34) displays two carbonate compositions, ankerite (Ank) (weakly luminescent) and manganese-rich ferroan calcite (Cmf) (brightly luminescent) (arrows). (**C**) The fracture exhibits a distinct internal change in carbonate composition (central black arrow) between non-luminescent ankerite (Ank) and luminescent manganese-rich ferroan calcite (Cmf). Both phases overgrow cubic sulfides, also filling the fracture (white arrows). Adjacent to the fracture, luminescent manganese-rich ferroan calcite fills intragranular porosity (black arrows). (**D**) Blue stained manganese-rich ferroan calcite (Cmf) clogs a primary pore and encloses quartz overgrowth cement (Qa) (arrows) in sample Ha-33. (**E**) Widespread sulfide cement in sample Ha-9 fills inter- and intragranular porosity. The quartz grains neighboring sulfide cement show syntaxial quartz overgrowth (arrows). Qtz: quartz grain, Qa: Authigenic quartz, Ank: Ankerite, Cmf: Manganese-rich ferroan carbonate, Kln: Kaolinite.

4.6.1.5 Authigenic clay minerals

Authigenic kaolinite and illite are the main clay minerals observed (0.0 to 2.3 %, mean 0.5 % in Bork-1; 0.0 to 5.3 %, mean 1.3 % in Haidberg-1), with coarse-grained samples from the delta front showing the highest contents (0.0 to 5.3 %, mean 1.1 %) compared to fine-grained samples from other depositional rock types (0.0 to 3.0 %, mean 0.4 %). Kaolinite displays aggregates of randomly oriented booklets ranging from extremely fine to fine crystalline (4-20 µm) to coarse crystalline size (Fig. 4.8 A to D). The prevalence of coarse-crystalline kaolinite occurs in higher volumes (0.0 to 1.3 %, mean 0.2 % in Bork-1; 0.0 to 4.0 %, mean 0.7 % in Haidberg-1) than the fine-crystalline kaolinite (0.0 to 0.7 %, mean 0.1 % in Bork-1; 0.0 to 2.0 %, mean 0.5 % in Haidberg-1). Kaolinite either replaces unstable grains such as igneous rock fragments or feldspar, outlined by residual grain limits or is widely occluding pores (pore-filling). Euhedral quartz delimits the growth of kaolinite (Fig. 4.8 A). CL analyses display that replacing and pore-filling kaolinite is overgrown by calcite adjacent to fracture-filling calcite (Fig.8 B, arrow). Similarly, adjacent to fracture-filling sulfide, kaolinite booklets are stained by goethite (Fig.8 C, arrows). Next to replacive and pore-filling kaolinite, coarse-crystalline kaolinite booklets locally fill fractures or cover fracture surfaces, encasing quartz overgrowth cement (Fig.8 D). Marcasite often accompanies kaolinite filling fractures (Fig. 4.8 E). Marcasite shows euhedral crystal faces (Fig.8 F, arrows) encased by kaolinite, but the booklets are not intergrown with marcasite.

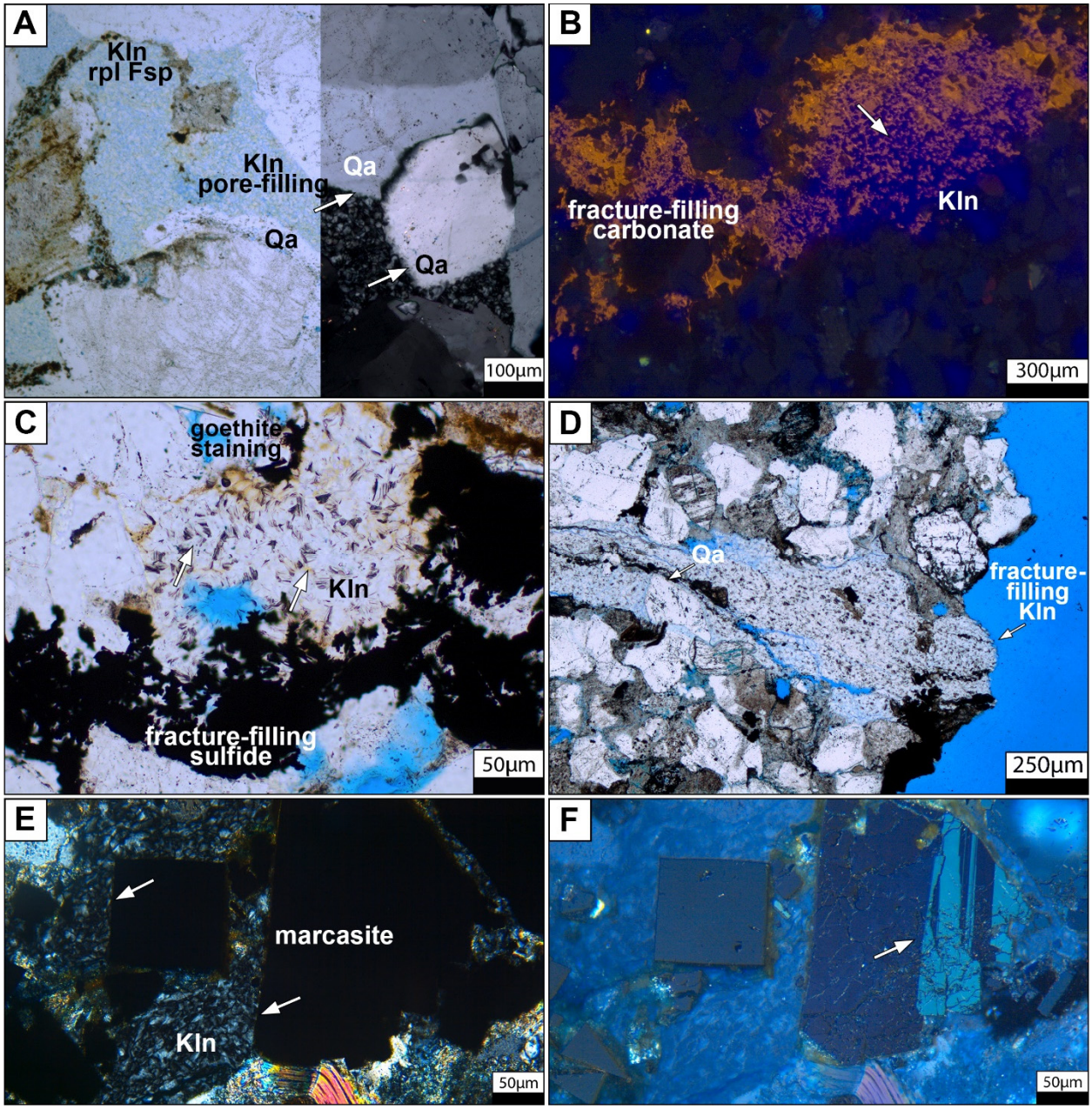

Figure 4.8 Kaolinite exhibits aggregates of randomly oriented coarse crystalline booklets and mostly replaces detrital feldspar but also appears pore filling (Pe-19). Euhedral quartz overgrowths delimit the growth of kaolinite but are also intergrown with its booklets (arrows). (**B**) The CL picture of sample Ha-27 displays that fracture-filling calcite (orange luminescing) is intergrown with kaolinite booklets (Kln) (arrow), indicated by the purple haze. (**C**) Goethite staining of kaolinite (Kln) and framework rock fragments is observed alongside the fracture-filling sulfide (Ha-9). Further, goethite stained the kaolinite booklets (arrows). (**D**) Fracture-filling kaolinite composed of coarse booklets covers a fractured surface, including quartz overgrowth cement (arrow) in sample Bo-13. (**E**) Transmitted light picture (xpl) shows marcasite with euhedral crystal faces (arrows) embedded in kaolinite (Kln). (**F**) Corresponding reflected light image (xpl) of marcasite displays its anisotropy, parallel twin structure, and dim gray-celadon interference color. Qa: Authigenic quartz, Kln rp Fsp: Kaolinite replacing feldspar.

The illitization of kaolinite booklets is rarely noticed (<0.7 % in all wells). Also, illite grain coatings occur exceptionally rarely (< 0.7 %) as finely disseminated aggregates upon detrital grains, forming tangential

illite aligned parallel to the grain surface as well as radial illite (Fig. 4.9 A and C). Mesh-like illite replaces feldspar (Fig. 4.9 B).

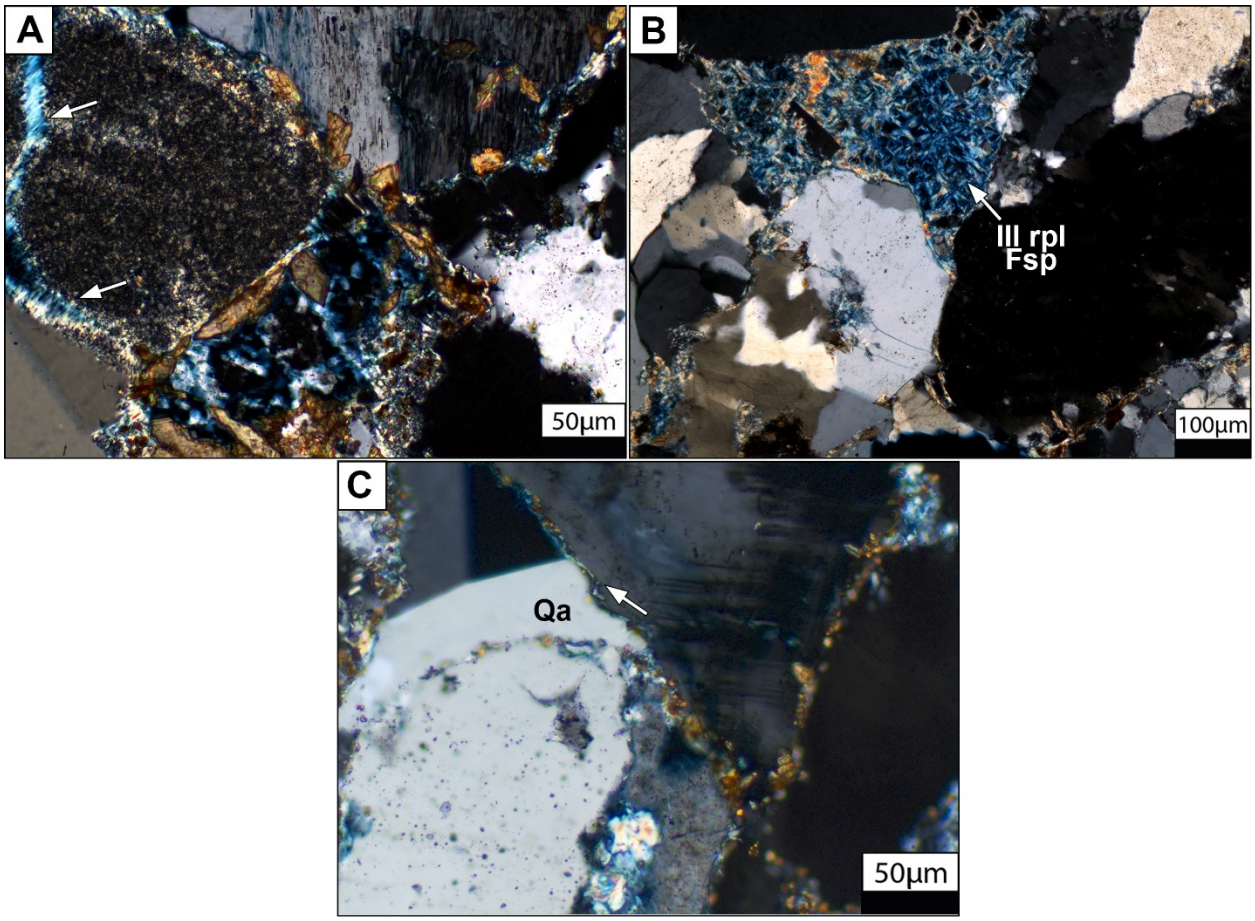

Figure 4.9 (**A**) Illite coatings on detrital grains in sample Bo-37, forming radial illite. (**B**) Illite (mesh) replacing a feldspar grain in sample Bo-32. (**C**) Illite coatings locally occur as finely disseminated aggregates on detrital grains (arrow), forming tangential illite parallel to the grain surface. Qa: Authigenic quartz, Ill rp Fsp: Illite replaces feldspar.

4.6.2 Compaction

The samples show low IGV values (0.0 to 8.7 %, mean 2.8 % in Bork-1; 0.0 to 5.7 %, mean 2.5 % in Haidberg-1) and low contents of intergranular cement (0.0 to 8.3 %, mean 2.6 % in Bork-1; 0.0 to 5.7 %, mean 2.5 % in Haidberg-1). Two outliers show high IGV values (Bo-10 = 16 % and Ha-17 = 38.3 %) and high contents of intergranular cement (Bo-10 = 16 % and Ha-17 = 38.3 %). Calculated COPL values range from 28.6 to 40.0 % (mean 38.2 %) in well Bork-1 and 2.7 to 40.0 % (mean 38.0 %) in well Haidberg-1, while low CEPL values vary from 0.0 to 11.4 % (mean 1.7 %) and 0.0 to 37.3 % (mean 2.0 %). Consequently, ICOMPACT values are high in both wells (mean > 0.9). Thus, in all samples, except for one outlier (Ha-17), the porosity loss can be classified as compaction-dominated (Fig. 4.10).

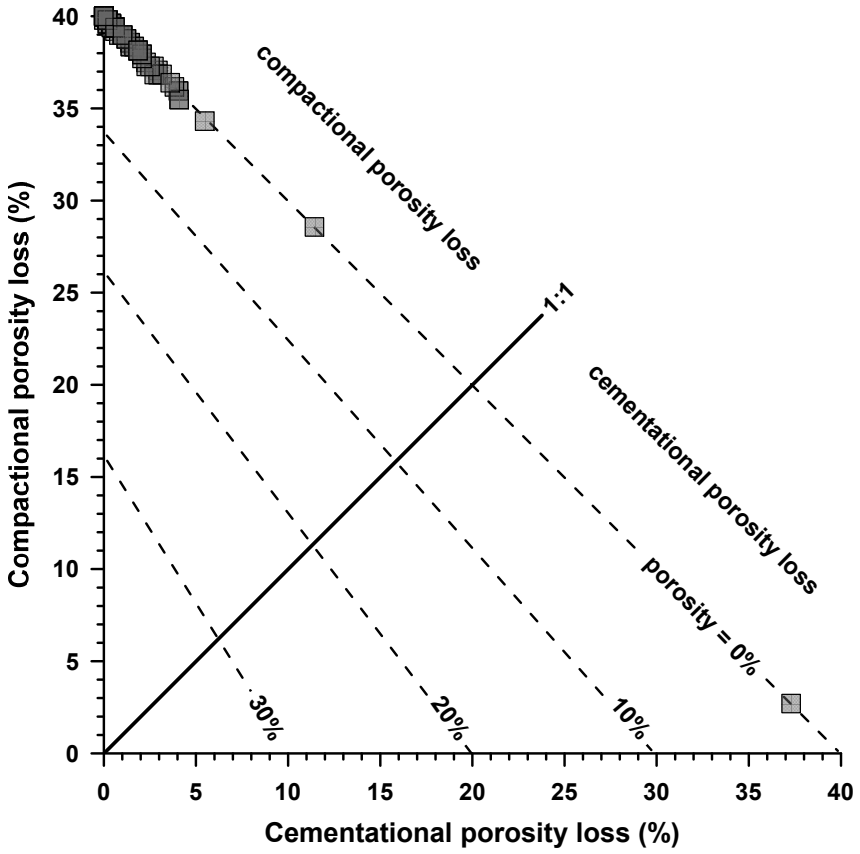

Figure 4.10 Evaluation of relative porosity loss due to compaction (COPL) and cementation (CEPL) for the present samples, after Lundegard (1992). In most samples, except for sample Ha-17, porosity loss is dominated by compaction.

4.6.3 Porosity and permeability

Porosity and permeability data produced in this study plot in the same range and extend the database provided by previous works on samples from the same studied well material (Fig. 4.11 A). The porosity ranges from 0.3 to 10.9 % (mean 5.5 %) in well Bork-1 and 0.3 to 11.1 % (mean 5.5 %) in well Haidberg-1, while permeabilities range from 0.0001 to 5.05 mD (mean 0.41 mD) and 0.0001 to 4.58 mD (mean 0.16 mD), respectively (Fig. 4.11 B). Samples from well Pelkum-1 used for comparison range from 0.5 to 15.6% porosity, while permeability ranges from 0.0001 to 4.43 mD. Little variation between stratigraphic units is seen (Fig. 4.11 C). Furthermore, samples of the delta front have better reservoir properties compared to the other delta facies (Fig. 4.11 D). Samples with low porosity but a permeability > 1 mD mostly contain a thin (~ 250 μm) coal layer or fractures on the plug scale (Fig. 4.3 C). Fine-grained samples tend to have cracks subparallel to the present lamination and are treated carefully, as, i.e. permeability might be amplified.

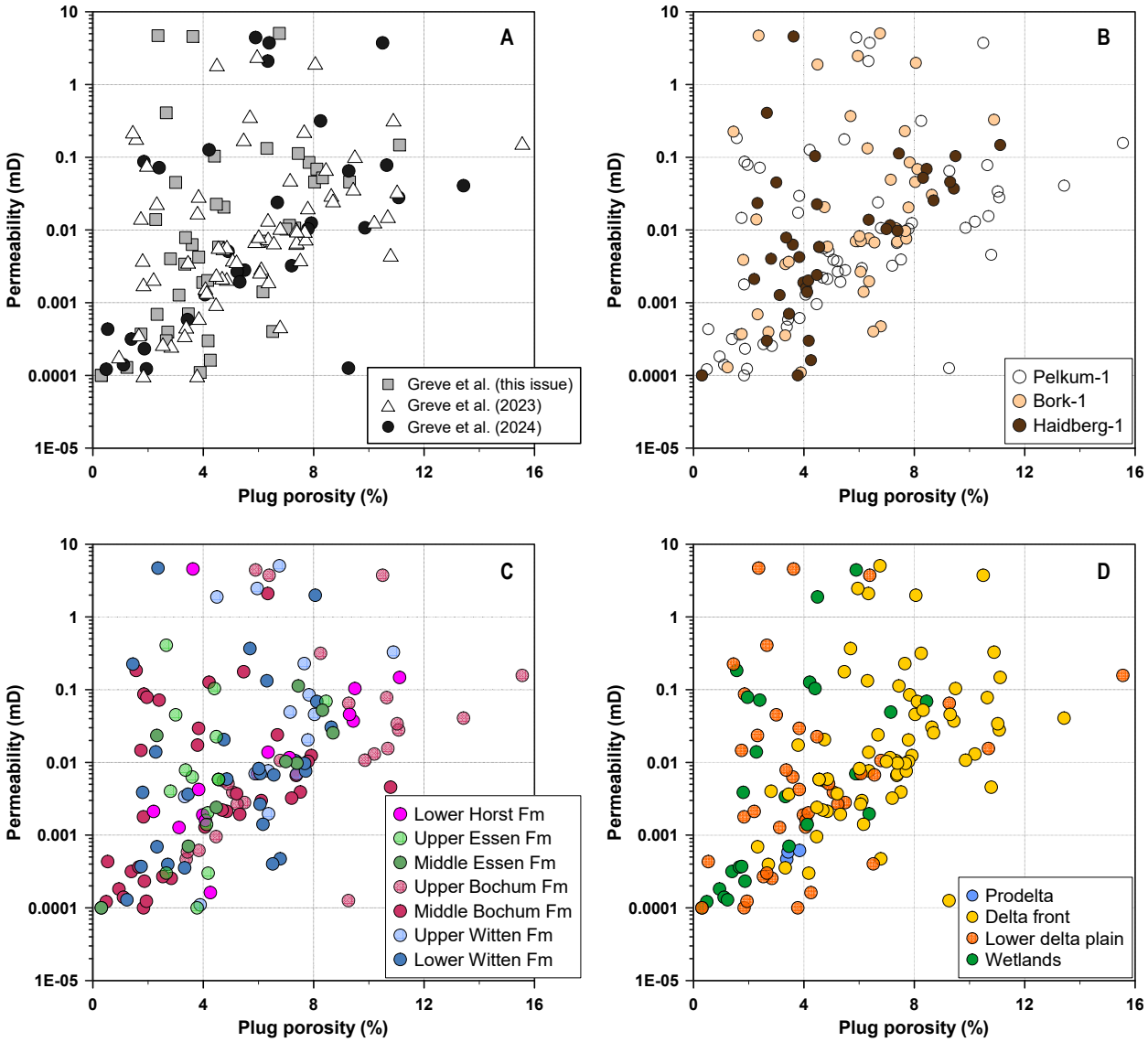

Figure 4.11 Porosity – permeability cross plot of the samples used in this and published studies (Greve et al., 2023; Greve et al., 2024), color-coded after issue. (**B**) Samples of the three studied wells plot in the same range, while no separation between any well is displayed. (**C**) Samples of this study color-coded by their stratigraphic position (in Fig. 4.2) show no clear separation, but some samples of the Bochum Formation show slightly higher reservoir properties. (**D**) Samples color-coded by their depositional rock type generally display better reservoir properties in delta front samples.

4.6.4 Correlations of petrography and petrophysics

An increase in grain size, from fine silt to very coarse sand, correlates with improved reservoir parameters, including higher permeability (> 0.01 mD) and porosity (> 7 %). (Fig. 4.12 A). Lower porosity and permeability is related to a higher quantity of ductile-behaving grains (> 42 %), such as shale and phyllite fragments, carbonatic rip-up clasts, micas, and ferric oxyhydroxides (Fig. 4.12 B). Higher reservoir quality also correlates with the amount of dissolution porosity (2.3 to 6.0 %). (Fig. 4.12 C). High amounts of authigenic clay minerals (> 1 %) are often present in samples with improved reservoir qualities as well as

ICOMPACT values below 0.95 (Fig. 4.12 E and F). Generally, samples with higher intergranular volumes (IGV) have better reservoir properties, similar to the characterization by ICOMPACT (Fig. 4.12 D). In samples Pe-21 and Ha-17, the lowest ICOMPACT values correspond to pervasive cementation by intergranular siderite (cf. Greve et al. 2023; their Fig. 6 A) and ankerite/ferroan calcite, respectively (Fig. 4.6 F). Despite their high difference in porosity (Pe-21 = 9.3 %; Ha-17 = 3.8 %), samples show similarly low permeability (~0.0001 mD). The reconstructed volumes of feldspar and rock fragments during deposition are correlated with reservoir properties. Better reservoir properties correspond with high reconstructed feldspar and rock fragment contents (Fig. 4.12 G). Furthermore, high volumes of secondary porosity correspond to coarser-grained samples (Fig. 4.12 H, red dots). In contrast, high volumes of ductile grains appear mainly in fine-grained samples (Fig. 4.12 H, black dots).

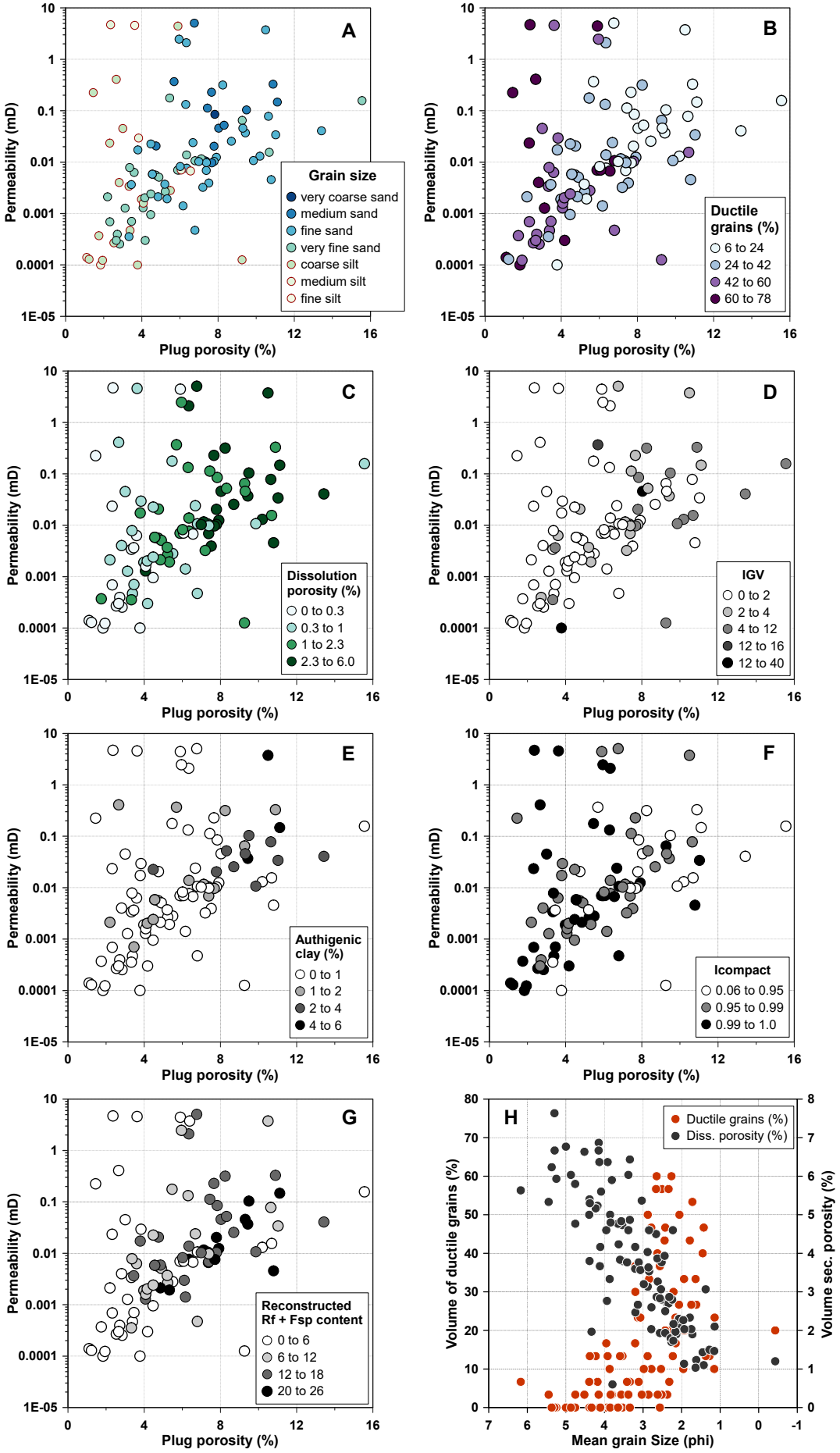
A
Permeability (mD)
Plug porosity (%)
Grain size
very coarse sand
medium sand
fine sand
very fine sand
coarse silt
medium silt
fine silt
B
Ductile grains (%)
6 to 24
24 to 42
42 to 60
60 to 78
C
Dissolution porosity (%)
0 to 0.3
0.3 to 1
1 to 2.3
2.3 to 6.0
D
IGV
0 to 2
2 to 4
4 to 12
12 to 16
12 to 40
E
Authigenic clay (%)
0 to 1
1 to 2
2 to 4
4 to 6
F
Icompact
0.06 to 0.95
0.95 to 0.99
0.99 to 1.0
G
Reconstructed Rf + Fsp content
0 to 6
6 to 12
12 to 18
20 to 26
H
Ductile grains (%)
Diss. porosity (%)
Volume of ductile grains (%)
Volume sec. porosity (%)
Mean grain Size (phi)

Figure 4.12 Porosity – permeability cross plots color-coded by: (**A**) The mean grain size, (**B**) volume of ductile grains, (**C**) volume of secondary porosity, (**D**) intergranular volume (IGV), (**E**) authigenic clay content, (**F**) ICOMPACT (=COPL/(COPL+CEPL)), (**G**) reconstructed rock fragment and feldspar content (counted + dissolved fragments), and (**H**) grain size vs ductile grains (shales, phyllites, carbonatic rip-up clasts) and secondary porosity from unstable grains (feldspars and rock fragments).

4.6.5 Porosity distribution

As the intragranular dissolution porosity strongly correlates with reservoir properties, the distribution of intragranular porosity along the wells is assessed. The point-counted intragranular dissolution porosity is separated by the grain mineralogy they are hosted in and displayed for all formations covered by the wells as well as compared with the measured plug porosity (Fig. 4.13 A). Generally, a good correlation between an increased volume of counted intragranular dissolution porosity and measured plug porosity is shown. Throughout the formations, variations in both intragranular dissolution porosity and the grains that host it are observable. In the Upper and Middle Bochum Formation, porosity originating from rock fragments (RFs) is predominant. In the other formations, the volume of intragranular dissolution porosity is dominantly hosted by K-feldspar (K-Fsp) and plagioclase (Plag) grains. The predominance of intragranular dissolution porosity hosted in RF in the Bochum Formation corresponds to the low to moderate reconstructed feldspar contents in this formation (Fig. 4.13 B). Generally, no clear trend for feldspar volumes along the studied formations can be noticed.

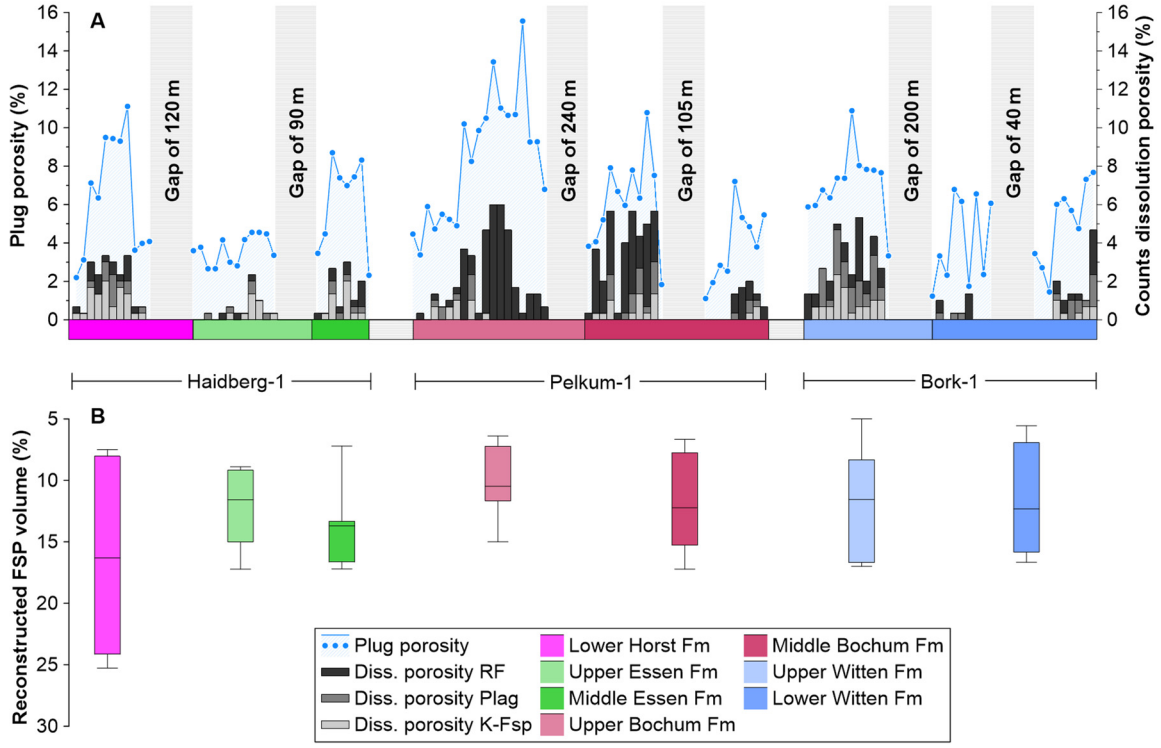

Figure 4.13(**A**) Stacked bars demonstrating the volumes of the different origins of intragranular porosity plotted for the formations encountered by the three studied wells. The volume of intragranular porosity is further compared with the measured plug porosity. (**B**) Reconstructed felspar content for each formation.

4.6.6 Whole-rock geochemistry

The distribution of major elements often correlates with the facies associations, displaying a trend from the delta front to the prodelta (Fig. 4.14 A). The SiO_2 concentration is greatest in samples of the delta front (n=20, 59.3 to 85.9 %, median 74.8 %). In contrast, volumes for the lower delta plain (n=10, 33.4 to 80.6 %, median 69.6 %), the wetlands (n=4, 59.6 to 71.8 %, median 65.7 %), and the prodelta (n=1, 62.8 %) are decreasing gradually. In comparison to lower contents in the wetlands (1.1 to 4.6 %, median 3.2 %) and prodelta (1.4 %) samples, the content of $CaCO_3$ is noticeably higher for samples taken from the delta front (0.2 to 7.7 %, median 1.4 %), which includes two positive outliers (9.1 and 24.5 %), and the lower delta plain (0.3 to 9.3%, median 3.4%), which includes one positive outlier (57.1 %). The TiO_2 content is low in all samples (max < 1.0 %) regardless of the facies association. Al_2O_3 concentrations are lowest in samples taken from the delta front (4.7 to 13.5 %, median 8.6 %), but are gradually increasing in samples from the lower delta plain (7.6 to 18.8 %, median 11.8 %), wetlands (10.5 to 18.7 %, median 14.9 %), and prodelta (17.5 %). Similarly, the lower delta plain (1.9 to 7.7 %, median 4.3 %), the wetlands (2.8 to 10.4 %, median 6.0 %), and the prodelta (5.3 %) display higher contents in Fe_2O_3 than samples from the delta front (1.2 to 7.4 %, median 3.3 %), which includes a positive outlier (17.8 %). Regardless of the facies associations, the content of MgO (median 0.9 to 1.7 %), CaO (median 0.3 to 0.4 %), and K_2O (median 1.7 to 2.8 %) are generally low in all samples. A positive outlier for MgO is observed in a sample of the delta front (4.2 %) and a sample of the lower delta plain (10.7 %). Positive outliers for CaO are displayed for samples of the delta front (0.8 and 6.7 %) and the lower delta plain (2.9 and 10.7 %).

Unlike the major elements, the distribution of minor elements correlates little with the facies associations, but outliers are restricted to the delta front samples (Fig 14 B). For the MnO content, values are slightly higher for the wetland samples (418 to 1823 ppm, median 984 ppm) compared to values of the lower delta plain (335 to 1174 ppm, median 726 ppm), prodelta (762 ppm) and delta front (58 to 1511 ppm, median 646 ppm), including one positive outlier (4038 ppm). The content of SrO is generally low regardless of the facies association (55 to 190 ppm, median 107 ppm), which also accounts for concentrations of BaO (10 to 741 ppm, median 332 ppm), except for a positive outlier (5300 ppm), and Rb_2O (37 to 168 ppm, median 75 ppm). ZrO_2 values of the delta front (84 to 328 ppm, median 168 ppm) are slightly lower compared to the lower delta plain (146 to 382 ppm, median 25 ppm), wetlands (248 to 484 ppm, median 326 ppm) and prodelta (290 ppm).

Comparing the Al_2O_3 wt% with the mean grain size, a negative correlation is shown, as with increasing grain size, the concentration of Al_2O_3 generally decreases (Fig. 4.14 C). A positive correlation between the SiO_2 wt% and the mean grain size is seen as the concentration of SiO_2 rises with increasing grain size (Fig. 4.14 D).

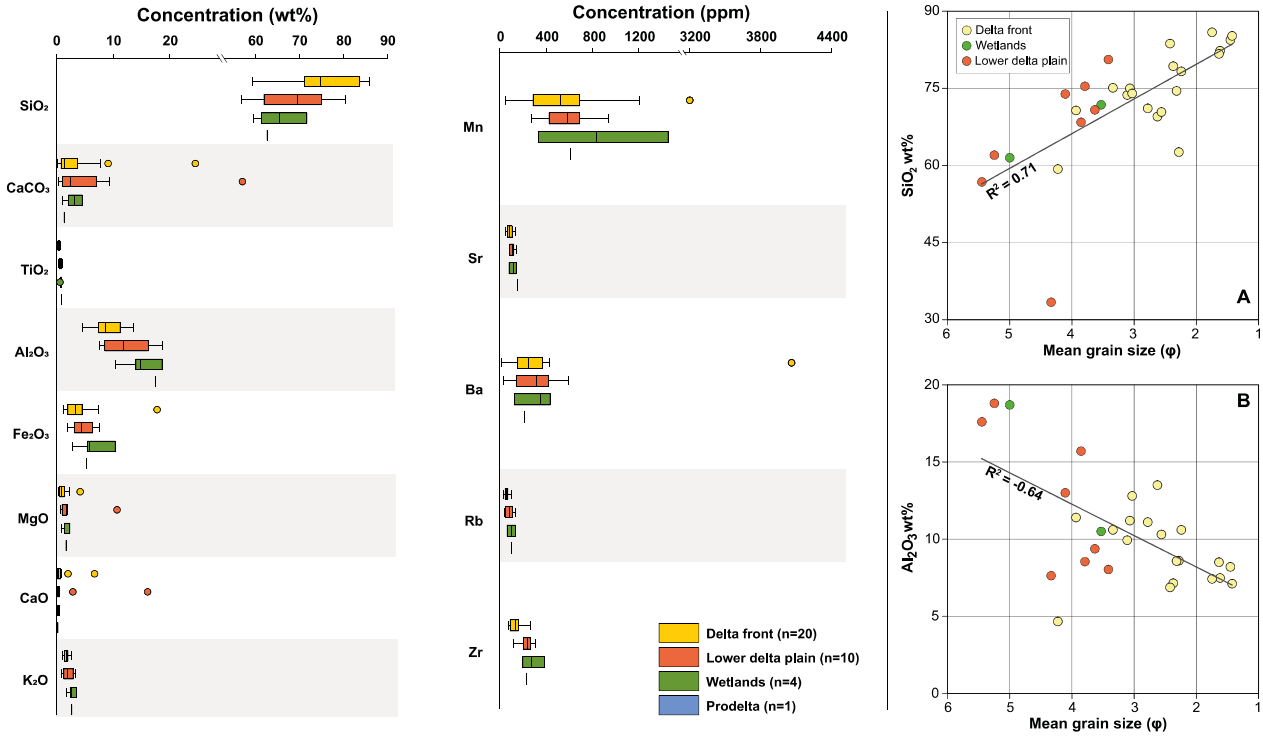

Figure 4.14 Box-and-whisker bars plotted for (**A**) Concentration in wt% of major and minor elements. (**B**) Concentration (ppm) of trace elements for samples of well Haidberg-1, Bork-1, and Pelkum-1 (appendix D.2-3: Modal data). (**C**) Comparison of SiO_2 wt% with the mean grain size visualizes a positive correlation (R^2=0.71). (**D**) Comparison of Al_2O_3 wt% with the mean grain size displays an opposing negative correlation (R^2=-0.64).

4.7 Discussion

4.7.1 Early diagenesis

During early diagenesis, the alteration of sediments is controlled by meteoric fluids and the physical, geochemical, as well as biological characteristics of the depositional environment (Morad et al., 2000; Worden & Burley, 2003). Early diagenetic modification can occur on the surface and as deep as 1 to 2 km in burial, corresponding to temperatures of 30 to 70°C in most basins (Morad et al., 2000).

The initial diagenetic alteration is the deposition of grain rimming phases of hematite or clay minerals (Ajdukiewicz & Lander, 2010; Molenaar, 1986; Van Houten, 1973). The observed tangential illite, which is aligned parallel to the grain surface (Busch et al., 2020; their Fig. 1), is most likely the result of recrystallization from clay rims, which acted as precursory minerals (Aagaard et al., 2000). Since the illitic grain coating is overgrown by syntaxial quartz cement overgrowths (Fig. 4.9 C), an early diagenetic emplacement of clay minerals is supported.

As the rarely observed hematite rims (Fig. 4.6 D) are encased by syntaxial quartz overgrowth cements, they are also interpreted to form during early diagenesis. This generally agrees with assessments on early diagenetic hematite rims on detrital quartz grains formed predominantly in arid environments by alteration

of iron-bearing grains, such as amphiboles or biotite (Walker, 1967). However, moist tropical climatic conditions, which lead to peat formation, prevailed during deposition in the Westphalian A and B (Strehlau, 1990). Still, red beds can form diagenetically in moist tropical climates if the interstitial chemical environment is favorable for the formation and preservation of iron oxide (Walker, 1974), the dehydration of detrital ferric oxyhydroxides, or by the oxidation of ferrous iron associated with organic material (Besly & Turner, 1983).

Since pyrite is widely encased by isopachous bladed siderite cement growing on carbonatic rip-up clasts (Fig. 4.4 E), an early emplacement of Fe-sulfides disseminated in the intergranular pore space is interpreted. The substantial organic input in the waterlogged sediments of the lower delta plain may promote an environment suitable for biogenic sulfate reduction, supporting anoxic, sulfidic pore water conditions favorable for pyrite precipitation (Coleman, 1985; Morad et al., 2000). Despite this, pyrite quantities are low (0.0 to 0.3 %, mean 0.0 % in Bork-1; 0.0 to 1.3 %, mean 0.0 % in Haidberg-1) compared to the quantity of organic material in Upper Carboniferous coal seams. Low levels of available sulfate due to the influence of freshwater may have limited H_2S production to maintain sulfate reduction, leading to methanic conditions with siderite precipitation (Gautier, 1982). In contrast, the absence of reactive organic matter in distal delta front sandstones most likely limits the presence of pyrite. All studied samples include remobilized sideritic rip-up clast and siderite cement, indicating meteorically impacted pore fluids (Curtis & Coleman, 1985). Siderite cement covering the intergranular pore space and coating detrital framework grains is also present at grain-to-grain contacts (Fig. 4.6 A), suggesting that it formed prior to intense mechanical compaction but subsequent to pyrite formation (Fig. 4.6 A). Siderite can form only where insufficient amounts of H_2S prevent the precipitation of the available reduced iron as pyrite (Curtis & Spears, 1968). However, siderite can also form when the iron reduction rate exceeds the sulfate reduction rate (Pye et al., 1990). The source of iron may be the alteration of iron-bearing silicates or the dewatering of iron-bearing clay minerals during early diagenesis (Haese et al., 1997; Postma & Brockenhuus-Schack, 1987).

Most siderite covering detrital quartz grains is encased by quartz cement (Fig. 4.6 A), indicating a formation before quartz cementation. However, since siderite can also be limited by quartz cement (Fig. 4.6 E), some siderite formation during burial diagenesis is interpreted.

The pervasively pore-filling ferroan calcite, restricted to sample Ha-17 (Fig. 4.6 F), fills all available pore space, while quartz overgrowth cement is absent. Thus, its formation is assigned to early diagenesis, predating quartz overgrowth cement formation, as ferroan calcite is common in sediments with marine-influenced pore fluid (Curtis & Coleman, 1985).

4.7.2 Burial diagenesis I

Once the depositional environment and meteoric fluids no longer control the sediment, burial diagenesis proceeds (Worden & Burley, 2003). Burial diagenesis I persisted within the context of this study until the Early Permian uplift (Bruns et al., 2013), which led to exposure to meteoric water.

In coarse-grained samples, syntaxial quartz overgrowth cements are prevalent. Regarding their paragenesis, most authigenic quartz postdates early siderite, ferroan calcite, and pyrite/marcasite cement. However, it is either contemporary with or postdates the recrystallization of pore-lining clay minerals to illite (Fig. 4.9 C). Since quartz overgrowths develop in dissolved rock fragments, the dissolution of framework grains that result in intragranular porosity in feldspars or plutonic rock fragments must have occurred before quartz precipitation. As quartz overgrowth cement is typically the predominant cement type in sandstone at temperatures over 70 to 100 °C, it is attributed to the burial diagenetic stage (Bjørlykke & Egeberg, 1993; Walderhaug, 1996). From the Late Carboniferous/Early Permian onwards, temperatures exceeded 70°C to enable quartz cementation for approximately 20 Ma, based on burial and heat flow reconstructions (Bruns et al., 2013). The comparisons between homogenization temperatures of fluid inclusions and calculated vitrinite reflectance temperatures indicate formation temperatures of quartz cements in the eastern Ruhr Basin ranging from 150 to 170°C for the upper Westphalian A (Büker, 1996). The apatite fission track analysis suggests that the maximum paleotemperatures prevailed only at the onset of burial followed by rapid cooling due to uplift (Büker, 1996). This pre-Permian burial is reconstructed to be the main control on measured vitrinite reflectance values (Büker, 1996).

The high heat flow of roughly 90 mW/m^2 was driven by crustal thinning during basin formation and subsequent mantle uplift (Littke et al., 2000; Ritter, 1986; Robert, 1989). Considering the maximum burial during the Early Permian with contemporaneous elevated heat flow, most quartz cementation is interpreted to have been formed during this burial phase. Clay mineral alteration, such as kaolinite reacting with K-feldspar to form illite and quartz, is common at similar temperatures (Bjorkum & Gjelsvik, 1988). Further, feldspar dissolution may have contributed to the silica necessary to produce authigenic quartz. Pressure dissolution at dissolution seams is also a suitable mechanism to provide silica (Rutter, 1976; Tada & Siever, 1989) but is usually not observed in the studied thin sections.

The dissolution of unstable rock fragments and feldspars and feldspar replacement by kaolinite is widely observed in the studied samples and a common early diagenetic alteration in humid climates in contact with meteoric waters (Bjørlykke et al., 1979; Hancock & Taylor, 1978; Lønøy et al., 1986). Since grain-shaped pores persist and ductile particles bend around the original grain, their dissolution is assumed to postdate the main phase of mechanical compaction. Furthermore, feldspar is stable at atmospheric pressure and low temperature under slightly alkaline pH conditions (Zhang et al., 1997; their Fig. 4), indicated by the widespread siderite production (Jackson & Sherman, 1953). A suitable mechanism for extensive burial

diagenetic feldspar dissolution that postdates mechanical compaction is the introduction of organic acid and carbonic acid generated during the thermal maturation of organic matter (Barth & Bjørlykke, 1993; Busch et al., 2019; Butala et al., 2000). According to Nöth et al. (2001), the coalification pattern shows that the studied region mostly underwent pre-tectonic maturation. Furthermore, by releasing organic acids during the maturation of organic matter (Gaupp et al., 1993; Platt, 1993), the low pH conditions significantly promote the replacement of feldspars by kaolinite (Lanson et al., 2002). SiO_2 is released into the solution due to the replacement reaction which is another source for quartz overgrowths.

The illitization of feldspar grains and pore-lining clay precursors is widespread (Fig. 4.9 B and C), while the illitization of kaolinite is hardly evident. Kaolinite booklets are intergrown with quartz overgrowths and either synchronous with or predate quartz cementation (Fig. 4.8 A). Furthermore, kaolinite and illite replacements of feldspars remained grain-shaped (Fig. 4.8 A), and their formation is interpreted to postdate mechanical compaction. If there is an acidity source that promotes extensive, simultaneous breakdown of K-feldspar, the illitization of K-feldspar is feasible at temperatures of 90 to 120°C as long as the supply of K^+ can be maintained to form illite rather than kaolinite (Berger et al., 1997; Lanson et al., 2002; Worden & Morad, 1999). In a closed geochemical system, acidic fluids derived from the maturation of organic matter within the Upper Carboniferous strata could facilitate the dissolution and replacement of feldspars during burial (Gaupp et al., 1993). The subsequent illitization of detrital clay rims, such as smectite, as well as the authigenic radial illite formation (Fig. 4.9 A), are likely incorporating the released K^+ from feldspar dissolution (McKinley et al., 1999).

4.7.3 Uplift diagenesis I/II

The thermal maturation of organic materials during burial diagenesis is assumed to primarily promote the dissolution of unstable rock fragments and feldspars and the kaolinization of feldspars. However, dissolution and kaolinitization are considered to have been partially driven by the flushing with meteoric waters at shallow depths during Permian and Early Cretaceous uplift (Bjørlykke et al., 1979; Hancock & Taylor, 1978; Loucks, 2005). According to Lanson et al. (2002) and Shaw (2006), the dissolution of K-feldspars might also be a source of pore-filling kaolinite cement (Fig. 4.8 A). However, the paragenetic relation with fracture-filling calcites suggests that the formation of replacive and pore-filling kaolinite predates fracturing (Fig. 4.8 B).

4.7.4 Burial diagenesis II/III

Due to the relatively shallow burial (2 km) and reduced heat flow during Triassic to Jurassic and Late Cretaceous (Bruns et al., 2013), burial diagenesis II/III includes little quartz cementation and some illitization of detrital K-feldspars and diagenetic kaolinite formation. Furthermore, minor dissolution of

unstable grains is interpreted to occur during burial diagenesis II. It is probably caused by continued coal maturation and degassing coal seams, which reintroduce carbonic acids into pore waters.

Most siderite in intergranular pore spaces is interpreted to form during early diagenesis. Yet, the paragenesis with authigenic quartz supports a formation locally postdating or synchronous to quartz cementation (Fig. 4.6 E). This second phase of siderite precipitation, occurring after quartz precipitation, is required to explain the observed paragenesis of siderite crystals being limited by quartz overgrowth cements and for the siderite filling dissolution porosity (Fig. 4.6 B).

Fracture-filling kaolinite encases quartz overgrowths and euhedral marcasite (Fig. 4.8 F, arrows, Fig. 4.8 E), suggesting an emplacement after fracture-filling quartz and marcasite formation. Fracture-filling kaolinite is rare but is described by Greve et al. (2024) in samples of well Pelkum-1 in the same study area. Fracture-filling kaolinite is also reported in core samples of Cretaceous shales from the Gibraltar Strait area at 2 to 3 km burial depths, which formed from smectite dissolution with simultaneous precipitation of I/S mixed-layers and quartz (Cruz & Reyes, 1998). Thus, the observed quartz overgrowth cement and kaolinite could have formed contemporaneously, while the low pH of formation fluids related to organic matter maturation may also have facilitated kaolinite to precipitate.

Cathodoluminescence analyses show two different phases of calcite precipitation in fractures. Non-luminescent ankerite (Ank) and brightly luminescent manganese-rich ferroan calcite (Cmf) (Fig. 4.7 B and C) both show a blue stain in plane-polarized transmitted light. The presence of ankerite is confirmed based on combined CL and XRD analyses on samples of well Pelkum-1 (Greve et al., 2024). Since the ankerite exhibits euhedral crystal faces (Fig. 4.7 C) and internal fractures filled by brightly luminescent manganese-rich ferroan calcite (Fig. 4.7 B), the manganese-rich ferroan calcite is interpreted to postdate the ankerite. Furthermore, brightly luminescent manganese-rich ferroan calcite, which fills intragranular porosity in feldspars and rock fragments as well as some intergranular porosity, is interpreted to be introduced through fracture conduits and forming contemporaneously since it also postdates quartz overgrowth cement (Fig. 4.7 C and D).

Both carbonate phases overgrow cubic marcasite, which is present at the host-rock vein interface (Fig. 4.7 C, white arrows), suggesting that the emplacement of fracture-filling sulfides predates the fracture-filling carbonates. Mineralization within coal cleats in the Ruhr Basin shows that ferroan dolomite/ankerite is accompanied by sulfide mineralization (Dawson et al., 2012). A basinal brine may be a suitable manganese source for the fracture-filling calcite (Larsen & Mann, 2005). Based on their paragenesis, the relative timing of fracture-filling carbonates postdates kaolinite formation (Fig. 4.7 D, Fig.4.8 B) and quartz overgrowths are late burial diagenetic features (Fig. 4.13).

In samples of well Pelkum-1, the timing of pyrite/marcasite in fractures was interpreted to predate quartz overgrowth precipitation since fractured quartz grains in pyrite/marcasite veins do not show quartz

overgrowth precipitation (Greve et al., 2024). The paragenesis in the samples of this study suggests that pyrite/marcasite predates the other fracture-filling cement. However, pyrite/marcasite is observed to encase quartz overgrowth cement (Fig. 4.7 E). Thus, the emplacement of fracture-filling sulfides is also a late diagenetic feature (Fig. 4.13). Generally, the fracturing of the Upper Carboniferous lithologies is widespread throughout its burial history (e.g. Drozdzewski, 1988; Drozdzewski & Wrede, 1994; Vinken, 1988) and thrust tectonics (e.g. Becker et al., 2011; Sindern et al., 2012; Sindern et al., 2007). Yet, the relative timing of fractures, regarding the textural relationships to other authigenic minerals and burial history points to a relatively late diagenetic formation (Fig. 4.13). Post-Carboniferous strata of the Ruhr Basin indicate different periods of active faulting (Drozdzewski, 1993) but likely periods are the early Kimmerian phase with normal faulting in the Late Triassic and the Late Cretaceous transpression, where pre-existing extensional faults in the Ruhr Basin were reactivated as reverse- and strike-slip faults (Becker et al., 2014; Drozdzewski, 1988; Kley & Voigt, 2008). Suitable pathways for fluids might have been NW-SE striking faults that primarily formed at the end of the Variscan deformation and partly before and during the deposition of the Zechstein (Lopingian) strata (Wolf, 1985).

The alteration of abundant fracture-filling iron sulfide minerals is evident by the formation of goethite (Abouessa & Morad, 2009; Bladh, 1982). The local presence of goethite near sulfide veins and their paragenetic relationship indicate it postdates all other authigenic minerals (Fig. 4.7 A, E, and Fig. 4.8 C).

4.7.5 Reservoir quality development

The samples from the studied wells have a similar detrital composition and are all affected by early siderite cementation and, to a minor degree, cubic pyrite/marcasite (Fig. 4.15 C). Ductile rock fragments enhance the effect of mechanical compaction, generally reducing the IGV and porosity (Fig. 4.15 D). Some samples contain detrital clay mineral grain coatings or rare hematite grain coatings (Fig. 4.15 B). Grain coatings and pigmented hematite rims are not well developed, resulting in the incomplete coverage of the grains, and do not inhibit syntaxial quartz overgrowth cementation (Fig. 4.15 D). Quartz cementation developed during burial on most detrital quartz surfaces and encases early diagenetic siderite as well as grain rimming phases (Fig. 4.15 C, D). The precursory grain coatings are transformed into incomplete tangential illitic grain coatings (Fig. 4.15 D). Furthermore, radial illite precipitates locally on uncoated grain surfaces can affect effective pore throat radii and reduce permeability (Howard, 1992). Feldspars or rock fragments mainly host intragranular dissolution porosity (Fig. 4.15 D-G), which formed since the initial phase of burial diagenesis. The major authigenic clay mineral is burial diagenetic kaolinite replacing feldspars (Fig. 4.15 D-F). Kaolinitization is interpreted to be driven by the maturation of organic material and the associated release of organic acids. Although temperatures were high enough to facilitate the kaolinite to illite transformation, and widespread feldspar dissolution, the availability of organic acids favors the preservation of kaolinite (Fig. 4.15 E-G). It explains the presence of kaolinite, while illite is rare. Intragranular

dissolution porosity is often filled by late burial diagenetic siderite and calcite phases introduced by fractures (Fig. 4.15 F, G). Locally, these uplift diagenetic fractures also host kaolinite and marcasite (Fig. 4.15 G).

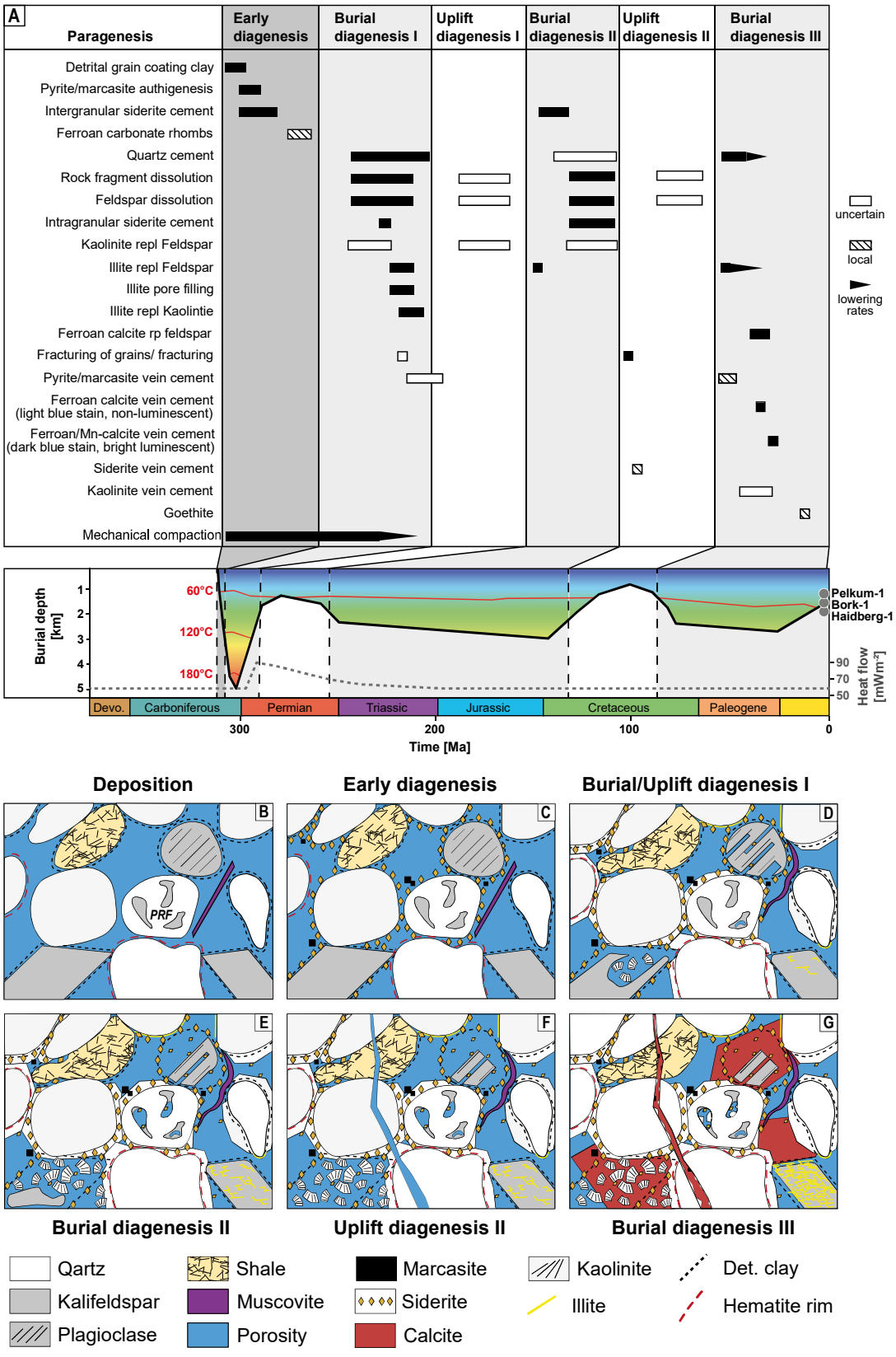

Figure 4.15 The paragenetic sequence of well Pelkum-1, based on petrographic evidence from this work, is associated with the burial and thermal reconstruction of the eastern and southern Ruhr Basin, modified after Littke et al. (1994) and Büker (1996). The burial path was projected based on their reconstruction regarding the stratigraphic units encountered by the well. (**B-G**) The sketch shows the main diagenetic processes affecting the reservoir quality of the studied wells. PRF: Plutonic rock fragment, Det. clay: Detrital clay.

4.7.6 Controls on reservoir properties and rock typing

The petrophysical data reported in this study indicate that Upper Carboniferous sandstones and siltstones of the Westphalian A and B are usually tight (mean porosity 5.5 %, mean permeability 0.28 mD). These data confirm measurements from previous studies in the Ruhr area (Brenne, 2016; Duda & Renner, 2013; Greve et al., 2023; Stöckhert et al., 2015) as well as from the adjacent Lower Saxony Basin (Becker et al., 2017; Busch et al., 2019; Quandt et al., 2022b; Wüstefeld et al., 2017), and can now be linked with detritral and authigenic composition. Enhanced reservoir properties can be related to subhorizontal cracks (Fig. 4.4 C), which enhance the permeability by two orders of magnitude in fine-grained samples under non-reservoir conditions (confining pressure of 1.2 MPa) (Bo-24, Bo-25, Bo-26, Bo-31). It also accounts for coal chips (mm to cm-scale), observed in some samples (Bo-40 and Ha-10) to enhance the permeability by two orders of magnitude (Greve et al., 2024). However, samples containing subhorizontal fractures are assumed to be tight at present-day pressures at depths of > 688 m and > 948 m (Fiebig, 1977; Sperber and Hettenberger, 1992).

Rock typing, which integrates petrographic data with porosity and permeability values of three studied wells (Bork-1, Haidberg-1, and Pelkum-1), was utilized to examine the controls on reservoir properties since it is a valuable tool for their classification (e.g., Busch et al., 2020; Monsees et al., 2020; Quandt et al., 2022a). The main aspect affecting reservoir parameters in Upper Carboniferous Westphalian A and B samples is the detrital grain size (Fig. 4.12 A). The transition from fine to coarse grain size correlates to changes in mineralogy from litharenites to lithic subarkoses (Fig. 4.5 A). Considering the reconstructed feldspar content in the samples (up to 28 %; Fig. 4.13 B), the mineralogical shift with grain size is even more pronounced. Sandstones are typically classified as feldspathic litharenites or lithic subarkoses and contain larger dissolution porosity volumes (> 1 %) than siltstones (< 1 %). Enhanced reservoir properties, therefore, are also related to grain size and mineralogy since the formation and distribution of dissolution porosity are driven by the dissolution of feldspars and unstable rock fragments (cf. Fig. 4.12 C and G). However, high volumes of burial diagenetic ankerite/ferroan calcite and siderite carbonate cement, filling primary as well as secondary porosity, again reducing porosity, are mainly present in coarse-grained samples (Fig. 4.7 D, Fig. 4.6 B). In well Pelkum-1 late burial diagenetic carbonate cements clog dissolution porosity. This process locally decreases the amount of intragranular dissolution porosity and consequently obstructs a correlation with higher permeabilities (Greve et al., 2024). Like intragranular dissolution porosity, coarser grain sizes correlate with larger volumes of authigenic clay (2 to 6 %) in sandstone. Next to the higher reconstructed feldspar content (Fig. 4.12 G), the presence of, e.g., replacive and pore-filling

kaolinite is related to fluid flow in sandstones since porosity and potential fluid flow was reduced by compaction in fine-grained sections. The presence of ductile rock fragments, such as shales and phyllites, enhances the effect of mechanical compaction, as suggested by higher ICOMPACT values (> 0.99) (Fig. 4.12 F). Siltstones, primarily categorized as litharenites, contain a greater number of ductile rock fragments (> 42 %) than most sandstones (< 42 %). Consequently, this shift in mineralogy is considered the primary control on IGV values (Fig. 4.12 D) since high quantities of ductile grains correlate with a rapid decline of IGV during burial (Paxton et al., 2002; Pittman & Larese, 1991). As a result, it is the primary mechanism responsible for porosity reduction in the analyzed samples (Fig 10). This is supported by petrographic observations, such as ductile shale rock fragments being distorted and compressed between rigid grains, which occurs less commonly in sandstones. Moreover, grain size and the consequent changes in detrital mineralogy appear to govern the distribution and quantities of cement since the lowermost ICOMPACT values (< 0.95; = high volumes of intergranular cement) occur in sandstones (Fig 12 F). Since sandstones that are poor in ductile rock fragments are less susceptible to porosity loss due to mechanical compaction, some primary porosity is preserved and cemented. This is also observed in core samples of well Pelkum-1 in the study area, where quartz overgrowths (> 0.3 %), ankerite/ferroan calcite (> 1 %), and early diagenetic siderite (up to 6.3 %), fill intergranular porosity and preserve slightly higher IGV values (2.8 to 7.0 %) (Greve et al., 2023b). However, due to low quantities of early diagenetic siderite and quartz cement precipitation primarily after the main compaction phase, their impact on mitigating the compactional porosity loss is limited. Regarding quartz overgrowths, in sandstones, fewer grain surfaces are covered and accessible for syntaxial cement precipitation. Most surfaces of detrital quartz in siltstones where cement might precipitate are in contact with ductile grains, and thus their reactive surface area is reduced (Bloch et al., 2002; Busch et al., 2020; Busch et al., 2017; Monsees et al., 2020). Siderite rimming detrital quartz grains does have little impact on quartz overgrowth cements. Hematite rims are not continuous and appear ineffective in inhibiting quartz cementation (Heald & Larese, 1974). Diagenetic, clay mineral grain coatings, e.g., pore-lining illite that may further retard quartz growth (Ajdukiewicz & Larese, 2012), commonly are not widespread or postdate quartz cementation.

Poor reservoir properties result from cementation and intense mechanical compaction analogously to other deeply buried tight reservoirs (e.g., Higgs et al., 2007). Porosity from mineral dissolution slightly enhances porosity by up to 6 %. However, the analogous increases in occluding carbonate cements reduce reservoir properties, and authigenic clay minerals, such as kaolinite and meshwork illite, impair intragranular dissolution porosity. Similarly, in Permian Rotliegend clastic reservoirs, pore-blocking carbonate cements reduce porosity, while permeability impairment is mainly due to authigenic clays (Gaupp & Okkerman, 2011).

The measured porosity and permeability range from 0.9 to 15.6 % and 0.0001 to 2.46 mD of the three studied wells are comparable (cp. Greve et al., 2023; Greve et al., 2024) and are related to the grain size

and facies associations. Sandstone-dominated delta front deposits generally show higher values (mean 6.8 %; 0.18 mD) than siltstone-dominated lower delta plain deposits (mean 4.6 %; 0.03 mD), mudstone-dominated wetland deposits (mean 3.9 %; 0.21 mD), or prodelta deposits (mean 3.6 %; 0.0005 mD). Furthermore, the effect of detrital and authigenic compositions on reservoir properties is comparable between the three wells. Samples containing abundant ductile rock fragments have experienced more pronounced mechanical compaction (low IGV) and, therefore, have poorer reservoir properties (Fig. 4.12 B, D) (cf. Greve et al., 2024). Similarly, samples containing larger authigenic clay mineral volumes (2 to 6 %, Fig. 4.12 E), due to alteration of unstable grains, have higher porosities and permeabilities than samples with lower clay mineral cement volumes (cf. Greve et al., 2024).

The comparison of petrographic sample mineralogy (Fig. 4.5) and geochemistry (Fig. 4.14) identified proxies for reservoir properties in the absence of petrophysical measurements. Since delta front deposits primarily consist of sandstone, siltstones can be attributed to the lower delta plain and the wetlands (Greve et al., 2023). When comparing the data, samples of the delta front with greater volumes of detrital quartz display higher concentrations of SiO_2, while lower quartz contents correlate with lower SiO_2 concentrations in the wetlands, the prodelta, and the lower delta plain, respectively (cf. Fig. 4.5 and Fig. 4.14 A). Thus, the SiO_2 content seems to be a proxy to identify coarse-grained sections (Fig. 4.14 A) that can be designated as sandstones of the delta front environment. However, deposits of other environments (fluvial or aeolian) in the Upper Carboniferous are not considered. Their relationship still needs to be investigated.

Coarse grain sizes are correlated with low Al_2O_3 content in delta front deposits (Fig. 4.14 A). A fining in grain sizes corresponds with an increase in Al_2O_3 concentration in samples of the lower delta plain, the wetlands, and the prodelta. It shows a relationship between detrital mineralogy and greater quantities of non-quartz rock fragments (i.e., shales and phyllites) in siltstone samples when considering the negative association between grain size and Al_2O_3 wt% (cf. Fig. 4.12 H and Fig. 4.14 D). Thus, the Al_2O_3 concentration may be a proxy for siltstone assigned to the lower delta plain and wetland environments. Like Al_2O_3, concentrations of Fe_2O_3, MgO, and K_2O show a similar distribution and are likely to result from clay minerals. In the case of Fe_2O_3, the present carbonatic rip-up clasts seem like a suitable source (Curtis & Coleman, 1985).

TiO_2, CaO, MnO, SrO, BaO, Rb_2O, and Zr_2O were previously discussed on samples of well Pelkum-1 and appear to be no diagnostic proxies to accurately assess depositional rock types or their reservoir properties in Upper Carboniferous samples (Greve et al., 2024).

4.7.7 Controls on the origin of porosity in the Westphalian A and B

The study investigated the distribution of intragranular dissolution porosity in the different formations of the Ruhr Basin, as it appears to be a main control on reservoir properties. The distribution was analyzed in all formations encountered by the wells, and the intragranular dissolution porosity was separated by the

grain types they are hosted in. A good correlation between increased volumes of point-counted intragranular dissolution porosity and measured plug porosity is shown (Fig. 4.13 A). However, the intragranular dissolution porosity and the grains it is hosted in are not uniform throughout the formations. In the Upper and Middle Bochum Formation of well Pelkum-1, dissolution porosity originating from altered rock fragments (RF) predominantly contributes (up to 6.0 %) to the measured plug porosity (up to 15.8 %). The predominance of dissolution porosity hosted in RF in the Bochum Formation corresponds to the low to moderate reconstructed feldspar contents (2 to 14 %) in this formation (Fig. 4.13 B).

In contrast, the volume of intragranular dissolution porosity hosted by K-feldspar and plagioclase dominates in the other formations (up to 2.3 %, respectively), but intragranular dissolution porosity hosted in RF is still present (Fig. 4.13 A). These findings correspond with an increase in reconstructed feldspar content, while in the Bochum Formation, the value is lower (Fig. 4.13 B). It suggests that the provenance of the investigated sandstones in the Ruhr Basin was not uniform throughout the Westphalian A and B or covered multiple source areas. According to previous studies, the sedimentary rocks in the Ruhr Basin were mainly sourced from the Variscan orogen in the south, the Central German Crystalline ridge, the Eastern European platform, and the reworking of the near surrounding during the Upper Carboniferous (Hedemann & Teichmüller, 1971; Hesemann, 1975). However, petrographic investigations concluded that the Ruhr Basin was mainly sourced by felsic plutonic and volcanic RF of the Central German Crystalline Ridge and metamorphic RF of a pre-Variscan basement during the Westphalian A and B (Frank et al., 1992). Since the Westphalian C, the Variscan Orogen has become the main sediment source (Drozdzewski, 1993).

The reconstructed feldspar content in Westphalian A and B sandstones of this study (Fig. 4.13 B) is lower (mean 8.4 % in Pelkum-1, mean 10.7 % in Bork-1; mean 11.7 % in Haidberg-1) than feldspar contents in outcrop samples (23 to 27 %) from the fluvial Namurian B to C Kaisberg sandstone (Brenne, 2016). On the contrary, the feldspar content in the Münsterland-1 well 50 km to the NW of this study decreases from up to 20 % at 2090 m in the Westphalian B to 2 to 3 % in the Namurian C at 4835 m depth due to increased diagenetic alteration, while contemporary increasing cementation by quartz cements is observed (Scherp, 1963). Low feldspar contents are related to burial diagenetic dissolution and the alteration to clay minerals. While kaolinitization of feldspars is pervasive in the coal-bearing strata of the Westphalian A, kaolinite is absent, and illitization of felspars is predominant in the barren and coal-bearing Namurian sediments, which provides silica for the increased quartz cementation (Scherp, 1963). Since no depth dependent correlation could be established between the reconstructed feldspar content in samples of this study and the depth of the studied formation, the relatively low feldspar content is interpreted to be related to the depositional environment and grain size (Fig. 4.16). Especially in transitional/shallow marine environments, the felspar content rapidly decreases due to mechanical destruction compared to fluvial environments (Mack, 1978), which are comparable to the deposition on the delta plain (Süss et al., 2007) of the studied sandstones. Even though previous studies suggest that feldspar appears to be preferentially destroyed during humid climates

(Nesbitt et al., 1997; Suttner et al., 1981), which prevailed throughout the Westphalian, this effect is not as effective as the mechanical destruction (Mack, 1978).

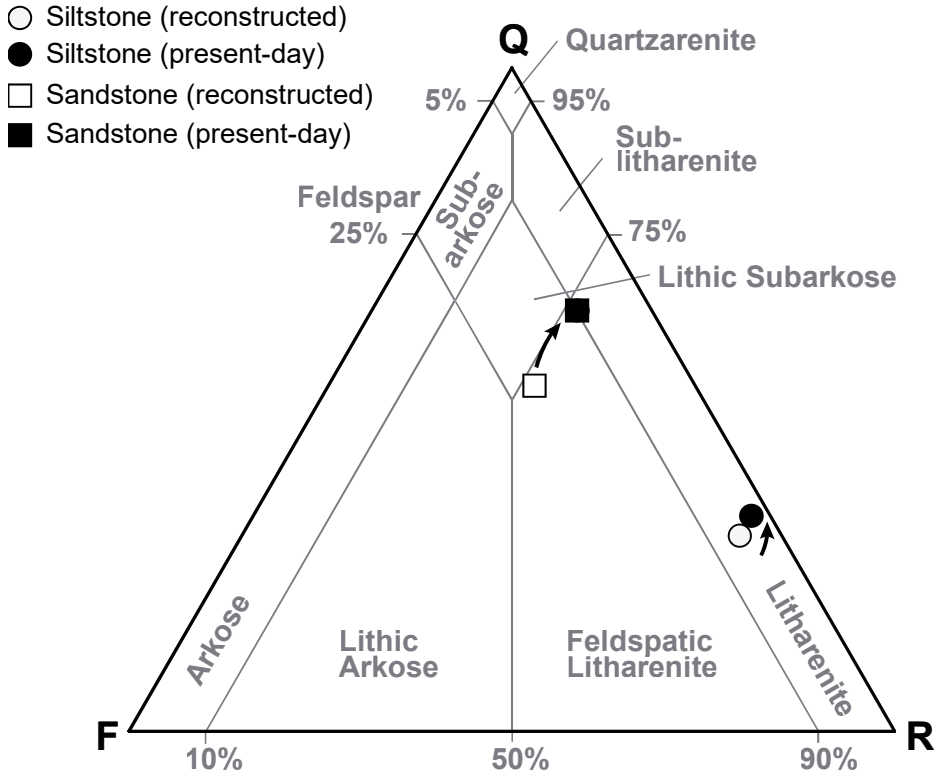

Figure 4.16 Average present-day composition of Westphalian A and B sandstones (open circle) and siltstones (closed circle) in comparison with the reconstructed composition to time of deposition of sandstones (open square) and siltstones (closed square) plotted on the sandstone classification of McBride (1963).

4.7.8 Conclusion

Upper Carboniferous sandstones and siltstones of the Westphalian A and B are generally tight (mean porosity 5.5 % in well Bork-1 and 5.1 % in well Haidberg-1; mean permeability 0.41 mD and 0.16 mD, respectively). Grain size and its correlated mineralogical composition is the main control on reservoir properties. Fine-grained litharenites (siltstones) contain lower intergranular dissolution porosity than coarse-grained lithic subarkoses (sandstones, up to 6 %). The locally enhanced dissolution by acidic pore waters during organic matter maturation is related to the provenance of siltstones and sandstones in the Ruhr Basin. While in the Upper and Middle Bochum Formation dissolution porosity originates from altered rock fragments (RF) (up to 6.0 %), it originates predominantly from feldspars in the other formations (up to 4.6 %).

Furthermore, ductile rock fragments, such as shales and phyllites, are responsible for porosity reduction due to mechanical compaction, leading to a rapid decline in IGV during burial (ICOMPACT > 0.99). The content of rock fragments is higher in siltstones (42 to 78 %) than in sandstones (6 to 42 %).

The SiO_2 content can be used to identify coarse-grained sections and designate them as sandstones of the delta front environment, whereas the Al_2O_3, Fe_2O_3, MgO, and K_2O concentration is a proxy for siltstones and clay minerals of the lower delta plain and wetland environments.

These findings provide valuable insights into the controls and origin of reservoir properties in Upper Carboniferous tight sandstones and siltstones for potential exploration and production strategies in similar geological settings. Nevertheless, tight sandstones and siltstones would require natural fracture networks or hydraulic stimulation to enable reservoir exploitation for different use cases. In the former mining areas in the Ruhr area, zones of enhanced permeabilities around galleries or the galleries themselves may be suitable targets for geothermal post-use cases.

Remark: For additional methodological considerations, see appendix B

5 Conclusions and Outlook

5.1 Conclusions

Fine to medium grained sandstones of the delta front generally contain fewer rock fragments, and higher quartz and feldspar contents compared to finer grained deposits of the lower delta plain, wetlands or prodelta. A clear correlation exists between grain size and mineralogical composition, as siltstones have higher contents of rock fragments, whereas sandstones are relatively enriched in quartz and feldspars, classifying them as lithic subarkoses.

Fine grained mud- and siltstones of the lower delta plain, wetlands and prodelta are primarily affected by mechanical compaction characterized by significant ductile clast deformation. In contrast, fine to medium sandstones of the delta front record a more complex diagenetic history including feldspar dissolution, kaolinite authigenesis and development of intragranular dissolution porosity (1.5–6%). Carbonate cements in sandstones, including siderite, ferroan dolomite/ankerite and ferroan calcite precipitate within pores and fractures, effectively reducing intergranular porosity. Quartz cementation is present but remains minor.

Reservoir properties vary significantly, with porosities of 0.3 to 15.6 % and permeabilities between 0.0001 and 5.05 mD, but overall, the siliciclastics are considered tight (< 1mD). Generally, grain size has the main influence on reservoir properties as high porosities are associated with larger grain size. A correlation between porosity and permeability is shown across the whole data set. Nevertheless, the enhancement in porosity does not necessarily yield a rise in permeability due to the clogging of primary and intragranular dissolution porosity by authigenic clays (i.e. kaolinite) and carbonates. The integration of lithology and characteristic sedimentary structures to appropriately characterize deltaic facies supports the established correlation. Delta front deposits dominated by sandstones exhibit higher porosity and permeability, while the lower delta plain siltstones, wetland mudstones and prodelta claystones have lower porosity. Coal fragments in plug samples enhance the permeability by approximately two orders of magnitude under non-reservoir conditions (1.2 MPa). However, under reservoir conditions (49 MPa) the permeability enhancing effect abates.

Delta front samples with high thermal conductivity correlate with high quartz content, while low values in lower delta plain and wetland sediments result from high contents of organic matter and sheet silicates. Porosity significantly affects thermal conductivity, with mineralogy playing a larger role in less porous samples. Compressional wave velocity (v_P) shows weak sensitivity to sedimentary attributes like mineralogy and grain size, while porosity and diagenesis, including mechanical compaction and

dissolution, have a primary impact. Cements, due to their low volumes, marginally affect reservoir properties and v_P values in Upper Carboniferous siliciclastics.

The v_P values can also be used as an indirect proxy in the absence of core material, representing porosity. Further, the Si/Al ratio is a suitable proxy for assessing grain size and distinguishing between delta front sandstones and lower delta plain siltstones in the Ruhr Basin. Additionally, Al_2O_3, Fe_2O_3, MgO, and K_2O concentrations serve as proxies for siltstones and clay minerals in the lower delta plain and wetland environments.

The tight reservoir nature of the Upper Carboniferous in the eastern Ruhr Basin demonstrates that the fluid flow, regardless of the application (i.e., mine flooding, geothermal applications, or gas extraction) will primarily rely on mined drifts and shafts, while natural faults may often be tight and natural fracture systems limited to tight sandstone horizons. Considering the rock composition of ductile behaving schist and shale rock fragments (often forming pseudomatrix), quartz and minor feldspar, alteration of tight rocks due to mine flooding is unlikely.

5.2 Outlook

For the Upper Carboniferous of the Ruhr Basin, the sedimentary attributes i.e., grain size and mineralogy are shown to act as a main controlling factor for reservoir quality by influencing the amount of porosity loss due to compaction and intragranular dissolution porosity, while the porosity enhancement has a minor influence on permeability. The paragenetic sequence established in this work (chapters 3 and 4) links data to a published burial history model for the Münsterland Basin and eastern Ruhr Basin (Bruns et al., 2013; Büker, 1996). However, radiometric dating of illite growth is missing for this area and can add absolute ages to the burial history and allows to pin the paragenetic framework for the various diagenetic processes, relative to the illite formation, that have affected the reservoir quality.

The results of this work highlight the tight reservoir characteristics, emphasizing that any utilization will rely on permeable faults and fracture systems. Therefore, it becomes crucial to conduct a more comprehensive examination of the mechanical properties and fracture patterns within the strata that facilitate fluid flow. Especially, the complex interplay of factors that may lead to mechanical anisotropy need to be investigated. Understanding these factors is essential for reservoir engineering (e.g. reservoir stimulation) and natural hazard assessment i.e. flooding of coal mines.

Late diagenetic carbonates play a significant role in the development of reservoir qualities by effectively sealing fractures. The analysis of fluid inclusions in cements of the fractures and surrounding rock matrix can provide information about P-T conditions during entrapment and therefore, insights into the fluid migration and the postdepositional reservoir evolution. Microthermometry and stable isotope measurements (i.e., Oxygen (δ18O) and Carbon (δ13C)) help to determine the composition and temperature

of the fluids involved and their interaction with the reservoir rocks, during cement precipitation. These findings can be integrated into the burial context to further constrain the timing and nature of fluid movements within the basin. Ultimately, this approach aims to better understand cementation trajectories and to identify potential patterns linking fracture orientation with cementation.

Lastly, conducting a comprehensive provenance analysis would provide valuable information about the source rocks contributing to sedimentation in the Upper Carboniferous, through petrographic and geochemical analysis (e.g., elemental composition, mineralogy and isotopes) of detrital grains analysis and heavy mineral studies. Such analysis would contribute to a better understanding of the depositional environments and sediment sources within the basin. As shown in this work, the feldspar content at deposition influences the intragranular dissolution porosity, and understanding the provenance may lead to a better understanding of lithologies that have favorable heat conductivities, which is negatively affected by dissolution porosity.

6 References

Aagaard, P., Jahren, J., Harstad, A., Nilsen, O., & Ramm, M. (2000). Formation of grain-coating chlorite in sandstones. Laboratory synthesized vs. natural occurrences. *Clay Minerals, 35*(1), 261–269. doi:https://doi.org/10.1180/000985500546639

Abouessa, A., & Morad, S. (2009). An integrated study of diagenesis and depositional facies in tidal sandstones: Hawaz Formation (Middle Ordovician), Murzuq Basin, Libya. *Journal of Petroleum Geology, 32*(1), 39–65. doi:https://doi.org/10.1111/j.1747-5457.2009.00434.x

Ajdukiewicz, J. M., & Lander, R. H. (2010). Sandstone reservoir quality prediction: The state of the art. *AAPG bulletin, 94*(8), 1083–1091. doi:https://doi.org/10.1306/intro060110

Ajdukiewicz, J. M., & Larese, R. E. (2012). How clay grain coats inhibit quartz cement and preserve porosity in deeply buried sandstones: Observations and experiments. *AAPG bulletin, 96*(11), 2091–2119. doi:https://doi.org/10.1306/02211211075

Allen, J. (1965). Late Quaternary Niger delta, and adjacent areas: sedimentary environments and lithofacies. *AAPG bulletin, 49*(5), 547–600. doi:https://doi.org/10.1306/A663363A-16C0-11D7-8645000102C1865D

Allgaier, F., Busch, B., Niederhuber, T., Quandt, D., Müller, B., & Hilgers, C. (2023). Fracture network characterization of the naturally fractured Upper Carboniferous sandstones combining outcrop and wellbore data, Ruhr Basin, Germany. *Journal of Applied and Regional Geology*. doi:10.1127/zdgg/2023/0369

Allison, M. A., Kineke, G. C., Gordon, E. S., & Goni, M. A. (2000). Development and reworking of a seasonal flood deposit on the inner continental shelf off the Atchafalaya River. *Continental Shelf Research, 20*(16), 2267–2294. doi:https://doi.org/10.1016/S0278-4343(00)00070-4

Andruleit, H., Bahr, A., Bönnemann, C., Erbacher, J., Franke, D., Gerling, J., Gestermann, N., Himmelsbach, T., Kosinowski, M., & Krug, S. (2012). NiKo-Projekt-Team (2012) Abschätzung des Erdgaspotenzials aus dichten Tongesteinen (Schiefergas) in Deutschland. *Bundesanstalt für Geowissenschaften und Rohstoffe*.

Arfai, J., Jähne, F., Lutz, R., Franke, D., Gaedicke, C., & Kley, J. (2014). Late Palaeozoic to Early Cenozoic geological evolution of the northwestern German North Sea (Entenschnabel): new results and insights. *Netherlands Journal of Geosciences- Geologie En Mijnbouw, 93*(4), 147–174. doi:https://doi.org/10.1017/njg.2014.22

Arndt, M., Fritschle, T., Thiel, A., & Salamon, M. (2021). The DGE-ROLLOUT project: Deep Geothermal Energy potential of Carboniferous carbonate rocks in North-West Europe – History, characterisation, modelling and exploration. *Journal of Applied and Regional Geology, 172*(3), 205–210. doi:10.1127/zdgg/2021/0309

Balcewicz, M., Ahrens, B., Lippert, K., & Saenger, E. H. (2021). Characterization of discontinuities in potential reservoir rocks for geothermal applications in the Rhine-Ruhr metropolitan area (Germany). *Solid Earth, 12*(1), 35–58. doi:https://doi.org/10.5194/se-12-35-2021

Barth, T., & Bjørlykke, K. (1993). Organic acids from source rock maturation: generation potentials, transport mechanisms and relevance for mineral diagenesis. *Applied Geochemistry, 8*(4), 325–337. doi:https://doi.org/10.1016/0883-2927(93)90002-X

Beard, D., & Weyl, P. (1973). Influence of texture on porosity and permeability of unconsolidated sand. *AAPG bulletin, 57*(2), 349–369. doi:https://doi.org/10.1306/819A4272-16C5-11D7-8645000102C1865D

Becker, I., Busch, B., Koehrer, B., Adelmann, D., & Hilgers, C. (2019). Reservoir quality evolution of Upper Carboniferous (Westphalian) tight gas sandstones, Lower Saxony Basin, NW Germany. *Journal of Petroleum Geology, 42*(4), 371–392. doi:https://doi.org/10.1111/jpg.12742

Becker, I., Wüstefeld, P., Koehrer, B., Felder, M., & Hilgers, C. (2017). Porosity and permeability variations in a tight gas sandstone reservoir analogue, Westphalian D, Lower Saxony Basin, NW Germany: Influence of depositional setting and diagenesis. *Journal of Petroleum Geology, 40*(4), 363–389. doi:https://doi.org/10.1111/jpg.12685

Becker, S., Hilgers, C., Kukla, P. A., & Urai, J. L. (2011). Crack-seal microstructure evolution in bi-mineralic quartz–chlorite veins in shales and siltstones from the RWTH-1 well, Aachen, Germany. *Journal of Structural Geology, 33*(4), 676-689. doi:https://doi.org/10.1016/j.jsg.2011.01.001

Becker, S., Nguyen, H. T., Nollet, S., Fernandez-Steeger, T. M., Laux, D., & Hilgers, C. (2014). Methods to analyse fracture orientation patterns in a Lower Carboniferous carbonate reservoir analogue in the Voreifel, Germany. *Journal of Applied and Regional Geology, 165*(3), 319–330. doi:https://10.1127/1860-1804/2014/0078

Berger, G., Lacharpagne, J.-C., Velde, B., Beaufort, D., & Lanson, B. (1997). Kinetic constraints on illitization reactions and the effects of organic diagenesis in sandstone/shale sequences. *Applied Geochemistry, 12*(1), 23–35. doi:https://doi.org/10.1016/S0883-2927(96)00051-0

Besly, B., & Turner, P. (1983). Origin of red beds in a moist tropical climate (Etruria Formation, Upper Carboniferous, UK). *Geological Society, London, Special Publications, 11*(1), 131–147. doi:https://doi.org/10.1144/GSL.SP.1983.011.01.14

Besly, B. M. (1998). Carboniferous. In K. W. Glennie (Ed.), *Petroleum geology of the North Sea: basic concepts and recent advances* (fourth ed. ed., pp. 104–136). Oxford, United Kingdom: Blackwell Science Ltd.

Best, A. I., Sothcott, J., & McCann, C. (2007). A laboratory study of seismic velocity and attenuation anisotropy in near-surface sedimentary rocks. *Geophysical Prospecting, 55*(5), 609–625. doi:https://doi.org/10.1111/j.1365-2478.2007.00642.x

Bhattacharya, J. P. (2006). Deltas. In H. W. Posamentier & R. G. Walker (Eds.), *Facies Models Revisited* (Vol. 84, pp. 237–292). Tulsa: SEPM Society for Sedimentary Geology.

Bisutti, I., Hilke, I., Schumacher, J., & Raessler, M. (2007). A novel single-run dual temperature combustion (SRDTC) method for the determination of organic, in-organic and total carbon in soil samples. *Talanta, 71*(2), 521–528. doi:https://doi.org/10.1016/j.talanta.2006.04.022

Bjorkum, P. A., & Gjelsvik, N. (1988). An isochemical model for formation of authigenic kaolinite, K-feldspar and illite in sediments. *Journal of sedimentary research, 58*(3), 506–511. doi:https://doi.org/10.1306/212F8DD2-2B24-11D7-8648000102C1865D

Bjørlykke, K., & Egeberg, P. K. (1993). Quartz cementation in sedimentary basins. *AAPG bulletin, 77*(9), 1538–1548. doi:https://doi.org/10.1306/BDFF8EE8-1718-11D7-8645000102C1865D

Bjørlykke, K., ElvekhøI, B. A., & Malm, A. O. (1979). Diagenesis in Mesozoic sandstones from Spitsbergen and the North Sea—a comparison. *Geologische Rundschau, 68*, 1152–1171. doi:https://doi.org/10.1007/BF02274692

Blackwell, D. D., & Steele, J. L. (1989). Thermal conductivity of sedimentary rocks: measurement and significance. In N. D. Naeser & T. H. McCulloh (Eds.), *Thermal History of Sedimentary Basins* (pp. 13–36). New York, NY: Springer New York.

Bladh, K. W. (1982). The formation of goethite, jarosite, and alunite during the weathering of sulfide-bearing felsic rocks. *Economic Geology, 77*(1), 176–184. doi:https://doi.org/10.2113/gsecongeo.77.1.176

Bless, M., Bouckaert, J., Conil, R., Groessens, E., Kasig, W., Paproth, E., Poty, E., Van Steenwinkel, M., Streel, M., & Walter, R. (1980). Pre-Permian depositional environments around the Brabant Massif in Belgium, the Netherlands and Germany. *Sedimentary Geology, 27*(1), 1–81. doi:https://doi.org/10.1016/0037-0738(80)90031-7

Bloch, S., Lander, R. H., & Bonnell, L. (2002). Anomalously high porosity and permeability in deeply buried sandstone reservoirs: Origin and predictability. *AAPG bulletin, 86*(2), 301–328. doi:https://doi.org/10.1306/61EEDABC-173E-11D7-8645000102C1865D

Boron, D. J., Evans, E. W., & Peterson, J. M. (1987). An overview of peat research, utilization, and environmental considerations. *International Journal of Coal Geology, 8*(1-2), 1–31. doi:https://doi.org/10.1016/0166-5162(87)90020-6

Brenne, S. (2016). *Hydraulic fracturing and flow experiments on anisotropic and pre-fractured rocks.* (PhD thesis Dissertation). Universtiy of Bochum, Bochum. (urn:nbn:de:hbz:294-49165)

Brix, M., Drozdzewski, G., Greiling, R., Wolf, R., & Wrede, V. (1988). The N Variscan margin of the Ruhr coal district (Western Germany): structural style of a buried thrust front? *Geologische Rundschau, 77*(1), 115–126. doi:https://doi.org/10.1007/BF01848679

Bruns, B., Di Primio, R., Berner, U., & Littke, R. (2013). Petroleum system evolution in the inverted Lower Saxony Basin, northwest Germany: a 3D basin modeling study. *Geofluids, 13*(2), 246–271. doi:https://doi.org/10.1111/gfl.12016

Büker, C. (1996). *Absenkungs-, Erosions-und Wärmeflußgeschichte des Ruhr-Beckens und des nordöstlichen Rechtsrheinischen Schiefergebirges.* (PhD thesis). Universtiy of Bochum, Jülich. (http://hdl.handle.net/2128/21785)

Busch, B., Becker, I., Koehrer, B., Adelmann, D., & Hilgers, C. (2019). Porosity evolution of two Upper Carboniferous tight-gas-fluvial sandstone reservoirs: Impact of fractures and total cement volumes on reservoir quality. *Marine and Petroleum Geology, 100*, 376–390. doi:https://doi.org/10.1016/j.marpetgeo.2018.10.051

Busch, B., Hilgers, C., & Adelmann, D. (2020). Reservoir quality controls on Rotliegend fluvio-aeolian wells in Germany and the Netherlands, Southern Permian Basin–Impact of grain coatings and cements. *Marine and Petroleum Geology, 112*, 104075. doi:https://doi.org/10.1016/j.marpetgeo.2019.104075

Busch, B., Hilgers, C., Gronen, L., & Adelmann, D. (2017). Cementation and structural diagenesis of fluvio-aeolian Rotliegend sandstones, northern England. *Journal of the Geological Society, 174*(5), 855–868. doi:https://doi.org/10.1144/jgs2016-122

Busch, B., Spitzner, A., Adelmann, D., & Hilgers, C. (2022). The significance of outcrop analog data for reservoir quality assessment: A comparative case study of Lower Triassic Buntsandstein sandstones in the Upper Rhine Graben. *Marine and Petroleum Geology, 141*, 105701. doi:https://doi.org/10.1016/j.marpetgeo.2022.105701

Bushell, T. (1986). Reservoir geology of the Morecambe Field. *Geological Society, London, Special Publications, 23*(1), 189–208. doi:https://doi.org/10.1144/GSL.SP.1986.023.01.1

Bussmann, G., Appelhans, K., Hahn, F., Jagert, F., Bracke, R., Seidel, T., & König, C. (2019). *Reutilization of mine water from heating and cooling in the abandoned colliery Dannebaum in Bochum.* Paper presented at the European Geothermal Congress.

Butala, S. J., Medina, J. C., Taylor, T. Q., Bartholomew, C. H., & Lee, M. L. (2000). Mechanisms and kinetics of reactions leading to natural gas formation during coal maturation. *Energy & fuels, 14*(2), 235–259. doi:https://doi.org/10.1021/ef990076k

Casshyap, S. M. (1975). Cyclic characteristics of coal-bearing sediments in the Bochumer Formation (Westphal A 2) Ruhrgebiet, Germany. *Sedimentology, 22*(2), 237–255. doi:https://doi.org/10.1111/j.1365-3091.1975.tb00292.x

Čermák, V., & Rybach, L. (1982). Thermal conductivity and specific heat of minerals and rocks. In G. Angenheister (Ed.), *Physical Properties of Rocks Subvolume A* (Vol. 1A, pp. 305–343). Germany: Springer-Verlag Berlin Heidelberg.

Clauser, C., & Huenges, E. (1995). Thermal conductivity of rocks and minerals. In T. J. Ahrens (Ed.), *Rock Physics & Phase Relations: A Handbook of Physical Constants* (Vol. 3, pp. 105–126): American Geophysical Union.

Coleman, M. L. (1985). Geochemistry of diagenetic non-silicate minerals: kinetic considerations. *Philosophical Transactions of the Royal Society of London. Series A, Mathematical and Physical Sciences, 315*(1531), 39–56. doi:https://doi.org/10.1098/rsta.1985.0028

Commission, G. S. (2016). *The Stratigraphic table of Germany*: GeoForschungsZentrum.

Conti, J., Holtberg, P., Diefenderfer, J., LaRose, A., Turnure, J. T., & Westfall, L. (2016). *International energy outlook 2016 with projections to 2040*. Retrieved from Washington, DC (United States): https://doi.org/10.2172/1296780

Cruz, M. R., & Reyes, E. (1998). Kaolinite and dickite formation during shale diagenesis: isotopic data. *Applied Geochemistry, 13*(1), 95–104. doi:https://doi.org/10.1016/S0883-2927(97)00056-5

Curtis, C. D., & Coleman, M. L. (1985). Controls on the precipitation of early diagenetic calcite, dolomite and siderite concretions in complex depositional sequences. In D. L. Gautier (Ed.), *Roles of Organic Matter in Sediment Diagenesis* (Vol. 38, pp. 23–33). Tulsa, Oklahoma: SEPM Society for Sedimentary Geology.

Curtis, C. D., & Spears, D. A. (1968). The formation of sedimentary iron minerals. *Economic Geology, 63*(3), 257–270. doi:https://doi.org/10.2113/gsecongeo.63.3.257

David, F. (1987). Sandkörper in fluviatilen Sandsteinen des Unteren Westfal D (Oberkarbon) am Piesberg bei Osnabrück. *Facies, 17*(1), 51–57. doi:https://doi.org/10.1007/BF02536769

Dawson, G., Golding, S., Esterle, J., & Massarotto, P. (2012). Occurrence of minerals within fractures and matrix of selected Bowen and Ruhr Basin coals. *International Journal of Coal Geology, 94*, 150–166. doi:https://doi.org/10.1016/j.coal.2012.01.004

Dickson, J. (1965). A modified staining technique for carbonates in thin section. *Nature, 205*(4971), 587–587. doi:10.1038/205587a0

Diessel, C. F. (1992). Coal facies and depositional environment. In C. F. K. Diessel (Ed.), *Coal-bearing depositional systems* (pp. 161–264). Berlin, Heidelberg: Springer Berlin Heidelberg.

Dölling, B., Dölling, M., Hiss, M., Berensmeier, M., & Püttmann, T. (2018). Upper Cretaceous shallow-marine deposits of the southwestern Münsterland (northwest Germany) influenced by synsedimentary tectonics. *Cretaceous Research, 87*, 261–276. doi:https://doi.org/10.1016/j.cretres.2017.05.002

Dowey, P. J., Worden, R. H., Utley, J., & Hodgson, D. M. (2017). Sedimentary controls on modern sand grain coat formation. *Sedimentary Geology, 353*, 46–63. doi:https://doi.org/10.1016/j.sedgeo.2017.03.001

Drozdzewski, G. (1988). Die Wurzel der Osning-Überschiebung und der Mechanismus herzynischer Inversionsstörungen in Mitteleuropa. *Geologische Rundschau, 77*(1), 127–141. doi:https://doi.org/10.1007/BF01848680

Drozdzewski, G. (1992). Zur Faziesentwicklung im Oberkarbon des Ruhrbeckens, abgeleitet aus Mächtigkeitskarten und lithostratigraphischen Gesamtprofilen. *Zeitschrift für angewandte Geologie, 38*(1), 41–48.

Drozdzewski, G. (1993). The Ruhr coal basin (Germany): Structural evolution of an autochthonous foreland basin. *International Journal of Coal Geology, 23*(1-4), 231–250. doi:https://doi.org/10.1016/0166-5162(93)90050-K

Drozdzewski, G. (2005). Zur sedimentären Entwicklung des Subvariscikums im Namurium und Westfalium Nordwestdeutschlands. In V. Wrede (Ed.), *Stratigraphie von Deutschland V - Das Oberkarbon (Pennsylvanium) in Deutschland* (Vol. 254, pp. 271–320). Frankfurt am Main: Courier Forschungsinstitut Senckenberg.

Drozdzewski, G., & Wrede, V. (1994). Faltung und Bruchtektonik–Analyse der Tektonik im Subvariscikum. In H. D. Hilden (Ed.), *Fortschritte in der Geologie von Rheinland und Westfalen* (Vol. 38, pp. 7–187). Krefeld: Geologisches Landesamt Nordrhein-Westfalen.

Duda, M., & Renner, J. (2013). The weakening effect of water on the brittle failure strength of sandstone. *Geophysical Journal International, 192*(3), 1091–1108. doi:https://doi.org/10.1093/gji/ggs090

Ehrenberg, S. N. (1989). Assessing the relative importance of compaction processes and cementation to reduction of porosity in sandstones: Discussion; Compaction and porosity evolution of Pliocene sandstones, Ventura Basin, California: Discussion. *AAPG bulletin, 73*(10), 1274–1276. doi:https://doi.org/10.1306/44B4AA1E-170A-11D7-8645000102C1865D

Ehrenberg, S. N. (1990). Relationship between diagenesis and reservoir quality in sandstones of the Garn Formation, Haltenbanken, mid-Norwegian continental shelf. *AAPG bulletin, 74*(10), 1538–1558. doi:https://doi.org/10.1306/0C9B2515-1710-11D7-8645000102C1865D

Elliott, T. (1976). Upper Carboniferous sedimentary cycles produced by river-dominated, elongate deltas. *Journal of the Geological Society, 132*(2), 199–208. doi:https://doi.org/10.1144/gsjgs.132.2.0199

Fiebig, H. (1971). *Untersuchungsergebnisse zur Bohrung Pelkum 1 - 1971*. Bearbeitung Karbon Nachtrag zur Schichtenbeschreibung der Tiefbohrung Pelkum 1. Bergbau AG Westfalen. Bochum.

Fiebig, H. (1977). *Schichtenschnitte und Untersuchungsergebnisse zur Bohrung Bork 1 - 1976*. Anlage 5 Karbon. Bergbau AG Westfalen. Bochum.

Folk, R. L. (1954). The distinction between grain size and mineral composition in sedimentary-rock nomenclature. *The Journal of Geology, 62*(4), 344–359. doi:https://doi.org/10.1086/626171

Folk, R. L. (1980). *Petrology of sedimentary rocks* (Second Edition ed.). Austin: Hemphill Publishing Company.

Folk, R. L., & Ward, W. C. (1957). Brazos River Bar: A study in the significance of grain size parameters. *Journal of sedimentary research, 27*(1), 3–26. doi:https://doi.org/10.1306/74D70646-2B21-11D7-8648000102C1865D

Frank, F., Albertsen, M., Blohm, M., Füchtbauer, H., & Zinkernagel, U. (1992). *Zur Liefergebietsfrage der Sandsteine des Nordwestdeutschen Oberkarbons* (Vol. 348-8). Hamburg: Deutsche Gesellschaft fuer Mineraloelwissenschaft und Kohlechemie e.V.

Fraser, H. (1935). Experimental study of the porosity and permeability of clastic sediments. *The Journal of Geology, 43*(8, Part 1), 910-1010. doi:https://doi.org/10.1086/624388

Fritschle, T., Strozyk, F., Oswald, T., Stubbe, H., & Salamon, M. (2021). Deep geothermal energy potential at Weisweiler, Germany: Exploring subsurface mid-Palaeozoic carbonate reservoir rocks. *Journal of Applied and Regional Geology, 172*(3), 325–338. doi:10.1127/zdgg/2021/0292

Fuchs, S., & Förster, A. (2010). Rock thermal conductivity of Mesozoic geothermal aquifers in the Northeast German Basin. *Geochemistry, 70*, 13–22. doi:https://doi.org/10.1016/j.chemer.2010.05.010

Gani, M. R., Bhattacharya, J. P., & Maceachern, J. A. (2007). Using ichnology to determine relative influence of waves, storms, tides, and rivers in deltaic deposits: examples from Cretaceous Western Interior Seaway, USA. In J. A. MacEachern (Ed.), *Applied Ichnology* (Vol. 52): SEPM (Society for Sedimentary Geology).

Gaupp, R., Matter, A., Platt, J., Ramseyer, K., & Walzebuck, J. (1993). Diagenesis and fluid evolution of deeply buried Permian (Rotliegende) gas reservoirs, northwest Germany. *AAPG bulletin, 77*(7), 1111–1128. doi:https://doi.org/10.1306/BDFF8E0C-1718-11D7-8645000102C1865D

Gaupp, R., & Okkerman, J. A. (2011). Diagenesis and reservoir quality of Rotliegend sandstones in the Northern Netherlands—a review. In J. Grötsch & R. Gaupp (Eds.), *The Permian Rotliegend of the Netherlands*. Tulsa: SEPM Society for Sedimentary Geology.

Gautier, D. L. (1982). Siderite concretions; indicators of early diagenesis in the Gammon Shale (Cretaceous). *Journal of sedimentary research, 52*(3), 859–871. doi:https://doi.org/10.1306/212F8076-2B24-11D7-8648000102C1865D

Gayer, R. A., Cole, J. E., Greiling, R. O., Hecht, C., & Jones, J. A. (1993). Comparative evolution of coal-bearing foreland basins along the Variscan northern margin in Europe. In R. A. Gayer, R. O. Greiling, & A. K. Vogel (Eds.), *Rhenohercynian and Subvariscan fold belts* (pp. 47–82). Braunschweig: Vieweg and Sons.

Geluk, M. (1999). Late Permian (Zechstein) rifting in the Netherlands; models and implications for petroleum geology. *Petroleum Geoscience, 5*(2), 189–199. doi:https://doi.org/10.1144/petgeo.5.2.189

Gong, L., Zeng, L., Gao, Z., Zhu, R., & Zhang, B. (2016). Reservoir characterization and origin of tight gas sandstones in the Upper Triassic Xujiahe formation, Western Sichuan Basin, China. *Journal of Petroleum Exploration and Production Technology, 6*, 319–329. doi:https://doi.org/10.1007/s13202-015-0203-9

Götze, J., Schertl, H.-P., Neuser, R. D., Kempe, U., & Hanchar, J. M. (2013). Optical microscope-cathodoluminescence (OM–CL) imaging as a powerful tool to reveal internal textures of minerals. *Mineralogy and Petrology, 107*, 373–392. doi:https://doi.org/10.1007/s00710-012-0256-0

Gray, A., & Uher, C. (1977). Thermal conductivity of mica at low temperatures. *Journal of Materials Science, 12*(5), 959–965. doi:https://doi.org/10.1007/BF00540978

Greve, J., Busch, B., Quandt, D., Knaak, M., Hartkopf-Fröder, C., & Hilgers, C. (2023). Coupling heat conductivity and lithofacies of the coal-bearing Upper Carboniferous in the eastern Ruhr Basin, NW Germany. *Journal of Applied and Regional Geology, 173*(4), 673–695. doi:https://10.1127/zdgg/2023/0350

Greve, J., Busch, B., Quandt, D., Knaak, M., & Hilgers, C. (2024). The influence of sedimentary facies, mineralogy, and diagenesis on reservoir properties of the coal-bearing Upper Carboniferous of NW Germany. *Petroleum Geoscience, 30*(1). doi:https://doi.org/10.1144/petgeo2023-020

Guion, P. D. (1987). Palaeochannels in mine workings in the High Hazles Coal (Westphalian B), Nottinghamshire Coalfield, England. *Journal of the Geological Society, 144*(3), 471–488. doi:https://doi.org/10.1144/gsjgs.144.3.0471

Guion, P. D., & Fielding, C. R. (1988). Westphalian A and B sedimentation in the Pennine Basin, UK. In B. Besly & G. Kelling (Eds.), *Sedimentation in a synorogenic basin complex, the Upper Carboniferous of Northwest Europe* (pp. 153–177). London: Blackie and Son.

Guo, P. Y., Zhang, N., He, M. C., & Bai, B. H. (2017). Effect of water saturation and temperature in the range of 193 to 373 K on the thermal conductivity of sandstone. *Tectonophysics, 699*, 121–128. doi:https://doi.org/10.1016/j.tecto.2017.01.024

Haese, R., Wallmann, K., Dahmke, A., Kretzmann, U., Müller, P., & Schulz, H. (1997). Iron species determination to investigate early diagenetic reactivity in marine sediments. *Geochimica et cosmochimica Acta, 61*(1), 63–72. doi:https://doi.org/10.1016/S0016-7037(96)00312-2

Hahn, F., Bussmann, G., Jagert, F., Ignacy, R., Bracke, R., & Seidel, T. (2018). *Reutilization of mine water as a heat storage medium in abandoned mines.* Paper presented at the 11th ICARD IMWA Conf.

Hahn, F., Jabs, T., Bracke, R., & Alber, M. (2018). Geomechanical characterization of the upper carboniferous under thermal stress for the evaluation of a High Temperature-Mine Thermal Energy Storage (HT-MTES). In V. Litvinenko (Ed.), *Geomechanics and Geodynamics of Rock Masses* (Vol. 1, pp. 287–293). London: CRC Press/Balkema.

Han, D.-h., Nur, A., & Morgan, D. (1986). Effects of porosity and clay content on wave velocities in sandstones. *Geophysics, 51*(11), 2093–2107. doi:https://doi.org/10.1190/1.1442062

Hancock, N., & Taylor, A. (1978). Clay mineral diagenesis and oil migration in the Middle Jurassic Brent Sand Formation. *Journal of the Geological Society, 135*(1), 69–72. doi:https://doi.org/10.1144/gsjgs.135.1.0069

Hannes, K. (1977). Engineering and construction of the Ruhr district heating supply line. *3 R international : RRR ; Rohre, Rohrleitungsbau, Rohrleitungstransport, 16*(10), 598–602.

Harding, A., Strebelle, S., Levy, M., Thorne, J., Xie, D., Leigh, S., Preece, R., & Scamman, R. (2005). Reservoir facies modelling: new advances in MPS. In O. Leuangthong & C. V. Deutsch (Eds.), *Geostatistics banff 2004* (pp. 559–568). Dordrecht: Springer.

Harlé, P., Kushnir, A. R., Aichholzer, C., Heap, M. J., Hehn, R., Maurer, V., Baud, P., Richard, A., Genter, A., & Duringer, P. (2019). Heat flow density estimates in the Upper Rhine Graben using laboratory measurements of thermal conductivity on sedimentary rocks. *Geothermal Energy, 7*(1), 1–36. doi:https://doi.org/10.1186/s40517-019-0154-3

Heald, M., & Larese, R. (1974). Influence of coatings on quartz cementation. *Journal of sedimentary research, 44*(4), 1269–1274. doi:https://doi.org/10.1306/212F6C94-2B24-11D7-8648000102C1865D

Hedemann, H. (1985). Das Nordwestdeutsche Oberkarbonbecken, sein Erdgas und seine Kohlerflöze. In *Dixième Congrès International de Stratigraphie et de Géologie du Carbonifère* (Vol. 2, pp. 15–29). Madrid.

Hedemann, H., & Teichmüller, R. (1971). Die paläogeographische Entwicklung des Oberkarbons. *Fortschritte in der Geologie von Rheinland und Westfalen, 19*, 129–142.

Hesemann, J. (1975). *Geologie Nordrhein-Westfalens*. Paderborn: Schöningh.

Higgs, K. E., Zwingmann, H., Reyes, A. G., & Funnell, R. H. (2007). Diagenesis, porosity evolution, and petroleum emplacement in tight gas reservoirs, Taranaki Basin, New Zealand. *Journal of sedimentary research, 77*(12), 1003–1025. doi:https://doi.org/10.2110/jsr.2007.095

Hofmann, P., Ricken, W., Schwark, L., & Leythaeuser, D. (2001). Geochemical signature and related climatic-oceanographic processes for early Albian black shales: Site 417D, North Atlantic Ocean. *Cretaceous Research, 22*(2), 243–257. doi:https://doi.org/10.1006/cres.2001.0253

Horai, K.-i., & Simmons, G. (1969). Thermal conductivity of rock-forming minerals. *Earth and planetary science letters, 6*(5), 359–368. doi:https://doi.org/10.1016/0012-821X(69)90186-1

Howard, J. J. (1992). Influence of Authigenic-Clay Minerals on Permeability. In D. W. Houseknecht & E. D. Pittman (Eds.), *Origin, Diagenesis, and Petrophysics of Clay Minerals in Sandstones* (Vol. 47, pp. 257–264). Tulsa: SEPM Society for Sedimentary Geology.

IEA. (2009). *World energy outlook*: OECD/IEA Paris.

Jackson, M., & Sherman, G. D. (1953). Chemical weathering of minerals in soils. *Advances in agronomy, 5*, 219–318. doi:https://doi.org/10.1016/S0065-2113(08)60231-X

Jasper, K., Krooss, B. M., Flajs, G., Hartkopf-Fröder, C., & Littke, R. (2009). Characteristics of type III kerogen in coal-bearing strata from the Pennsylvanian (Upper Carboniferous) in the Ruhr Basin, Western Germany: Comparison of coals, dispersed organic matter, kerogen concentrates and coal–mineral mixtures. *International Journal of Coal Geology, 80*(1), 1–19. doi:https://doi.org/10.1016/j.coal.2009.07.003

Jerrett, R. M., Hodgson, D. M., Flint, S. S., & Davies, R. C. (2011). Control of relative sea level and climate on coal character in the Westphalian C (Atokan) Four Corners Formation, central Appalachian Basin, USA. *Journal of sedimentary research, 81*(6), 420–445. doi:https://doi.org/10.2110/jsr.2011.37

Jessen, W. (1956). Allgemeine Erkenntnisse aus feinstratigraphisch erarbeiteten Faunen- und Sediment-Zyklen des Ruhrkarbons. *Geologische Rundschau, 45*(1), 119–128. doi:https://doi.org/10.1007/BF01792756

Kineke, G., Sternberg, R., Trowbridge, J., & Geyer, W. (1996). Fluid-mud processes on the Amazon continental shelf. *Continental shelf research, 16*(5-6), 667–696. doi:https://doi.org/10.1016/0278-4343(95)00050-X

Kley, J., & Voigt, T. (2008). Late Cretaceous intraplate thrusting in central Europe: Effect of Africa-Iberia-Europe convergence, not Alpine collision. *Geology, 36*(11), 839–842. doi:https://doi.org/10.1130/G24930A.1

Kombrink, H. (2008). *The Carboniferous of the Netherlands and surrounding areas; a basin analysis. Geologica Ultraiectina (294).* (Ph.D. Dissertation). Utrecht University,

Kombrink, H., Van Lochem, H., & Van Der Zwan, K. J. (2010). Seismic interpretation of Dinantian carbonate platforms in the Netherlands; implications for the palaeogeographical and structural development of the Northwest European Carboniferous Basin. *Journal of the Geological Society, 167*(1), 99–108. doi:https://doi.org/10.1144/0016-76492008-149

Kretschmann, J., Efremenkov, A. B., & Khoreshok, A. A. (2017). *From mining to post-mining: the sustainable development strategy of the German Hard Coal Mining Industry.* Paper presented at the IOP Conference Series: Earth and Environmental Science.

Krull, P., & Wrede, V. (2005). Paläogeographischer Rahmen. In V. Wrede (Ed.), *Stratigraphie von Deutschland V - Das Oberkarbon (Pennsylvanium) in Deutschland* (Vol. 254, pp. 13–24). Frankfurt am Main: Courier Forschungsinstitut Senckenberg.

Kruszewski, M., Montegrossi, G., Backers, T., & Saenger, E. H. (2021). In Situ Stress State of the Ruhr Region (Germany) and Its Implications for Permeability Anisotropy. *Rock Mechanics and Rock Engineering, 54*(12), 6649–6663. doi:https://doi.org/10.1007/s00603-021-02636-3

Kummerow, J. (2006). *The influence of intergranular, supercritical water on the elastic properties of rocks.* (PhD). Freie Universität Berlin Berlin. Retrieved from https://refubium.fu-berlin.de/handle/fub188/5720

Labus, M., & Labus, K. (2018). Thermal conductivity and diffusivity of fine-grained sedimentary rocks. *Journal of Thermal Analysis and Calorimetry, 132*(3), 1669–1676. doi:https://doi.org/10.1007/s10973-018-7090-5

Lai, J., Wang, G., Ran, Y., Zhou, Z., & Cui, Y. (2016). Impact of diagenesis on the reservoir quality of tight oil sandstones: The case of Upper Triassic Yanchang Formation Chang 7 oil layers in Ordos Basin, China. *Journal of petroleum science and Engineering, 145*, 54–65. doi:https://doi.org/10.1016/j.petrol.2016.03.009

Lander, R. H., Larese, R. E., & Bonnell, L. M. (2008). Toward more accurate quartz cement models: The importance of euhedral versus noneuhedral growth rates. *AAPG bulletin, 92*(11), 1537–1563. doi:https://doi.org/10.1306/07160808037

Lanson, B., Beaufort, D., Berger, G., Bauer, A., Cassagnabere, A., & Meunier, A. (2002). Authigenic kaolin and illitic minerals during burial diagenesis of sandstones: a review. *Clay Minerals, 37*(1), 1–22. doi:https://doi.org/10.1180/0009855023710014

Larsen, D., & Mann, R. (2005). Origin of high manganese concentrations in coal mine drainage, eastern Tennessee. *Journal of Geochemical Exploration, 86*(3), 143–163. doi:https://doi.org/10.1016/j.gexplo.2005.06.001

Littke, R., Büker, C., Hertle, M., Karg, H., Stroetmann-Heinen, V., & Oncken, O. (2000). Heat flow evolution, subsidence and erosion in the Rheno-Hercynian orogenic wedge of central Europe. *Geological Society, London, Special Publications, 179*(1), 231–255. doi:https://doi.org/10.1144/GSL.SP.2000.179.01.1

Littke, R., Büker, C., Lückge, A., Sachsenhofer, R., & Welte, D. (1994). A new evaluation of palaeo-heat flows and eroded thicknesses for the Carboniferous Ruhr Basin, western Germany. *International Journal of Coal Geology, 26*(3-4), 155–s183. doi:https://doi.org/10.1016/0166-5162(94)90009-4

Littke, R., Krooss, B., Uffmann, A. K., Schulz, H.-M., & Horsfield, B. (2011). Unconventional gas resources in the Paleozoic of Central Europe. *Oil & Gas Science and Technology–Revue d'IFP Energies nouvelles, 66*(6), 953–977. doi:https://doi.org/10.2516/ogst/2010033

Littke, R., & Zieger, L. (2019). Deposition, diagenesis and petroleum generation potential of Pennsylvanian coals and coal-bearing strata in Western Germany: A review. *Journal of Applied and Regional Geology, 170*(3-4), 289–309. doi:10.1127/zdgg/2019/0199

Lønøy, A., Akselsen, J., & Rønning, K. (1986). Diagenesis of a deeply buried sandstone reservoir: Hild Field, Northern North Sea. *Clay Minerals, 21*(4), 497–511. doi:https://doi.org/10.1180/claymin.1986.021.4.06

Loucks, R. G. (2005). Revisiting the importance of secondary dissolution pores in Tertiary sandstones along the Texas Gulf Coast. *Gulf Coast Association of Geological Societies Transactions, 55*, 447–455.

Lundegard, P. D. (1992). Sandstone porosity loss; a" big picture" view of the importance of compaction. *Journal of sedimentary research, 62*(2), 250–260. doi:https://doi.org/10.1306/D42678D4-2B26-11D7-8648000102C1865D

MacEachern, J. A., Bann, K. L., Bhattacharya, J. P., Howell, C. D., Jr., Giosan, L., & Bhattacharya, J. P. (2005). Ichnology of Deltas: Organism Responses to the Dynamic Interplay of Rivers, Waves, Storms, and Tides. In L. Giosan & J. P. Bhattacharya (Eds.), *River Deltas–Concepts, Models, and Examples* (Vol. 83): SEPM Society for Sedimentary Geology.

Mack, G. H. (1978). The survivability of labile light-mineral grains in fluvial, aeolian and littoral marine environments: the Permian Cutler and Cedar Mesa Formations, Moab, Utah. *Sedimentology, 25*(5), 587–604. doi:https://doi.org/10.1111/j.1365-3091.1978.tb00321.x

McBride, E. F. (1963). A classification of common sandstones. *Journal of sedimentary research, 33*(3), 664–669. doi:https://doi.org/10.1306/74D70EE8-2B21-11D7-8648000102C1865D

McKinley, J., Worden, R. H., & Ruffell, A. H. (1999). Smectite in sandstones: a review of the controls on occurrence and behaviour during diagenesis. In R. H. Worden & S. Morad (Eds.), *Clay mineral cements in sandstones* (Vol. 34, pp. 109–128). New York: Wiley.

Meisl, S., Aanderle, H., & Strecker, G. (1982). Niedrigtemperierte Metamorphose im Taunus und im Soonwald. [METAMORPHISME DE BASSE TEMPERATURE DANS LE TAUNUS ET LE SOONWALD (fr)]. *Fortschritte Mineral., Beihefte, 60*(2), 43–69.

Meissner, R., Bartelsen, H., & Murawski, H. (1981). Thin-skinned tectonics in the northern Rhenish Massif, Germany. *Nature, 290*(5805), 399–401. doi:https://doi.org/10.1038/290399a0

Melehan, S., Botziolis, C., Maravelis, A. G., Catuneanu, O., Ruming, K., Holmes, E., & Collins, W. J. (2021). Sedimentology and Stratigraphy of an Upper Permian Sedimentary Succession: Northern Sydney Basin, Southeastern Australia. *Geosciences, 11*(7), 273. doi:https://doi.org/10.3390/geosciences11070273

Miall, A. D. (1977). Lithofacies types and vertical profile models in braided river deposits: A summary. In A. D. Miall (Ed.), *Fluvial Sedimentology: Memoir* (pp. 597–604). Stacs Data Service Ltd: Canadian Society of Petroleum Geologists.

Miller, S. L., & Stewart, R. R. (1991). The relationship between elastic-wave velocities and density in sedimentary rocks: A proposal. *Crewes Res. Rep*, 260–273.

Miocic, J. M., Girard, J.-P., Schoener, R., & Gaupp, R. (2020). Mudstone/sandstone ratio control on carbonate cementation and reservoir quality in Upper Permian Rotliegend sandstones, offshore the Netherlands. *Marine and Petroleum Geology, 115*, 104293.

Molenaar, N. (1986). The interrelation between clay infiltration, quartz cementation, and compaction in Lower Givetian terrestrial sandstones, northern Ardennes, Belgium. *Journal of sedimentary research, 56*(3), 359–369. doi:https://doi.org/10.1306/212F8913-2B24-11D7-8648000102C1865D

Monsees, A. C., Busch, B., Schöner, N., & Hilgers, C. (2020). Rock typing of diagenetically induced heterogeneities–A case study from a deeply-buried clastic Rotliegend reservoir of the Northern German Basin. *Marine and Petroleum Geology, 113*, 104163. doi:https://doi.org/10.1016/j.marpetgeo.2019.104163

Morad, S., De Ros, L., Nystuen, J., & Bergan, M. (1998). Carbonate diagenesis and porosity evolution in sheet-flood sandstones: evidence from the Middle and Lower Lunde Members (Triassic) in the Snorre Field, Norwegian North Sea. In S. Morad (Ed.), *Carbonate Cementation in Sandstones: Distribution Patterns and Geochemical Evolution* (Vol. 26, pp. 53–85): Special Publication-International Association of Sedimentologists.

Morad, S., Ketzer, J., & De Ros, L. F. (2000). Spatial and temporal distribution of diagenetic alterations in siliciclastic rocks: implications for mass transfer in sedimentary basins. *Sedimentology, 47*(1), 95–120. doi:https://doi.org/10.1046/j.1365-3091.2000.00007.x

Mountney, N. P. (2006). Eolian facies models. In H. W. Posamentier & R. G. Walker (Eds.), *Facies models revisited* (Vol. 84, pp. 19–84). Tulsa: SEPM Society for Sedimentary Geology.

Mulder, T., & Syvitski, J. P. (1995). Turbidity currents generated at river mouths during exceptional discharges to the world oceans. *The Journal of Geology, 103*(3), 285–299. doi:https://www.jstor.org/stable/30071222

Mumm, A. S., & Wolfgramm, M. (2002). Diagenesis and fluid mobilisation during the evolution of the North German Basin—evidence from fluid inclusion and sulphur isotope analysis. *Marine and Petroleum Geology, 19*(3), 229–246. doi:https://doi.org/10.1016/S0264-8172(02)00015-6

Nesbitt, H. W., Fedo, C. M., & Young, G. M. (1997). Quartz and feldspar stability, steady and non-steady-state weathering, and petrogenesis of siliciclastic sands and muds. *The Journal of Geology, 105*(2), 173–192. doi:https://doi.org/10.1086/515908

Niederhuber, T., Kruszewski, M., Röckel, T., Rische, M., Alber, M., & Müller, B. (2023). Stress orientations from hydraulic fracturing tests in the Ruhr area in comparison to stress orientations from borehole observations and earthquake focal mechanism. *Journal of Applied and Regional Geology, 173*(4), 625–635. doi:10.1127/zdgg/2022/0352

Nöth, S., Karg, H., & Littke, R. (2001). Reconstruction of Late Paleozoic heat flows and burial histories at the Rhenohercynian-Subvariscan boundary, Germany. *International Journal of Earth Sciences, 90*(2), 234–256. doi:https://doi.org/10.1007/s005310000114

Oncken, O., Von Winterfeld, C., & Dittmar, U. (1999). Accretion of a rifted passive margin: The Late Paleozoic Rhenohercynian fold and thrust belt (Middle European Variscides). *Tectonics, 18*(1), 75–91. doi:https://doi.org/10.1029/98TC02763

Pasternak, M., Kosinowski, M., Loesch, J., Meyer, H., Porth, H., & Sedlacek, R. (1998). Crude oil and natural gas in the Federal Republic of Germany 1997; Erdoel und Erdgas in der Bundesrepublik Deutschland 1997.

Paxton, S., Szabo, J., Ajdukiewicz, J., & Klimentidis, R. (2002). Construction of an intergranular volume compaction curve for evaluating and predicting compaction and porosity loss in rigid-grain sandstone reservoirs. *AAPG bulletin, 86*(12), 2047–2067. doi:https://doi.org/10.1306/61EEDDFA-173E-11D7-8645000102C1865D

Philippe, G., Abdoulaye, G., Haïkel, B. H., Hassen, B., & Farid, L. (2019). Installation of a thermal energy storage site in an abandoned mine in Picardy (France). Part 1: Selection criteria and equipment of the experimental site. *Environmental Earth Sciences, 78*(5), 1–16. doi:https://doi.org/10.1007/s12665-019-8128-0

Pijnenburg, R., Verberne, B., Hangx, S., & Spiers, C. (2019). Inelastic deformation of the Slochteren sandstone: Stress-strain relations and implications for induced seismicity in the Groningen gas field. *Journal of Geophysical Research: Solid Earth, 124*(5), 5254–5282. doi:https://doi.org/10.1029/2019JB017366

Pittman, E. D., & Larese, R. E. (1991). Compaction of lithic sands: experimental results and applications. *AAPG bulletin, 75*(8), 1279–1299. doi:https://doi.org/10.1306/0C9B292F-1710-11D7-8645000102C1865D

Platt, J. (1993). Controls on clay mineral distribution and chemistry in the early Permian Rotliegend of Germany. *Clay Minerals, 28*(3), 393–416. doi:https://doi.org/10.1180/claymin.1993.028.3.05

Popov, Y., Tertychnyi, V., Romushkevich, R., Korobkov, D., & Pohl, J. (2003). Interrelations Between Thermal Conductivity and Other Physical Properties of Rocks: Experimental Data. In H.-J. Kümpel (Ed.), *Thermo-Hydro-Mechanical Coupling in Fractured Rock* (pp. 1137–1161). Basel: Birkhäuser Basel.

Popov, Y. A., Pribnow, D. F., Sass, J. H., Williams, C. F., & Burkhardt, H. (1999). Characterization of rock thermal conductivity by high-resolution optical scanning. *Geothermics, 28*(2), 253–276. doi:https://doi.org/10.1016/S0375-6505(99)00007-3

Porębski, S. J., & Steel, R. J. (2003). Shelf-margin deltas: their stratigraphic significance and relation to deepwater sands. *Earth-Science Reviews, 62*(3-4), 283–326. doi:https://doi.org/10.1016/S0012-8252(02)00161-7

Postma, D., & Brockenhuus-Schack, B. S. (1987). Diagenesis of iron in proglacial sand deposits of late- and post-Weichselian age. *Journal of sedimentary research, 57*(6), 1040–1053. doi:https://doi.org/10.1306/212F8CE2-2B24-11D7-8648000102C1865D

Prajapati, N., Abad Gonzalez, A., Selzer, M., Nestler, B., Busch, B., & Hilgers, C. (2020). Quartz cementation in polycrystalline sandstone: Insights from phase-field simulations. *Journal of Geophysical Research: Solid Earth, 125*(2), e2019JB019137. doi:https://doi.org/10.1029/2019JB019137

Pusch, G., Gaupp, R., & Liermann, N. (2005). Integrated research contributions for screening the tight gas potential in the Rotliegendes formation of North-Germany. *Erdöl, Erdgas, Kohle, 121*(12), 187–193.

Pye, K., Dickson, J. A. D., Schiavon, N., Coleman, M. L., & Cox, M. (1990). Formation of siderite-Mg-calcite-iron sulphide concretions in intertidal marsh and sandflat sediments, north Norfolk, England. *Sedimentology, 37*(2), 325–343. doi:https://doi.org/10.1111/j.1365-3091.1990.tb00962.x

Quandt, D., Busch, B., Fuchs, H., Alvarado de la Barrera, A., Greve, J., & Hilgers, C. (2022b). Petrographical and petrophysical properties of tight siliciclastic rocks from the Ibbenbueren coal mine with regard to mine flooding. *Journal of Applied and Regional Geology, 173*(4), 653–672. doi:https://10.1127/zdgg/2022/0343

Quandt, D., Busch, B., Schmidt, C., & Hilgers, C. (2022a). Diagenesis and controls on reservoir quality of Lower Triassic red bed sandstones (Buntsandstein) from a marginal basin facies, southwest Germany. *Marine and Petroleum Geology*, 105744. doi:https://doi.org/10.1016/j.marpetgeo.2022.105744

Raymond, J. (2018). Colloquium 2016: Assessment of subsurface thermal conductivity for geothermal applications. *Canadian Geotechnical Journal, 55*(9), 1209–1229. doi:https://doi.org/10.1139/cgj-2017-0447

Raymond, J., Sirois, C., Nasr, M., & Malo, M. (2017). Evaluating the geothermal heat pump potential from a thermostratigraphic assessment of rock samples in the St. Lawrence Lowlands, Canada. *Environmental Earth Sciences, 76*(2), 1–15. doi:https://doi.org/10.1007/s12665-017-6398-y

Reinieck, H. E., & Wunderlich, F. (1968). Classification and origin of flaser and lenticular bedding. *Sedimentology, 11*(1-2), 99–104. doi:https://doi.org/10.1111/j.1365-3091.1968.tb00843.x

Rieken, R. (1988). *Lösungs-Zusammensetzung und Migrationsprozesse von Paläo-Fluidsystemen in Sedimentgesteinen des Norddeutschen Beckens:(Mikrothermometrie, Laser-Raman-Spektroskopie und Isotopen-Geochemie)*: Im Selbstverlag der Geologischen Institute der Georg-August-Universität ….

Rische, M., Fischer, K., & Friederich, W. (2023). Induced microseismicity due to rising mine water level in abandoned coal mines in the eastern Ruhr area (Germany). *Journal of Applied and Regional Geology, 173*(4), 551–564. doi:10.1127/zdgg/2023/0346

Ritter, U. (1986). Heat flow during the Carboniferous and Mesozoic of the Northwest German Basin. *Geologische Rundschau, 75*(2), 293–300. doi:https://doi.org/10.1007/BF01820612

Robert, P. (1989). The thermal setting of Carboniferous basins in relation to the Variscan orogeny in Central and Western Europe. *International Journal of Coal Geology, 13*(1-4), 171–206. doi:https://doi.org/10.1016/0166-5162(89)90094-3

Rushing, J. A., Newsham, K. E., & Blasingame, T. A. (2008). *Rock typing—Keys to understanding productivity in tight gas sands.* Paper presented at the SPE Unconventional Resources Conference/Gas Technology Symposium.

Rutter, E. (1976). A discussion on natural strain and geological structure - the kinetics of rock deformation by pressure solution. *Philosophical Transactions of the Royal Society of London. Series A, Mathematical and Physical Sciences, 283*(1312), 203–219. doi:https://doi.org/10.1098/rsta.1976.0079

Rygel, M. C., Fielding, C. R., Frank, T. D., & Birgenheier, L. P. (2008). The magnitude of Late Paleozoic glacioeustatic fluctuations: a synthesis. *Journal of sedimentary research, 78*(8), 500–511. doi:https://doi.org/10.2110/jsr.2008.058

Scherp, A. (1963). Die Petrographie der paläozoischen Sandsteine in der Bohrung Münsterland 1 und ihre Diagenese in Abhängigkeit von der Teufe. *Fortschritte in der Geologie von Rheinland und Westfalen, 11*, 251–282.

Schmidt, C., Busch, B., & Hilgers, C. (2021). Lateral variations of detrital, authigenic and petrophysical properties in an outcrop analog of the fluvial Plattensandstein, Lower Triassic, Central S-Germany. *Journal of Applied and Regional Geology, 172*(4), 541–564. doi:10.1127/zdgg/2020/0234

Schulte, H. (1975). The Ruhr district-heating grid as predecessor of a supra-district heat transmission grid in West Germany. *3 R international : RRR ; Rohre, Rohrleitungsbau, Rohrleitungstransport, 14*(2), 84–87.

Shaw, H. (2006). Clay mineralogy of Carboniferous sandstone reservoirs, onshore and offshore UK. *Clay Minerals, 41*(1), 417–432. doi:https://doi.org/10.1180/0009855064110202

Sindern, S., Meyer, F., Lögering, M., Kolb, J., Vennemann, T., & Schwarzbauer, J. (2012). Fluid evolution at the Variscan front in the vicinity of the Aachen thrust. *International Journal of Earth Sciences, 101*, 87–108. doi:https://doi.org/10.1007/s00531-011-0662-2

Sindern, S., Stanjek, H., Hilgers, C., & Etoundi, Y. (2007). Short-term hydrothermal effects on the 'crystallinities' of illite and chlorite in the footwall of the Aachen-Faille du midi thrust fault : first results of the RWTH-1 drilling project. *Clays and Clay Minerals, 55*(2), 200–212. doi:https://doi.org/10.1346/CCMN.2007.0550209

Stewart, R., & Peselnick, L. (1977). Velocity of compressional waves in dry Franciscan rocks to 8 KB. *Journal of Geophysical Research, 82*(14), 2027–2039. doi:https://doi.org/10.1029/JB082i014p02027

Stewart, R., & Peselnick, L. (1978). Systematic behavior of compressional velocity in Franciscan rocks at high pressure and temperature. *Journal of Geophysical Research: Solid Earth, 83*(B2), 831–839. doi:https://doi.org/10.1029/JB083iB02p00831

Stöckhert, F., Molenda, M., Brenne, S., & Alber, M. (2015). Fracture propagation in sandstone and slate–Laboratory experiments, acoustic emissions and fracture mechanics. *Journal of Rock Mechanics and Geotechnical Engineering, 7*(3), 237–249. doi:https://doi.org/10.1016/j.jrmge.2015.03.011

Strehlau, K. (1990). Facies and genesis of Carboniferous coal seams of Northwest Germany. *International Journal of Coal Geology, 15*(4), 245–292. doi:https://doi.org/10.1016/0166-5162(90)90068-A

Sundborg, Å. (1956). The river Klarälven a study of fluvial processes. *Geografiska annaler, 38*(2-3), 125–316. doi:https://doi.org/10.1080/20014422.1956.11880887

Surdam, R., Jiao, Z., & Heasler, H. (1997). Anomalously pressured gas compartments in Cretaceous rocks of the Laramide basins of Wyoming: A new class of hydrocarbon accumulation. In R. C. Surdam (Ed.), *AAPG Memoir 67: Seals, Traps, and the Petroleum System* (pp. 199–222): American Association of Petroleum Geologists.

Süss, M. P. (1996). *Sedimentologie und Tektonik des Ruhr-Beckens: Sequenzstratigraphische Interpretation und Modellierung eines Vorlandbeckens der Varisciden.* (Dissertation). Rhenish Friedrich Wilhelm University of Bonn, Wiehl Galunder. (Bonner geowissenschaftliche Schriften Band 20)

Süss, M. P. (2005). Zyklotheme, Zyklen und Sequenzen-Steuernde Faktoren der Sedimentation im Ruhr-Becken. In V. Wrede (Ed.), *Stratigraphie von Deutschland V - Das Oberkarbon (Pennsylvanium) in Deutschland* (Vol. 254, pp. 161–168). Frankfurt am Main: Courier Forschungsinstitut Senckenberg.

Süss, M. P., Drozdzewski, G., & Schäfer, A. (2000). Sequenzstratigraphie des kohleführenden Oberkarbons im Ruhr-Becken. In M. Menning, D. Weyer, G. Drozdzewski, & M. P. Süss (Eds.), *Karbon: Zeitskala und Sequenzstratigraphie* (Vol. 156, pp. 45–106). Stuttgart: Bundesanstalt für Geowissenschaften und Rohstoffe und den Geologischen Landesämtern in der Bundesrepublik Deutschland.

Süss, M. P., Drozdzewski, G., & Schäfer, A. (2007). Sedimentary environment dynamics and the formation of coal in the Pennsylvanian Variscan foreland in the Ruhr Basin (Germany, Western Europe). *International Journal of Coal Geology, 69*(4), 267–287. doi:https://doi.org/10.1016/j.coal.2006.05.003

Süss, M. P., Schäfer, A., Drozdzewski, G., & Kasper, F. (2008). Modelling tectonics and sedimentation of the Late Carboniferous Variscan Foreland in Northwestern Europe. *Journal of Applied and Regional Geology, 159*(4), 671–686. doi:https://10.1127/1860-1804/2008/0159-0671

Suttner, L. J., Basu, A., & Mack, G. H. (1981). Climate and the origin of quartz arenites. *Journal of sedimentary research, 51*(4), 1235–1246. doi:https://doi.org/10.1306/212F7E73-2B24-11D7-8648000102C1865D

Tada, R., & Siever, R. (1989). Pressure solution during diagenesis. *Annual Review of Earth and Planetary Sciences, 17*, 89–118. doi:https://doi.org/10.1146/annurev.ea.17.050189.000513

Teichmüller, M. (1986). Coalification and natural gas deposits in northwestern Germany. *Geological Society, London, Special Publications, 23*(1), 101–112. doi:https://doi.org/10.1144/GSL.SP.1986.023.01.07

Teichmüller, M., & Teichmüller, R. (1982). The geological basis of coal formation. In E. Stach, M. T. Mackowsky, M. Teichmüller, G. H. Taylor, D. Chandra, & R. Teichmüller (Eds.), *Stach's textbook of coal petrology* (3 ed., pp. 5–86). Berlin, Stuttgart: Gebrüder Borntraeger.

Thielemann, T., Cramer, B., & Schippers, A. (2004). Coalbed methane in the Ruhr Basin, Germany: a renewable energy resource? *Organic Geochemistry, 35*(11-12), 1537–1549. doi:https://doi.org/10.1016/j.orggeochem.2004.05.004

Tucker, M. E. (2001). *Sedimentary petrology: an introduction to the origin of sedimentary rocks*: John Wiley & Sons.

Udden, J. A. (1914). Mechanical composition of clastic sediments. *Bulletin of the geological society of America, 25*(1), 655–744. doi:https://doi.org/10.1130/GSAB-25-655

Ulmer-Scholle, D. S., Scholle, P. A., Schieber, J., & Raine, R. J. (2014). *A color guide to the petrography of sandstones, siltstones, shales and associated rocks* (Vol. 109): The American Association of Petroleum Geologists.

Van Houten, F. B. (1973). Origin of red beds a review-1961-1972. *Annual Review of Earth and Planetary Sciences, 1*(1), 39–61. doi:https://doi.org/10.1146/annurev.ea.01.050173.000351

Van Yperen, A. E., Holbrook, J. M., Poyatos-Moré, M., & Midtkandal, I. (2019). Coalesced Delta-front Sheet-like Sandstone Bodies from Highly Avulsive Distributary Channels: The Low-accommodation Mesa Rica Sandstone (Dakota Group, New Mexico, U.S.A.). *Journal of sedimentary research, 89*(7), 654–678. doi:https://doi.org/10.2110/jsr.2019.27

Vinken, R. (1988). *The Northwest European Tertiary Basin: Results of the International Geological Correlation-Programme, Project No. 124* (Vol. 100). Stuttgart: Bundesanstalt für Geowissenschaften und Rohstoffe und den Geologischen Landesämtern in der Bundesrepublik Deutschland.

Von Sperber, M., & Hettenberger, R. (1992). *Abschlussbericht Tiefbohrung Haidberg 1 (1992)*. Stratigraphie und Tektonik. DMT-Gesellschaft für Forschung und Prüfung GmbH. Bochum.

Voß, H.-W. (2018). Last Shift for the Mine in the deep North-the Ibbenbüren Coal Mining District looks back on nearly 500 Years of History. *Mining Report, 154*(6), 538–546.

Walderhaug, O. (1996). Kinetic modeling of quartz cementation and porosity loss in deeply buried sandstone reservoirs. *AAPG bulletin, 80*(5), 731–745. doi:https://doi.org/10.1306/64ED88A4-1724-11D7-8645000102C1865D

Walker, T. R. (1967). Formation of red beds in modern and ancient deserts. *Geological Society of America Bulletin, 78*(3), 353–368. doi:https://doi.org/10.1130/0016-7606(1967)78[353:FORBIM]2.0.CO;2

Walker, T. R. (1974). Formation of red beds in moist tropical climates: a hypothesis. *Geological Society of America Bulletin, 85*(4), 633–638. doi:https://doi.org/10.1130/0016-7606(1974)85<633:FORBIM>2.0.CO;2

Wentworth, C. K. (1922). A scale of grade and class terms for clastic sediments. *The Journal of Geology, 30*(5), 377–392. doi:https://doi.org/10.1086/622910

Wilkinson, M., Milliken, K. L., & Haszeldine, R. S. (2001). Systematic destruction of K-feldspar in deeply buried rift and passive margin sandstones. *Journal of the Geological Society, 158*(4), 675–683. doi:https://doi.org/10.1144/jgs.158.4.675

Wimmers, K., & Koehrer, B. (2014). Integration of sedimentology, petrophysics and rock typing as key to understanding a tight gas reservoir. *Oil Gas European Magazine, 40*(4), 196–200.

Wolf, R. (1985). Tiefentektonik des linksniederrheinischen Steinkohlengebietes. In Günter Drozdzewski (Ed.), *Beiträge zur Tiefentektonik westdeutscher Steinkohlenlagerstätten* (pp. 105–167). Krefeld: Geologischer Dienst Nordrhein-Westfalen - Landesbetrieb.

Worden, R. H., & Burley, S. D. (2003). Sandstone Diagenesis: The Evolution of Sand to Stone. In S. D. Burley & R. H. Worden (Eds.), *Sandstone diagenesis: Recent and ancient* (Vol. 4, pp. 3–44). Hoboken: Wiley-Blackwell.

Worden, R. H., & Morad, S. (1999). Clay minerals in sandstones: controls on formation, distribution and evolution. In R. H. Worden & S. Morad (Eds.), *Clay mineral cements in sandstones* (Vol. 34, pp. 1–41). Hoboken: Wiley-Blackwell.

Wrede, V., Drozdzewski, G., & Dvorak, J. (1993). On the structure of the Variscan front in the Eifel-Ardennes area. In R. A. Gayer, R. O. Greiling, & A. K. Vogel (Eds.), *Rhenohercynian and Subvariscan Fold Belts* (Vol. 6, pp. 269–296). Braunschweig: Friedrich Vieweg & Sohn Verlag.

Wrede, V., & Hilden, H. (1988). Geologische Entwicklung. In G. L. Nordrhein-Westfalen (Ed.), *Geologie am Niederrhein* (pp. 7–14). Krefeld.

Wrede, V., & Ribbert, K. (2005). Das Oberkarbon (Silesium) am Nordrand des rechtsrheinischen Schiefergebirges (Ruhrkarbon). In V. Wrede (Ed.), *Stratigraphie von Deutschland V - Das Oberkarbon (Pennsylvanium) in Deutschland* (Vol. 254, pp. 225–254). Frankfurt am Main: Courier-Forschungsinstitut Senckenberg.

Wrede, V., & Zeller, M. (1988). *Geologie der Aachener Steinkohlenlagerstätte (Wurm-und Inde-Revier)*: Geologisches Landesamt Nordrhein-Westfalen.

Wüstefeld, P., Hilse, U., Koehrer, B., Adelmann, D., & Hilgers, C. (2017). Critical evaluation of an Upper Carboniferous tight gas sandstone reservoir analog: Diagenesis and petrophysical aspects. *Marine and Petroleum Geology, 86*, 689–710. doi:https://doi.org/10.1016/j.marpetgeo.2017.05.034

Yin, P., Qi, L., Zhu, Q., Luo, L., Tang, J., Ruan, C., Zhao, L., & Liang, H. (2018). Application of element logging to lithologic identification of key horizons in Sichuan–Chongqing gas provinces. *Natural Gas Industry B, 5*(2), 132–138. doi:https://doi.org/10.1016/j.ngib.2018.01.005

Zhang, C., Liu, S., Phelps, T. J., Cole, D. R., Horita, J., Fortier, S. M., Elless, M., & Valley, J. W. (1997). Physiochemical, mineralogical, and isotopic characterization of magnetite-rich iron oxides formed by thermophilic iron-reducing bacteria. *Geochimica et cosmochimica Acta, 61*(21), 4621–4632. doi:https://doi.org/10.1016/S0016-7037(97)00257-3

Zhang, D., Ranjith, P., & Perera, M. (2016). The brittleness indices used in rock mechanics and their application in shale hydraulic fracturing: A review. *Journal of petroleum science and Engineering, 143*, 158–170. doi:https://doi.org/10.1016/j.petrol.2016.02.011

Zhu, R., Zou, C., Zhang, N., Wang, X., Cheng, R., Liu, L., Zhou, C., & Song, L. (2008). Diagenetic fluids evolution and genetic mechanism of tight sandstone gas reservoirs in Upper Triassic Xujiahe Formation in Sichuan Basin, China. *Science in China Series D: Earth Sciences, 51*, 1340–1353. doi:https://doi.org/10.1007/s11430-008-0102-8

Ziegler, P. A., Cloetingh, S., & van Wees, J.-D. (1995). Dynamics of intra-plate compressional deformation: the Alpine foreland and other examples. *Tectonophysics, 252*(1-4), 7–59. doi:https://doi.org/10.1016/0040-1951(95)00102-6

Zierfuss, H., & Van der Vliet, G. (1956). Laboratory measurements of heat conductivity of sedimentary rocks. *AAPG bulletin, 40*(10), 2475–2488. doi:https://doi.org/10.1306/5CEAE5A4-16BB-11D7-8645000102C1865D

Zou, C., Zhang, G., Tao, S., Hu, S., Li, X., Li, J., Dong, D., & Zhu, R. (2010). Geological features and exploration discoveries of unconventional resources and the petroleum geological theory. *Petroleum Exploration and Development, 37*(2), 641–653. doi:https://doi.org/10.1016/S1876-3804(10)60021-3

Zou, C., Zhu, R., Liu, K., Su, L., Bai, B., Zhang, X., Yuan, X., & Wang, J. (2012). Tight gas sandstone reservoirs in China: characteristics and recognition criteria. *Journal of petroleum science and Engineering, 88-89*, 82–91. doi:https://doi.org/10.1016/j.petrol.2012.02.001

7 Appendix

Appendix A Lithologs well Pelkum-1

Appendix A.1. Litholog of the upper part of well Pelkum-1 (p. 126) containing information about grins size, lithology, sedimentary structures and accessories, the facies and depositional environment. Further it includes the depth of samples with porosity and permeability measurements as well as geochemical data.

Appendix A.1. (continue p. 127).

Appendix A.2. Litholog of the middle part of well Pelkum-1 (p. 128) containing information about grins size, lithology, sedimentary structures and accessories, the facies and depositional environment. Further it includes the depth of samples with porosity and permeability measurements as well as geochemical data.

Appendix A.2. (continue p. 129).

Appendix A.3. Litholog of the lower part of well Pelkum-1 (p. 130) containing information about grins size, lithology, sedimentary structures and accessories, the facies and depositional environment. Further it includes the depth of samples with porosity and permeability measurements as well as geochemical data.

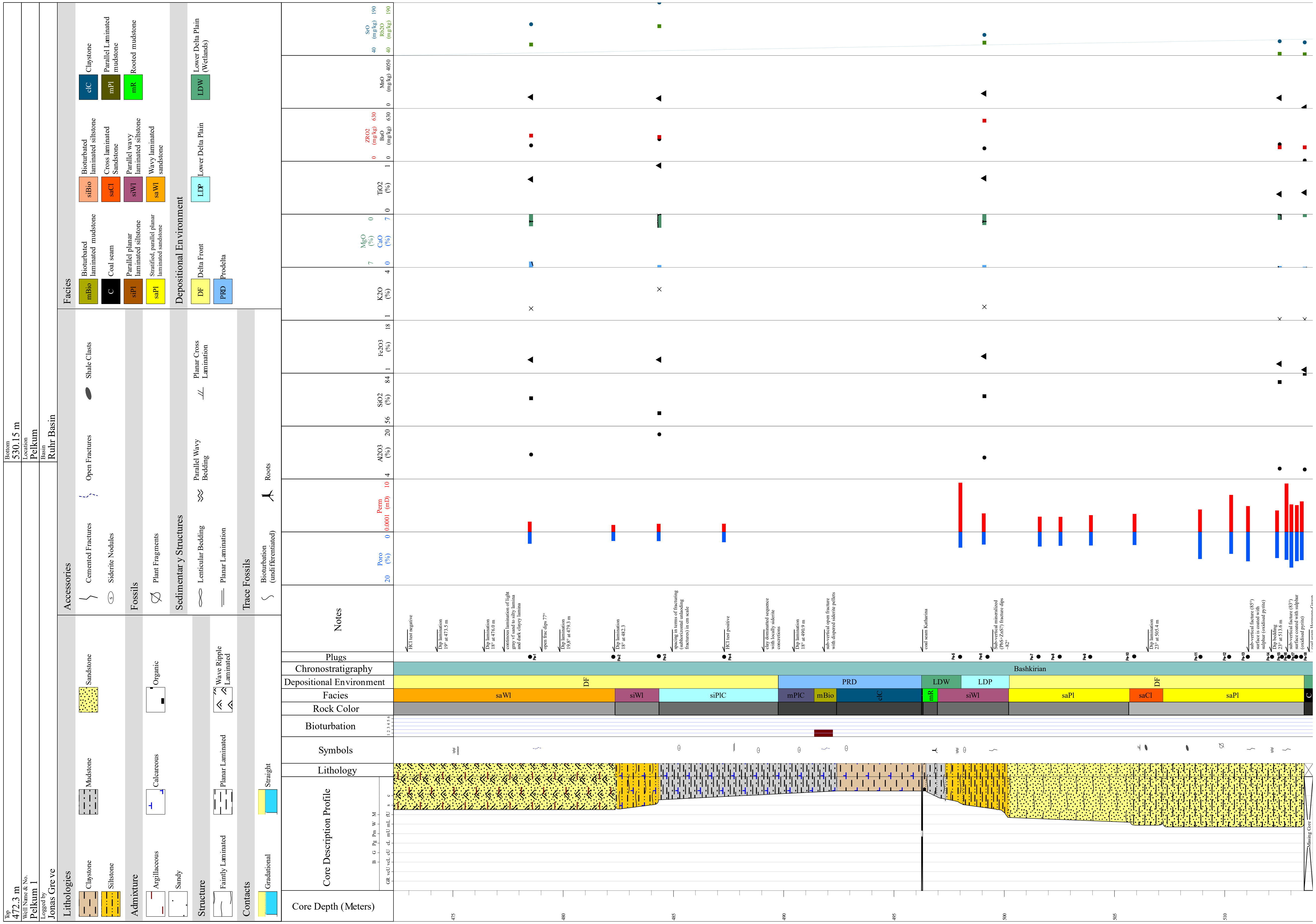

Top 472.3 m
Bottom 530.15 m
Well Name & No. Pelkum 1
Location Pelkum
Logged by Jonas Greve
Basin Ruhr Basin
Lithologies
Admixture
Structure
Contacts
Accessories
Fossils
Sedimentary Structures
Trace Fossils
Facies
Depositional Environment
Notes
Plugs
Chronostratigraphy
Depositional Environment
Facies
Rock Color
Bioturbation
Symbols
Lithology
Core Description Profile
Core Depth (Meters)
Bashkirian

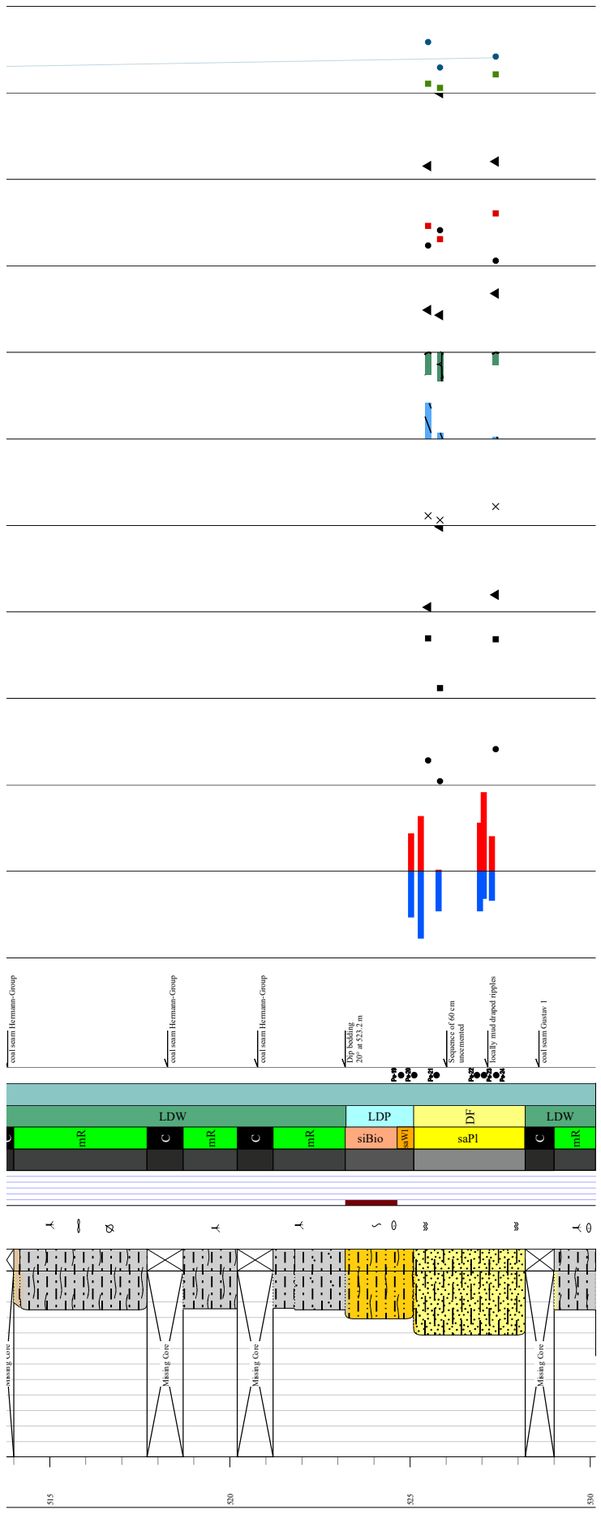
coal seam Hermann-Group
coal seam Hermann-Group
coal seam Hermann-Group
Dip bedding
20° at 1323.2 m
Sequence of 60 cm
uncorrected
locally mud-draped ripples
coal seam Gustav 1
LDW
LDP
DF
LDW
mR
C
mR
C
mR
siBio
saWI
saPl
C
mR
Missing Core
Missing Core
Missing Core
Missing Core
515
520
525
530

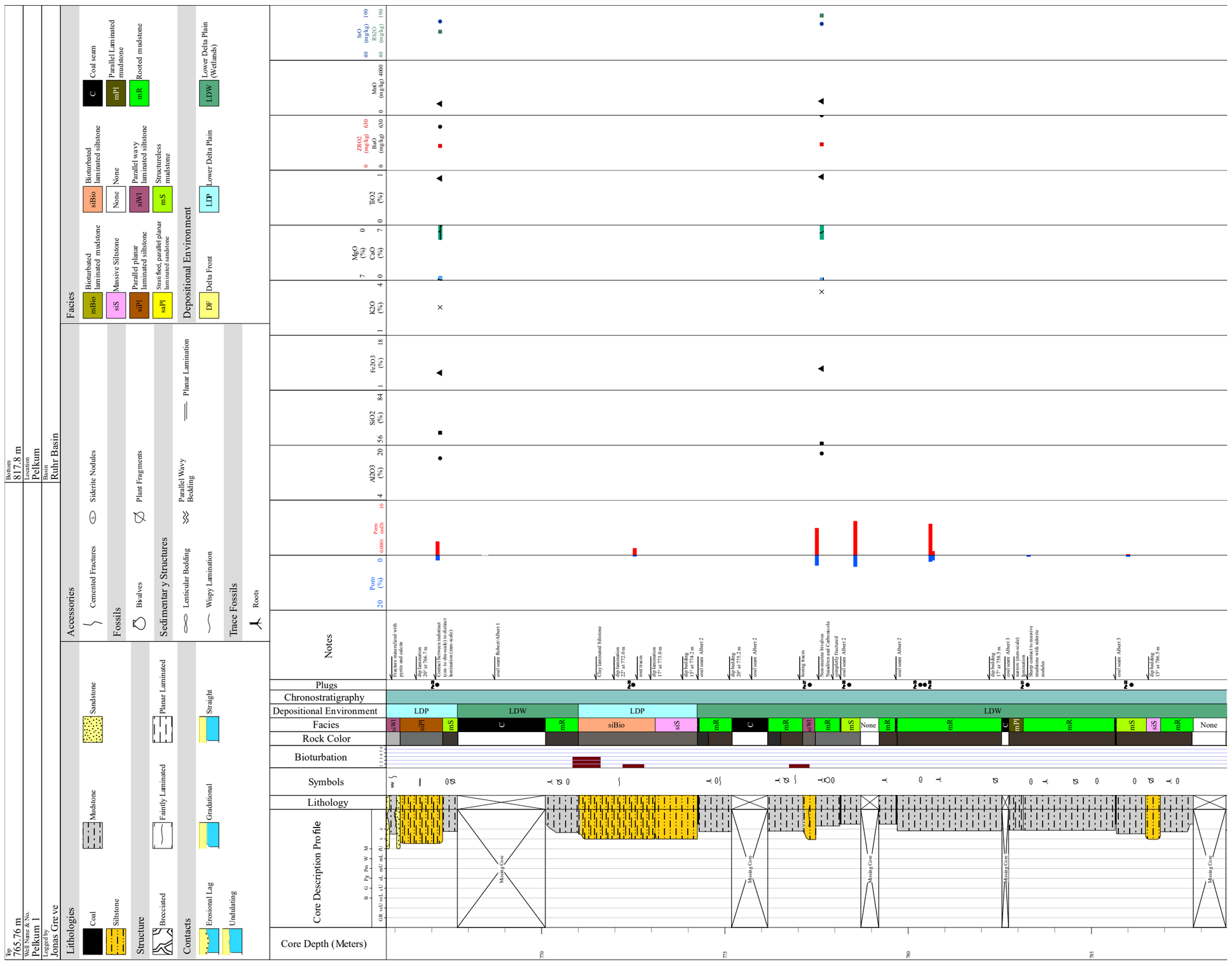
Top
765.76 m
Well Name & No.
Pelkum 1
Logged by
Jonas Greve
Bottom
817.8 m
Location
Pelkum
Basin
Ruhr Basin
Lithologies
Coal
Mudstone
Sandstone
Siltstone
Structure
Brecciated
Fainly Laminated
Planar Laminated
Contacts
Erosional Lag
Gradational
Undulating
Straight
Accessories
Cemented Fractures
Siderite Nodules
Fossils
Bivalves
Plant Fragments
Sedimentary Structures
Lenticular Bedding
Wispy Lamination
Parallel Wavy Bedding
Planar Lamination
Trace Fossils
Roots
Facies
mBio Bioturbated laminated mudstone
siS Massive Siltstone
siPl Parallel planar laminated siltstone
saPl Strati fied, parallel planar laminated sandstone
siBio Bioturbated laminated siltstone
None None
siWl Parallel wavy laminated siltstone
mS Structureless mudstone
C Coal seam
mPl Parallel Laminated mudstone
mR Rooted mudstone
Depositional Environment
DF Delta Front
LDP Lower Delta Plain
LDW Lower Delta Plain (Wetlands)
Core Description Profile
Lithology
Symbols
Bioturbation
Rock Color
Facies
Depositional Environment
Chronostratigraphy
Plugs
Notes
Core Depth (Meters)
Poro (%)
Perm (mD)
Al2O3 (%)
SiO2 (%)
Fe2O3 (%)
K2O (%)
MgO (%)
CaO (%)
TiO2 (%)
ZrO2 (mg/kg)
BaO (mg/kg)
MnO (mg/kg)
SrO (mg/kg)
RbO (mg/kg)
Missing Core

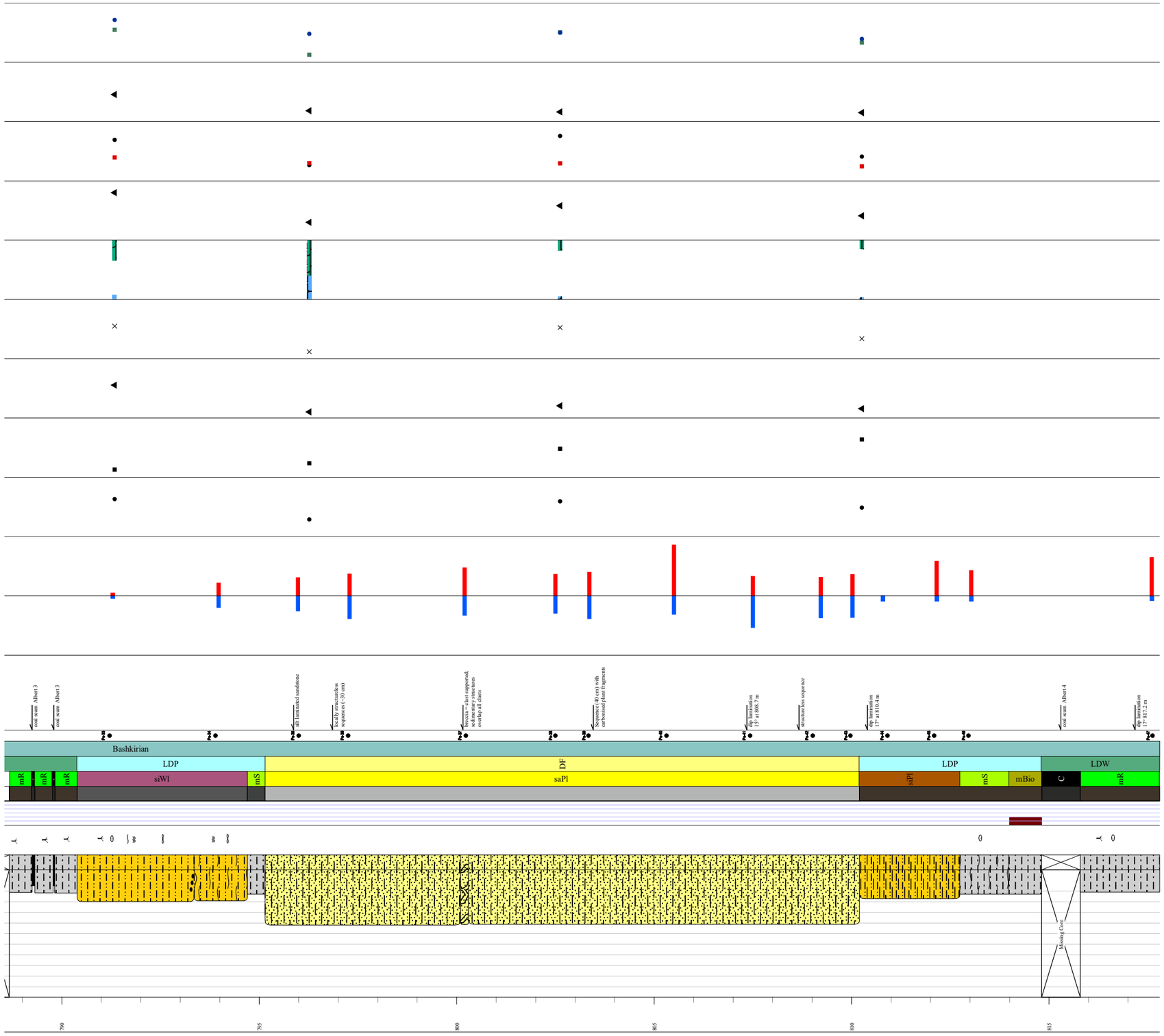
coal seam Albert 3
coal seam Albert 3
silt laminated sandstone
locally structureless sequences (~30 cm)
massive – but supported; sedimentary structures overlap all clasts
Sequences (40 cm) with carbonised plant fragments
dip lamination 15° at 808.7 m
structureless sequence
dip lamination 17° at 810.4 m
coal seam Albert 4
dip lamination 15° 817.2 m
Bashkirian
LDP
DF
LDP
LDW
mR
mR
mR
siWl
mS
saPl
siPl
mS
mBio
C
mR
Missing Core
790
795
800
805
810
815

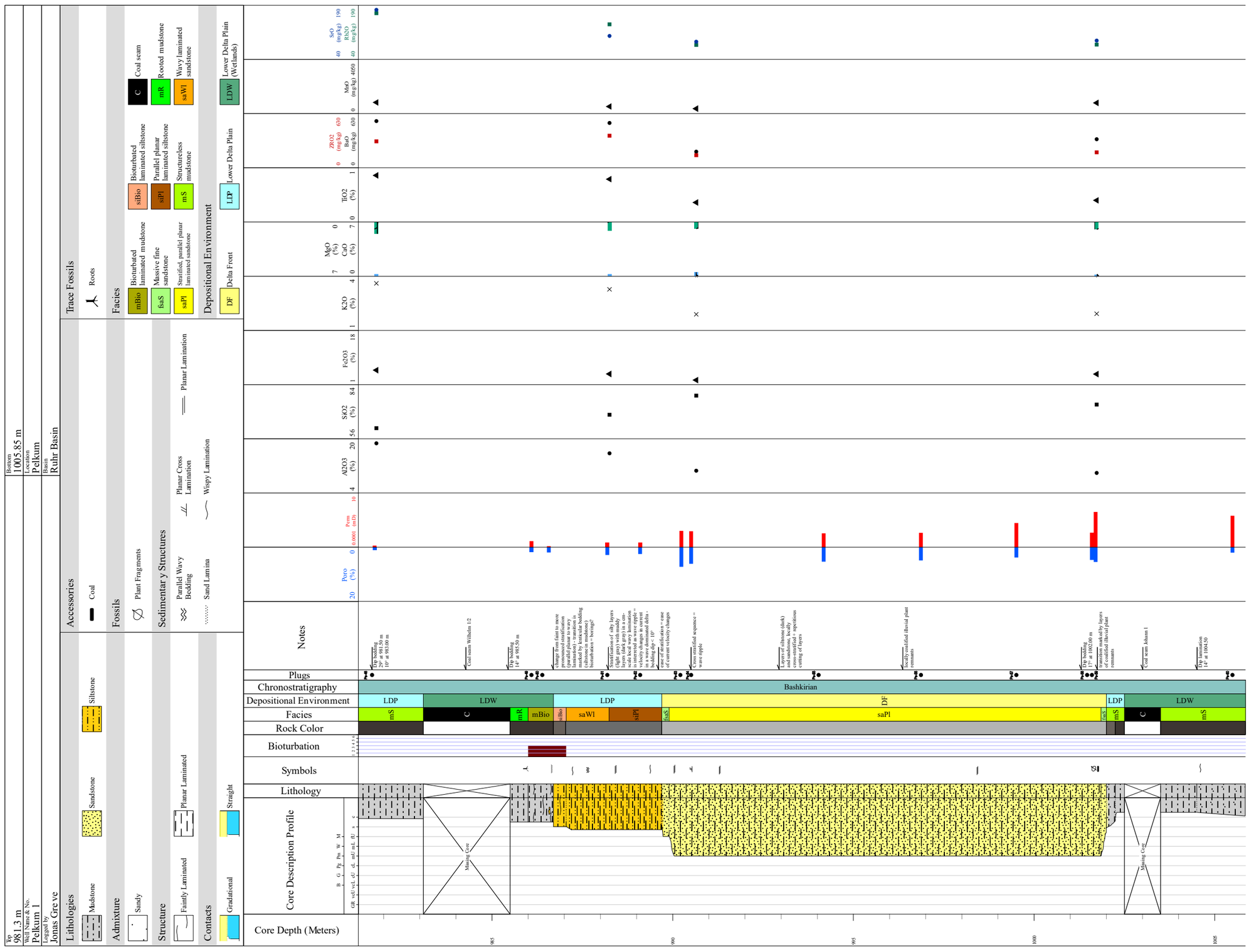
Top
981.3 m
Well Name & No.
Pelkum 1
Logged by
Jonas Greve
Bottom
1005.85 m
Location
Pelkum
Basin
Ruhr Basin
Lithologies
Mudstone
Sandstone
Siltstone
Admixture
Sandy
Structure
Faintly Laminated
Planar Laminated
Contacts
Gradational
Straight
Trace Fossils
Roots
Facies
mBio Bioturbated laminated mudstone
fsaS Massive fine sandstone
saPl Stratified, parallel planar laminated sandstone
siBio Bioturbated laminated siltstone
siPl Parallel planar laminated siltstone
mS Structureless mudstone
Depositional Environment
DF Delta Front
LDP Lower Delta Plain
LDW Lower Delta Plain (Wetlands)
Accessories
Coal
Fossils
Plant Fragments
Sedimentary Structures
Parallel Wavy Bedding
Sand Lamina
Planar Cross Lamination
Planar Lamination
Wispy Lamination
Core Depth (Meters)
Core Description Profile
Lithology
Symbols
Bioturbation
Rock Color
Facies
Depositional Environment
Chronostratigraphy
Plugs
Notes
Poro (%)
Perm (mD)
Al2O3 (%)
SiO2 (%)
Fe2O3 (%)
K2O (%)
MgO (%)
CaO (%)
TiO2 (%)
ZrO2 (mg/kg)
BaO (mg/kg)
MnO (mg/kg)
SrO (mg/kg)
B2O3 (mg/kg)
Bashkirian
LDP
LDW
DF
mS
C
mR
mBio
siBio
saWl
siPl
fsaS
saPl
Missing Core
Missing Core
985
990
995
1000
1005

Appendix B Lithologs of well Bork-1

Appendix B.1. Litholog of the upper part of well Bork-1 (p. 132) containing information about grins size, lithology, sedimentary structures and accessories, the facies and depositional environment. Further it includes the depth of samples with porosity and permeability measurements as well as geochemical data.

Appendix B.2. Litholog of the middle part of well Bork-1 (p. 133) containing information about grins size, lithology, sedimentary structures and accessories, the facies and depositional environment. Further it includes the depth of samples with porosity and permeability measurements as well as geochemical data.

Appendix B.3. Litholog of the lower part of well Bork-1 (p. 134) containing information about grins size, lithology, sedimentary structures and accessories, the facies and depositional environment. Further it includes the depth of samples with porosity and permeability measurements as well as geochemical data.

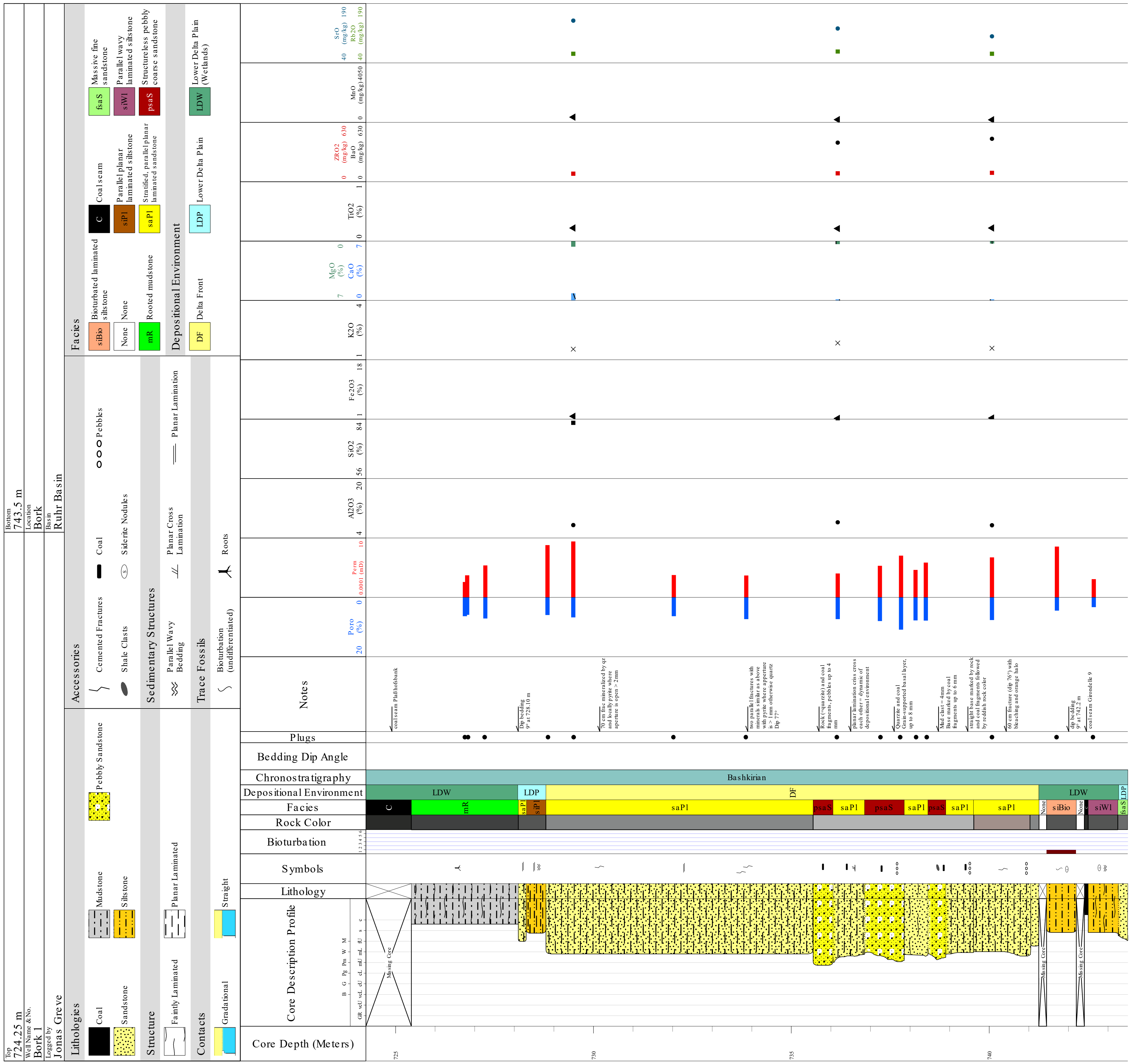
Top
724.25 m
Well Name & No.
Bork 1
Logged by
Jonas Greve
Bottom
743.5 m
Location
Bork
Basin
Ruhr Basin
Lithologies
Coal
Sandstone
Mudstone
Siltstone
Pebbly Sandstone
Structure
Faintly Laminated
Planar Laminated
Contacts
Gradational
Straight
Accessories
Cemented Fractures
Shale Clasts
Coal
Siderite Nodules
Pebbles
Sedimentary Structures
Parallel Wavy Bedding
Planar Cross Lamination
Planar Lamination
Trace Fossils
Bioturbation (undifferentiated)
Roots
Facies
Bioturbated laminated siltstone
None
Rooted mudstone
Coal seam
Parallel planar laminated siltstone
Stratified, parallel planar laminated sandstone
Massive fine sandstone
Parallel wavy laminated siltstone
Structureless pebbly coarse sandstone
Depositional Environment
Delta Front
Lower Delta Plain
Lower Delta Plain (Wetlands)
Core Depth (Meters)
Core Description Profile
Lithology
Symbols
Bioturbation
Rock Color
Facies
Depositional Environment
Chronostratigraphy
Bedding Dip Angle
Plugs
Notes
Poro (%)
Perm
Al2O3 (%)
SiO2 (%)
Fe2O3 (%)
K2O (%)
MgO (%)
CaO (%)
TiO2 (%)
ZRO2 (mg/kg)
BaO (mg/kg)
MnO (mg/kg)
SrO (mg/kg)
Rb2O (mg/kg)
Bashkirian
LDW
LDP
DF
Missing Core
725
730
735
740

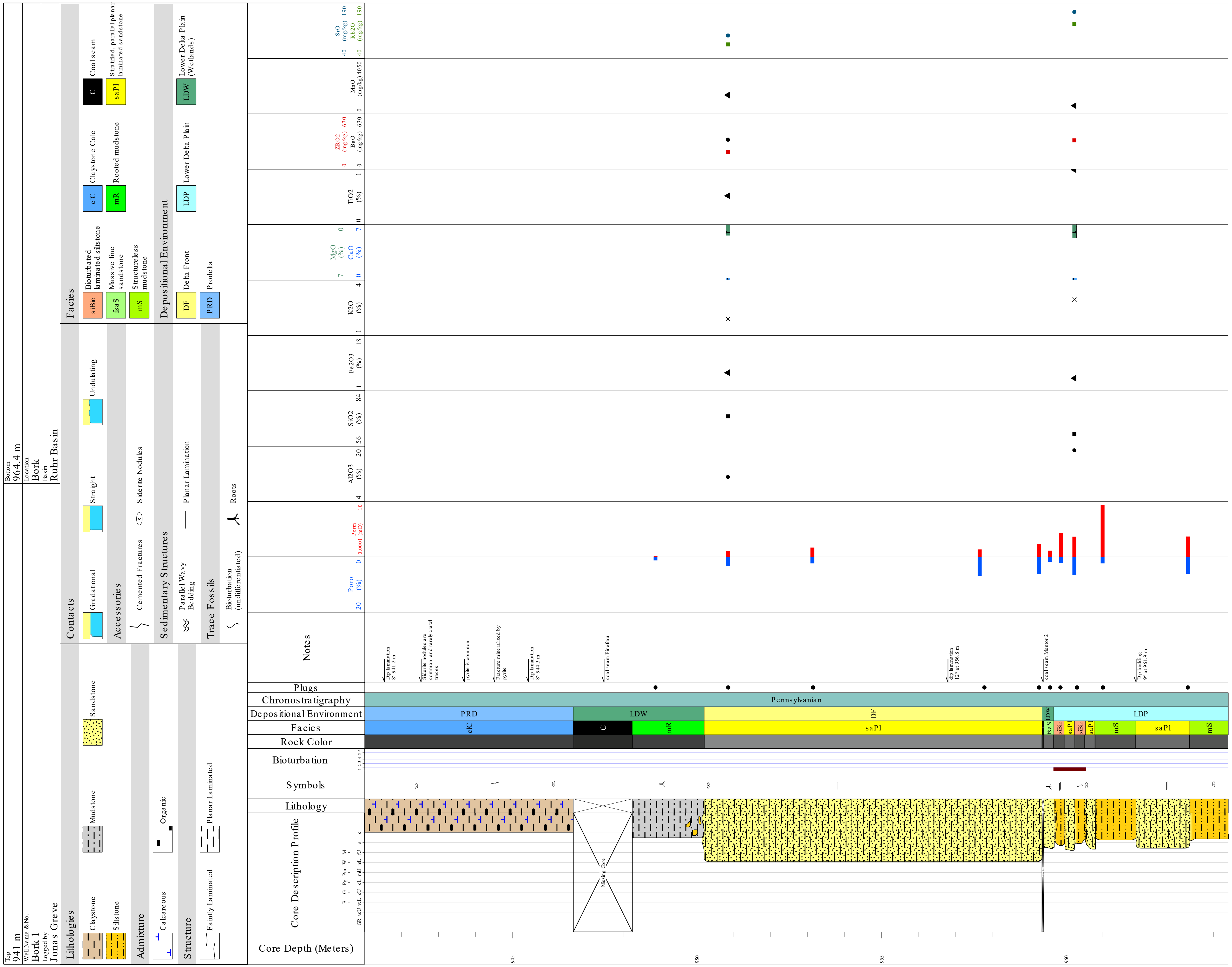
Plugs
Chronostratigraphy
Depositional Environment
Facies
Rock Color
Bioturbation
Symbols
Lithology
Core Depth (Meters)
Pennsylvanian
PRD
LDW
DF
LDP
saPl
mS

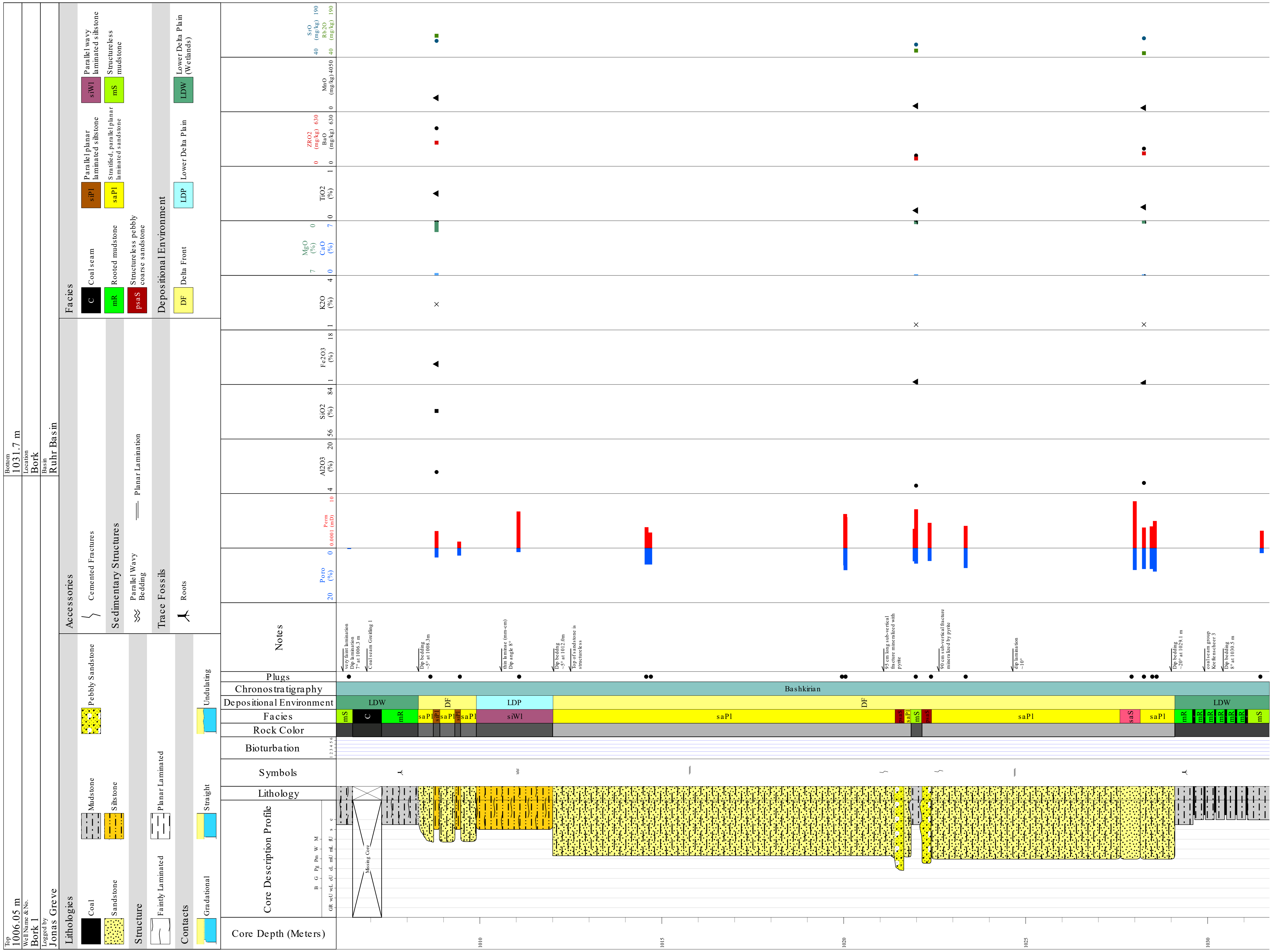
Top
1006.05 m
Well Name & No.
Bork 1
Logged by
Jonas Greve
Bottom
1031.7 m
Location
Bork
Basin
Ruhr Basin
Lithologies
Coal
Sandstone
Mudstone
Siltstone
Pebbly Sandstone
Structure
Faintly Laminated
Planar Laminated
Contacts
Gradational
Straight
Undulating
Accessories
Cemented Fractures
Sedimentary Structures
Parallel Wavy Bedding
Planar Lamination
Trace Fossils
Roots
Facies
Coal seam
Rooted mudstone
Structureless pebbly coarse sandstone
Parallel planar laminated siltstone
Stratified, parallel planar laminated sandstone
Parallel wavy laminated siltstone
Structureless mudstone
Depositional Environment
Delta Front
Lower Delta Plain
Lower Delta Plain (Wetlands)
Notes
Plugs
Chronostratigraphy
Depositional Environment
Facies
Rock Color
Bioturbation
Symbols
Lithology
Core Description Profile
Core Depth (Meters)
Bashkirian
LDW
DF
LDP
saPl
siWl
mS
mR
saS
Missing Core
1010
1015
1020
1025
1030
Poro (%)
Perm (mD)
Al2O3 (%)
SiO2 (%)
Fe2O3 (%)
K2O (%)
MgO (%)
CaO (%)
TiO2 (%)
ZRO2 (mg/kg)
BaO (mg/kg)
MnO (mg/kg)
SrO (mg/kg)
Rb2O (mg/kg)

Appendix C Lithologs of well Haidberg-1

Appendix C.1. Litholog of the upper part of well Haidberg-1 (p. 136) containing information about grins size, lithology, sedimentary structures and accessories, the facies and depositional environment. Further it includes the depth of samples with porosity and permeability measurements as well as geochemical data

Appendix C.2. Litholog of the middle part of well Haidberg-1 (p. 137) containing information about grins size, lithology, sedimentary structures and accessories, the facies and depositional environment. Further it includes the depth of samples with porosity and permeability measurements as well as geochemical data.

Appendix C.3. Litholog of the lower part of well Haidberg-1 (p. 138) containing information about grins size, lithology, sedimentary structures and accessories, the facies and depositional environment. Further it includes the depth of samples with porosity and permeability measurements as well as geochemical data.

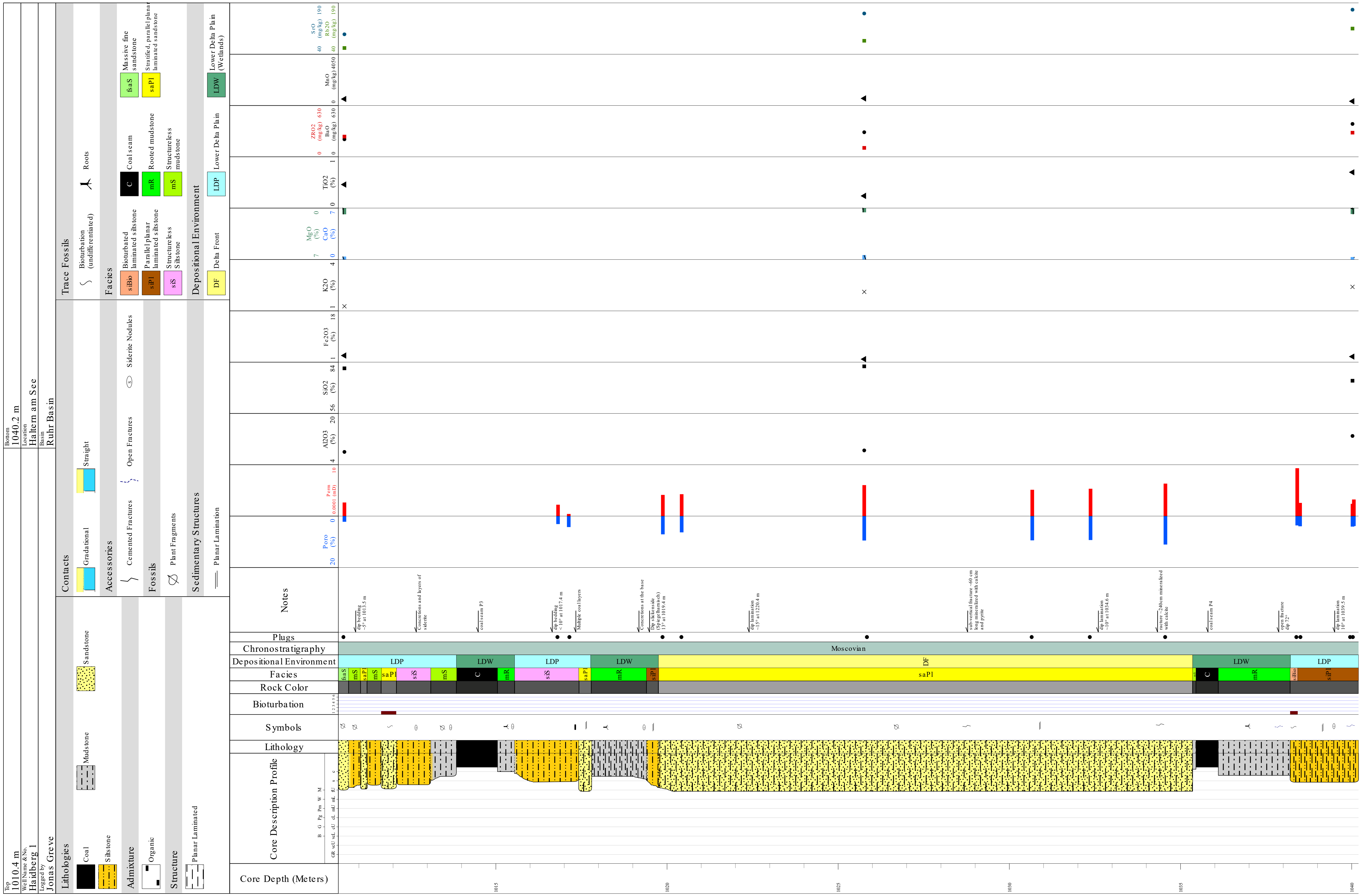
Top
1010.4 m
Bottom
1040.2 m
Well Name & No.
Haidberg 1
Location
Haltern am See
Basin
Ruhr Basin
Logged by
Jonas Greve
Lithologies
Coal
Siltstone
Mudstone
Sandstone
Admixture
Organic
Structure
Planar Laminated
Contacts
Gradational
Straight
Accessories
Cemented Fractures
Open Fractures
Siderite Nodules
Fossils
Plant Fragments
Sedimentary Structures
Planar Lamination
Trace Fossils
Bioturbation (undifferentiated)
Roots
Facies
siBio Bioturbated laminated siltstone
siPl Parallel planar laminated siltstone
siS Structureless Siltstone
C Coal seam
mR Rooted mudstone
mS Structureless mudstone
fsaS Massive fine sandstone
saPl Stratified, parallel planar laminated sandstone
Depositional Environment
DF Delta Front
LDP Lower Delta Plain
LDW Lower Delta Plain (Wetlands)
Notes
Plugs
Chronostratigraphy
Depositional Environment
Facies
Rock Color
Bioturbation
Symbols
Lithology
Core Description Profile
Core Depth (Meters)
Moscovian
Poro (%)
Perm (mD)
Al2O3 (%)
SiO2 (%)
Fe2O3 (%)
K2O (%)
MgO (%)
CaO (%)
TiO2 (%)
ZRO2 (mg/kg)
BaO (mg/kg)
MnO (mg/kg)
SrO (mg/kg)
Rb2O (mg/kg)
1015
1020
1025
1030
1035
1040

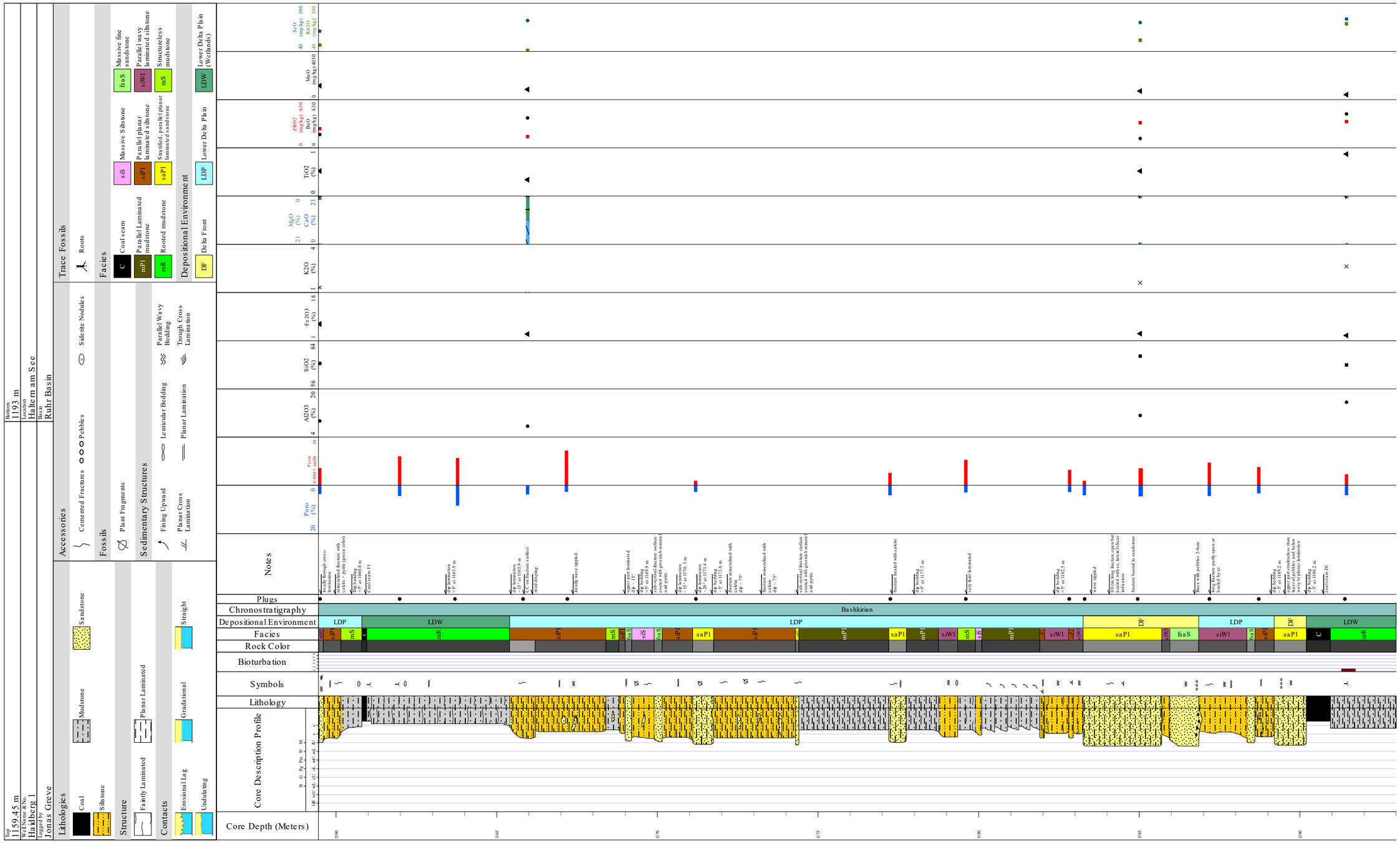
Bottom
1193 m
Location
Hallenham See
Base
Ruhr Basin
Trace Fossils
Pebbles
Siderite Nodules
Roots
Facies
C Coal seam
mPl Parallel Laminated mudstone
mR Rooted mudstone
siS Massive Siltstone
siPl Parallel planar laminated siltstone
saPl Stratified, parallel planar laminated sandstone
fsaS Massive fine sandstone
siWl Parallel wavy laminated siltstone
mS Structureless mudstone
Depositional Environment
DF Delta Front
LDP Lower Delta Plain
LDW Lower Delta Plain (Wetlands)
Accessories
Cemented Fractures
Fossils
Plant Fragments
Sedimentary Structures
Lenticular Bedding
Parallel Wavy Bedding
Planar Lamination
Trough Cross Lamination
Fining Upward
Planar Cross Lamination
Top
1159.45 m
Well Name & No.
Hallberg 1
Logged by
Jonas Greve
Lithologies
Coal
Mudstone
Sandstone
Siltstone
Structure
Fainly laminated
Planar Laminated
Contacts
Erosional Lag
Gradational
Straight
Undulating
Notes
Plugs
Chronostratigraphy
Bashkirian
Depositional Environment
Facies
Rock Color
Bioturbation
Symbols
Lithology
Core Description Profile
Core Depth (Meters)
Poro (%)
Perm (Klinkenberg) (mD)
Al2O3 (%)
SiO2 (%)
Fe2O3 (%)
K2O (%)
MgO (%)
CaO (%)
TiO2 (%)
ZrO2 (mg/kg)
BaO (mg/kg)
MnO (mg/kg)
S+O (mg/kg)
Rb2O (mg/kg)

Top	Bottom
1281.5 m	1305.9 m
Well Name & No.	**Location**
Haidberg 1	Haltern am See
Logged by	**Basin**
Jonas Greve	Ruhr Basin

Lithologies

Coal · Mudstone · Sandstone · Siltstone

Structure

Planar Laminated

Contacts

Gradational · Straight

Accessories

Cemented Fractures · Siderite Nodules

Fossils

Plant Fragments

Sedimentary Structures

Fining Upward · Lenticular Bedding · Planar Cross Lamination · Planar Lamination

Trace Fossils

Roots

Facies

C	Coal seam	siS	Massive Siltstone	mPl	Parallel Laminated mudstone
siPl	Parallel planar laminated siltstone	mR	Rooted mudstone	saPl	Stratified, parallel planar laminated sandstone
mS	Structureless mudstone				

Depositional Environment

DF Delta Front · LDP Lower Delta Plain · LDW Lower Delta Plain (Wetlands)

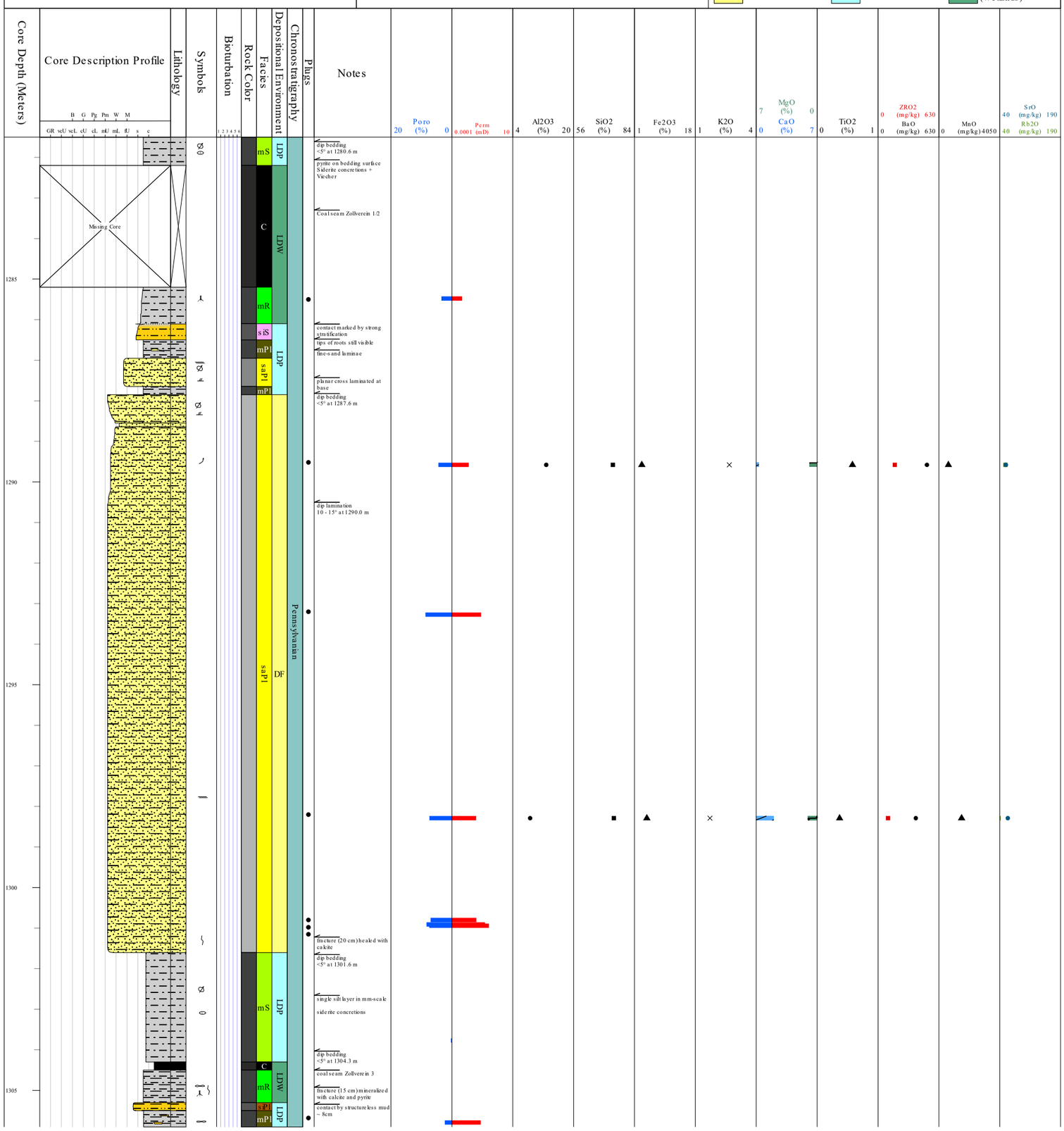

Appendix D Data tables

Table D.1. Table (p. 140-141) with supplementary point-counting, petrographic and petrophysical data table for well Pelum-1. Abbreviations in order of appearance. RF: rock fragment, PRF: Plutonic rock fragment, VRF: Volcanic rock fragment, sid: siderite, carbo: carbonate, rp: replaces, Fe-OH: Iron hydroxide, poro: Porosity, IGV: intergranular volume, COPL: Compactional porosity loss, CEPL: Cementational porosity loss, Recon: Reconstructed.

Table D.2. Table (p. 142-143) with supplementary point-counting, petrographic and petrophysical data table for well Bork-1. Abbreviations in order of appearance. RF: rock fragment, PRF: Plutonic rock fragment, VRF: Volcanic rock fragment, sid: siderite, carbo: carbonate, rp: replaces, Fe-OH: Iron hydroxide, poro: Porosity, IGV: intergranular volume, COPL: Compactional porosity loss, CEPL: Cementational porosity loss, Recon: Reconstructed.

Table D.3. Table (p. 144-145) with supplementary point-counting, petrographic and petrophysical data table for well Haidberg-1. Abbreviations in order of appearance. RF: rock fragment, PRF: Plutonic rock fragment, VRF: Volcanic rock fragment, sid: siderite, carbo: carbonate, rp: replaces, Fe-OH: Iron hydroxide, poro: Porosity, IGV: intergranular volume, COPL: Compactional porosity loss, CEPL: Cementational porosity loss, Recon: Reconstructed.

	Sample No.	Core Depth (m)	Stage	Formation	Grain size	Mean GS (ϕ)	Mean GS (mm)	Sorting	Sorting (ϕ)	Sorting (mm)	Skewness	Facies	Facies Association	Helium Porosity (%)	Permeability horizontal (mD)	Comments Plug	Quartz mono	Quartz poly	Plag	K-fsp	PRF	VRF	SRF	Shale	Phyllite	Shist	Quartzite	MRF	Chert	Org. matter	Carbonatic rip-up	Mica	Zirkon	Turmaline	Clay rip-up clast	Opaque	Pyrite	Biotite	Chlorite	Altered MRF	Fe-OH inter
Pelkum-1	Pe-1	478.48	Westph. A	Upper Bochum	very fine sand	3.9	0.07	moderately sorted	0.8	0.6	-0.18	saWl	Delta front	4.46	0.0010	minor outbreak	9.7	45.7	0.7	1.0	1.0	2.7	2.7	7.7	3.0	3.7	1.3	0.0	0.7	0.0	14.3	1.3	0.3	0.0	0.0	0.0	0.0	0.0	0.0	0.0	1.3
	Pe-2	482.27	Westph. A	Upper Bochum	coarse silt	4.8	0.04	moderately sorted	0.7	0.6	0.02	siWlC	Prodelta	3.38	0.0005	healed fracture	11.7	34.3	0.7	1.0	0.0	0.0	0.0	19.0	3.7	3.0	0.0	0.0	0.3	0.0	17.7	5.3	0.7	0.0	0.0	0.3	0.0	0.0	0.3	0.0	1.7
	Pe-3	484.33	Westph. A	Upper Bochum								siPlC	Prodelta	3.43	0.0006	outbreak																										
	Pe-4	487.29	Westph. A	Upper Bochum								mPlC	Prodelta	3.84	0.0006	massiv																										
	Pe-5	498.01	Westph. A	Upper Bochum	coarse silt	4.1	0.06	moderately sorted	0.9	0.5	-0.25	siWl	Wetlands	5.90	4.4320	cracks	6.0	17.3	0.3	0.3	0.7	0.0	1.0	2.7	0.3	2.0	0.7	0.0	0.0	0.0	65.0	0.7	0.0	0.0	0.0	0.7	0.0	0.0	0.0	0.0	0.0
	Pe-6	499.07	Westph. A	Upper Bochum	very fine sand	3.5	0.09	moderately sorted	0.7	0.6	0.10	siWlBio	Wetlands	4.73	0.0056	little outbreak	12.0	37.0	1.3	2.7	1.3	1.0	0.7	23.7	1.0	1.7	1.3	0.3	0.0	0.0	12.3	1.0	0.0	0.0	0.0	0.3	0.0	0.0	0.0	0.0	0.0
	Pe-7	501.61	Westph. A	Upper Bochum	coarse silt	4.2	0.06	moderately sorted	0.9	0.5	-0.21	saWl	Lower delta plain	5.50	0.0028	massiv	9.7	31.3	0.3	1.3	0.7	0.0	0.3	46.7	1.0	0.7	0.0	0.0	0.0	0.0	2.0	2.7	0.3	0.0	0.0	2.0	0.0	0.0	0.0	0.0	0.0
	Pe-8	502.55	Westph. A	Upper Bochum	very fine sand	3.9	0.07	moderately well sorted	0.7	0.6	-0.12	saWl	Lower delta plain	5.23	0.0027	massiv	9.3	45.7	0.0	4.0	1.3	0.3	0.3	26.0	2.0	2.0	1.3	0.0	0.0	0.0	4.0	0.7	0.7	0.7	0.0	0.0	0.0	0.0	0.3	0.0	0.3
	Pe-9	503.93	Westph. A	Upper Bochum								saWl	Lower delta plain	5.07	0.0039	massiv																										
	Pe-10	505.91	Westph. A	Upper Bochum	very fine sand	3.2	0.11	moderately well sorted	0.7	0.6	-0.26	saWl	Lower delta plain	4.90	0.0051	massiv	9.3	40.0	1.3	3.3	1.0	0.3	1.0	26.0	2.0	0.7	2.7	0.0	0.3	0.0	6.0	1.7	0.0	0.3	0.0	0.0	0.0	0.0	0.0	0.0	0.3
	Pe-11	508.88	Westph. A	Upper Bochum	fine sand	2.6	0.17	moderately well sorted	0.5	0.7	-0.27	saPl	Delta front	10.20	0.0130	massiv	15.7	32.0	0.0	0.7	0.0	1.0	2.0	9.3	1.0	5.7	0.0	0.3	2.3	0.0	7.0	1.3	0.0	0.0	0.0	0.0	0.0	0.0	0.0	3.0	0.7
	Pe-12	510.29	Westph. A	Upper Bochum	fine sand	2.8	0.14	moderately well sorted	0.7	0.6	-0.42	saPl	Delta front	8.25	0.3163	organic-rich layers	9.0	29.7	0.7	4.3	2.0	2.0	1.0	18.3	0.7	2.0	1.7	0.0	0.7	0.7	12.7	0.7	0.3	0.0	0.0	0.0	0.0	0.0	0.0	0.0	2.3
	Pe-13	511.05	Westph. A	Upper Bochum								saPl	Delta front	11.08	0.0280	massiv																										
	Pe-14	512.37	Westph. A	Upper Bochum	fine sand	2.4	0.19	moderately well sorted	0.6	0.6	-0.30	saPl	Delta front	9.86	0.0107	massiv	8.3	32.3	0.0	6.7	3.7	1.3	4.3	18.0	0.7	1.3	3.0	0.0	0.7	0.0	7.3	0.7	0.0	0.0	0.0	0.7	0.0	0.0	0.3	0.0	0.0
	Pe-15	512.80	Westph. A	Upper Bochum	fine sand	2.8	0.15	moderately sorted	0.8	0.6	-0.22	saPl	Delta front	10.50	3.7441	central coal layer	14.0	26.7	1.7	1.7	0.3	2.0	9.0	12.0	1.3	5.7	3.0	0.7	0.0	0.0	4.0	1.0	0.0	0.0	0.0	0.0	0.0	0.0	0.0	1.3	2.3
	Pe-16	513.02	Westph. A	Upper Bochum	fine sand	2.3	0.21	well sorted	0.5	0.7	-0.28	saPl	Delta front	13.43	0.0407	marginal healed fracture	8.7	38.7	1.0	1.3	0.3	3.7	4.3	14.7	1.3	3.3	1.3	0.7	0.7	0.0	0.3	0.7	0.0	0.0	0.0	0.3	0.0	0.0	0.0	3.7	0.0
	Pe-17	513.27	Westph. A	Upper Bochum	fine sand	2.6	0.16	moderately well sorted	0.7	0.6	-0.38	saPl	Delta front	11.02	0.0340	massiv	13.3	30.7	0.0	0.3	0.0	1.3	6.0	22.0	1.3	3.0	2.3	0.7	0.3	0.3	3.0	2.0	0.0	0.0	0.0	0.3	0.0	0.0	0.0	2.7	0.0
	Pe-18	513.49	Westph. A	Upper Bochum	fine sand	2.4	0.19	moderately well sorted	0.5	0.7	-0.24	saPl	Delta front	10.65	0.0779	central healed fracture	14.0	35.0	0.3	4.3	0.7	1.7	2.3	13.3	0.3	3.0	2.3	0.0	0.0	0.0	5.0	0.7	0.3	0.0	0.0	1.0	0.0	0.0	0.0	0.3	0.0
	Pe-19	525.03	Westph. A	Upper Bochum	very fine sand	4.0	0.06	moderately well sorted	0.7	0.6	-0.17	saWl	Lower delta plain	10.69	0.0155	-	12.7	23.3	0.0	2.3	0.0	1.3	0.3	15.0	1.7	2.0	0.0	0.0	1.3	0.0	23.0	3.7	0.0	0.0	1.7	0.7	0.0	0.0	0.3	0.0	0.7
	Pe-20	525.30	Westph. A	Upper Bochum	very fine sand	3.8	0.07	moderately well sorted	0.7	0.6	-0.27	saWl	Lower delta plain	15.56	0.1571	massiv	25.3	25.0	0.0	0.0	0.0	2.0	1.0	4.0	0.3	1.7	0.0	0.0	0.3	0.0	0.3	1.3	0.0	0.0	0.0	0.0	0.0	0.0	0.0	3.7	0.0
	Pe-21	525.79	Westph. A	Upper Bochum	coarse silt	4.2	0.05	moderately sorted	0.8	0.6	-0.03	saPl	Delta front	9.26	0.0001	massiv	16.0	17.7	0.0	0.0	0.0	0.3	0.7	2.3	0.3	0.7	0.3	0.0	0.7	0.3	48.3	0.3	0.3	0.3	0.0	0.3	0.0	0.0	0.0	0.3	0.0
	Pe-22	526.80	Westph. A	Upper Bochum								saPl	Delta front	9.27	0.0649	single organic-rich layer																										
	Pe-23	527.05	Westph. A	Upper Bochum	very fine sand	3.6	0.08	moderately well sorted	0.7	0.6	-0.12	saPl	Delta front	6.39	3.7445	discontinous coal flakes	9.3	37.3	0.3	1.3	0.0	1.3	1.7	15.0	2.0	2.7	1.7	0.0	0.7	1.7	15.7	2.0	0.0	0.0	0.0	0.3	0.0	0.0	0.0	0.7	2.0
	Pe-24	527.27	Westph. A	Upper Bochum	very fine sand	3.3	0.10	moderately sorted	0.9	0.5	-0.43	saWl	Lower delta plain	6.79	0.0106	tiny (<mm) coal flakes	9.7	16.7	0.0	0.7	0.3	0.0	1.3	5.7	1.0	2.3	0.0	0.0	1.0	0.0	54.7	1.3	0.0	0.3	0.3	0.0	0.0	0.0	0.0	0.3	1.3
	Pe-25	761.16	Westph. A	Middle Bochum								siPl	Lower delta plain	1.83	0.0018	massiv																										
	Pe-26	772.54	Westph. A	Middle Bochum								siPl	Lower delta plain	0.54	0.0004	minor outbreaks																										
	Pe-27	777.51	Westph. A	Middle Bochum	medium silt	5.4	0.02	moderately sorted	1.0	0.5	0.08	siWl	Lower delta plain	3.83	0.0294	major outbreaks	11.3	28.0	0.3	0.3	0.0	0.0	1.3	23.3	2.0	3.0	0.3	0.0	0.0	0.3	18.0	5.7	0.3	0.0	2.3	0.0	0.0	0.0	0.3	0.0	1.3
	Pe-28	778.56	Westph. A	Middle Bochum								mR	Wetlands	4.21	0.1265	minor outbreaks																										
	Pe-29	780.61	Westph. A	Middle Bochum								mR	Wetlands	2.40	0.0719	outbreak																										
	Pe-30	780.67	Westph. A	Middle Bochum								mR	Wetlands	1.87	0.0002	outbreak																										
	Pe-31	783.29	Westph. A	Middle Bochum								mR	Wetlands	0.48	0.0001	outbreak - healed fractures																										
	Pe-32	768.44	Westph. A	Middle Bochum								mR	Wetlands	1.40	0.0003	massiv																										
	Pe-33	791.29	Westph. A	Middle Bochum								siWl	Wetlands	0.94	0.0002	massiv																										
	Pe-34	793.97	Westph. A	Middle Bochum	very fine sand	3.2	0.11	moderately sorted	0.7	0.6	0.00	siWl	Lower delta plain	4.06	0.0013	<mm discontinous coal flakes	16.3	15.3	3.7	4.3	1.0	0.0	2.0	11.3	8.3	7.3	1.3	0.7	0.0	0.0	15.0	5.3	0.3	0.0	0.3	0.0	0.0	0.0	1.3	0.7	0.0
	Pe-35	795.98	Westph. A	Middle Bochum	fine sand	2.3	0.21	moderately well sorted	0.6	0.7	-0.27	saPl	Delta front	5.21	0.0037	massiv	16.0	22.7	2.7	3.7	1.3	2.0	0.3	10.3	3.7	4.0	2.7	0.3	0.0	0.0	1.3	2.3	0.0	0.0	0.3	0.0	0.0	0.0	0.0	1.7	0.0
	Pe-36	397.05	Westph. A	Middle Bochum	fine sand	2.5	0.18	moderately well sorted	0.6	0.7	-0.17	saPl	Delta front	7.91	0.0124	massiv	13.7	24.7	1.0	10.3	2.0	0.0	0.7	11.3	4.3	8.0	2.0	0.3	0.7	0.0	8.0	4.3	0.0	0.0	0.0	0.0	0.0	0.0	0.0	1.3	0.0
	Pe-37	800.20	Westph. A	Middle Bochum	fine sand	2.5	0.17	moderately well sorted	0.7	0.6	0.04	saPl	Delta front	6.68	0.0239	breccia - massiv	19.7	27.3	1.7	4.3	0.3	0.3	1.7	19.7	6.7	5.0	0.7	0.3	0.3	0.0	8.0	3.0	0.3	0.0	0.0	0.0	0.0	0.0	0.3	0.0	0.0
	Pe-38	802.50	Westph. A	Middle Bochum	fine sand	2.6	0.16	moderately well sorted	0.5	0.7	-0.24	saPl	Delta front	5.96	0.0070	massiv	19.0	17.7	3.7	3.0	2.0	1.7	1.0	16.3	6.0	7.0	0.3	0.3	0.0	0.0	8.3	7.7	0.0	0.0	0.0	0.0	0.0	0.0	0.0	0.0	0.3
	Pe-39	803.36	Westph. A	Middle Bochum	fine sand	2.7	0.16	moderately well sorted	0.5	0.7	-0.01	saPl	Delta front	7.79	0.0103	massiv	14.0	15.7	3.7	5.7	0.7	0.0	1.7	19.7	9.0	4.3	0.0	0.3	0.0	0.0	14.7	1.7	0.0	0.0	0.0	0.0	0.0	0.0	0.0	0.3	0.0
	Pe-40	805.50	Westph. A	Middle Bochum	fine sand	2.4	0.18	moderately well sorted	0.6	0.7	-0.17	saPl	Delta front	6.34	2.1020	plenty coal layers	13.7	22.7	1.7	4.7	3.0	0.3	2.0	16.0	3.7	3.7	2.0	0.0	1.0	3.3	11.0	3.0	0.0	0.0	0.0	0.0	0.0	0.0	0.0	0.7	2.3
	Pe-41	807.50	Westph. A	Middle Bochum	fine sand	2.9	0.14	well sorted	0.5	0.7	0.04	saPl	Delta front	10.79	0.0046	massiv	14.7	23.7	4.7	6.3	4.7	0.0	0.7	16.3	5.7	6.0	1.3	0.7	0.0	0.0	6.7	2.7	0.0	0.0	0.0	0.0	0.0	0.0	0.0	0.0	0.0
	Pe-42	809.22	Westph. A	Middle Bochum								saPl	Delta front	7.52	0.0039	massiv																										
	Pe-43	810.02	Westph. A	Middle Bochum	fine sand	2.3	0.20	well sorted	0.4	0.7	-0.17	saPl	Delta front	7.37	0.0066	massiv	12.3	27.0	3.0	8.3	3.7	2.0	0.3	13.3	4.0	6.0	3.3	0.0	0.0	0.0	8.3	1.3	0.0	0.0	0.0	0.0	0.0	0.0	0.3	0.0	
	Pe-44	810.79	Westph. A	Middle Bochum	medium silt	5.3	0.03	moderately sorted	0.8	0.6	-0.03	siPl	Lower delta plain	1.83	0.0001	massiv	7.7	14.0	1.3	1.3	0.7	0.0	1.0	24.7	5.0	6.7	0.3	0.0	0.0	0.3	17.7	15.7	0.0	0.0	0.0	0.0	0.0	0.0	0.7	0.0	2.7
	Pe-45	812.15	Westph. A	Middle Bochum								siPl	Lower delta plain	1.85	0.0870	massiv																										
	Pe-46	813.03	Westph. A	Middle Bochum								mS	Lower delta plain	1.74	0.0147	massiv																										
	Pe-47	817.98	Westph. A	Middle Bochum								mR	Wetlands	1.57	0.1839	minor outbreak																										
	Pe-48	981.75	Westph. A	Middle Bochum	medium silt	5.0	0.03	moderately sorted	1.0	0.5	-0.09	mS	Wetlands	1.11	0.0001	massiv	9.3	14.7	0.7	1.3	0.0	0.0	0.0	30.3	4.7	6.0	0.0	0.0	0.0	0.3	17.7	11.3	0.3	0.0	0.0	0.0	0.0	0.0	0.0	0.0	3.3
	Pe-49	986.09	Westph. A	Middle Bochum								mR	Wetlands	1.67	0.0004	minor outbreak																										
	Pe-50	986.57	Westph. A	Middle Bochum	coarse silt	4.8	0.04	moderately sorted	0.8	0.6	-0.17	siBio	Lower delta plain	1.94	0.0001	massiv	14.7	18.0	0.0	1.3	0.7	0.0	0.3	32.7	7.0	6.3	0.3	0.0	0.0	0.3	3.7	11.3	0.0	0.0	0.0	0.0	0.0	0.0	1.7	0.0	1.3
	Pe-51	988.19	Westph. A	Middle Bochum	very fine sand	3.9	0.07	moderately well sorted	0.5	0.7	0.02	siWl	Lower delta plain	2.84	0.0003	massiv	11.3	28.3	1.0	2.0	1.7	0.0	0.7	25.0	7.7	4.3	0.0	0.0	0.0	0.7	11.7	4.7	0.0	0.0	0.0	0.0	0.0	0.0	0.3	0.0	0.0
	Pe-52	989.10	Westph. A	Middle Bochum	coarse silt	4.1	0.06	moderately well sorted	0.6	0.7	-0.13	siPl	Lower delta plain	2.53	0.0003	massiv	10.0	21.3	1.0	1.3	1.7	0.3	0.7	23.3	9.3	5.7	0.7	0.0	0.3	0.0	14.7	7.7	0.3	0.7	0.3	0.0	0.0	0.0	0.3	0.0	0.3
	Pe-53	990.24	Westph. A	Middle Bochum								saCl	Delta front	7.20	0.0032	massiv																										
	Pe-54	990.51	Westph. A	Middle Bochum	fine sand	2.2	0.21	moderately well sorted	0.6	0.7	-0.18	saCl	Delta front	6.10	0.0030	minor outbreak	11.7	31.7	3.3	4.7	5.0	0.3	1.3	14.3	5.0	6.3	2.0	0.3	0.3	0.0	6.7	1.7	0.0	0.0	0.0	0.0	0.0	0.0	0.0	0.0	0.3
	Pe-55	994.18	Westph. A	Middle Bochum	fine sand	2.2	0.22	moderately well sorted	0.5	0.7	-0.12	saPl	Delta front	5.32	0.0019	massiv	10.0	36.3	3.7	7.0	6.0	1.0	1.3	13.7	4.3	6.3	2.3	0.0	0.0	0.0	2.0	1.0	0.0	0.0	0.0	0.0	0.0	0.0	0.0	0.0	0.0
	Pe-56	996.87	Westph. A	Middle Bochum	fine sand	2.4	0.19	moderately well sorted	0.5	0.7	-0.17	saPl	Delta front	4.85	0.0021	massiv	13.3	32.7	4.0	7.3	4.3	1.0	2.7	14.3	6.0	5.0	0.7	0.0	0.0	0.0	3.7	0.7	0.0	0.0	0.0	0.3	0.0	0.0	0.3	0.0	0.0
	Pe-57	999.51	Westph. A	Middle Bochum	fine sand	2.9	0.14	moderately well sorted	0.6	0.7	-0.17	saPl	Delta front	3.79	0.0173	massiv	9.3	28.7	1.3	7.3	2.3	1.3	1.7	18.3	10.7	3.3	1.0	0.0	0.3	0.0	8.0	3.3	0.0	0.0	0.0	0.0	0.0	0.0	0.0	0.0	0.0
	Pe-58	1001.60	Westph. A	Middle Bochum								saPl	Delta front	4.68	0.0022	massiv																										
	Pe-59	1001.70	Westph. A	Middle Bochum	very fine sand	3.1	0.12	poorly sorted	1.3	0.4	-0.01	saPl	Delta front	5.46	0.1766	plenty coal layers	7.3	36.3	1.7	4.0	1.3	1.0	2.7	14.0	2.3	2.0	3.0	0.0	0.3	3.0	11.3	2.7	0.0	0.0	0.0	0.0	0.0	0.0	0.3	0.0	4.3
	Pe-60	1005.49	Westph. A	Middle Bochum								mS	Wetlands	1.96	0.0786	outbreak																										
					Min	*2.2*	*0.0*		*0.4*	*0.4*	*-0.43*			*0.48*	*0.0001*		*6.0*	*14.0*	*0.0*	*0.0*	*0.0*	*0.0*	*0.0*	*2.3*	*0.3*	*0.7*	*0.0*	*0.0*	*0.0*	*0.0*	*0.3*	*0.3*	*0.0*	*0.0*	*0.0*	*0.0*	*0.0*	*0.0*	*0.0*	*0.0*	*0.0*
					Mean	*3.3*	*0.1*		*0.7*	*0.6*	*-0.15*			*5.55*	*0.2615*		*12.3*	*27.8*	*1.4*	*3.2*	*1.4*	*0.9*	*1.6*	*17.2*	*3.6*	*3.9*	*1.2*	*0.2*	*0.3*	*0.3*	*12.8*	*3.2*	*0.1*	*0.1*	*0.1*	*0.2*	*0.0*	*0.0*	*0.2*	*0.5*	*0.8*
					Max	*5.4*	*0.2*		*1.3*	*0.7*	*0.10*			*15.56*	*4.4320*		*25.3*	*45.7*	*4.7*	*10.3*	*6.0*	*3.7*	*9.0*	*46.7*	*10.7*	*8.0*	*3.3*	*0.7*	*2.3*	*3.3*	*65.0*	*15.7*	*0.7*	*0.7*	*2.3*	*2.0*	*0.0*	*0.0*	*1.7*	*3.7*	*4.3*

Authigenic components (%)

Sample No.	Qzo	Sid inter	Sid intra	Non-ferroan cc	Ferroan cc	Qz intra	Non-ferroan dolo	Ferroan dolo	Carbo rpl	Early rpl kao	Late rpl kao	Ill rpl kaol	Illite inter	Illite rpl fsp	Illite pore-linening	Frac-filling carbonate	Frac-filling sulfide
Pe-1	0.7	0.3	0.7	0.0	0.0	0.0	0.0	0.0	0.3	0.0	0.0	0.0	0.0	0.0	0.0	0.7	0.3
Pe-2	0.0	0.0	0.0	0.0	0.0	0.0	0.0	0.0	0.0	0.0	0.0	0.0	0.0	0.0	0.0	0.0	0.0
Pe-3																	
Pe-4																	
Pe-5	0.3	0.7	0.0	0.0	0.0	0.0	0.0	0.0	0.0	0.0	0.0	0.0	0.0	0.0	0.0	0.3	0.0
Pe-6	0.7	0.0	0.3	0.0	0.0	0.0	0.0	0.0	0.0	0.0	0.0	0.0	0.0	0.0	0.0	0.0	0.0
Pe-7	0.0	0.0	0.3	0.0	0.0	0.0	0.0	0.0	0.0	0.0	0.0	0.0	0.0	0.0	0.0	0.0	0.0
Pe-8	0.0	0.0	0.0	0.0	0.0	0.0	0.0	0.0	0.0	0.0	0.0	0.0	0.0	0.0	0.0	0.0	0.0
Pe-9																	
Pe-10	0.0	1.0	0.7	0.0	0.0	0.0	0.0	0.0	0.0	0.3	0.0	0.0	0.0	0.0	0.0	0.0	0.0
Pe-11	1.3	5.0	7.0	0.0	0.0	0.0	0.0	0.0	0.0	0.3	0.0	0.0	0.0	0.0	0.0	0.0	0.0
Pe-12	0.3	4.3	1.7	0.0	0.0	0.0	0.0	0.0	0.0	1.0	0.7	0.0	0.0	0.0	0.0	0.0	0.0
Pe-13																	
Pe-14	1.3	3.3	3.3	0.0	0.0	0.0	0.0	0.0	0.0	1.3	0.7	0.0	0.0	0.0	0.0	0.0	0.0
Pe-15	1.7	0.7	1.0	0.0	0.0	0.0	0.0	0.0	0.0	1.3	1.7	0.7	0.0	0.7	0.0	0.0	0.7
Pe-16	4.7	0.0	0.3	0.0	0.0	0.0	0.0	0.0	0.0	1.0	2.7	0.0	0.0	0.0	0.0	0.0	0.0
Pe-17	0.3	0.0	0.0	0.0	0.0	0.0	0.0	0.0	0.0	0.7	2.3	0.0	0.0	0.0	0.0	0.0	0.7
Pe-18	0.7	0.0	0.0	0.0	0.0	0.0	0.0	0.0	0.0	1.7	1.3	0.0	0.0	0.0	0.0	0.0	6.0
Pe-19	0.3	3.7	4.0	0.0	0.0	0.0	0.0	0.0	0.0	0.0	0.0	0.0	0.0	0.0	0.3	0.0	0.0
Pe-20	0.0	0.0	0.0	0.3	5.7	0.0	0.3	0.0	28.0	0.0	0.0	0.0	0.0	0.0	0.0	0.0	0.3
Pe-21	0.0	6.3	2.7	0.0	0.0	0.0	0.0	0.0	0.0	0.0	0.0	0.0	0.0	0.3	0.0	0.0	0.0
Pe-22																	
Pe-23	0.0	0.3	1.0	0.0	0.0	0.0	0.0	0.0	0.0	0.0	1.3	0.0	0.0	0.3	0.0	0.0	0.0
Pe-24	0.0	0.3	1.0	0.0	0.0	0.0	0.0	0.0	0.0	0.3	0.0	0.0	0.0	0.3	0.0	0.0	0.0
Pe-25																	
Pe-26																	
Pe-27	0.0	1.0	0.3	0.0	0.0	0.0	0.0	0.0	0.0	0.0	0.0	0.0	0.0	0.0	0.0	0.0	0.0
Pe-28																	
Pe-29																	
Pe-30																	
Pe-31																	
Pe-32																	
Pe-33																	
Pe-34	0.0	1.7	0.0	0.0	0.0	0.0	0.0	0.0	0.0	0.0	0.0	0.0	0.0	0.0	0.0	0.0	0.0
Pe-35	0.0	0.0	0.0	0.0	3.3	0.0	0.0	0.0	34.7	0.0	0.0	0.0	0.0	0.7	0.0	0.0	0.0
Pe-36	0.0	0.0	0.3	0.0	0.0	0.3	0.0	0.0	0.0	0.0	0.3	0.0	0.0	0.0	0.3	0.0	0.0
Pe-37	0.0	0.0	0.0	0.0	0.0	0.0	0.0	0.0	0.0	0.0	0.0	0.0	0.0	0.0	0.0	0.0	0.0
Pe-38	1.0	0.0	0.0	0.0	0.0	0.3	0.0	0.0	0.0	0.0	0.0	0.0	0.0	0.0	0.0	0.0	0.0
Pe-39	0.7	0.0	0.0	0.0	1.3	0.0	0.0	0.0	0.0	0.0	0.0	0.0	0.0	0.0	0.0	1.0	0.0
Pe-40	0.0	0.0	0.0	0.0	0.0	0.0	0.0	0.0	0.0	0.7	0.0	0.0	0.0	0.0	0.0	0.0	0.0
Pe-41	0.0	0.0	0.0	0.0	0.3	0.0	0.0	0.0	0.0	0.0	0.0	0.0	0.0	0.7	0.0	0.0	0.0
Pe-42																	
Pe-43	0.7	0.0	0.3	0.0	0.0	0.0	0.0	0.0	0.0	0.0	0.0	0.0	0.0	0.0	0.0	0.0	0.0
Pe-44	0.0	0.0	0.0	0.0	0.0	0.0	0.0	0.0	0.0	0.3	0.0	0.0	0.0	0.0	0.0	0.0	0.0
Pe-45																	
Pe-46																	
Pe-47																	
Pe-48	0.0	0.0	0.0	0.0	0.0	0.0	0.0	0.0	0.0	0.0	0.0	0.0	0.0	0.0	0.0	0.0	0.0
Pe-49																	
Pe-50	0.0	0.0	0.3	0.0	0.0	0.0	0.0	0.0	0.0	0.0	0.0	0.0	0.0	0.0	0.0	0.0	0.0
Pe-51	0.0	0.0	0.3	0.0	0.3	0.0	0.0	0.0	0.0	0.0	0.0	0.0	0.0	0.0	0.0	0.0	0.0
Pe-52	0.0	0.0	0.0	0.0	0.0	0.0	0.0	0.0	0.0	0.0	0.0	0.0	0.0	0.0	0.0	0.0	0.0
Pe-53																	
Pe-54	1.3	0.7	0.7	0.0	1.0	0.0	0.0	0.0	0.0	0.0	0.0	0.0	0.0	0.0	0.0	0.0	0.0
Pe-55	1.3	0.0	0.0	0.0	1.0	0.0	0.0	0.0	0.7	0.0	0.0	0.0	0.3	0.0	0.0	0.0	0.0
Pe-56	0.3	0.0	1.0	0.0	0.0	0.0	0.0	0.0	0.3	0.0	0.0	0.0	0.0	0.0	0.0	0.0	0.0
Pe-57	0.3	0.0	0.0	0.0	0.3	0.0	0.0	0.0	1.0	0.0	0.0	0.0	0.0	0.0	0.0	0.0	0.0
Pe-58																	
Pe-59	0.0	0.0	1.0	0.0	0.0	0.3	0.0	0.0	0.0	0.0	0.0	0.0	0.3	0.0	0.0	0.0	0.0
Pe-60																	
Min	*0.0*	*0.0*	*0.0*	*0.0*	*0.0*	*0.0*	*0.0*	*0.0*	*0.0*	*0.0*	*0.0*	*0.0*	*0.0*	*0.0*	*0.0*	*0.0*	*0.0*
Mean	*0.5*	*0.8*	*0.7*	*0.0*	*0.3*	*0.0*	*0.0*	*0.0*	*1.7*	*0.2*	*0.3*	*0.0*	*0.0*	*0.1*	*0.0*	*0.1*	*0.2*
Max	*4.7*	*6.3*	*7.0*	*0.3*	*5.7*	*0.3*	*0.3*	*0.0*	*34.7*	*1.7*	*2.7*	*0.7*	*0.3*	*0.7*	*0.3*	*1.0*	*6.0*

Optical porosity (%)

Sample No.	Primary porosity	Sec. poro Kfs	Sec. poro RF	Sec. poro Plag	Fracture porosity
Pe-1	0.0	0.0	0.0	0.0	0.0
Pe-2	0.0	0.0	0.3	0.0	0.0
Pe-3					
Pe-4					
Pe-5	0.0	0.0	0.0	0.0	1.0
Pe-6	0.0	0.7	0.3	0.3	0.0
Pe-7	0.0	0.0	0.0	0.7	0.0
Pe-8	0.0	0.7	0.3	0.0	0.0
Pe-9					
Pe-10	0.0	1.0	0.3	0.3	0.0
Pe-11	0.7	0.0	3.7	0.0	0.0
Pe-12	0.0	1.0	1.0	1.3	0.0
Pe-13					
Pe-14	0.3	0.0	0.3	0.0	0.0
Pe-15	0.3	0.3	4.3	0.0	0.0
Pe-16	0.3	0.0	6.0	0.0	0.0
Pe-17	0.3	0.0	6.0	0.0	0.0
Pe-18	0.3	0.0	4.7	0.0	0.7
Pe-19	0.0	0.0	1.7	0.0	0.0
Pe-20	0.0	0.0	0.3	0.0	0.0
Pe-21	0.0	0.0	1.3	0.0	0.0
Pe-22					
Pe-23	0.0	0.0	1.3	0.0	0.0
Pe-24	0.0	0.0	0.7	0.0	0.3
Pe-25					
Pe-26					
Pe-27	0.0	0.0	0.3	0.0	0.0
Pe-28					
Pe-29					
Pe-30					
Pe-31					
Pe-32					
Pe-33					
Pe-34	0.0	0.3	3.3	0.0	0.0
Pe-35	0.0	0.3	1.7	0.0	0.0
Pe-36	0.3	1.0	3.3	1.3	0.0
Pe-37	0.0	0.0	0.3	0.0	0.0
Pe-38	0.3	0.0	3.7	0.3	0.0
Pe-39	0.0	0.3	4.3	1.0	0.0
Pe-40	0.3	1.3	1.7	1.3	0.0
Pe-41	0.0	0.3	4.3	0.3	0.0
Pe-42					
Pe-43	0.0	1.3	2.7	1.7	0.0
Pe-44	0.0	0.0	0.0	0.0	0.0
Pe-45					
Pe-46					
Pe-47					
Pe-48	0.0	0.0	0.0	0.0	0.0
Pe-49					
Pe-50	0.0	0.0	0.0	0.0	0.0
Pe-51	0.0	0.0	0.0	0.0	0.0
Pe-52	0.0	0.0	0.0	0.0	0.0
Pe-53					
Pe-54	0.0	0.0	1.0	0.3	0.0
Pe-55	0.0	0.0	1.7	0.0	0.0
Pe-56	0.0	0.3	1.0	0.7	0.0
Pe-57	0.0	0.7	0.3	0.3	0.0
Pe-58					
Pe-59	0.0	0.0	0.7	0.0	0.0
Pe-60					
Min	*0.0*	*0.0*	*0.0*	*0.0*	*0.0*
Mean	*0.1*	*0.2*	*1.6*	*0.3*	*0.1*
Max	*0.7*	*1.3*	*6.0*	*1.7*	*1.0*

Additional information

Sample No.	Q	F	R	IGV (%)	COPL	CEPL	Icompact	Recon Q	Recon F	Recon R
Pe-1	60.3	2.8	36.9	1.0	38.8	0.6	0.97	60.4	2.8	36.8
Pe-2	50.4	1.8	47.8	0.0	40.0	0.0	1.00	50.7	1.8	47.4
Pe-3										
Pe-4										
Pe-5	24.9	1.4	73.7	1.0	39.2	0.8	0.97	24.9	0.7	74.4
Pe-6	52.2	5.5	42.2	0.7	39.6	0.4	0.99	51.5	5.5	43.0
Pe-7	43.6	2.5	53.9	0.0	40.0	0.0	1.00	43.2	2.8	54.0
Pe-8	58.5	5.5	36.0	0.0	40.0	0.0	1.00	58.1	4.8	37.1
Pe-9										
Pe-10	55.3	6.0	38.7	1.0	39.4	0.6	0.98	54.3	7.3	38.4
Pe-11	61.9	0.9	37.2	7.0	35.5	4.1	0.87	59.3	9.5	31.2
Pe-12	47.6	8.3	44.1	4.7	37.1	2.9	0.91	45.4	11.8	42.8
Pe-13										
Pe-14	49.8	11.8	38.4	5.0	36.8	2.9	0.90	47.7	12.9	39.4
Pe-15	53.3	4.5	42.3	2.7	37.9	1.4	0.95	50.2	9.6	40.2
Pe-16	60.6	3.3	36.1	5.0	36.8	2.9	0.90	58.5	7.5	34.0
Pe-17	54.9	0.4	44.7	0.7	39.2	0.2	0.99	53.4	3.8	42.7
Pe-18	62.3	6.5	31.2	1.0	35.5	0.4	0.98	60.2	9.0	30.9
Pe-19	42.5	2.8	54.7	4.3	37.3	2.7	0.91	42.1	7.1	50.8
Pe-20	83.9	0.0	16.1	6.3	35.7	4.1	0.86	57.6	31.8	10.6
Pe-21	38.9	0.0	61.1	6.3	35.9	4.1	0.85	38.4	3.3	58.3
Pe-22					39.8	0.2				
Pe-23	54.3	1.9	43.8	0.3	39.8	0.2	0.99	53.5	4.7	41.8
Pe-24	28.1	1.1	70.8	0.3	39.8	0.2	0.99	28.7	2.4	68.9
Pe-25										
Pe-26										
Pe-27	43.9	0.7	55.4	1.0	39.4	0.6	0.98	43.8	1.1	55.1
Pe-28										
Pe-29										
Pe-30										
Pe-31										
Pe-32										
Pe-33										
Pe-34	37.9	10.3	51.7	1.7	39.0	1.0	0.96	37.8	9.5	52.7
Pe-35	57.9	10.7	31.3	3.3	37.9	2.1	0.93	45.4	28.6	26.0
Pe-36	46.4	15.3	38.3	0.7	39.6	0.2	0.99	45.6	15.9	38.5
Pe-37	49.7	6.6	43.8	0.0	40.0	0.0	1.00	50.0	6.3	43.8
Pe-38	42.9	10.0	47.1	1.3	39.2	0.6	0.98			
Pe-39	33.2	11.2	55.6	2.0	38.1	1.9	0.94	42.7	8.1	49.2
Pe-40	44.9	10.9	44.1	0.3	39.8	0.0	1.00	32.7	11.8	55.5
Pe-41	43.4	17.2	39.4	0.3	39.8	0.2	0.99	44.4	10.9	44.7
Pe-42								42.8	13.3	43.9
Pe-43	46.5	16.4	37.1	0.7	39.6	0.4	0.99			
Pe-44	27.4	4.1	68.5	0.0	40.0	0.0	1.00	44.9	15.4	39.6
Pe-45								27.3	3.7	69.0
Pe-46										
Pe-47										
Pe-48	28.3	2.4	69.3	0.0	40.0	0.0	1.00			
Pe-49								28.3	2.4	69.3
Pe-50	38.8	2.4	58.8	0.0	40.0	0.0	1.00			
Pe-51	42.3	5.0	52.7	0.3	39.8	0.2	0.99	38.7	2.0	59.4
Pe-52	35.3	4.4	60.3	0.0	40.0	0.0	1.00	42.2	3.5	54.3
Pe-53								35.7	2.6	61.8
Pe-54	48.7	14.0	37.3	3.0	38.1	1.9	0.95			
Pe-55	51.8	17.7	30.5	2.7	38.4	1.6	0.95	48.6	9.6	41.8
Pe-56	49.1	16.5	34.4	0.3	39.8	0.2	0.99	51.4	12.0	36.6
Pe-57	41.6	11.7	46.6	0.7	39.6	0.4	0.99	47.9	14.0	38.0
Pe-58								41.1	11.1	47.7
Pe-59	53.4	8.0	38.5	0.3	39.8	0.2	0.99			
Pe-60								53.2	7.5	39.2
Min	*24.9*	*0.0*	*16.1*	*0.0*	*35.5*	*0.0*	*0.9*	24.9	0.7	10.6
Mean	*47.4*	*6.7*	*45.9*	*1.7*	*38.8*	*1.0*	*1.0*	45.7	8.4	45.9
Max	*83.9*	*17.7*	*73.7*	*7.0*	*40.0*	*4.1*	*1.0*	60.4	31.8	74.4

Geochemical data

Sample No.	CO3 therm	CaCO3 therm	SiO2 (%)	TiO2 (%)	Al2O3 (%)	Fe2O3 (%)	Cr2O3 (%)	MgO (%)	CaO (%)	K2O (%)	MnO (ppm)	SrO (ppm)	BaO (ppm)	Rb2O (ppm)	ZRO2 (ppm)
Pe-1	2.24	3.70	70.70	0.66	11.40	5.29	0.02	1.59	0.73	1.66	855	128	189	71	306
Pe-2															
Pe-3	0.85	1.40	62.80	0.92	17.50	5.31	0.02	1.76	0.27	2.75	762	190	264	123	290
Pe-4															
Pe-5															
Pe-6	2.74	4.60	71.80	0.68	10.50	6.40	0.02	1.44	0.28	1.76	1138	98	155	76	484
Pe-7															
Pe-8															
Pe-9															
Pe-10															
Pe-11															
Pe-12															
Pe-13															
Pe-14	0.48	0.80	79.30	0.38	7.14	3.96	0.02	0.71	0.14	1.06	799	80	202	45	168
Pe-15															
Pe-16															
Pe-17															
Pe-18	0.10	0.20	83.70	0.41	6.87	2.08	0.02	0.37	0.06	1.05	58	77	10	43	168
Pe-19															
Pe-20	5.55	9.30	75.40	0.49	8.54	1.90	0.02	1.83	2.89	1.33	620	128	148	56	292
Pe-21	5.49	9.10	59.30	0.43	4.66	17.75	0.02	2.32	0.48	1.18	4038	84	260	49	195
Pe-22															
Pe-23															
Pe-24	0.15	0.30	75.10	0.68	10.60	4.35	0.02	1.00	0.17	1.65	834	103	37	72	382
Pe-25	2.03	3.40	62.30	0.85	16.20	6.36	0.02	1.86	0.53	2.52	832	146	498	118	279
Pe-26															
Pe-27	4.18	7.00	56.80	0.88	17.60	7.66	0.02	1.87	0.31	3.37	1020	139	631	162	297
Pe-28															
Pe-29															
Pe-30															
Pe-31															
Pe-32															
Pe-33	2.46	4.10	59.60	0.80	14.10	10.42	0.02	2.42	0.54	2.65	1823	147	435	122	248
Pe-34															
Pe-35	14.72	24.50	62.60	0.30	8.60	2.74	0.02	4.16	6.70	1.35	732	112	167	59	187
Pe-36															
Pe-37															
Pe-38	0.80	1.30	69.50	0.58	13.50	4.48	0.02	1.21	0.37	2.58	653	115	477	116	185
Pe-39															
Pe-40															
Pe-41															
Pe-42															
Pe-43	0.64	1.10	73.90	0.41	11.80	3.67	0.02	1.06	0.24	2.01	603	99	258	90	154
Pe-44															
Pe-45															
Pe-46															
Pe-47															
Pe-48	1.31	2.20	61.50	0.86	18.70	5.52	0.02	1.54	0.27	3.61	830	177	543	168	307
Pe-49															
Pe-50															
Pe-51	0.95	1.60	68.40	0.79	15.70	4.34	0.02	1.14	0.27	3.27	529	105	521	137	373
Pe-52															
Pe-53															
Pe-54	0.84	1.40	78.30	0.36	10.60	2.42	0.02	0.87	0.50	1.89	373	89	188	80	146
Pe-55															
Pe-56															
Pe-57															
Pe-58	0.77	1.30	73.70	0.40	9.93	4.29	0.02	0.96	0.21	1.92	801	92	332	81	181
Pe-59	0.77	1.30	73.70	0.40	9.93	4.29	0.02	0.96	0.21	1.92	801	92	332	81	181
Pe-60															
Min	*0.10*	*0.20*	*56.80*	*0.30*	*4.66*	*1.90*	*0.02*	*0.37*	*0.06*	*1.05*	*58.00*	*77.00*	*10.00*	*43.00*	*146.00*
Mean	*2.48*	*4.14*	*69.39*	*0.59*	*11.78*	*5.43*	*0.02*	*1.53*	*0.80*	*2.08*	*952.68*	*115.84*	*297.21*	*92.05*	*253.84*
Max	*14.72*	*24.50*	*83.70*	*0.92*	*18.70*	*17.75*	*0.02*	*4.16*	*6.70*	*3.61*	*4038.00*	*190.00*	*631.00*	*168.00*	*484.00*

	Sample No.	Core Depth (m)	Stage	Formation	Grain size	Mean GS (ϕ)	Mean GS (mm)	Sorting	Sorting (ϕ)	Sorting (mm)	Skewness	Facies	Facies Association	Helium Porosity (%)	Permeability horizontal (mD)	Comments Plug	Quartz mono	Quartz poly	Plag	K-fsp	PRF	VRF	SRF	Shale	Phyllite	Shist	Quarzite	MRF	Chert	Org. matter	Carbonatic ripup	Mica	Zirkon	Turmaline	Clay rip-up clast	Opaque	Pyrite	Biotite	Chlorite	Fe-OH inter
Bork-1	Bo-1	726.75	Westph. A	Upper Witten								mR	Wetlands	6.36	0.0020	partly open fracture																									
	Bo-2	726.81	Westph. A	Upper Witten	very fine sand	3.9	0.1	moderately well sorted	0.5	0.7	-0.1	mR	Wetlands	5.88	0.0070	massiv	4.3	18.0	1.0	0.3	1.7	0.3	1.7	26.0	8.0	5.0	0.3	0.0	0.0	0.0	21.7	7.7	0.0	0.0	0.0	1.7	0.0	0.0	0.3	0.0
	Bo-3	727.27	Westph. A	Upper Witten								mR	Wetlands	7.15	0.0492	massiv																									
	Bo-4	728.84	Westph. A	Upper Witten	fine sand	2.2	0.2	poorly sorted	1.0	0.5	-0.18	saPl	Delta front	5.95	2.4643	contact massiv	8.0	26.7	2.3	4.7	1.7	0.0	1.7	20.7	6.3	4.0	2.0	0.0	0.0	0.0	14.0	4.3	0.7	0.0	0.0	0.0	0.0	0.0	0.0	0.7
	Bo-5	729.49	Westph. A	Upper Witten	medium sand	1.6	0.3	moderately well sorted	0.7	0.6	-0.11	saPl	Delta front	6.76	5.0542	central healed fracture	7.3	46.3	5.0	6.3	2.0	1.3	2.7	6.7	1.0	2.3	5.0	0.0	1.3	0.0	2.3	1.7	0.3	0.0	0.0	0.0	0.3	0.0	0.0	0.7
	Bo-6	732.03	Westph. A	Upper Witten	fine sand	2.1	0.2	well sorted	0.4	0.7	0.11	saPl	Delta front	6.35	0.0076	massiv	8.0	38.0	5.0	9.7	3.3	1.3	3.7	13.3	2.3	1.3	3.0	0.3	0.0	0.0	1.0	1.7	0.3	0.0	0.0	0.0	0.0	0.0	0.7	0.0
	Bo-7	733.86	Westph. A	Upper Witten	fine sand	2.1	0.2	well sorted	0.5	0.7	-0.06	saPl	Delta front	7.38	0.0069	massiv	15.0	31.0	3.0	5.7	1.3	2.0	3.0	11.0	5.3	3.7	3.0	0.7	0.3	0.0	3.7	0.3	0.0	0.0	0.0	0.0	0.0	0.0	0.7	0.0
	Bo-8	736.17	Westph. A	Upper Witten	medium sand	1.5	0.4	moderately well sorted	0.5	0.7	-0.03	psaS	Delta front	7.37	0.0103	massiv	7.7	43.3	4.0	9.7	2.7	0.3	2.3	7.0	4.3	2.0	7.0	0.3	0.3	0.0	0.0	2.7	0.0	0.0	0.0	0.0	0.0	0.0	0.3	0.0
	Bo-9	737.77	Westph. A	Upper Witten	medium sand	1.1	0.5	moderately sorted	0.9	0.5	0.27	psaS	Delta front	10.89	0.3285	massiv	10.3	38.0	3.3	5.0	1.7	0.7	3.0	17.7	1.7	2.0	6.0	0.0	0.3	0.0	0.7	1.0	0.0	0.0	0.0	0.0	0.0	0.0	0.0	0.0
	Bo-10	737.24	Westph. A	Upper Witten	medium sand	1.7	0.3	moderately sorted	0.8	0.6	-0.12	psaS	Delta front	8.03	0.0458	single coal layer <mm	7.7	30.7	1.3	3.7	1.7	0.7	3.7	6.0	1.0	1.3	5.3	0.3	0.3	0.0	11.3	0.7	0.0	0.0	0.0	0.7	0.0	0.0	0.0	0.0
	Bo-11	738.40	Westph. A	Upper Witten	very coarse sand	-0.4	1.3	moderately sorted	0.8	0.6	-0.25	psaS	Delta front	7.83	0.0850	massiv	2.0	50.0	2.0	2.0	6.0	0.7	8.0	10.7	1.3	0.0	7.7	0.0	2.3	0.0	0.0	0.0	0.0	0.0	0.0	0.0	0.7	0.0	0.0	0.0	0.0
	Bo-12	738.14	Westph. A	Upper Witten	medium sand	1.8	0.3	moderately well sorted	0.6	0.7	-0.22	saPl	Delta front	7.79	0.0204	massiv	11.7	34.0	4.0	6.7	3.0	0.7	1.0	15.7	1.7	1.0	2.3	0.3	0.3	0.0	2.0	1.7	0.0	0.3	2.3	0.0	0.0	0.0	0.0	0.0
	Bo-13	740.07	Westph. A	Upper Witten	medium sand	1.7	0.3	moderately well sorted	0.5	0.7	-0.19	saPl	Delta front	7.66	0.2287	marginal healed fracture	12.0	38.7	3.0	7.7	3.0	0.7	1.3	19.0	0.3	2.3	2.7	0.0	0.7	0.0	0.3	0.3	0.0	0.0	0.0	1.7	0.0	0.0	0.3	0.0
	Bo-14	741.71	Westph. A	Upper Witten								mBio	Wetlands	4.49	1.8861	massiv																									
	Bo-15	742.64	Westph. A	Upper Witten	coarse silt	4.4	0.0	moderately sorted	0.8	0.6	-0.03	siWl	Wetlands	3.33	0.0034	massiv	9.7	24.3	1.3	3.7	0.7	0.0	0.0	37.7	2.7	5.0	0.7	0.0	0.0	0.3	0.0	6.7	0.0	0.3	0.0	0.3	0.0	0.0	2.3	4.3
	Bo-16	945.35	Westph. A	Upper Witten								clC	Pro Delta	3.89	0.0001	broken long axis																									
	Bo-17	948.88	Westph. A	Lower Witten	coarse silt	4.1	0.1	moderately well sorted	0.7	0.6	-0.08	mR	Wetlands	1.23	0.0001	minor outbreak	5.7	19.0	0.3	0.3	0.0	0.3	0.0	27.0	4.3	5.3	0.0	0.0	0.0	0.0	0.0	5.3	0.0	0.0	0.0	0.7	0.0	0.0	0.0	0.0
	Bo-18	950.84	Westph. A	Lower Witten	fine sand	2.8	0.1	moderately well sorted	0.5	0.7	-0.14	saWl	Delta front	3.33	0.0004	massiv	10.3	30.7	0.7	4.7	0.3	0.7	1.7	18.3	3.3	8.7	1.0	0.0	0.0	0.0	0.0	2.7	0.0	0.0	0.0	0.0	0.0	0.0	1.7	0.0
	Bo-19	953.13	Westph. A	Lower Witten	very fine sand	3.5	0.1	moderately well sorted	0.6	0.7	0.03	saPl	Delta front	2.32	0.0007	massiv	12.3	27.0	0.3	2.7	1.0	0.0	1.0	33.7	7.0	6.7	0.7	0.0	0.0	0.0	1.3	5.0	0.0	0.0	0.0	0.0	0.0	0.0	0.3	0.0
	Bo-20	957.66	Westph. A	Lower Witten	fine sand	2.8	0.1	moderately well sorted	0.5	0.7	-0.10	saPl	Delta front	6.79	0.0005	massiv	7.7	24.3	2.0	5.7	1.0	1.7	2.0	14.7	4.3	6.3	1.3	0.7	0.0	1.0	23.0	1.0	0.0	0.0	0.0	0.0	0.0	0.0	0.7	1.3
	Bo-21	959.27	Westph. A	Lower Witten	fine sand	2.6	0.2	well sorted	0.5	0.7	-0.18	saPl	Delta front	6.16	0.0014	massiv	9.7	33.3	3.7	5.7	3.0	0.0	2.3	20.0	6.3	6.7	1.0	0.0	0.0	0.0	4.0	2.0	0.0	0.0	0.0	0.0	0.0	0.0	0.3	0.0
	Bo-22	959.56	Westph. A	Lower Witten	coarse silt	4.4	0.0	moderately well sorted	0.7	0.6	-0.12	fsaS	Wetlands	1.75	0.0004	massiv	8.3	27.7	1.0	1.3	0.0	0.0	0.0	34.0	4.3	4.7	0.0	0.0	0.0	5.0	0.0	9.3	0.0	0.0	0.0	1.7	0.0	1.0	0.3	0.0
	Bo-23	959.86	Westph. A	Lower Witten								fsaS	Wetlands	2.28	0.0139	massiv																									
	Bo-24	960.23	Westph. A	Lower Witten	medium silt	5.2	0.0	moderately well sorted	0.6	0.7	-0.01	siBio	Lower delta plain	6.56	0.0067	marginal crack	3.7	30.0	1.7	0.7	0.0	0.0	0.0	29.3	1.7	3.7	0.0	0.0	0.0	2.0	6.0	17.3	0.3	0.0	0.0	0.3	0.0	0.0	1.3	1.7
	Bo-25	960.99	Westph. A	Lower Witten	medium silt	5.3	0.0	moderately sorted	0.8	0.6	-0.21	mS	Lower delta plain	2.36	4.7046	central crack	2.0	21.0	0.0	0.0	0.0	0.0	0.3	28.0	0.7	0.3	0.0	0.0	0.0	1.0	36.0	8.0	0.0	0.0	0.0	0.0	0.0	0.0	0.0	2.7
	Bo-26	963.31	Westph. A	Lower Witten	medium silt	5.4	0.0	moderately well sorted	0.6	0.7	-0.05	siS	Lower delta plain	6.07	0.0070	marginal crack	6.7	29.0	0.0	0.7	0.0	0.0	0.0	29.3	0.7	0.7	0.0	0.0	0.0	1.0	14.0	13.3	0.3	0.0	0.0	0.3	0.0	0.0	0.3	3.7
	Bo-27	964.37	Westph. A	Lower Witten								mS	Lower delta plain	6.51	0.0004	no cylindric shape																									
	Bo-28	1006.41	Westph. A	Lower Witten								mS	Wetlands	0.31	0.0001	massiv																									
	Bo-29	1008.81	Westph. A	Lower Witten	fine sand	2.6	0.2	well sorted	0.5	0.7	0.06	saPl	Delta front	3.45	0.0037	massiv	11.3	35.0	3.0	6.3	2.7	0.3	0.7	13.7	1.7	3.0	1.3	0.0	0.3	0.0	6.0	7.0	0.0	0.0	0.0	0.7	0.0	0.0	0.0	0.0
	Bo-30	1009.43	Westph. A	Lower Witten	very fine sand	3.3	0.1	well sorted	0.5	0.7	0.14	saPl	Delta front	2.71	0.0004	massiv	12.3	29.3	1.3	2.3	0.3	0.0	0.7	23.7	3.0	1.3	0.3	0.0	0.0	0.7	14.7	5.7	0.0	0.0	0.0	1.0	0.0	0.0	0.0	1.0
	Bo-31	1011.06	Westph. A	Lower Witten	coarse silt	4.1	0.1	moderately well sorted	0.5	0.7	0.08	siWl	Lower delta plain	1.45	0.2250	minor central crack	6.0	22.7	0.3	0.7	0.0	0.0	0.3	30.3	1.3	4.3	0.0	0.0	0.0	0.3	17.0	11.3	0.0	0.0	0.0	0.3	0.0	0.0	0.0	3.7
	Bo-32	1014.58	Westph. A	Lower Witten	fine sand	2.1	0.2	moderately well sorted	0.7	0.6	-0.16	saPl	Delta front	6.01	0.0082	minor coal flakes	16.3	36.3	4.0	6.3	3.0	0.3	1.0	14.7	2.3	1.3	3.0	0.3	0.0	1.0	4.0	1.0	0.0	0.0	0.0	0.0	0.0	0.0	0.0	0.0
	Bo-33	1014.68	Westph. A	Lower Witten								saPl	Delta front	6.06	0.0027	massiv																									
	Bo-34	1020.04	Westph. A	Lower Witten	fine sand	2.5	0.2	moderately well sorted	0.6	0.7	-0.02	saPl	Delta front	6.30	0.1326	central healed fracture	13.3	36.3	3.7	4.7	1.3	0.3	1.3	19.0	3.7	2.0	1.7	0.0	0.0	0.0	3.3	4.7	0.0	0.0	0.0	2.0	0.0	0.0	0.0	0.0
	Bo-35	1020.05	Westph. A	Lower Witten								saPl	Delta front	8.11	0.0687	central healed fracture																									
	Bo-36	1021.95	Westph. A	Lower Witten	medium sand	1.3	0.4	moderately sorted	0.8	0.6	-0.10	psaS	Delta front	4.86	0.0059	massiv	8.3	40.7	3.7	2.0	5.0	3.7	1.0	11.7	0.3	1.7	6.3	0.0	0.0	0.3	0.7	0.7	0.0	0.0	1.0	0.0	0.0	0.0	0.0	0.3
	Bo-37	1021.99	Westph. A	Lower Witten								psaS	Delta front	5.69	0.3678	coal flakes minor outbreak																									
	Bo-38	1022.36	Westph. A	Lower Witten	medium sand	1.4	0.4	moderately sorted	0.7	0.6	0.19	psaS	Delta front	4.75	0.0206	single minor coal flake	10.0	33.0	1.7	4.0	2.3	4.0	1.7	22.7	1.7	1.3	3.7	0.0	0.0	0.0	0.7	1.3	0.3	0.0	4.3	0.0	0.0	0.0	0.0	0.0
	Bo-39	1023.35	Westph. A	Lower Witten	medium sand	1.2	0.4	well sorted	0.5	0.7	-0.10	saS	Delta front	7.32	0.0106	minor outbreaks	8.0	45.3	5.0	5.3	5.3	0.7	1.0	13.0	0.0	1.7	5.7	0.0	0.0	0.0	0.0	1.7	0.0	0.0	0.0	0.0	0.0	0.0	0.0	0.0
	Bo-40	1028.00	Westph. A	Lower Witten								saS	Delta front	8.06	1.9881	single coal layer																									
	Bo-41	1028.25	Westph. A	Lower Witten	medium sand	1.4	0.4	well sorted	0.5	0.7	-0.11	saS	Delta front	7.71	0.0076	massiv	12.3	43.3	5.3	5.0	3.3	0.7	1.7	10.7	0.0	0.7	4.3	0.0	0.0	0.0	0.0	0.3	0.0	0.0	0.0	0.0	0.0	0.0	0.0	0.0
	Bo-42	1028.46	Westph. A	Lower Witten								saS	Delta front	7.68	0.0097	massiv																									
	Bo-43	1028.55	Westph. A	Lower Witten								saS	Delta front	8.64	0.0304	big coal flake																									
	Bo-44	1031.49	Westph. A	Lower Witten								mS	Wetlands	1.80	0.0039	massiv																									
					Min	*-0.4*	*0.0*		*0.4*	*0.5*	*-0.3*			*0.3*	*0.0001*		*2.0*	*18.0*	*0.0*	*0.0*	*0.0*	*0.0*	*0.0*	*6.0*	*0.0*	*0.0*	*0.0*	*0.0*	*0.0*	*0.0*	*0.0*	*0.0*	*0.0*	*0.0*	*0.0*	*0.0*	*0.0*	*0.0*	*0.0*	*0.0*
					Mean	*2.7*	*0.2*		*0.6*	*0.7*	*-0.1*			*5.5*	*0.41*		*8.9*	*32.8*	*2.4*	*4.1*	*1.9*	*0.7*	*1.6*	*19.5*	*2.8*	*3.0*	*2.5*	*0.1*	*0.2*	*0.4*	*6.3*	*4.2*	*0.1*	*0.0*	*0.3*	*0.4*	*0.0*	*0.0*	*0.3*	*0.7*
					Max	*5.4*	*1.3*		*1.0*	*0.7*	*0.3*			*10.9*	*5.05*		*16.3*	*50.0*	*5.3*	*9.7*	*6.0*	*4.0*	*8.0*	*37.7*	*8.0*	*8.7*	*7.7*	*0.7*	*2.3*	*5.0*	*36.0*	*17.3*	*0.7*	*0.3*	*4.3*	*2.0*	*0.3*	*1.0*	*2.3*	*4.3*

Sample No.	Authigenic components (%)																Optical porosity (%)					Additional information									Geochemichal data													
	Qzo	Sid inter	Sid intra	Cc non-ferroan	Ferroan cc	Quartz intra	Dolo non-ferroan	Ferroan dolo	Carbo rpl	Early rpl kao	Late rpl kao	Ill rpl kaol	Illite inter	Illite rpl fsp	Illite pore-linening	Frac-filling carbonate	Frac-filling sulfide	Primary porosity	Sec. poro Kfs	Sec. poro RF	Sec. poro Plag	Fracture porosity	Q	F	R	IGV (%)	COPL	CEPL	Icompact	Recon Q	Recon F	Recon R	CO3 therm	CaCO3 therm	SiO2 (%)	TiO2 (%)	Al2O3 (%)	Fe2O3 (%)	Cr2O3 (%)	MgO (%)	CaO (%)	K2O (%)	MnO (ppm)	SrO (ppm)	BaO (ppm)	Rb2O (ppm)	ZRO2 (ppm)
Bo-1																																												
Bo-2	0.0	0.3	0.0	0.0	0.0	0.0	0.0	0.0	0.0	0.3	0.0	0.0	0.0	0.0	0.0	0.0	0.0	0.0	0.0	1.3	0.0	0.0	25.7	1.5	72.8	0.3	39.8	0.2	0.99	25.6	1.9	72.6														
Bo-3																																												
Bo-4	0.3	0.0	0.7	0.0	0.0	0.0	0.0	0.0	0.0	0.0	0.0	0.0	0.0	0.0	0.0	0.0	0.0	0.0	0.7	0.7	0.0	0.0	39.9	7.6	52.5	0.3	39.8	0.2	0.99	39.3	8.9	51.8														
Bo-5	2.0	0.0	2.0	0.0	0.0	0.0	0.0	0.0	0.7	0.0	0.0	0.0	0.0	0.0	0.0	0.0	0.0	0.0	0.7	0.0	2.0	0.0	66.7	12.6	20.7	2.3	38.6	1.4	0.96	62.9	17.5	19.6	1.41	2.30	82.30	0.22	7.48	1.83	0.02	0.66	0.83	1.54	355	147	5300	63	84
Bo-6	1.0	0.3	0.0	0.0	1.0	0.0	0.0	0.0	2.0	0.3	0.0	0.0	0.0	0.3	0.0	0.0	0.0	0.0	0.7	1.0	0.3	0.0	54.2	16.2	29.5	2.3	38.6	1.4	0.96	52.1	19.5	28.4														
Bo-7	1.7	0.7	0.7	0.0	0.0	0.0	0.0	0.0	1.0	0.0	0.3	0.3	0.7	0.0	0.0	0.0	0.0	0.0	2.3	0.3	2.3	0.0	55.6	9.8	34.6	3.0	38.1	1.9	0.95	51.7	16.1	32.2														
Bo-8	1.7	0.0	0.0	0.0	0.0	0.0	0.0	0.0	0.0	0.0	0.3	0.0	0.0	0.0	0.0	0.0	0.0	0.0	1.7	1.0	1.3	0.0	64.1	15.0	20.9	1.7	39.0	1.0	0.97	61.8	18.0	20.1	< 0,10	< 0,2	84.40	0.21	8.20	1.22	0.02	0.36	0.13	1.85	190	127	415	69	89
Bo-9	3.7	0.0	0.7	0.0	0.0	0.0	0.0	0.0	0.0	1.0	0.7	0.0	0.0	0.0	0.0	0.0	0.0	0.3	0.3	0.7	1.3	0.0	60.5	9.2	30.3	4.0	37.5	2.3	0.94	58.0	13.1	29.0														
Bo-10	5.0	11.0	1.7	0.0	0.0	0.0	0.0	0.0	0.0	0.3	0.3	0.0	0.0	0.0	0.0	0.0	0.0	0.0	0.7	3.3	1.3	0.0	58.7	6.7	34.7	16.0	28.6	11.4	0.71	55.5	11.8	32.8														
Bo-11	3.7	0.0	0.0	0.0	0.0	0.0	0.0	0.0	0.0	0.3	0.0	0.0	0.0	0.0	0.0	0.0	0.0	0.7	0.7	0.7	0.7	0.0	66.9	4.3	28.8	4.3	37.3	2.3	0.94	65.7	6.0	28.3														
Bo-12	3.0	1.3	0.0	0.0	0.0	0.0	0.0	0.0	0.0	1.3	0.3	0.0	0.0	0.3	0.0	0.0	0.0	0.7	1.0	1.0	2.3	0.0	55.8	12.3	31.9	5.0	36.8	2.7	0.93	52.5	17.4	30.1														
Bo-13	2.3	0.0	0.0	0.0	0.0	0.0	0.0	0.0	0.0	0.7	0.0	0.0	0.0	0.0	0.0	0.0	0.0	0.3	1.0	1.0	0.7	0.0	58.9	11.6	29.5	2.7	38.4	1.4	0.96	57.4	13.8	28.7	< 0,10	< 0,2	85.90	0.22	7.42	1.33	0.02	0.32	0.13	1.58	174	107	455	63	93
Bo-14																																												
Bo-15	0.0	0.0	0.0	0.0	0.0	0.0	0.0	0.0	0.0	0.0	0.0	0.0	0.0	0.0	0.0	0.0	0.0	0.0	0.0	0.0	0.0	0.0	40.5	5.8	53.7	0.0	40.0	0.0	1.00	40.5	5.8	53.7														
Bo-16																																												
Bo-17	0.0	0.0	0.0	0.0	0.0	0.0	0.0	0.0	31.7	0.0	0.0	0.0	0.0	0.0	0.0	0.0	0.0	0.0	0.0	0.0	0.0	0.0	39.6	1.1	59.4	0.0	40.0	0.0	1.00	26.2	34.4	39.4														
Bo-18	0.3	4.3	3.0	0.7	0.7	0.0	0.0	0.0	5.3	0.0	0.0	0.0	0.0	0.0	0.0	0.0	0.0	0.0	0.0	0.7	0.3	0.0	52.3	6.6	41.1	6.0	36.2	3.8	0.90	47.2	15.7	37.1	2.17	3.60	71.10	0.52	11.10	6.55	0.02	1.38	0.24	1.89	1371	102	335	78	199
Bo-19	0.3	0.0	0.0	0.0	0.0	0.0	0.0	0.0	0.0	0.7	0.0	0.0	0.0	0.0	0.0	0.0	0.0	0.0	0.0	0.0	0.0	0.0	42.7	3.2	54.1	0.3	39.8	0.2	0.99	42.4	3.9	53.7														
Bo-20	0.0	0.3	0.0	0.0	0.0	0.0	0.0	0.0	0.0	0.0	0.3	0.0	0.0	0.0	0.0	0.0	0.0	0.3	0.0	0.0	0.3	0.0	35.2	8.1	56.7	0.7	39.6	0.2	0.99	35.0	8.7	56.3														
Bo-21	1.0	0.0	0.3	0.0	0.0	0.0	0.0	0.0	0.0	0.3	0.0	0.0	0.0	0.0	0.0	0.0	0.0	0.0	0.0	0.0	0.3	0.0	46.0	9.8	44.3	1.0	39.4	0.6	0.98	45.5	10.7	43.8														
Bo-22	0.0	0.0	0.0	0.0	0.0	0.0	0.0	0.0	0.0	0.0	0.0	0.0	0.0	0.0	0.0	0.0	0.0	0.0	0.0	1.3	0.0	0.0	44.3	2.9	52.9	0.0	40.0	0.0	1.00	44.3	2.9	52.9														
Bo-23																																												
Bo-24	0.0	0.0	0.0	0.0	0.0	0.0	0.0	0.0	0.0	0.0	0.0	0.0	0.0	0.0	0.0	0.0	0.0	0.0	0.0	0.0	0.0	0.3	43.9	3.0	53.0	0.0	40.0	0.0	1.00	43.9	3.0	53.0	0.66	1.10	62.00	0.99	18.80	4.84	0.02	1.73	0.24	2.93	595	166	741	134	329
Bo-25	0.0	0.0	0.0	0.0	0.0	0.0	0.0	0.0	0.0	0.0	0.0	0.0	0.0	0.0	0.0	0.0	0.0	0.0	0.0	0.0	0.0	0.0	26.0	0.0	74.0	0.0	40.0	0.0	1.00	26.0	0.0	74.0														
Bo-26	0.0	0.0	0.0	0.0	0.0	0.0	0.0	0.0	0.0	0.0	0.0	0.0	0.0	0.0	0.0	0.0	0.0	0.0	0.0	0.0	0.0	0.0	44.0	0.8	55.1	0.0	40.0	0.0	1.00	44.0	0.8	55.1														
Bo-27																																												
Bo-28																																												
Bo-29	2.3	0.3	0.3	0.0	2.3	0.0	0.0	0.0	1.3	0.0	0.0	0.0	0.0	0.3	0.0	0.0	0.0	0.0	0.0	0.0	0.0	0.0	56.3	10.9	32.8	5.0	36.8	3.2	0.92	55.0	13.0	32.1	4.63	7.70	70.40	0.50	10.30	7.36	0.02	1.45	0.29	2.41	1026	85	439	99	272
Bo-30	0.0	0.0	0.0	0.0	2.0	0.0	0.0	0.0	0.3	0.0	0.0	0.0	0.0	0.0	0.0	0.0	0.0	0.0	0.0	0.0	0.0	0.0	47.0	4.1	48.9	2.0	38.8	1.2	0.97	46.8	4.5	48.7														
Bo-31	0.0	0.0	0.0	0.0	0.7	0.0	0.0	0.0	0.7	0.0	0.0	0.0	0.0	0.0	0.0	0.0	0.0	0.0	0.0	0.0	0.0	0.0	34.5	1.2	64.3	0.7	39.6	0.4	0.99	34.3	2.0	63.7														
Bo-32	1.0	0.0	1.0	0.0	0.3	0.0	0.0	0.0	0.3	0.0	0.0	0.0	0.0	0.0	0.0	0.0	0.0	0.3	1.0	0.7	0.3	0.0	59.9	11.1	29.0	1.7	39.0	0.8	0.98	58.2	13.6	28.2														
Bo-33																																												
Bo-34	0.3	0.0	0.7	0.0	0.0	0.0	0.0	0.0	0.0	0.0	0.3	0.0	0.0	0.3	0.0	0.0	0.0	0.0	0.3	0.7	0.0	0.0	56.6	9.2	34.2	0.3	39.8	0.2	0.99	55.6	10.8	33.6														
Bo-35																																												
Bo-36	4.3	3.3	2.3	0.0	0.0	0.0	0.0	0.0	0.0	0.0	0.0	0.0	0.7	0.3	0.0	0.0	0.0	0.3	0.0	0.3	1.0	0.0	64.3	6.6	29.1	8.7	34.3	5.5	0.86	61.7	10.4	27.9														
Bo-37																																	0.13	0.20	85.90	0.19	6.32	1.78	0.02	0.43	0.13	1.29	427	75	124	58	90
Bo-38	2.0	1.3	1.7	0.0	0.0	0.7	0.0	0.0	0.0	0.0	0.0	0.0	0.0	0.3	0.0	0.0	0.0	0.0	0.3	0.3	0.7	0.0	52.6	6.4	41.0	3.3	37.9	2.1	0.95	49.6	9.2	41.1														
Bo-39	3.3	0.0	0.0	0.0	0.0	0.3	0.0	0.0	0.0	0.0	0.0	0.0	0.7	1.7	0.0	0.0	0.0	0.3	0.7	0.0	0.3	0.0	64.8	11.4	23.8	4.3	37.3	2.5	0.94	63.0	13.9	23.1														
Bo-40																																												
Bo-41	5.7	0.0	0.3	0.0	0.0	0.0	0.0	0.0	0.0	0.0	0.0	0.0	0.7	0.3	0.0	0.0	0.0	0.7	0.7	2.3	1.7	0.0	68.7	11.8	19.5	7.0	35.5	4.1	0.90	66.4	14.8	18.8	0.11	< 0,2	85.20	0.25	7.11	1.43	0.02	0.37	0.16	1.30	292	92	204	51	148
Bo-42																																												
Bo-43																																												
Bo-44																																												
Min	*0.0*	*0.0*	*0.0*	*0.0*	*0.0*	*0.0*	*0.0*	*0.0*	*0.0*	*0.0*	*0.0*	*0.0*	*0.0*	*0.0*	*0.0*	*0.0*	*0.0*	*0.0*	*0.0*	*0.0*	*0.0*	*0.0*	*25.7*	*0.0*	*19.5*	*0.0*	*28.6*	*0.0*	*0.71*	*25.6*	*0.0*	*18.8*	*0.1*	*0.2*	*62.0*	*0.2*	*6.3*	*1.2*	*0.0*	*0.3*	*0.1*	*1.3*	*174.0*	*75.0*	*124.0*	*51.0*	*84*
Mean	*1.5*	*0.8*	*0.5*	*0.0*	*0.2*	*0.0*	*0.0*	*0.0*	*1.4*	*0.2*	*0.1*	*0.0*	*0.1*	*0.1*	*0.0*	*0.0*	*0.0*	*0.1*	*0.4*	*0.6*	*0.6*	*0.0*	*50.9*	*7.4*	*41.8*	*2.8*	*38.2*	*1.7*	*0.96*	*48.9*	*10.7*	*40.3*	*1.5*	*3.0*	*78.4*	*0.4*	*9.6*	*3.3*	*0.0*	*0.8*	*0.3*	*1.8*	*553.8*	*112.6*	*1001.6*	*76.9*	*163*
Max	*5.7*	*11.0*	*3.0*	*0.7*	*2.3*	*0.7*	*0.0*	*0.0*	*31.7*	*1.3*	*0.7*	*0.3*	*0.7*	*1.7*	*0.0*	*0.0*	*0.0*	*0.7*	*2.3*	*3.3*	*2.3*	*0.3*	*68.7*	*16.2*	*74.0*	*16.0*	*40.0*	*11.4*	*1.00*	*66.4*	*34.4*	*74.0*	*4.6*	*7.7*	*85.9*	*1.0*	*18.8*	*7.4*	*0.0*	*1.7*	*0.8*	*2.9*	*1371.0*	*166.0*	*5300.0*	*134.0*	*329*

	Sample No.	Core Depth (m)	Stage	Formation		Grain size	Mean GS (ϕ)	Mean GS (mm)	Sorting	Sorting (ϕ)	Sorting (mm)	Skewness	Facies	Facies Association		Helium Porosity (%)	Permeability horizontal (mD)	Comments Plug		Quartz mono	Quartz poly	Plag	K-fsp	PRF	VRF	SRF	Shale	Phyllite	Shist	Quarzite	MRF	Chert	Org. matter	Carbo ripup	Mica	Zirkon	Turmaline	Clay rip-up clast	Opaque	Pyrite	Chlorite	Biotite	Fe-OH inter
Haidberg-1	Ha-1	1010.58	Westph. B	Lower Horst	Depositional parameter	very fine sand	3.4	0.1	moderately well sorted	0.5	0.7	-0.23	fsaS	Lower delta plain	Petrophysical data	2.20	0.0021	massiv	Detrital components (%)	10.7	39.0	0.0	1.3	1.0	1.7	0.0	18.0	1.0	2.7	1.7	0.0	0.0	0.0	17.3	1.3	0.7	0.0	0.0	0.0	0.0	0.0	0.0	0.0
	Ha-2	1016.82	Westph. B	Lower Horst		very fine sand	3.4	0.1	moderately well sorted	0.6	0.7	-0.06	siS	Lower delta plain		3.12	0.0013	single coal layers		7.0	22.7	0.3	1.7	2.3	0.7	0.3	8.7	2.3	3.3	0.0	0.0	0.3	0.0	35.0	3.3	0.0	0.0	0.0	0.0	0.0	0.0	0.0	11.0
	Ha-3	1017.13	Westph. B	Lower Horst									siS	Lower delta plain		4.26	0.0002	massiv																									
	Ha-4	1019.88	Westph. B	Lower Horst		very fine sand	3.2	0.1	well sorted	0.4	0.8	-0.05	saPl	Delta front		7.12	0.0116	minor outbreak		14.3	27.7	3.7	9.0	3.3	2.0	1.3	13.7	1.7	3.3	1.7	0.0	0.0	0.0	5.0	4.3	0.0	0.0	0.0	0.0	0.0	0.0	0.0	0.0
	Ha-5	1020.43	Westph. B	Lower Horst		very fine sand	3.1	0.1	well sorted	0.5	0.7	-0.07	saPl	Delta front		6.35	0.0138	massiv		18.3	29.3	4.0	7.3	2.3	1.0	1.0	17.7	3.7	1.3	1.7	0.0	0.0	0.0	2.0	3.0	0.0	0.0	0.0	0.0	0.0	0.0	0.0	0.3
	Ha-6	1025.76	Westph. B	Lower Horst		medium sand	1.6	0.3	well sorted	0.5	0.7	-0.10	saPl	Delta front		9.49	0.1037	massiv		12.3	31.3	4.0	9.3	5.7	1.7	3.3	7.0	0.7	1.3	4.3	0.0	0.7	0.0	2.0	0.7	0.0	0.0	0.0	0.0	0.0	0.0	0.0	0.0
	Ha-7	1030.67	Westph. B	Lower Horst		fine sand	2.2	0.2	well sorted	0.5	0.7	-0.02	saPl	Delta front		9.43	0.0371	massiv		15.0	27.0	3.3	11.0	4.0	2.0	1.3	9.7	1.7	1.7	3.7	0.0	0.0	0.0	3.7	2.0	0.0	0.0	0.3	0.3	0.0	0.0	0.0	0.0
	Ha-8	1032.37	Westph. B	Lower Horst		fine sand	2.2	0.2	moderately well sorted	0.5	0.7	-0.17	saPl	Delta front		9.30	0.0457	massiv		12.3	30.0	4.7	14.3	4.0	1.3	2.7	11.7	2.0	1.3	2.0	0.0	0.0	0.0	2.7	3.0	0.0	0.0	0.0	0.0	0.0	0.0	0.0	0.3
	Ha-9	1034.56	Westph. B	Lower Horst		medium sand	1.9	0.3	well sorted	0.5	0.7	-0.18	saPl	Delta front		11.11	0.1474	fracture		10.0	33.3	4.0	8.0	4.3	2.3	2.3	7.3	0.7	2.3	2.3	0.0	0.0	0.0	1.3	0.7	0.0	0.0	0.0	0.0	0.0	0.0	0.0	1.3
	Ha-10	1038.41	Westph. B	Lower Horst		fine silt	6.2	0.0	moderately sorted	0.7	0.6	0.12	siPl	Lower delta plain		3.63	4.5751	coal layers		10.7	21.3	1.3	1.3	0.3	0.0	0.7	18.7	0.0	1.3	0.0	0.0	0.0	0.0	32.7	3.3	0.0	0.0	0.0	0.0	0.0	0.0	0.0	1.7
	Ha-11	1038.49	Westph. B	Lower Horst		coarse silt	4.4	0.0	moderately well sorted	0.6	0.7	-0.08	siPl	Lower delta plain		3.98	0.0019	massiv		19.7	32.3	0.7	3.0	1.0	2.0	0.7	31.3	2.0	1.0	0.3	0.0	0.0	0.0	1.0	3.3	0.3	0.0	0.0	0.0	0.0	0.0	0.0	0.3
	Ha-12	1040.02	Westph. B	Lower Horst		coarse silt	4.1	0.1	moderately well sorted	0.5	0.7	-0.06	siPl	Lower delta plain		4.08	0.0016	massiv		12.0	33.3	0.7	5.7	0.3	1.3	1.7	27.7	1.0	0.3	0.0	0.0	0.3	0.0	7.0	4.7	0.0	0.0	0.0	0.0	0.0	0.0	0.0	1.3
	Ha-13	1040.06	Westph. B	Lower Horst									siPl	Lower delta plain		3.83	0.0042	massiv																									
	Ha-14	1159.49	Westph. B	Upper Essen		very fine sand	3.6	0.1	moderately well sorted	0.5	0.7	-0.13	siWl	Lower delta plain		3.60	0.0063	massiv		10.0	34.0	0.7	3.7	0.3	1.3	1.7	19.0	0.3	0.7	1.3	0.0	0.7	3.0	16.0	3.7	0.3	0.0	0.0	0.0	0.0	0.0	0.0	0.3
	Ha-15	1161.98	Westph. B	Upper Essen									siR	Wetlands		4.40	0.1037	massiv																									
	Ha-16	1163.78	Westph. B	Upper Essen									siR	Wetlands		8.45	0.0691	massiv																									
	Ha-17	1165.96	Westph. B	Upper Essen		coarse silt	4.3	0.0	moderately well sorted	0.7	0.6	-0.13	siPl	Lower delta plain		3.78	0.0001	massiv		12.0	19.0	0.0	1.0	1.3	0.7	0.0	5.7	1.3	1.0	0.3	0.0	0.0	0.3	7.0	3.0	0.3	0.0	0.0	0.0	0.0	0.0	0.3	2.7
	Ha-18	1167.17	Westph. B	Upper Essen		coarse silt	4.5	0.0	moderately well sorted	0.7	0.6	0.06	siPl	Lower delta plain		2.66	0.4085	massiv		4.0	24.7	0.3	0.3	0.3	0.7	0.0	30.7	2.7	1.0	0.3	0.0	0.3	0.7	17.0	10.0	0.0	0.0	0.0	0.0	0.0	0.7	0.3	4.7
	Ha-19	1171.19	Westph. B	Upper Essen		very fine sand	3.6	0.1	moderately well sorted	0.6	0.7	-0.26	siPl	Lower delta plain		2.66	0.0003	massiv		8.7	32.7	1.3	3.0	0.3	0.7	0.7	14.3	3.3	1.0	0.7	0.0	0.0	0.0	21.0	8.0	0.0	0.0	0.0	0.7	0.0	0.3	0.0	0.7
	Ha-20	1177.24	Westph. B	Upper Essen		very fine sand	3.6	0.1	moderately sorted	0.9	0.5	-0.23	saPl	Lower delta plain		4.16	0.0020	massiv		8.7	24.3	1.3	2.7	1.0	2.3	2.0	15.3	1.7	4.0	0.7	0.0	0.3	0.0	22.0	5.7	0.0	0.0	0.0	0.3	0.0	0.3	0.0	3.3
	Ha-21	1179.60	Westph. B	Upper Essen		coarse silt	4.4	0.0	moderately sorted	0.9	0.5	-0.08	mS	Lower delta plain		3.00	0.0451	massiv		6.3	33.3	0.3	3.0	1.0	0.7	2.0	23.0	1.3	1.3	0.0	0.0	0.0	0.0	13.7	8.3	0.0	0.0	0.0	0.0	0.0	0.7	0.0	3.0
	Ha-22	1182.83	Westph. B	Upper Essen		coarse silt	4.2	0.1	moderately well sorted	0.5	0.7	-0.06	siWl	Delta front		2.81	0.0040	massiv		6.0	18.7	1.3	3.0	0.3	0.0	1.0	12.0	1.0	0.7	0.0	0.0	0.0	0.0	38.3	8.7	0.0	0.0	0.0	0.0	0.0	0.0	0.3	6.7
	Ha-23	1183.29	Westph. B	Upper Essen		very fine sand	3.8	0.1	moderately sorted	0.7	0.6	-0.22	saWl	Delta front		4.18	0.0003	massiv		7.0	23.7	0.3	3.0	1.0	0.3	0.7	25.3	1.3	1.7	1.7	0.0	0.0	0.0	21.3	8.0	0.0	0.0	0.0	0.0	0.0	0.0	0.0	3.0
	Ha-24	1185.03	Westph. B	Upper Essen		fine sand	3.1	0.1	moderately well sorted	0.5	0.7	0.00	saWl	Delta front		4.55	0.0058	massiv		9.7	25.3	4.3	7.3	3.3	1.0	0.3	20.0	1.7	2.0	1.3	0.0	0.0	0.0	8.7	5.3	0.0	0.0	0.0	0.0	0.0	0.0	0.0	0.0
	Ha-25	1185.06	Westph. B	Upper Essen		fine sand	3.0	0.1	well sorted	0.5	0.7	-0.16	saWl	Delta front		4.55	0.0058	massiv		11.3	33.3	3.7	7.3	1.3	0.7	2.7	15.0	2.3	2.0	1.0	0.0	0.0	0.0	8.3	5.3	0.0	0.0	0.0	0.0	0.0	0.0	0.0	1.0
	Ha-26	1187.18	Westph. B	Upper Essen		fine sand	2.9	0.1	moderately well sorted	0.5	0.7	0.00	siWl	Lower delta plain		4.47	0.0226	massiv		9.0	30.7	3.3	4.0	1.7	0.7	1.7	12.0	1.3	2.7	1.0	0.0	0.0	0.0	16.0	5.3	0.0	0.0	0.0	0.0	0.0	0.0	0.0	1.7
	Ha-27	1188.72	Westph. B	Upper Essen		very fine sand	3.4	0.1	moderately well sorted	0.5	0.7	0.12	siPl	Lower delta plain		3.36	0.0078	massiv		6.0	29.7	2.7	3.3	2.7	1.3	3.3	19.3	1.0	1.3	1.0	0.0	0.0	0.3	20.3	3.7	0.0	0.0	0.0	0.0	0.0	0.0	0.0	2.0
	Ha-28	1191.45	Westph. B	Upper Essen									siR	Wetlands		4.12	0.0014	massiv																									
	Ha-29	1285.48	Westph. B	Middle Essen		very fine sand	3.8	0.1	well sorted	0.5	0.7	0.04	mR	Wetlands		3.46	0.0007	massiv		10.7	33.0	0.3	2.0	0.0	0.3	0.7	30.7	2.7	1.3	0.0	0.0	0.0	0.0	5.0	8.3	0.3	0.0	0.0	0.0	0.0	0.3	0.0	1.0
	Ha-30	1289.58	Westph. B	Middle Essen		very fine sand	3.0	0.1	moderately well sorted	0.7	0.6	-0.03	saPl	Delta front		4.47	0.0024	massiv		9.7	16.3	2.0	6.3	0.7	1.0	2.7	23.0	7.7	3.0	2.3	0.0	0.3	0.0	12.7	9.7	0.0	0.0	0.0	0.0	0.0	0.3	0.0	0.3
	Ha-31	1293.27	Westph. B	Middle Essen		fine sand	2.1	0.2	moderately well sorted	0.6	0.7	-0.05	saPl	Delta front		8.70	0.0255	massiv		7.3	40.7	2.7	6.0	3.0	1.3	4.3	17.0	1.7	2.3	2.0	0.0	0.0	0.0	2.7	1.7	0.3	0.0	0.0	0.0	0.0	0.0	0.0	0.0
	Ha-32	1298.29	Westph. B	Middle Essen		fine sand	2.3	0.2	well sorted	0.5	0.7	-0.01	saPl	Delta front		7.39	0.0098	massiv		5.0	38.3	2.0	4.3	3.0	1.7	2.0	15.3	1.7	2.7	2.7	0.0	0.0	0.0	7.7	3.7	0.0	0.0	0.0	0.0	0.0	0.0	0.0	0.3
	Ha-33	1300.80	Westph. B	Middle Essen		fine sand	2.2	0.2	well sorted	0.5	0.7	-0.04	saPl	Delta front		6.99	0.0103	massiv		6.3	44.0	1.3	7.3	3.0	0.7	2.7	11.7	2.0	1.3	2.7	0.0	0.0	0.0	3.3	4.7	0.0	0.3	0.0	0.0	0.0	0.0	0.0	0.0
	Ha-34	1300.84	Westph. B	Middle Essen		medium sand	2.0	0.3	moderately well sorted	0.6	0.7	0.00	saPl	Delta front				marginal healed fracture		5.7	39.3	2.0	6.3	2.7	0.3	4.0	18.7	1.0	4.0	1.3	0.0	0.0	0.0	1.7	0.3	0.0	0.0	0.0	0.0	1.3	0.0	0.0	1.0
	Ha-35	1300.91	Westph. B	Middle Essen		medium sand	1.9	0.3	moderately well sorted	0.6	0.7	-0.09	saPl	Delta front		8.32	0.0522	caol layers		4.7	46.0	1.3	5.0	4.7	1.7	3.0	17.0	0.3	1.3	2.0	0.0	0.0	0.0	2.0	1.0	0.0	0.0	0.0	0.0	0.0	0.0	0.0	0.0
	Ha-36	1300.94	Westph. B	Middle Essen									saPl	Delta front		7.44	0.1127	minor caol layers																									
	Ha-37	1303.77	Westph. B	Middle Essen									mS	Lower delta plain		0.31	0.0001	massiv																									
	Ha-38	1305.79	Westph. B	Middle Essen		coarse silt	4.9	0.0	moderately well sorted	0.7	0.6	-0.09	mPl	Lower delta plain		2.32	0.0235	massiv		4.3	29.7	1.0	1.3	0.3	0.0	1.0	21.7	1.0	0.7	0.3	0.0	0.0	0.0	18.0	12.7	0.3	0.0	0.0	0.0	0.0	0.0	0.3	7.0
						Min	*1.6*	*0.0*		*0.4*	*0.5*	*-0.3*				*0.3*	*0.0001*			*4.0*	*16.3*	*0.0*	*0.3*	*0.0*	*0.0*	*0.0*	*5.7*	*0.0*	*0.3*	*0.0*	*0.0*	*0.0*	*0.0*	*1.0*	*0.3*	*0.0*	*0.0*	*0.0*	*0.0*	*0.0*	*0.0*	*0.0*	*0.0*
						Mean	*3.3*	*0.1*		*0.6*	*0.7*	*-0.1*				*5.1*	*0.16*			*9.5*	*30.5*	*1.9*	*4.9*	*2.0*	*1.1*	*1.7*	*17.4*	*1.7*	*1.8*	*1.3*	*0.0*	*0.1*	*0.1*	*12.0*	*4.7*	*0.1*	*0.0*	*0.0*	*0.0*	*0.0*	*0.1*	*0.0*	*1.8*
						Max	*6.2*	*0.3*		*0.9*	*0.8*	*0.1*				*11.1*	*4.58*			*19.7*	*46.0*	*4.7*	*14.3*	*5.7*	*2.3*	*4.3*	*31.3*	*7.7*	*4.0*	*4.3*	*0.0*	*0.7*	*3.0*	*38.3*	*12.7*	*0.7*	*0.3*	*0.3*	*0.7*	*1.3*	*0.7*	*0.3*	*11.0*

Sample No.	Authigenic components (%)																	Optical porosity (%)					Additional information										Geochemical data														
	Qzo	Sid inter	Sid intra	Cc non-ferroan	Ferroan cc	Quartz intra	Dolo non-ferroan	Ferroan dolo	Carbo rpl	Early rpl kao	Late rpl kao	Kao pore-filling	Ill rpl kaol	Illite inter	Illite rpl fsp	Illite pore-linening	Frac-filling carbonate	Frac-filling sulfide	Primary porosity	Sec. poro Kfs	Sec. poro RF	Fracture porosity	Sec. poro Plag	Q	F	R	IGV (%)	COPL	CEPL	Icompact	Recon Q	Recon F	Recon R	CO3 therm	CaCO3 therm	SiO2 (%)	TiO2 (%)	Al2O3 (%)	Fe2O3 (%)	Cr2O3 (%)	MgO (%)	CaO (%)	K2O (%)	MnO (ppm)	SrO (ppm)	BaO (ppm)	Rb2O (ppm)	ZRO2 (ppm)
Ha-1	1.0	0.3	0.3	0.0	0.3	0.0	0.0	0.0	0.0	0.0	0.7	0.0	0.0	0.0	0.3	0.0	0.0	0.0	0.0	0.3	0.3	0.0	0.0	54.4	1.4	44.2	1.7	39.0	1.0	0.97	53.5	3.1	43.4	0.91	1.50	80.60	0.46	8.03	3.20	0.02	0.82	0.41	1.26	518	98	215	58	248
Ha-2	0.0	0.3	0.0	0.0	0.3	0.0	0.0	0.0	0.0	0.0	0.0	0.0	0.0	0.0	0.0	0.0	0.0	0.0	0.0	0.3	0.0	0.0	0.0	35.4	2.4	62.2	0.7	39.6	0.4	0.99	35.3	2.7	62.0															
Ha-3																																															
Ha-4	1.7	1.3	1.7	0.0	0.0	0.0	0.0	0.0	0.3	0.0	0.7	0.0	0.3	0.0	0.0	0.0	0.0	0.0	0.0	1.7	1.0	0.0	0.3	50.4	14.6	35.0	3.0	38.1	1.9	0.95	47.8	19.0	33.2															
Ha-5	1.0	0.3	0.0	0.0	0.3	0.0	0.0	0.0	1.3	0.7	0.7	0.0	0.3	0.0	0.0	0.0	0.0	0.0	0.0	1.3	1.0	0.0	0.0	55.0	12.6	32.3	1.7	39.0	1.0	0.97	52.7	16.4	31.0															
Ha-6	5.0	0.3	1.0	0.0	0.3	0.0	0.0	0.0	2.7	2.3	0.7	0.0	0.0	0.0	0.0	0.0	0.0	0.0	0.0	2.0	0.3	0.0	1.0	58.2	15.9	25.9	5.7	36.4	3.6	0.91	52.1	24.6	23.2	1.07	1.80	81.70	0.24	8.50	2.01	0.02	0.55	0.59	2.11	558	159	302	79	109
Ha-7	2.0	0.7	1.7	0.0	0.0	0.0	0.0	0.0	1.7	3.3	0.7	0.0	0.0	0.0	0.3	0.0	0.0	0.0	0.0	0.7	0.7	0.0	1.7	54.2	17.0	28.9	2.7	38.4	1.6	0.96	48.4	25.8	25.8															
Ha-8	0.7	0.3	0.3	0.0	0.0	0.0	0.0	0.0	0.7	1.7	1.7	0.0	0.0	0.0	0.0	0.0	0.0	0.0	0.0	1.7	0.3	0.0	0.3	49.8	21.3	28.8	1.0	39.4	0.6	0.98	46.5	26.6	26.9															
Ha-9	3.3	0.0	0.7	0.0	0.0	0.0	0.0	0.0	2.0	4.0	1.3	0.0	0.0	0.0	0.0	0.0	3.7	1.0	0.3	1.3	1.3	0.0	0.7	58.3	15.3	26.4	3.7	37.7	2.1	0.95	51.7	24.9	23.4															
Ha-10	0.0	0.0	0.0	0.0	0.0	0.0	0.0	0.0	0.7	0.0	0.0	0.0	0.0	0.0	0.0	0.0	3.0	2.3	0.0	0.3	0.3	0.0	0.0	36.2	3.0	60.8	0.0	40.0	0.0	1.00	35.8	4.1	60.1															
Ha-11	0.0	0.0	0.3	0.0	0.0	0.0	0.0	0.0	0.0	0.0	0.0	0.0	0.0	0.0	0.0	0.0	0.0	0.0	0.0	0.3	0.0	0.0	0.3	55.1	3.9	41.1	0.0	40.0	0.0	1.00	54.5	4.9	40.6															
Ha-12	0.3	0.3	0.0	0.0	0.0	0.0	0.0	0.0	2.0	0.0	0.0	0.0	0.0	0.0	0.0	0.0	0.0	0.0	0.0	0.0	0.0	0.0	0.0	50.0	6.9	43.1	0.7	39.6	0.4	0.99	48.9	8.9	42.1	0.45	0.70	73.90	0.70	13.00	2.82	0.02	0.80	0.34	2.40	335	170	405	115	297
Ha-13																																															
Ha-14	0.3	1.7	0.3	0.0	0.0	0.0	0.0	0.0	0.3	0.0	0.3	0.0	0.0	0.0	0.0	0.0	0.0	0.0	0.0	0.0	0.0	0.0	0.0	51.3	4.8	43.9	2.0	38.8	1.2	0.97	50.7	5.9	43.4	2.83	4.70	70.80	0.52	9.37	6.89	0.02	1.64	0.36	1.31	1174	103	175	60	250
Ha-15																																															
Ha-16																																															
Ha-17	0.0	0.0	0.0	0.0	38.3	0.0	0.0	0.0	5.7	0.0	0.0	0.0	0.0	0.0	0.0	0.0	0.0	0.0	0.0	0.0	0.0	0.0	0.0	63.5	2.0	34.5	38.3	2.7	37.3	0.07	57.0	12.1	30.9	34.23	57.10	33.40	0.34	7.63	3.34	0.02	10.70	16.10	0.93	859	136	392	43	146
Ha-18	0.0	0.0	0.0	0.0	0.0	0.0	0.0	0.0	0.0	1.0	0.0	0.0	0.0	0.0	0.0	0.0	0.0	0.0	0.0	0.0	0.0	0.0	0.3	35.6	0.8	63.6	0.0	40.0	0.0	1.00	35.1	2.4	62.5															
Ha-19	0.3	0.7	0.3	0.0	0.0	0.0	0.0	0.0	0.7	0.3	0.3	0.0	0.0	0.0	0.0	0.0	0.0	0.0	0.0	0.0	0.0	0.0	0.0	47.9	4.9	47.1	1.0	39.4	0.6	0.98	47.0	6.7	46.3															
Ha-20	0.0	0.7	1.7	0.0	0.0	0.0	0.0	0.0	0.0	1.3	0.0	0.0	0.0	0.0	0.0	0.0	0.0	0.0	0.0	0.0	0.3	0.0	0.0	39.4	4.6	56.0	0.7	39.6	0.4	0.99	38.1	7.8	54.1															
Ha-21	0.0	0.3	0.0	0.0	0.0	0.0	0.0	0.0	0.7	0.3	0.0	0.0	0.0	0.0	0.0	0.0	0.0	0.0	0.0	0.3	0.0	0.0	0.3	46.1	3.9	50.0	0.3	39.8	0.2	0.99	45.2	5.7	49.0															
Ha-22	0.0	0.0	0.0	0.0	1.0	0.0	0.0	0.0	0.0	0.3	0.3	0.0	0.0	0.0	0.0	0.0	0.0	0.0	0.0	0.0	0.3	0.0	0.0	30.0	5.3	64.8	1.0	39.4	0.6	0.98	29.7	6.0	64.3															
Ha-23	0.0	0.0	0.3	0.0	0.3	0.0	0.0	0.0	0.0	0.7	0.0	0.0	0.0	0.0	0.0	0.0	0.0	0.0	0.0	0.3	0.0	0.0	0.0	37.0	3.8	59.2	0.3	39.8	0.2	0.99	36.5	5.3	58.3															
Ha-24	0.7	0.3	2.0	0.0	0.0	0.0	0.0	0.0	0.0	1.3	2.0	0.0	0.0	0.0	0.0	0.0	1.0	0.0	0.0	1.3	0.3	0.0	0.7	42.7	13.7	43.5	1.0	39.4	0.6	0.98	39.4	20.6	40.1	1.42	2.40	75.00	0.52	11.20	3.48	0.02	0.91	0.70	1.61	723	130	123	75	328
Ha-25	0.0	0.0	1.3	0.0	0.0	0.0	0.0	0.0	0.0	0.7	0.7	0.0	0.0	0.0	0.0	0.0	0.7	0.0	0.0	1.0	0.0	0.3	0.0	51.3	12.4	36.3	0.0	40.0	0.0	1.00	49.3	15.8	34.9															
Ha-26	0.0	1.0	1.3	0.0	0.0	0.0	0.0	0.0	0.3	1.0	1.7	0.0	0.3	0.0	0.0	0.0	3.0	0.0	0.0	0.0	0.0	0.0	0.3	48.4	8.7	42.9	1.0	39.4	0.6	0.98	45.9	13.5	40.6															
Ha-27	0.0	0.0	0.3	0.0	0.0	0.0	0.0	0.0	0.0	0.7	0.0	0.0	0.0	0.0	0.0	0.0	0.7	0.0	0.0	0.3	0.0	0.0	0.0	39.9	6.5	53.6	0.0	40.0	0.0	1.00	39.3	7.9	52.9															
Ha-28																																		0.68	1.10	69.90	0.87	15.60	2.84	0.02	1.01	0.51	2.63	418	141	444	126	344
Ha-29	0.0	0.3	1.3	0.0	0.0	0.0	0.0	0.0	0.0	0.7	0.7	0.0	0.0	0.0	0.0	0.0	0.0	0.0	0.0	0.0	0.3	0.0	0.0	50.4	2.7	46.9	0.3	39.8	0.2	0.99	48.9	5.6	45.5															
Ha-30	0.3	0.0	0.3	0.0	0.0	0.0	0.0	0.0	0.0	0.3	0.3	0.0	0.0	0.0	0.3	0.0	0.0	0.0	0.0	0.3	0.0	0.0	0.0	32.7	9.5	57.8	0.3	39.8	0.2	0.99	32.1	11.2	56.7	0.75	1.20	74.00	0.58	12.80	3.05	0.02	0.86	0.29	2.67	638	55	507	54	175
Ha-31	1.0	0.0	0.7	0.0	0.0	0.3	0.0	0.0	0.0	0.0	2.0	0.0	0.0	0.0	0.3	0.0	0.0	0.0	0.0	1.3	0.7	0.0	0.7	54.9	9.5	35.5	1.0	39.4	0.6	0.98	52.1	14.2	33.7															
Ha-32	1.3	2.0	2.7	0.0	0.0	0.0	0.0	0.0	2.3	0.0	0.0	0.0	0.0	0.0	0.7	0.0	0.0	0.0	0.0	0.0	0.3	0.0	0.3	53.3	7.3	39.4	3.3	37.9	2.1	0.95	49.8	13.4	36.8	3.19	5.30	74.50	0.37	8.58	4.44	0.02	1.09	2.01	1.72	1511	60	391	37	104
Ha-33	1.3	0.0	0.7	0.0	0.3	0.3	0.0	0.0	2.7	0.0	0.0	0.0	0.0	0.0	0.3	0.0	0.0	0.0	0.0	2.0	0.7	0.0	0.3	61.4	10.0	28.6	1.7	39.0	1.0	0.97	57.4	15.9	26.7															
Ha-34	1.7	0.0	0.3	0.0	0.0	0.3	0.0	0.0	4.3	0.0	0.3	0.0	0.0	0.0	0.0	0.0	1.7	0.7	0.0	0.3	0.3	0.0	0.3	53.3	9.6	37.2	3.0	38.1	1.9	0.95	50.0	15.1	34.9															
Ha-35	2.3	0.0	0.0	0.0	0.0	0.7	0.0	0.0	2.7	0.0	1.0	0.0	0.0	0.3	0.7	0.3	0.0	0.0	0.0	0.3	1.3	0.0	0.3	59.2	7.1	33.7	3.0	38.1	1.9	0.95	56.0	12.1	31.9															
Ha-36																																															
Ha-37																																															
Ha-38	0.0	0.0	0.0	0.0	0.0	0.0	0.0	0.0	0.0	0.3	0.0	0.0	0.0	0.0	0.0	0.0	0.0	0.0	0.0	0.0	0.0	0.0	0.0	43.3	2.9	53.8	0.0	40.0	0.0	1.00	43.1	3.3	53.6															
Min	*0.0*	*0.0*	*0.0*	*0.0*	*0.0*	*0.0*	*0.0*	*0.0*	*0.0*	*0.0*	*0.0*	*0.0*	*0.0*	*0.0*	*0.0*	*0.0*	*0.0*	*0.0*	*0.0*	*0.0*	*0.0*	*0.0*	*0.0*	*30.0*	*0.8*	*25.9*	*0.0*	*2.7*	*0.0*	*0.07*	*29.7*	*2.4*	*23.2*	*0.5*	*0.7*	*33.4*	*0.2*	*7.6*	*2.0*	*0.02*	*0.6*	*0.3*	*0.9*	*335.0*	*55.0*	*123.0*	*37.0*	*104.0*
Mean	*0.8*	*0.4*	*0.6*	*0.0*	*1.3*	*0.1*	*0.0*	*0.0*	*1.0*	*0.7*	*0.5*	*0.0*	*0.0*	*0.0*	*0.1*	*0.0*	*0.4*	*0.1*	*0.0*	*0.6*	*0.3*	*0.0*	*0.3*	*48.3*	*7.9*	*43.8*	*2.5*	*38.0*	*2.0*	*0.95*	*46.1*	*11.7*	*42.2*	*5.1*	*8.4*	*70.4*	*0.5*	*10.5*	*3.6*	*0.02*	*2.0*	*2.4*	*1.8*	*748.2*	*116.9*	*328.2*	*71.9*	*222.3*
Max	*5.0*	*2.0*	*2.7*	*0.0*	*38.3*	*0.7*	*0.0*	*0.0*	*5.7*	*4.0*	*2.0*	*0.0*	*0.3*	*0.3*	*0.7*	*0.3*	*3.7*	*2.3*	*0.3*	*2.0*	*1.3*	*0.3*	*1.7*	*63.5*	*21.3*	*64.8*	*38.3*	*40.0*	*37.3*	*1.00*	*57.4*	*26.6*	*64.3*	*34.2*	*57.1*	*81.7*	*0.9*	*15.6*	*6.9*	*0.02*	*10.7*	*16.1*	*2.7*	*1511.0*	*170.0*	*507.0*	*126.0*	*344.0*

8 Addendum

Addendum A – Compressional wave velocity

A study was was conducted to compare the compressional wave velocity (v_P) measurements using a Proceq Pundit 200 device at 54 kHz (with coupling paste) and a stationary device (DMA Netzsch Gabo “Eplexor 500N”, Technische Petrophysik) at 1 MHz on tight sandstone plugs (diameter ~25.4 mm). Results show that most data points closely follow the 1:1 correlation at lower velocities (grey line, Fig. 8.1). As velocities increase, data points tend to fall above this line, suggesting that the stationary device systematically records higher velocities (Fig. 8.1). Overall, the 1-inch (~25.4 mm) core plugs of tight sandstones measured with a Proceq Pundit 200 show good agreement between the two methods but reveal a systematic bias.

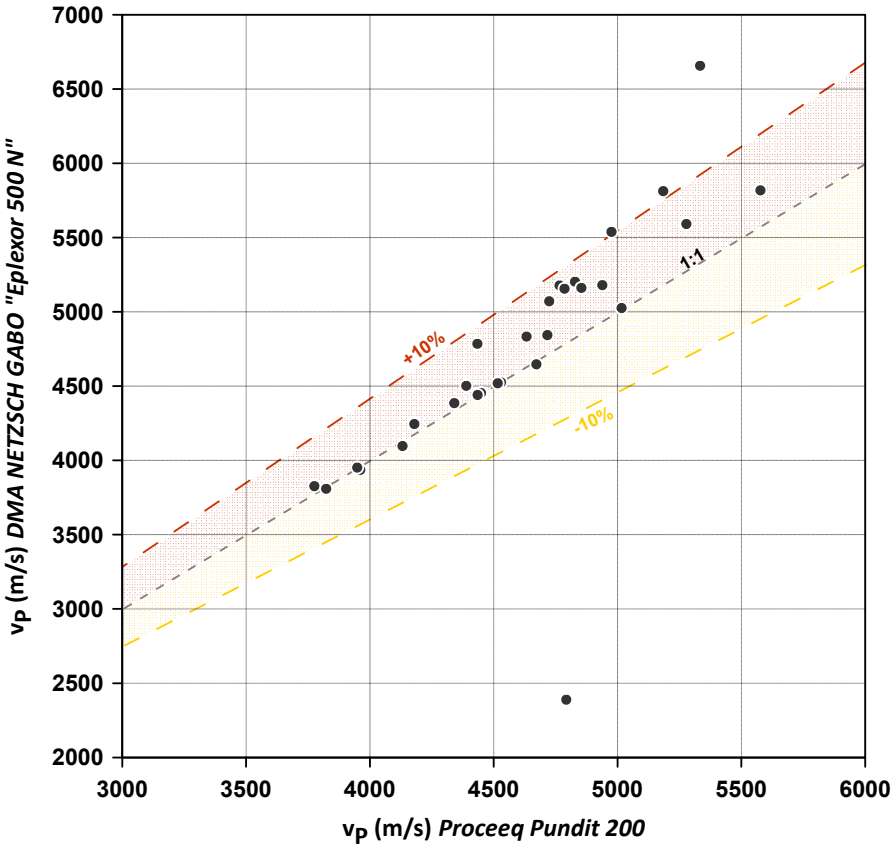

Figure 8.1 Comparison of compressional (P) wave velocity (v_P) measurements obtained using a Proceq Pundit 200 device (with coupling paste) and a stationary device (DMA Netzsch Gabo “Eplexor 500N”, Technische Petrophysik) on 1-inch plugs of tight sandstone. The grey line represents the ideal 1:1 correlation. While most data points are close to the correlation line at lower velocities, the stationary device generally records higher velocities as velocity increases. The observed deviations and outliers suggest potential influences from material properties, coupling conditions, or waveform conversion effects.

Core plug diameters pose significant limitations on the compressional wave velocity measurements, as shown by Kummerow (2006) shown in Fig. 8.2. The longer wavelength at 54 kHz should, in theory, reduce attenuation effects from grain boundaries, making it suitable for bulk velocity measurement (Fig. 8.2 B). Additionally, sidewall reflections, which are a major issue in small-diameter samples at higher frequencies (1 MHz or more), are generally less significant at lower frequencies. However, the correlation between frequency and sample diameter (Fig. 8.2 A) suggests that lower frequencies require larger sample diameters to produce a resolvable signal. At 54 kHz, the required sample diameter for a clear P-wave signal must be larger than 1 inch (~25.4 mm) (Kummerow, 2006) otherwise, the signal would not be physically resolvable. Since the sample diameter used in this study (1 inch) is too small for the applied low frequency, the direct P-wave phase may be superimposed by noise or sidewall reflections, suggesting that the measured velocity does not represent a true bulk rock property.

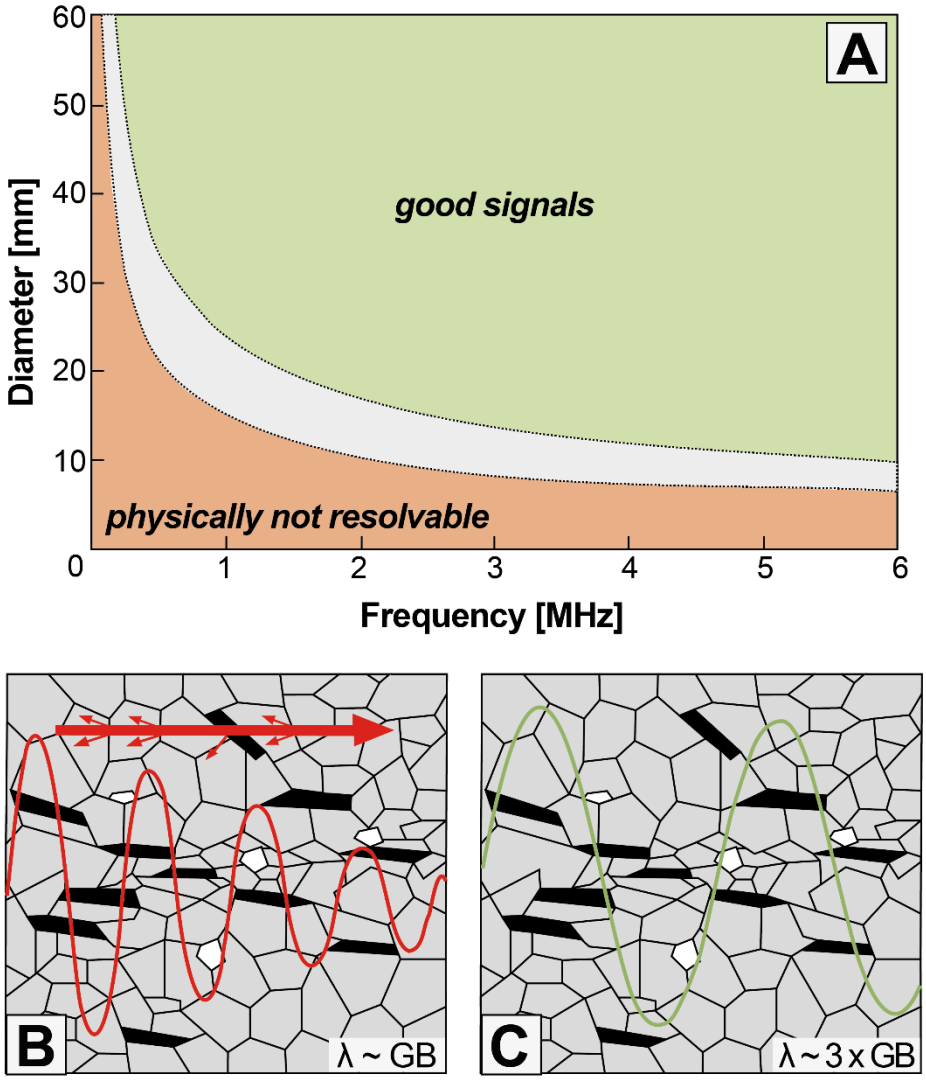

Figure 8.2 (**A**) The minimum usable sample diameter for a given compressional wave velocity (v_P) depends on the applied frequency, where a critical d^2/λ ratio was derived from tests on Al and Al_2O_3 rods (Kummerow, 2006). (**B**) The effect of grain boundaries (GB) at the micrometer scale, where wavelengths comparable to grain size cause strong

signal attenuation due to energy scattering. (**C**) To minimize attenuation, the wavelength λ should be at least three times the grain size. Images modified after Kummerow (2006).

However, the calibration (Fig. 8.1) shows that the Pundit 200 device at 54 kHz for 1-inch tight sandstone plugs provides reasonable results within a 10% variation. To improve measurement accuracy at 54 kHz, a larger sample diameter may be used.

Addendum B – X-ray fluorescence (XRF)

The calcium carbonate content ($CaCO_3$) determined via XRF is estimated based on the measured calcium content (Ca). However, this value can only be directly attributed to $CaCO_3$ if the sample consists exclusively of calcium carbonate or components with known compositions. Hydroxyl groups in such compounds are indirectly accounted for through the oxygen and hydrogen signals, but they are not specifically detected by the XRF system, which measures only elemental concentrations (e.g., Ca, Si, P) but not functional groups like hydroxyl (-OH). Consequently, the quantitative assignment of calcium to a specific phase (e.g., $CaCO_3$) relies either on calculations or on assumptions based on the mineralogical composition of the sample. In this study the $CaCO_3$ concentration was determined thermally. As a result, siderite is not included because it decomposes at 550°C, whereas calcite remains thermally stable (Bisutti et al., 2007). However, other carbonates (e.g., dolomite, siderite) and abundant clay minerals can affect the results, leading to an overestimation of $CaCO_3$ content, as heating to 1050°C induces various reactions (i.e., clay minerals lose structurally bound water and may transform into amorphous phases or mullite; hydroxides decompose into oxides and H_2O; gypsum looses crystalline water and converts into anhydrite, organic material combusts completely) which can alter the mineralogical composition and, consequently, affect the analytical data.